Transport of Turbulence in the Solar Wind

A thesis
submitted in partial fulfilment
of the requirements for the Degree
of
Master of Science in Mathematics
at
The University of Waikato
by

Mark Bishop

THE UNIVERSITY OF
WAIKATO
Te Whare Wānanga o Waikato

2022

Abstract

Charged particles are ejected from the sun and transported radially outward to the edge of the solar system, this plasma is called the solar wind. In the solar wind, turbulent fluctuations and waves form, and their transport can be modelled using the Magnetohydrodynamic (MHD) equations. This thesis displays several different options for building an MHD turbulence model including nonlinear phenomenologies, and turbulence source driving like interstellar pickup ions and velocity shear. The options are extended from existing models that express a range of variables from the forward and backward propagating energies, the energy difference and the respective correlation lengths. Nonlinear phenomenologies are built from analogies to Hydrodynamic (HD) von Kármán-Taylor phenomenologies extended to MHD. Additional phenomenological models are needed for the energy difference (and its correlation length). These models are evaluated from 0.29 to 100 AU, analytically where possible, otherwise numerical solutions are sought after and compared to simulation data, and satellite data obtained from the Helios 2, Ulysses and Voyager 2 spacecraft.

Acknowledgements

I would like to thank my supervisor, Professor Sean Oughton for providing me with the opportunity to do this research. Working with you has been an absolute blast. I would also like to thank my parents for their continual support, this would not be possible without you. Lastly, thank you to my Nana and late Grandad for their encouragement and support. Also, thank you to Dr Laxman Adhikari for providing us with most of the observational data used in this thesis.

Contents

List of Acronyms

HD	Hydrodynamic
MHD	Magnetohydrodynamic
KAW	Kinetic Alfvén Wave
AU	Astronomical Units
ODE	ordinary differential equation
PDE	partial differential equation
RHS	right hand side
LHS	left hand side

Chapter 1

Introduction

The existence of the solar wind was first predicted by Parker [45] in 1958. There have since been many observations that have confirmed the solar wind existence from direct in-situ spacecraft observations [27, 48, 49]. We can also observe the solar wind acting on objects in the solar system, like comet tails [11, 17] and can even see the effects of the solar wind on earth, via the auroras [30, 47]. The solar wind is commonly modelled using an MHD turbulence approximation which seems to agree with the spacecraft observations. Much like HD turbulence, there is a great degree of complexity surrounding MHD turbulence. The addition of the magnetic field to the turbulence modelling adds significant complexity. There are still many important mysteries the solar wind holds with regards to both itself, in the purest sense, and to MHD turbulence, so much so, that both NASA and ESA have recently launched spacecraft (the Parker Solar Probe in 2018 and the Solar Orbiter in 2020 respectively) with the missions of investigating various solar wind and sun phenomena. Both the Parker Solar Probe [2, 6, 56, 65] and the Solar Orbiter [3, 56] have provided more evidence for the MHD turbulence in the solar wind and have started to help expound on the complex interactions present.

There have been many attempts to model and evaluate the solar wind using MHD models. Matthaeus et al. and Breech et al. provide some numerical [13, 35] and analytical [36] solutions to a simplified five (and three) equation model [66]. Adhikari et al. [1, 4] provides numerical solutions to a six equation model constructed with the assistance a Cauchy-Schwarz inequality [19, 62]. These models have a degree of variability between them providing ambiguity in the behaviour of the modelled solar wind, particularly with the nonlinear dissipation terms. These nonlinear terms end up having a big effect on the behaviour of the turbulence [26].

The aim of this thesis is to develop and examine the behaviour of some solar wind models commonly proposed in the literature [1, 13, 35], along with some additional nonlinear models. These models should describe the transport of the turbulence, characterised via the energy fluctuations and their correlation lengths, over the radial distance out to the edge of the solar system, matching the in-situ observations from the Helios 2, Ulysses and Voyager 2 satellites, and qualitatively, the simulation data.

Chapter 2 will focus on the background of this thesis; providing context to the solar wind as it is emitted from the Sun. Then, delving into the typical turbulence characteristics for an HD fluid that can be extended to the solar wind flow via the MHD approximation.

Chapter 3 (with the addition of Appendices A to D) introduces the equations we will be using to model the solar wind. The resulting model is expressed as a set of six coupled, nonlinear ordinary differential equations. The nonlinear terms will be discussed in depth as their modelling is integral to the behaviour of the solar wind, likewise for the source driving terms. Lastly, the model for the temperature is introduced with motivation, adding an additional ordinary differential equation to the solar wind model.

Chapter 4 will examine some simulation data to help provide estimations for the behaviour of the MHD turbulence. Additionally, in-situ observational data will be looked at and used to verify the models in the subsequent chapters.

In Chapter 5, the six equation solar wind model will be reduced appropriately until analytical solutions can be found. The analytical solutions will be discussed in the context of the behaviour seen in the observational data. In this chapter, we have found sets of nonlinear and linear solutions.

Chapter 6 will evaluate the numerical solutions for the full six equation (plus one for the temperature), solar wind models. We will be iterating over various nonlinear and source driving models and discussing their effects on the behaviour of the evolution of the solar wind.

Lastly, Chapter 7 summarises our results and conclusions.

Chapter 2

Solar Wind Background

This section discusses the context for this thesis; the origin of the solar wind and its evolution via turbulent processes as it spreads out across the solar system.

2.1 The Sun and the Solar Wind

The solar wind is a flow of plasma that exudes from the sun due to the overwhelming difference between the gravitational and magnetic forces holding the plasma in the atmosphere of the sun (the corona) and the outward pressure gradient of space *i.e.,* the large difference in the pressures between interstellar space and the sun's atmosphere. The solar wind streams off the sun, mostly radially in all directions, and is an electrically neutral, fully ionized plasma of low density (see section 4.2). The solar wind ends at the edge of the solar system (called the heliosphere) after the density (of the solar wind) has fallen off so much that velocity decreases dramatically (the termination shock) and clashes with the plasma from interstellar space.

Due to the highly electrically conductive solar wind, magnetic field lines are implanted and frozen into the outward flow of plasma. As the sun rotates, and the solar wind continues expanding radially, the magnetic field is dragged along and twists into a large Archimedean-like spiral (the Parker Spiral [45]). The Parker Spiral forms an appropriate model for the behaviour of the large-scale magnetic field. The angle between the solar wind radial direction and the magnetic field is around 45° at Earth's distance (1 Astronomical Units (AU)) and 89° at the edge of the heliosphere (75-100 AU, Figure 2.1). The equation for the Parker Spiral [45], expressed in spherical polar coordinates is the following

$$B_r(r,\theta,\phi) = B_0 \left(\frac{R_0}{r}\right)^2 \tag{2.1}$$

$$B_\theta(r,\theta,\phi) = 0 \tag{2.2}$$

$$B_\phi(r,\theta,\phi) = B_0 \left(\frac{\Omega R_0}{U}\right) \left(\frac{r}{R_0} - 1\right) \left(\frac{R_0}{r}\right)^2 \sin\theta \tag{2.3}$$

where Ω is the angular velocity of the sun, U is the outward (radial) velocity and R_0 is the point where beyond that distance, the solar gravitation and outward acceleration by high coronal pressure is neglected. Figure 2.2 shows an example of the large-scale magnetic fields in the solar wind at different speeds, along with the approximate orbit of Earth and Mars.

This thesis is interested in the solar wind as it evolves as it travels through to the edge of the heliosphere (75-100 AU).

2.2 Taking Data from Space

Understanding how measurements are taken from spacecraft is useful to understanding some of the decisions related to composing the quantities in the later sections of this thesis (subsection 3.1.1). The first question to ask is; how do we measure turbulent eddies? As a time series, the flow of a fluid is measured from sensors record useful properties of a fluid; for example the temperature or the velocity. The fluid velocity field changes in both position and time, in order to properly reconstruct the full turbulence correlations from the measurements between any two points in the relevant region, a mesh of sensors would be required to measure the velocity at each point in time at each point in space. This is impractical so instead, we assume there is a strong mean flow and use a frozen-in flow approximation (Taylor's Hypothesis [55]); the

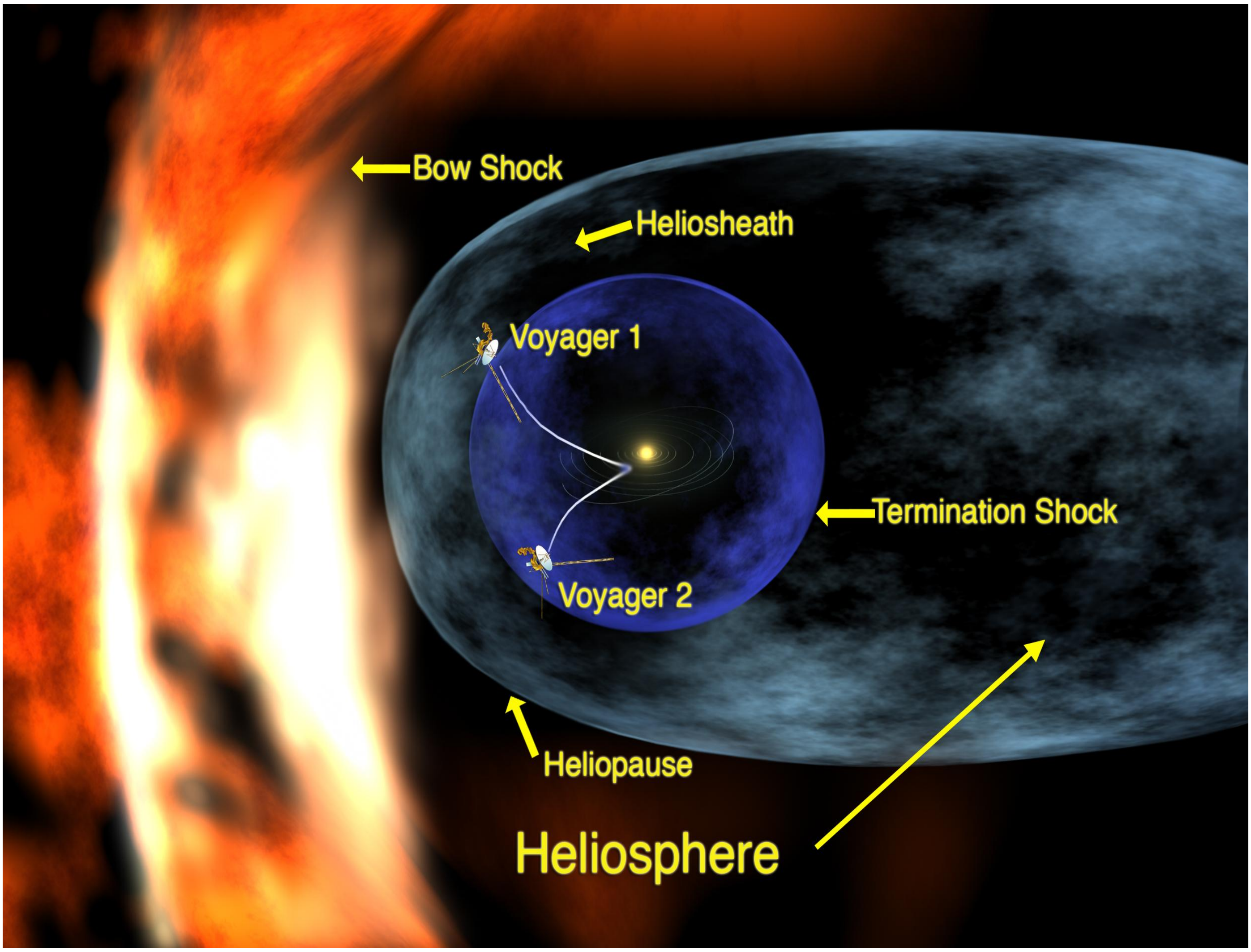

Figure 2.1: Depiction of the solar system encased in the heliosphere as it travels through interstellar space. Taken from [39].

Figure 2.2: Diagram of the magnetic field in fast (1000 [km/s], purple) and slow (400 [km/s], blue) solar wind, stretching out to 2 AU.

fluid transport is due solely to the large scale motion (advection due to the small-scale turbulence is small and therefore neglected). The numbers of sensors can be reduced to one that captures the velocity (and temperature) as the *steady* turbulent eddy flows past at the mean speed. A correlation with spatial lag can now be constructed as a correlation with time lag instead; however, this still only allows for correlations to be taken in a single direction, in the direction of the mean flow. Therefore, in the solar wind with one spacecraft measuring a frozen-in flow, correlations between two points in the fluctuating field can only be constructed in the radial direction (as the solar wind is primarily radially expanding). There are a couple of sets of satellites that fly in groups, for example NASA's Magnetospheric Multiscale (MMS) Mission uses four spacecraft flying in a tetrahedral formation. These MMS spacecraft (and others) can be used to construct correlations in different directions. Unfortunately they will not be relevant to this thesis as they fly in an orbit around Earth, popping in and out of the magnetosphere. Whereas we are interested in the solar wind as it is transported out to the edge of the solar system.

2.3 Turbulence

A turbulent flow does not have an exact definition but can typically be recognized by a few key characteristics. The two main features of a turbulent flow we will talk about are the irregularity and the energy cascade. The turbulence is the motion of a fluid characterized by chaotic changes in the pressure/temperature and velocity. Even though the turbulence is chaotic, it is deterministic and can be fully described by the Navier-Stokes equations, along with Maxwell's equations in the case of MHD (Appendix A). Turbulence is dissipative, meaning the energies in the smallest eddies transition into internal energy (temperature). The smallest eddies receive their energies from the slightly larger eddies and so on until the largest eddies receive their energy from the bulk motion. The process of the transfer of energy from the bulk motion to the smallest scales is called the *energy cascade*.

2.3.1 The Energy Cascade

The energy cascade defines the transfer of the energy from the largest scale to the smallest scales. This process requires nonlinear couplings and local, transfer of energy from one scale to the next smallest scales. Once the structures are small enough, molecular diffusion becomes a factor and the dissipation of energy can take place. The energy spectrum, $E(k)$, is a key quantity in discussion and modelling of the energy cascade. It has dimensions of energy per wavenumber and can be interpreted as just that: the energy per wavenumber associated with scales of order $1/k$. The total energy is given by $\int_0^\infty E(k)\,\mathrm{d}k$.

In HD, the energy cascade stops when the turbulent structures are small enough for molecular diffusion. In MHD theory, there are multiple scales where the energy dissipation can occur resulting from the proton and electron (in the ionized hydrogen). Current theories predict, once the MHD cascade reaches the proton gyroradius, a transition occurs from the MHD scheme to a new Kinetic Alfvén Wave (KAW) scheme. At this point, we can say that the energy has dissipated from the perspective of MHD; however the energy might not be fully transitioned into the temperature at the proton gyroradius scale. KAW might carry some of the energy to even smaller scales like the electron gyroradius. For the purposes of this thesis, we are ignoring the effects of the KAW in the solar wind and focusing solely on an MHD approximation.

In terms of the cascade, the energy spectrum is roughly divided up into three ranges (see Figure 2.3 where k is the wave number and proportional to 1/length scale), the range for the energy containing eddies, the inertial subrange and lastly, the dissipation range. The energy containing range (occurring around the integral length scale L) carries most of the energy in the turbulence. It extracts energy from the mean flow and passes it onto the smaller scales. The dissipation range is where scales are smaller than those characteristic of dissipation, denoted with a velocity scale v, a length scale η and a time scale

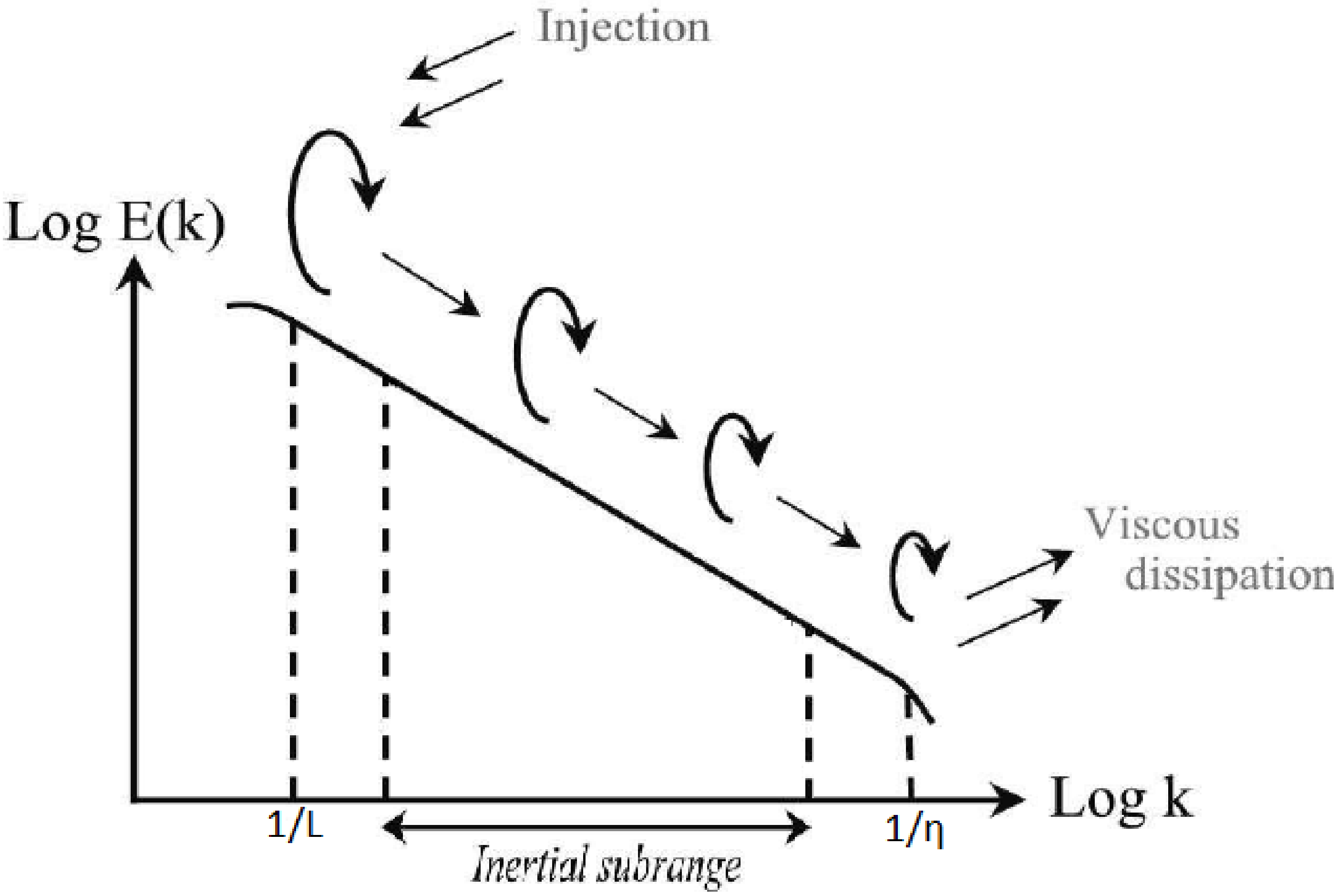

Figure 2.3: Spectrum for the wave number k and the energy $E(k)$ for turbulence showing the energy cascade. Taken from [60].

τ. From dimensional analysis, these scales can be determined by the viscosity ν [SI units of m^2/s] and the energy dissipation rate per unit mass ϵ [units: m^2/s^3]

$$v = (\nu\epsilon)^{1/4} \tag{2.4}$$

$$\eta = \left(\frac{\nu^3}{\epsilon}\right)^{1/4} \tag{2.5}$$

$$\tau = \left(\frac{\nu}{\epsilon}\right)^{1/2} \tag{2.6}$$

The inertial subrange is the transport region of the cascade process. The energy comes in from the energy containing range at a rate ϵ and passes through to the dissipation range. The inertial subrange occurs in the wavenumber range $1/L \ll k \ll 1/\eta$. An important result to note comes from Kolmogorov's 1941 Theory [31, 32, 33], where the energy spectra in the inertial range decays with a power of $-5/3$

$$E(k) \propto \epsilon^{2/3} k^{-5/3} \tag{2.7}$$

It is important for the discussion on phenomenologies, to remember the idea of constructing the quantities in the inertial and dissipation ranges in terms of the wave number k (proportional to 1/length scale) and the dissipation rate ϵ. This helps reinforce the energy cascade being driven at the largest scales at the rate ϵ and flowing down the cascade at the rate ϵ, ending in the energy dissipating at the rate ϵ. Conceptually these three ϵ's are clearly physically distinct quantities. However in a statistically steady system their average values will be equal. Additionally, the following relation can be derived from the Navier-Stokes equations [22], where $\boldsymbol{f}$ is the force driving

$$\frac{\partial}{\partial \mathrm{t}} \frac{1}{2} \left\langle \boldsymbol{v}^2 \right\rangle = \langle \boldsymbol{f} \cdot \boldsymbol{v} \rangle + \nu \left\langle \boldsymbol{v} \cdot \nabla^2 \boldsymbol{v} \right\rangle \tag{2.8}$$

In words, the only changes in the mean kinetic energy come from the force driving at the large scale (first term on the right hand side (RHS)) and the viscous energy dissipation at the small scale (second term on the RHS). The energy cascade transfers energy from the forcing range to the dissipation range (via an inertial range if the flow is turbulent) but does not actually change the energy. Formally this transfer of energy between scales would appear in Equation 2.8 as the term $-\langle \boldsymbol{v} \cdot (\boldsymbol{v} \cdot \nabla)\boldsymbol{v} \rangle$ which can be shown to be zero.

2.3.2 Phenomenologies

A phenomenology is a modelling approach that seeks to give tractable equations that adequately represent the system.

Firstly, the nonlinear couplings in the Navier-Stokes equations provide the means for the cascade of energy. This gives rise to the following notation, $\left.\frac{\partial(\cdot)}{\partial \mathrm{t}}\right|_{NL}$ representing the time rate of change from the nonlinear terms in the Navier-Stokes equation. From the energy cascade, the time rate of change of the kinetic energy is the energy dissipation rate

$$\left.\frac{\partial u^2}{\partial \mathrm{t}}\right|_{NL} \propto -\epsilon \tag{2.9}$$

Here, the kinetic energy per unit mass u^2 is the mean-square of the velocity $u^2 = \langle |\boldsymbol{u}|^2 \rangle$. The next idea introduces the eddy turnover time $\tau \approx \frac{\lambda}{u}$, which is the typical time for a structure of size λ to undergo a distortion due to the relative motion of the fluid particles. Think of a vortex of size λ decreasing in size or breaking up due to the velocities of the different particles. In other words, the vortex transitions to a smaller scale at a rate $1/\tau$. From the energy cascade, the dissipation rate (or the force driving rate or the inertial range energy flux) is the kinetic energy over the eddy turnover time

$$\epsilon \propto \frac{u^2}{\tau} \tag{2.10}$$

Similarly, the length scale evolves according to the eddy turn over time

$$\left.\frac{\mathrm{d}\lambda}{\mathrm{d}t}\right|_{NL} = \frac{\lambda}{\tau} \tag{2.11}$$

This gives us the Kármán-Taylor phenomenology [16, 20, 54] (Taylor [54] and de Kármán and Howarth [16] implicitly contain the following model and Dryden [20] explicitly)

$$\left.\frac{\mathrm{d}u^2}{\mathrm{d}t}\right|_{NL} = -\alpha\frac{u^3}{\lambda} \tag{2.12}$$

$$\left.\frac{\mathrm{d}\lambda}{\mathrm{d}t}\right|_{NL} = \beta u \tag{2.13}$$

The parameters α and β are the Kármán-Taylor constants, and are strictly positive. These Kármán-Taylor constants play an important role in the energy cascade process [36] and are left as generalized parameters. In fact, it is possible to reconstruct a number of theories on turbulence through choices in the α and β constants [36], particularly, Kolmogorov's model [32] (with $\alpha = 5\beta$).

These Kármán-Taylor equations and the discussion in this section has been focusing on the HD process, this is mostly generalizable to the MHD description. The discussion will be extended in the next chapter (chapter 3). The Kármán-Taylor equations are one example of an energy-containing range phenomenology; we focus on the Kármán-Taylor equations in this thesis but there other phenomenologies do exist.

2.3.3 Plasma Turbulence

The complexity of plasma interactions runs deep, and there are a vast amount of instabilities and phenomena that can occur in a plasma fluid. As the plasma in the solar wind is described using the Navier-Stokes equations with the addition of Maxwell's equations we get the usual fluid velocity-velocity interactions in addition to velocity-magnetic field and magnetic field-magnetic field interactions. Some of these phenomena have been observed to occur in the solar wind like magnetic reconnection [23, 24] but, for the most part, these phenomena will be ignored since we are only interested in the average behaviour of the fluctuation correlations. Some of the effects that might play a part in increasing the overall energy of the solar wind are captured in the source driving terms (section 2.5).

Due to the couplings between the fluid velocity and the magnetic field, with an ideal conductor in the form of ions and electrons in a near vacuum, we arrive at the Alfvén effect; the magnetic field lines are frozen into and move with the fluid. From the Alfvén effect, any perturbation in one of the fields will result in a perturbation in the other field. This means that waves both transverse and parallel (to the mean magnetic field) can form through an oscillation of the fluid and the magnetic field perturbations. So, in addition to the analogous HD eddies [14], there are waves present in MHD turbulence [9]. In this thesis, these two turbulent quantities will be considered equivalent and in terms of describing specific aspects, we will alternate between an analogous HD eddy or a propagating wave. Some research has been done by separating out the turbulence into a two component model in the form of a wave piece and quasi-2D-turbulence [43].

2.4 Elsässer Variables

To simplify the description of MHD fluids, it helps to construct Elsässer variables from the flow velocity field and the magnetic field [21]. The magnetic field is divided by the square root of the mass density ρ; this converts the magnetic field $\boldsymbol{b}$ (in units of gauss, say) to an Alfvén velocity $\boldsymbol{v}_A$ (in units of cm/s, say):

$$\boldsymbol{z}_{\pm} = \boldsymbol{u} \pm \frac{\boldsymbol{b}}{\sqrt{4\pi\rho}} = \boldsymbol{u} \pm \boldsymbol{v}_A \tag{2.14}$$

This leads to a symmetric form of the MHD equations (chapter 3) and also separates the equations into parts that depict the wave propagation direction. $\boldsymbol{z}_+$ represents an inward propagating wave (anti-parallel to the mean magnetic field) and $\boldsymbol{z}_-$ represents an outward propagating wave (parallel to the mean magnetic field). The use of the Elsässer variables in the MHD equations does *not* imply that the fluctuations must be waves; they represent general fluctuations which, in some circumstances may be Alfvén waves. The Elsässer representation can be easily converted to the kinetic and magnetic representation (with the addition of the cross helicity H_c). The energies (per unit mass) for the kinetic, magnetic and the cross helicity are the following

$$u^2 = \langle \boldsymbol{u} \cdot \boldsymbol{u} \rangle \tag{2.15}$$

$$b^2 = \langle \boldsymbol{v}_A \cdot \boldsymbol{v}_A \rangle \tag{2.16}$$

$$H_c = \langle \boldsymbol{u} \cdot \boldsymbol{v}_A \rangle \tag{2.17}$$

Really, the correct value for the energies (per unit mass) is a half of the above quantities, for example $E_u = \frac{1}{2}u^2$ is the kinetic energy. These energies can be converted into the Elsässer variable representation by the following identities:

$$Z_\pm^2 = \langle \boldsymbol{z}_\pm \cdot \boldsymbol{z}_\pm \rangle = u^2 + b^2 \pm 2H_c \tag{2.18}$$

$$D = \langle \boldsymbol{z}_+ \cdot \boldsymbol{z}_- \rangle = u^2 - b^2 \tag{2.19}$$

The same goes for the correlation integrals of the Elsässer representation if we assume that $\langle \boldsymbol{u} \cdot \boldsymbol{v}_A' \rangle = \langle \boldsymbol{v}_A \cdot \boldsymbol{u}' \rangle$ where the primed variables indicate spatial lag *e.g.,* $\boldsymbol{z}^{\pm\prime} = \boldsymbol{z}^\pm(\boldsymbol{x} + \boldsymbol{w})$ (see Appendix B)

$$L_\pm = \int_0^\infty \left\langle \boldsymbol{z}_\pm \cdot \boldsymbol{z}_\pm' \right\rangle \mathrm{d}w = L_u + L_b \pm 2L_c \tag{2.20}$$

$$L_D = \int_0^\infty \frac{1}{2} \left\langle \boldsymbol{z}_+ \cdot \boldsymbol{z}_-' \right\rangle + \left\langle \boldsymbol{z}_- \cdot \boldsymbol{z}_+' \right\rangle \mathrm{d}w = L_u - L_b \tag{2.21}$$

All the correlation integrals can be used with their respective energies to construct a correlation length that has solely length units, for example the Elsässer correlation lengths are

$$\lambda_\pm = \frac{L_\pm}{Z_\pm^2} \tag{2.22}$$

$$\lambda_D = \frac{L_D}{D} \tag{2.23}$$

2.5 Driven Turbulence Sources

There are potentially many sources for additional turbulence driving and some are necessary for accurately describing the solar wind evolution (section 4.2) [25]. We will focus on three primary sources of turbulence in the heliosphere in this thesis [1, 4, 13, 29, 35, 53, 63]; the first is the turbulence driven by the shear interaction between fast and slow solar wind streams. The second source is from the compressive effects (*e.g.,* due to shock waves in the solar wind). Lastly, the charge exchange between the neutral interstellar hydrogen and the solar wind protons creates additional turbulence in the solar wind.

2.5.1 Stream Shear Driving

Although the solar wind is mostly constant along the radial directions, it varies according to the helio-latitude allowing for a shear interaction of a fast stream rubbing against a slower stream. The stream shear driving can be thought of as analogous to HD shear, as the fast stream rubs against the slow stream, instabilities arise and add more energy to the system. The equation for the stream shear driven turbulence is modelled as [13, 63]

$$S_{\pm}^{shear} = C_{shear} U \frac{Z_{\pm}^2}{r} \tag{2.24}$$

where C_{shear} represents the strength of the shear interaction which acts on the slow solar wind speed U by the difference between the fast and the slow speed δU over the distance they interact δr

$$C_{shear} = \frac{\delta U}{U} \frac{r}{\delta r} \tag{2.25}$$

2.5.2 Shock Wave Driving

We can also model the compression effects of shocks that occur in the plasma. The shocks have been observed around 1 AU and enhance the pressure and the magnetic field along with increasing the level of fluctuations in the solar wind [59]. It is important to note that the shocks do not occur continuously, but a region of the solar wind can develop/cross over into a shock region so the equation models the effects of the shock over a region δr. The equation for the shock driven turbulence is modelled similarly to the stream shear turbulence [63]

$$S_{\pm}^{shock} = C_{shock} U \frac{Z_{\pm}^2}{r} \tag{2.26}$$

2.5.3 Pickup Ion Driving

In the outer parts of the heliosphere, the neutral protons from the interstellar medium flow into the heliosphere and get ionized by charge exchange with the solar wind protons or via the solar radiation. Once ionized, the interstellar particles gyrate around the magnetic field and are then scattered by the inertial range turbulence. The scattering of the interstellar pickup ions generates waves that act as an additional driving force for the turbulence [13, 29, 53]. The pickup ion driving can be estimated as the following equation

$$S^{PID} = \frac{f_D n_H^{\infty} U V_A}{n_{SW}^1 \tau_{ion}^1} e^{-\frac{L_{cav}}{r}} \tag{2.27}$$

where $n_H^{\infty} = 0.1 \text{ cm}^{-3}$ is the density of the incoming interstellar hydrogen, $n_{SW}^1 = 5 \text{ cm}^{-3}$ is the solar wind density at 1 AU, $\tau_{ion}^1 = 10^6$ s is the ionization time of the hydrogen at 1 AU and $L_{cav} = \lambda\theta/\sin\theta = 8$ AU is the scale of the ionization cavity around the sun (λ is *not* the inertial range correlation length). In the heliosphere, the ionization cavity is sphere in the inner heliosphere where there are minimal interstellar neutrals. As the neutral atoms come into the heliosphere at a fixed rate and are ionized at the rate $\frac{\mathrm{d}n_{PI}}{\mathrm{d}t}$, as the radial distance decreases there are less and less neutral atoms to ionize. The ionization cavity is represented by the exponential term $e^{-L_{cav}/r}$ in S^{PID}.

Chapter 3

Solar Wind Models

This section discusses the equations used to model the solar wind. First, a coupled set of evolution equations are needed to model the transport of the turbulent fluctuations. These equations contain nonlinear couplings that are difficult to analytically solve and require more evolution equations, instead, they will be replaced with phenomenologies based off the decay of the turbulence and the transfer of the energy to higher wave numbers. This section will also cover additional processes that need to be included to account for the interactions of the solar wind plasma particles in the heliosphere.

3.1 Evolution Equations

The dynamics of the solar wind can be approximated with an MHD one-fluid approximation [66]. For an apt description of the solar wind fluctuations, we will need the total energy which is the kinetic energy plus the magnetic energy $E_T = E_u + E_b$, the energy difference (sometimes called the residual energy) which is the difference between the kinetic and magnetic energies $E_D = E_u - E_b$, and the cross helicity E_C. These three quantities can be easily obtained by ensemble averaging the velocity and magnetic fields, where the

Alfvén field $\boldsymbol{v}_A$ is the magnetic field in speed units $\frac{1}{\sqrt{4\pi\rho}}\boldsymbol{b} = \boldsymbol{v}_A$ (in km/s, say)

$$E_T = \frac{1}{2}\langle \boldsymbol{u} \cdot \boldsymbol{u} \rangle + \frac{1}{2}\langle \boldsymbol{v}_A \cdot \boldsymbol{v}_A \rangle \tag{3.1}$$

$$E_D = \frac{1}{2}\langle \boldsymbol{u} \cdot \boldsymbol{u} \rangle - \frac{1}{2}\langle \boldsymbol{v}_A \cdot \boldsymbol{v}_A \rangle \tag{3.2}$$

$$E_C = \frac{1}{2}\langle \boldsymbol{u} \cdot \boldsymbol{v}_A \rangle \tag{3.3}$$

The MHD equations contain a conservation of mass equation,

$$\frac{\partial \rho}{\partial \mathrm{t}} + \nabla \cdot (\boldsymbol{V}\rho) = 0 \tag{3.4}$$

an equation of motion,

$$\rho\left(\frac{\partial \boldsymbol{V}}{\partial \mathrm{t}} + \boldsymbol{V} \cdot \nabla \boldsymbol{V}\right) = -\nabla p + \frac{1}{c}\boldsymbol{J} \times \boldsymbol{B} + \boldsymbol{D} \tag{3.5}$$

and an induction equation,

$$\frac{\partial \boldsymbol{B}}{\partial \mathrm{t}} = \nabla \times (\boldsymbol{V} \times \boldsymbol{B}) + \boldsymbol{D'} \tag{3.6}$$

Obtaining the equations for the fluctuations requires considerable algebra which is relegated to Appendices A to D. Appendix A discusses the MHD equations further and converts them to a symmetrical Elsässer variable form (Equation A.35). Next, in Appendix B, the MHD equations are taken with ensemble averages to obtain evolution equations of the statistical properties (Equations (B.10) and (B.21)) which obtain the evolution equations of the energies. To complete the model derivation, the nonlinear couplings in Equations (B.10) and (B.21) need to be resolved (section 3.2). To form the nonlinear closure, models for the turbulent length scales (λ_u, λ_b, λ_C) are required. The evolution equations for the turbulent length scales can also be obtained from Equations (B.10) and (B.21). Equations (B.10) and (B.21) are developed further in Appendix C and Appendix D, to obtain a six equation, steady-state system of equations for the fluctuating energy and their length scales (section D.5).

This thesis evaluates the models in section D.5 and will additionally compare it to a simpler, three equation Breech et al. [13] model (section E.2) and with a model constructed using a Cauchy-Scharwz' inequality, the Adhikari et al. [1] model (section E.1).

3.1.1 Energy and length-scale Evolution Equations

Due to the assumptions in the symmetries of the turbulence (Appendix C), there are multiple models that could be composed from Equations (B.10) and (B.21). Furthermore, the length scales can be measured differently depending on the alignment of the separation vector $\hat{\boldsymbol{w}}$ with respect to the local Cartesian coordinate system and the radial and magnetic fields resulting in different length scale equations. In this thesis we will focus on two dimensional isotropy (axisymmetry) as solar wind observations suggest that there is an anisotropy invoked due to the large scale magnetic field [10, 15, 34, 41, 42]. Choosing two dimensional isotropy means that the wave vectors and fluctuations lie in the plane perpendicular to the mean magnetic field. The three dimensional isotropic equations will be used as a simpler reference for the more complicated two dimensional case. When it comes to resolving the length scale equations, we will choose the local Cartesian coordinate system such that the correlation length is measured in the radial direction as this is more relevant to in situ space craft measurements (Section 2.2). Assuming the constant spherically symmetric outward flow $\boldsymbol{U} = U\hat{\boldsymbol{r}}$, conservation of mass yields $\rho = \rho_0 \left(R_0/r\right)^2$. With $\boldsymbol{B}_0$ defined as an outwardly directed Parker Spiral, $V_{Ar} = \frac{B_0}{\sqrt{4\pi\rho}}\left(\frac{R_0}{r}\right)^2 = \frac{B_0}{\sqrt{4\pi\rho_0}}\left(\frac{R_0}{r}\right) = V_{Ar0}\left(\frac{R_0}{r}\right)$. The one dimensional and steady-state evolution equations are the following

$$\frac{\mathrm{d}Z_\pm^2}{\mathrm{d}r} = -\frac{U \pm V_{Ar}}{U \mp V_{Ar}}\frac{Z_\pm^2}{r} - \frac{1}{U \mp V_{Ar}}M^\pm D + \frac{1}{U \mp V_{Ar}}N_\pm + \frac{1}{U \mp V_{Ar}}S_\pm \tag{3.7}$$

$$\frac{\mathrm{d}D}{\mathrm{d}r} = -\frac{D}{r} - \frac{1}{2}\frac{1}{U}\left(M^+ Z_-^2 + M^- Z_+^2\right) + \frac{1}{U}N_D + \frac{1}{U}S_D \tag{3.8}$$

$$\frac{\mathrm{d}L_\pm}{\mathrm{d}r} = -\frac{U \pm V_{Ar}}{U \mp V_{Ar}}\frac{L_\pm}{r} - \frac{1}{U \mp V_{Ar}}M_L^\pm L_D + \frac{1}{U \mp V_{Ar}}N_\pm^L + \frac{1}{U \mp V_{Ar}}S_\pm^L \tag{3.9}$$

$$\frac{\mathrm{d}L_D}{\mathrm{d}r} = -\frac{L_D}{r} - \frac{1}{2U}\left(M_L^- L_+ + M_L^+ L_-\right) + \frac{1}{U}N_D^L + \frac{1}{U}S_D^L \tag{3.10}$$

where the 2 dimensional mixing terms are

$$M_{2D}^{\pm} = \frac{1}{r}\left[U\cos^2\Psi \pm V_{Ar}\left(3\cos^2\Psi - 2\right) \pm V_{Ar0}\left(\frac{\Omega R_0}{U}\right)\left(1 - \frac{3R_0}{2r}\right)\sin\theta\sin 2\Psi\right] \tag{3.11}$$

$$M_{2D,L}^{\pm} = \frac{1}{r}\left[U\left(2\cos^2\Psi - 1\right) \pm V_{Ar}\left(6\cos^2\Psi - 5\right) \pm V_{Ar0}\left(\frac{\Omega R_0}{U}\right)\left(\frac{3R_0}{2r} - 1\right)\sin\theta\sin 2\Psi\right] \tag{3.12}$$

3.2 Nonlinear Phenomenologies

As section 2.3 discusses, in the hydrodynamic case, the fluctuations in a turbulent flow can be described by the characteristic length scale and the energy - an energy containing range phenomenology. From these two quantities, the characteristic velocity and timescale can be derived and used to explain the decay due to the nonlinear interactions. In the MHD case, more timescales are required. In this thesis we will focus on four characteristic timescales following Matthaeus et al. [35]. The nonlinear timescale $\tau_{nl} = \lambda/Z$ is the first, and is analogous to the hydrodynamic eddy turnover time. The second timescale is the Alfvén timescale $\tau_A = \lambda/V_A$, associated with the propagation of the Alfvén waves along the mean magnetic field V_A. These Alfvén waves have a potential to effect the spectral transfer. Next, the triple correlation timescale τ_3 is used for the decay of the energy-containing eddies via spectral transfer. In the hydrodynamic case, the spectral timescale is equal to the nonlinear timescale $\tau_3^{-1} = \tau_{nl}^{-1}$. In MHD, we could assume that the triple correlations decay at a rate that is instead the sum of the Alfvén and nonlinear rates

$$\tau_3^{-1} = \tau_{nl}^{-1} + \tau_A^{-1} \tag{3.13}$$

We will discuss whether to assume the hydrodynamic case for the triple correlation timescale later in this section when discussing the specific nonlinear forms for each of the evolution variables. The last timescale is the spectral timescale τ_S; sometimes called the cascade timescale, and is associated with the decay of the MHD variables. The triple correlation in Matthaeus et al.

[35] is described as $\tau_S = (\tau_{nl})^2/\tau_3$. In the analogous hydrodynamic case, the spectral timescale reduces down to the nonlinear timescale $\tau_S = \tau_{nl}$.

The nonlinear terms will be described in terms of the timescales effecting them, therefore the energies and the correlation lengths. The notation has been changed for the nonlinear terms to the following

$$N_\pm = \left.\frac{\mathrm{d}Z_\pm^2}{\mathrm{d}t}\right|_{NL} \tag{3.14}$$

$$N_D = \left.\frac{\mathrm{d}D}{\mathrm{d}t}\right|_{NL} \tag{3.15}$$

$$N_\pm^L = \left.\frac{\mathrm{d}L_\pm}{\mathrm{d}t}\right|_{NL} \tag{3.16}$$

$$N_D^L = \left.\frac{\mathrm{d}L_D}{\mathrm{d}t}\right|_{NL} \tag{3.17}$$

3.2.1 Energy $Z_\pm^2$ Models

The estimates for the decay of the Elsässer fields $\epsilon_\pm$ can be assembled as the following

$$\epsilon_\pm \propto \frac{Z_\pm^2}{\tau_S^\pm} \tag{3.18}$$

Therefore the nonlinear decay of the turbulent Elsässer energies can be written as the following

$$\left.\frac{\mathrm{d}Z_\pm^2}{\mathrm{d}t}\right|_{NL} = -\alpha_\pm \frac{Z_\pm^2}{\tau_S^\pm} \tag{3.19}$$

where $\alpha_\pm$ are the Kármán-Taylor constants for the Elsässer energies. We will also need the nonlinear timescales for the Elsässer fields that are proportional to their own length scale divided by the opposing Elsässer field; $\tau_{nl}^\pm = \lambda_\pm/Z_\mp$. The form for the nonlinear timescale comes from the following term in the dynamical vector evolution equations for $\boldsymbol{z}^\pm$ (Equation A.35)

$$\boldsymbol{z}^\mp \cdot \nabla \boldsymbol{z}^\pm \tag{3.20}$$

An MHD case, analogous to the HD case takes $\tau_S^\pm = \tau_{nl}^\pm$, and then the nonlinear turbulent decay takes the form

$$\left.\frac{\mathrm{d}Z_\pm^2}{\mathrm{d}t}\right|_{NL} = -\alpha_\pm \frac{Z_\pm^2 Z_\mp}{\lambda_\pm} \tag{Model A}$$

If we assume that the Alfvén timescale is present in the spectral transfer, the following term

$$\boldsymbol{V}_A \cdot \nabla \boldsymbol{z}^{\pm} \tag{3.21}$$

gives $\tau_A^{\pm} = \lambda_{\pm}/V_A$ and assuming $\tau_3^{-1} = \tau_{nl}^{-1} + \tau_A^{-1}$, the nonlinear decay follows

$$\left.\frac{\mathrm{d}Z_{\pm}^2}{\mathrm{d}t}\right|_{NL} = -\alpha_{\pm}\frac{Z_{\pm}^2 Z_{\mp}^2}{\lambda_{\pm}\left(V_A + Z_{\mp}\right)} \tag{Model A (V_A)}$$

Most models; particularly the Adhikari et al. [1] and Breech et al. [13] models, ignore the Alfvén timescale for the spectral transfer of the Elsässer fields and use Model A. This can be justified if the turbulence is (largely) 2D, so that the Alfvén wave propagation effects are weak.

3.2.2 Length Scale $\lambda_{\pm}$ Models

The evolution for the Elsässer correlation lengths $\lambda_{\pm}$ also needs to be developed. Since the hydrodynamic correlation length has the nonlinear evolution proportional to the correlation length over the timescale $\frac{\mathrm{d}\ell}{\mathrm{d}t}\big|_{NL} = \ell/\tau = u$ it is simple to follow the same idea for the Elsässer correlation lengths. Again, assuming that $\tau_S^{\pm} = \tau_{nl}^{\pm}$

$$\left.\frac{\mathrm{d}\lambda_{\pm}}{\mathrm{d}t}\right|_{NL} = \frac{\lambda_{\pm}}{\tau_S^{\pm}} = \beta_{\pm} Z_{\mp} \tag{Model B}$$

where $\beta_{\pm}$ is the Kármán-Taylor constant for the correlation lengths. Like the hydrodynamic case, Model B contains a class of conservation laws,

$$\frac{\mathrm{d}\left(Z_{\pm}^{a_{\pm}}\lambda_{\pm}\right)}{\mathrm{d}t} = 0 \tag{3.22}$$

where $a_{\pm} = 2\beta_{\pm}/\alpha_{\pm}$. Having conservation laws makes it easier to obtain analytical results and relations between the Kármán-Taylor constants $\alpha_{\pm}, \beta_{\pm}$ [36]. A specific case of the conservation laws can be constructed where it can be interpreted that the area under the correlation tensor (as defined in Appendices B and D) $L_{\pm} = \int_0^{\infty} \boldsymbol{H}_{ii}^{\pm}\mathrm{d}w = Z_{\pm}^2\lambda_{\pm}$ is constant in time

$$\frac{\mathrm{d}L_{\pm}}{\mathrm{d}t} = 0 \tag{Model 0}$$

Model 0 corresponds to a choice of the Kármán-Taylor constants $\alpha_\pm = \beta_\pm$. Adhikari et al. [1] uses Model 0 as its length scale nonlinear models. Model B also introduces an inconsistency, if one of the Elsässer fields vanishes, it is expected that all the turbulent spectral transfer will halt. With Equation Model B the opposite Elsässer field correlation length would still continue to evolve. As a result, Matthaeus et al. [35] suggests that the evolution for the correlation lengths can be rewritten to depend on the correlation length $\lambda_\pm$ and the decay rate $\epsilon_\pm$

$$\left.\frac{\mathrm{d}\lambda_\pm}{\mathrm{d}t}\right|_{NL} = \left(\lambda_\pm \epsilon_\pm\right)^{1/3} \tag{3.23}$$

this equation still maintains the expected hydrodynamic limit $\left.\frac{\mathrm{d}\ell}{\mathrm{d}t}\right|_{NL} = u$. If we assume that the spectral timescale is only the nonlinear timescale then

$$\left.\frac{\mathrm{d}\lambda_\pm}{\mathrm{d}t}\right|_{NL} = \beta_\pm \left(Z_\pm^2 Z_\mp\right)^{1/3} \tag{Model A}$$

If the spectral timescale depends on the Alfvén timescale as well, then

$$\left.\frac{\mathrm{d}\lambda_\pm}{\mathrm{d}t}\right|_{NL} = \beta_\pm \left(\frac{Z_\pm^2 Z_\mp^2}{V_A + Z_\mp}\right)^{1/3} \tag{Model A (V_A)}$$

As an extension of Model A, it is possible to construct distinct models that maintain the same behaviour of halting spectral transfer when one of the Elsässer fields vanishes and obtaining the hydrodynamic limit. Hossain et al. [26] analyses the above models and also

$$\left.\frac{\mathrm{d}\lambda_\pm}{\mathrm{d}t}\right|_{NL} = \beta_\pm \left(Z_\pm Z_\mp\right)^{1/2} \tag{3.24}$$

Instead, we will define a generalized model for the correlation lengths that encompasses the $\lambda_\pm$ models, when the spectral timescale only depends on the nonlinear timescale

$$\left.\frac{\mathrm{d}\lambda_\pm}{\mathrm{d}t}\right|_{NL} = \beta_\pm \left(Z_\pm^m Z_\mp^n\right)^{\frac{1}{m+n}} \tag{Model $C_{m,n}$}$$

Setting $m = 0, n = 1$ obtains Model B (Model $C_{0,1}$) and $m = 2, n = 1$ obtains Model A (Model $C_{2,1}$).

3.2.3 Extra Discussion on the Conservation Laws

We touched on the idea of conservation laws with $\lambda_\pm$ Model 0; constraining the area under the correlation tensor $L_\pm$. Using $Z_\pm^2$ Model A and $\lambda_\pm$ Model B, a general conservation law can be constructed for $Z_\pm^{a_\pm}\lambda_\pm$ requiring the $\alpha_\pm$ and $\beta_\pm$ relations $a_\pm = 2\beta_\pm/\alpha_\pm$

$$\frac{\mathrm{d}(Z_\pm^{a_\pm}\lambda_\pm)}{\mathrm{d}t} = 0 \tag{3.25}$$

$$= \lambda_\pm \frac{\mathrm{d}Z_\pm^{a_\pm}}{\mathrm{d}t} + Z_\pm^{a_\pm}\frac{\mathrm{d}\lambda_\pm}{\mathrm{d}t} \tag{3.26}$$

$$= \lambda_\pm a_\pm Z_\pm^{a_\pm - 1}\frac{\mathrm{d}Z_\pm}{\mathrm{d}t} + Z^{a_\pm}\frac{\mathrm{d}\lambda_\pm}{\mathrm{d}t} \tag{3.27}$$

$$= \lambda_\pm a_\pm Z_\pm^{a_\pm - 1}\left(-\frac{\alpha_\pm}{2}\frac{Z_\pm Z_\mp}{\lambda_\pm}\right) + Z^{a_\pm}\beta_\pm Z_\mp \tag{3.28}$$

$$= -\frac{a_\pm \alpha_\pm}{2} Z_\pm^{a_\pm} Z_\mp + Z_\pm^{a_\pm}\beta_\pm Z_\mp \tag{3.29}$$

$$\implies a_\pm = \frac{2\beta_\pm}{\alpha_\pm} \tag{3.30}$$

To retrieve $\lambda_\pm$ Model 0, set $\alpha_\pm = \beta_\pm$. The conservation of $Z_\pm^{a_\pm}\lambda_\pm$ depends on the Kármán-Taylor parameter relation and therefore the nonlinear model used.

If we use $\lambda_\pm$ Model A; for the + equations, we can calculate an expression of the energies as a function of a_+, using $Z_+^{a_+}\lambda_+ = const$

$$\frac{\mathrm{d}(Z_+^{a_+}\lambda_+)}{\mathrm{d}t} = 0 \tag{3.31}$$

$$= Z_+^{a_+}\frac{\mathrm{d}\lambda_+}{\mathrm{d}t} + \lambda_+\frac{\mathrm{d}Z_+^{a}}{\mathrm{d}t} \tag{3.32}$$

$$= Z_+^{a_+}\beta_+\left(Z_+^2 Z_-\right)^{1/3} + \lambda_+ a_+ Z_+^{a_+ - 1}\left(-\frac{\alpha_+}{2}\frac{Z_+ Z_-}{\lambda_+}\right) \tag{3.33}$$

$$= \beta_+\left(Z_+^2 Z_-\right)^{1/3} - \frac{a_+\alpha_+}{2} Z_- \tag{3.34}$$

$$= \beta_+^3 Z_+^2 - \frac{a_+^3\alpha_+^3}{2^3} Z_-^2 \tag{3.35}$$

$$\implies \frac{Z_+^2}{Z_-^2} = \left(\frac{a_+\alpha_+}{2\beta_+}\right)^3 \tag{3.36}$$

Likewise, we can calculate a distinct expression for the energy ratio as a function of a_-, using $Z_-^{a_-}\lambda_- = const$:

$$\frac{\mathrm{d}(Z_-^{a_-}\lambda_-)}{\mathrm{d}t} = 0 = \beta_-^3 Z_-^2 - \frac{a_-^3\alpha_-^3}{2} Z_+^2 \tag{3.37}$$

$$\implies \frac{Z_-^2}{Z_+^2} = \left(\frac{a_-\alpha_-}{2\beta_-}\right)^3 \tag{3.38}$$

Equation 3.36 and Equation 3.38 imply

$$\frac{a_-\alpha_-}{2\beta_-} = \frac{2\beta_+}{a_+\alpha_+} \tag{3.39}$$

If we denote the normalized cross helicity σ_c to $\sigma_c^\pm$ to indicate whether we are factoring out $Z_\mp^2$ respectively from the numerator and denominator

$$\sigma_c^+ = \frac{Z_+^2 - Z_-^2}{Z_+^2 + Z_-^2} = \frac{\frac{Z_+^2}{Z_-^2} - 1}{\frac{Z_+^2}{Z_-^2} + 1} = \frac{\left(\frac{a_+\alpha_+}{2\beta_+}\right)^3 - 1}{\left(\frac{a_+\alpha_+}{2\beta_+}\right)^3 + 1} \tag{3.40}$$

$$\sigma_c^- = \frac{Z_+^2 - Z_-^2}{Z_+^2 + Z_-^2} = \frac{1 - \frac{Z_-^2}{Z_+^2}}{1 + \frac{Z_-^2}{Z_+^2}} = \frac{1 - \left(\frac{a_-\alpha_-}{2\beta_-}\right)^3}{1 + \left(\frac{a_-\alpha_-}{2\beta_-}\right)^3} \tag{3.41}$$

we can construct an expression for a_+ as a function of the cross helicity

$$\sigma_c^+ = \frac{\left(\frac{a_+\alpha_+}{2\beta_+}\right)^3 - 1}{\left(\frac{a_+\alpha_+}{2\beta_+}\right)^3 + 1} \tag{3.42}$$

$$\implies \sigma_c^+\left(\left(\frac{a_+\alpha_+}{2\beta_+}\right)^3 + 1\right) = \left(\frac{a_+\alpha_+}{2\beta_+}\right)^3 - 1 \tag{3.43}$$

$$\implies \sigma_c^+ a_+^3\left(\frac{\alpha_+}{2\beta_+}\right)^3 + \sigma_c^+ = a_+^3\left(\frac{\alpha_+}{2\beta_+}\right)^3 - 1 \tag{3.44}$$

$$\implies \sigma_c^+\left(\frac{\alpha_+}{2\beta_+}\right)^3 + \frac{\sigma_c^+}{a_+^3} = \left(\frac{\alpha_+}{2\beta_+}\right)^3 - \frac{1}{a_+^3} \tag{3.45}$$

$$\implies \sigma_c^+\left(\frac{\alpha_+}{2\beta_+}\right)^3 - \left(\frac{\alpha_+}{2\beta_+}\right)^3 = -\frac{\sigma_c^+}{a_+^3} - \frac{1}{a_+^3} \tag{3.46}$$

$$\implies \left(\frac{\alpha_+}{2\beta_+}\right)^3\left(\sigma_c^+ - 1\right) = -\frac{1}{a_+^3}\left(\sigma_c^+ + 1\right) \tag{3.47}$$

$$\implies -\left(\frac{\alpha_+}{2\beta_+}\right)^3\frac{\sigma_c^+ - 1}{\sigma_c^+ + 1} = \frac{1}{a_+^3} \tag{3.48}$$

$$\therefore a_+ = \left(\frac{2\beta_+}{\alpha_+}\right)\left(\frac{1+\sigma_c^+}{1-\sigma_c^+}\right)^{1/3} \tag{3.49}$$

Similarly, we can construct an expression for a_- as a function of the cross helicity

$$\sigma_c^- = \frac{1-\left(\frac{a_-\alpha_-}{2\beta_-}\right)^3}{1+\left(\frac{a_-\alpha_-}{2\beta_-}\right)^3} \tag{3.50}$$

$$\implies \sigma_c^- \left(1+\left(\frac{a_-\alpha_-}{2\beta_-}\right)^3\right) = 1-\left(\frac{a_-\alpha_-}{2\beta_-}\right)^3 \tag{3.51}$$

$$\implies \sigma_c^- + a_-^3\sigma_c^- \left(\frac{\alpha_-}{2\beta_-}\right)^3 = 1 - a_-^3\left(\frac{\alpha_-}{2\beta_-}\right)^3 \tag{3.52}$$

$$\implies \frac{\sigma_c^-}{a_-^3} + \sigma_c^- \left(\frac{\alpha_-}{2\beta_-}\right)^3 = \frac{1}{a_-^3} - \left(\frac{\alpha_-}{2\beta_-}\right)^3 \tag{3.53}$$

$$\implies \sigma_c^- \left(\frac{\alpha_-}{2\beta_-}\right)^3 + \left(\frac{\alpha_-}{2\beta_-}\right)^3 = \frac{1}{a_-^3} - \frac{\sigma_c^-}{a_-^3} \tag{3.54}$$

$$\implies \left(\frac{\alpha_-}{2\beta_-}\right)^3 \left(\sigma_c^- + 1\right) = \frac{1}{a_-^3}\left(1-\sigma_c^-\right) \tag{3.55}$$

$$\implies \left(\frac{\alpha_-}{2\beta_-}\right)^3 \frac{\sigma_c^- + 1}{1-\sigma_c^-} = \frac{1}{a_-^3} \tag{3.56}$$

$$\therefore a_- = \left(\frac{2\beta_-}{\alpha_-}\right)\left(\frac{1-\sigma_c^-}{1+\sigma_c^-}\right)^{1/3} \tag{3.57}$$

The values for $a_\pm$ show that the phenomenology predicts that the conservation of $Z_\pm^{a_\pm}\lambda_\pm$ is a function of σ_c. At $\sigma_c = 0$, we obtain the hydrodynamic conservation $a_{HD} = 2\beta/\alpha$. The other way of looking at this is to say that the phenomenology used is incorrect by some factor (as a function of σ_c) compared to the expected conservation constant. Figure 3.1 shows the values of the correction factors. As expected, the correction factors converge at $\sigma_c = 0$ and a_- the mirror of a_+ about the origin $\sigma_c = 0$. As σ_c increases to 1 (there is only backwards propagating modes now), the forwards constant a_- turns off, whereas the backwards constant a_+ rises above 2. The opposite happens for $\sigma \to -1$. If we wish to enforce a proper conservation law (with constant $a_\pm$), we can construct an equation for the appropriate nonlinear equation for the energy based off the general form of the nonlinear $\lambda_\pm$ Model $C_{m,n}$

$$\frac{\mathrm{d}\lambda_\pm}{\mathrm{d}t} = \beta_\pm \left(Z_\pm^m Z_\mp^n\right)^{\frac{1}{n+m}} \tag{3.58}$$

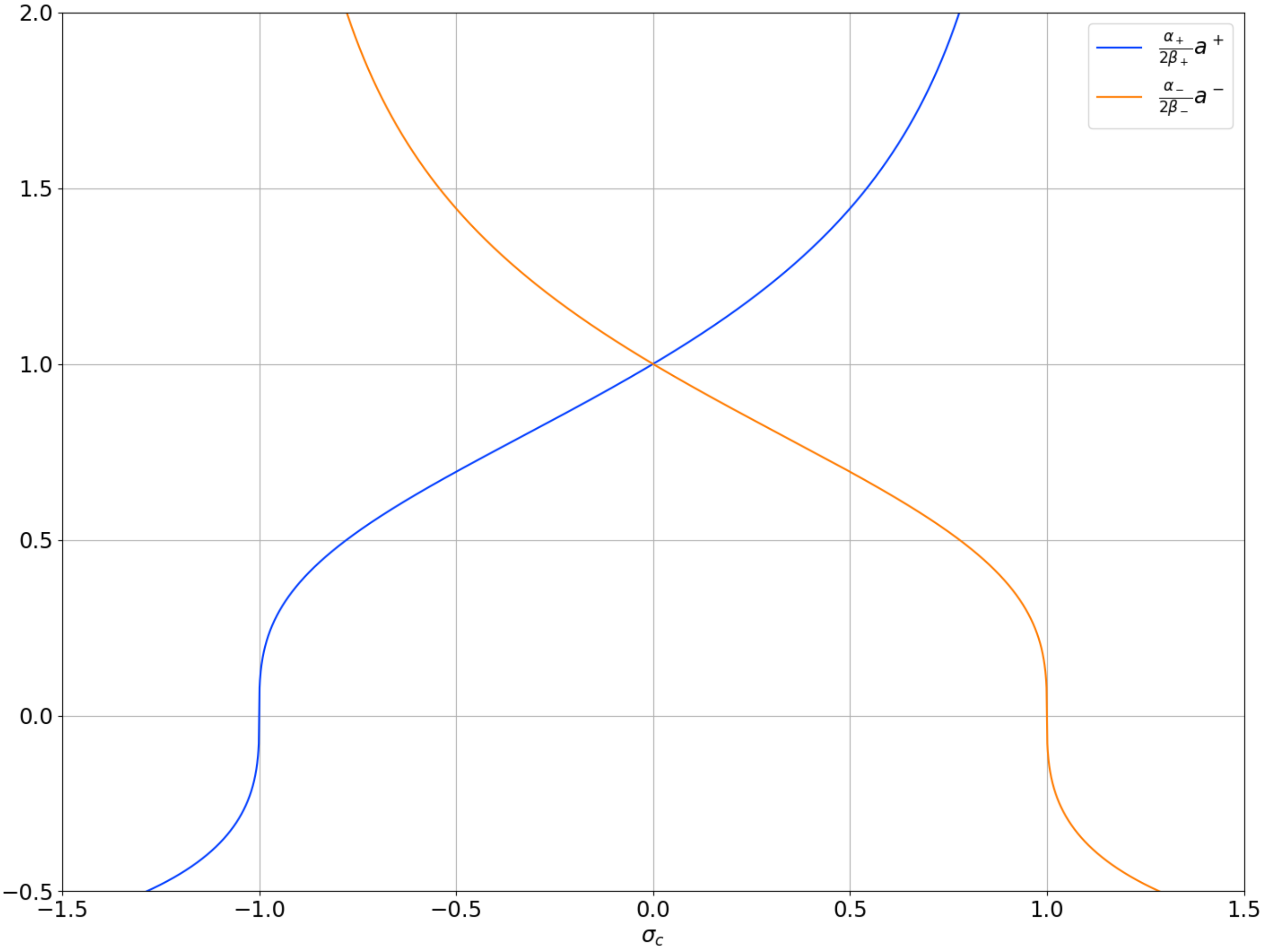

Figure 3.1: Plot of the conservation constants a_+ (blue) and a_- (orange) scaled to only the correction factors as a function of σ_c.

Using $Z_\pm^{a_\pm^{m,n}} \lambda_\pm = const$, the form of $a_\pm^{m,n}$ is the following

$$a_+^{m,n} = \frac{2\beta_+}{\alpha_+}\left(\frac{1+\sigma_c}{1-\sigma_c}\right)^{\frac{m}{2(m+n)}} \tag{3.59}$$

$$a_-^{m,n} = \frac{2\beta_-}{\alpha_-}\left(\frac{1-\sigma_c}{1+\sigma_c}\right)^{\frac{m}{2(m+n)}} \tag{3.60}$$

In order for there to be no correction factor in the conservation power, $a_\pm^{m,n} = \frac{2\beta_\pm}{\alpha_\pm}$, the nonlinear term for $Z_\pm^2$ needs to be

$$\left.\frac{\mathrm{d}Z_\pm^2}{\mathrm{d}t}\right|_{NL} = -\alpha_\pm \frac{Z_\pm^2\left(Z_\pm^m Z_\mp^n\right)^{\frac{1}{m+n}}}{\lambda_\pm} \tag{Model $A_{m,n}$}$$

3.2.4 Energy Difference D Models

Constructing a nonlinear phenomenology for the energy difference D is not as simple as for the Elsässer fields as the energy difference is not conserved by nonlinear interactions in the energy containing, and inertial ranges. Another aspect to note is that solar wind observations suggest that the normalized energy difference is approximately constant $\sigma_D = E_D/E_T \approx -1/3$ [46]. Matthaeus et al. [35] notes that the energy difference increases toward zero due to the Alfvén effect at the Alfvén timescale $\tau_A^D = \lambda/V_A$. The Alfvén effect growth is assumed to be counteracted by the spectral transfer of the total energy (to reach the equilibrium at $\sigma_D \approx 1/3$). Therefore, the nonlinear model for the Matthaeus et al. [35] equation is depicted as the following

$$\left.\frac{\mathrm{d}D}{\mathrm{d}t}\right|_{NL} = -\alpha_D \frac{D}{\tau_A^D} - \frac{1}{2}\left(\alpha_+ \frac{Z_+^2}{\tau_S^+} + \alpha_- \frac{Z_-^2}{\tau_S^-}\right) \tag{3.61}$$

The first term is the Alfvén effect, that pushes D towards 0 whether D is positive or negative; the second, negative term corresponds to the decrease in the energy difference due to the spectral transfer. Matthaeus et al. [35] finds that Equation 3.61 does not always behave physically and so modifies it to the following

$$\left.\frac{\mathrm{d}D}{\mathrm{d}t}\right|_{NL} = -\alpha_D \frac{D}{\tau_A^D} - \frac{1}{2}\frac{u^2}{\tau_*} \tag{3.62}$$

where τ_* is the timescale for the decay of the total energy

$$\tau_* = \left| \frac{Z_+^2 + Z_-^2}{\frac{\mathrm{d}Z_+^2}{\mathrm{d}t}\Big|_{NL} + \frac{\mathrm{d}Z_-^2}{\mathrm{d}t}\Big|_{NL}} \right| \tag{3.63}$$

The denominator of τ_* is negative, hence the absolute value is applied to ensure that the timescale is positive. The Adhikari et al. [1] model takes its energy difference model from Dosch et al. [19]. Wherein, the nonlinear energy difference term is simply derived from the equations according to Zank et al. [64]

$$\frac{\mathrm{d}D}{\mathrm{d}t}\bigg|_{NL} = -\alpha_D D \left(\frac{Z_+}{\lambda_-} + \frac{Z_-}{\lambda_+} \right) \tag{Model C}$$

In connection with the equations introduced in subsection 3.1.1, we will focus on energy difference phenomenologies derived in the styles of Equations (3.61) and (3.62) [35]. Matthaeus et al. [35] assumed that the energy difference Alfvén timescale τ_A^D occurs with the energy difference correlation length $\tau_A^D = \lambda_D/V_A$. This might not be the case, in this thesis we test whether the correlation length in the energy difference Alfvén timescale is associated with the energy difference correlation length $\tau_A^D = \lambda_D/V_A$ or the average Elsässer variable correlation length $\tau_A^D = \lambda/V_A$ where $\lambda = \frac{1}{2}(\lambda_+ + \lambda_-)$. Equation 3.61 now becomes the following models

$$\frac{\mathrm{d}D}{\mathrm{d}t}\bigg|_{NL} = -\alpha_D \frac{D}{\tau_A^D} + \alpha_{D,2} \left(\frac{\mathrm{d}Z_+^2}{\mathrm{d}t}\bigg|_{NL} + \frac{\mathrm{d}Z_-^2}{\mathrm{d}t}\bigg|_{NL} \right) \tag{Model A}$$

$$\overset{\tau_A^D \to \lambda_D/V_A}{=} -\alpha_D \frac{DV_A}{\lambda_D} + \alpha_{D,2} \left(\frac{\mathrm{d}Z_+^2}{\mathrm{d}t}\bigg|_{NL} + \frac{\mathrm{d}Z_-^2}{\mathrm{d}t}\bigg|_{NL} \right) \tag{Model A_{λ_D}}$$

$$\overset{\tau_A^D \to \lambda/V_A}{=} -\alpha_D \frac{DV_A}{\lambda} + \alpha_{D,2} \left(\frac{\mathrm{d}Z_+^2}{\mathrm{d}t}\bigg|_{NL} + \frac{\mathrm{d}Z_-^2}{\mathrm{d}t}\bigg|_{NL} \right) \tag{Model A_{λ}}$$

and Equation 3.62 becomes

$$\frac{\mathrm{d}D}{\mathrm{d}t}\bigg|_{NL} = -\alpha_D \frac{D}{\tau_A^D} - \alpha_{D,2} \frac{u^2}{\tau^*} \tag{Model B}$$

$$\overset{\tau_A^D \to \lambda_D/V_A}{=} -\alpha_D \frac{DV_A}{\lambda_D} - \alpha_{D,2} \frac{u^2}{\tau^*} \tag{Model B_{λ_D}}$$

$$\overset{\tau_A^D \to \lambda/V_A}{=} -\alpha_D \frac{DV_A}{\lambda} - \alpha_{D,2} \frac{u^2}{\tau^*} \tag{Model B_{λ}}$$

In Model A and Model B the negative sign needed in order to relax the normalized energy difference towards $-1/3$ is in the nonlinear terms for the Elsässer energies (the second terms on the RHS). Since we do not really know how much the Elsässer spectral cascade effects the energy difference equilibrium with the Alfvén effect, $\alpha_{D,2}$ has been added to the equation.

3.2.5 Energy Difference Length Scale λ_D Models

Models for λ_D are a bit different from the models for the other variables. There is not much literature on phenomenologies for λ_D and, like D there is no pure hydrodynamic relation to compare to. Matthaeus et al. [35] uses only a five equation evolution model, λ_D is chosen such that it is determined by the Elsässer correlation lengths $\lambda_\pm$

$$\lambda_D = \frac{\lambda_+ Z_\pm^2 + \lambda_- Z_-^2}{Z_+^2 + Z_-^2} \tag{3.64}$$

Adhikari et al. [1] uses the same idea as Model 0, wherein it is assumed the area under the curve of the cross-correlation tensor $L_D = \int_0^\infty \boldsymbol{R}_{ii}^{Ds}(w)\mathrm{d}w = D\lambda_D$ (see Appendices B and D) is constant

$$\left.\frac{\mathrm{d}L_D}{\mathrm{d}t}\right|_{NL} = 0 \tag{Model 0}$$

Another method for forming the nonlinear transport term for the correlation scale is to separate L_D into its kinetic L_u and magnetic L_b components $L_D = L_u - L_b$. We can then use the phenomenologies for L_u and L_b to construct the phenomenology for L_D

$$\begin{align}
\left.\frac{\mathrm{d}L_D}{\mathrm{d}t}\right|_{NL} &= \left.\frac{\mathrm{d}L_u}{\mathrm{d}t}\right|_{NL} - \left.\frac{\mathrm{d}L_b}{\mathrm{d}t}\right|_{NL} \tag{3.65}\\
&= u^2 \left.\frac{\mathrm{d}\lambda_u}{\mathrm{d}t}\right|_{NL} + \lambda_u \left.\frac{\mathrm{d}u^2}{\mathrm{d}t}\right|_{NL} - b^2 \left.\frac{\mathrm{d}\lambda_b}{\mathrm{d}t}\right|_{NL} - \lambda_b \left.\frac{\mathrm{d}b^2}{\mathrm{d}t}\right|_{NL} \tag{3.66}\\
&= u^2 \left(\beta_u u\right) + \lambda_u \left(-\alpha_u \frac{u^3}{\lambda_u}\right) - b^2 \left(\beta_b u\right) - \lambda_b \left(-\alpha_b \frac{ub^2}{\lambda_b}\right) \tag{3.67}\\
&= \left(\beta_u - \alpha_u\right) u^3 - \left(\beta_b - \alpha_b\right) ub^2 \tag{Model A}
\end{align}$$

Model A gives four parameters $\alpha_{u,b}$ and $\beta_{u,b}$. Choosing $\alpha_u = \beta_u$ and $\alpha_b = \beta_b$ we obtain Model 0. If we assume that $\alpha_D = \alpha_u = \alpha_b$ and $\beta_D = \beta_u = \beta_b$ then Model A becomes $\left(\beta_D - \alpha_D\right)\left(u^3 - ub^2\right) = \left(\beta_D - \alpha_D\right) uD$. The last option would be to consider the energy difference correlation length evolves proportional to itself over a timescale (similar to the Elsässer correlation length $\lambda_\pm$ Model B). In this case, as the energy difference is affected by the Alfvén timescale, we shall assume that its correlation integral does as well

$$\left.\frac{\mathrm{d}L_D}{\mathrm{d}t}\right|_{NL} = -\beta_D \frac{L_D}{\tau_A} \tag{Model B}$$

As mentioned in subsection 3.2.5, the Alfvén timescale can either occur with the energy difference correlation length $\tau_A = \lambda_D / V_A$, or the total energy $\tau_A = \lambda / V_A$

$$\left.\frac{\mathrm{d}L_D}{\mathrm{d}t}\right|_{NL} = -\beta_D V_A D \tag{Model B_{λ_D}}$$

$$\left.\frac{\mathrm{d}L_D}{\mathrm{d}t}\right|_{NL} = -\beta_D V_A D \frac{\lambda_D}{\lambda} \tag{Model B_λ}$$

3.3 Source Driving

As previous and later sections have described (Sections 2.5 and 4.2), there are additional phenomena that increase the energy in the solar wind. Since the shear sources $S_\pm^{shear}$ and shock sources $S_\pm^{shock}$ have the same form, we will encapsulate both of the effects into a single source term $S_\pm^{sh}$ with the constant parameter C_{sh} which will have a typical value $C_{sh} = 0.5$ [13]. In this thesis we will be including only the shear (and shock) and pickup ion driving sources. We will also assume that the pickup ion and shear sources will increase the kinetic and magnetic energies equally, therefore the source terms for the energy evolution equations are

$$\left.\frac{\mathrm{d}Z_\pm^2}{\mathrm{d}t}\right|_S = S_\pm^{sh} + S^{PID} \tag{3.68}$$

$$\left.\frac{\mathrm{d}D}{\mathrm{d}t}\right|_S = 0 \tag{3.69}$$

Here, there is no change due to the sources for the energy difference as the changes to the magnetic and kinetic energies cancel out.

Unfortunately there is more nuance to the source terms required for the correlation lengths. There are several arguments for the source terms for the correlation lengths that are discussed in the following three subsections and examined in this thesis.

3.3.1 No Length Scale Sources

A simple assumption to make for the correlation lengths is to examine the ranges that the sources involve. The pickup ion driving occurs due to the interstellar neutral atoms being ionized, resulting in a gyration around the magnetic field at the ion gyroradius ρ_i. The smallest scale in the MHD cascade is where the dissipation starts to occur, which is theorized to be around the ion gyroradius therefore the increase in the energy due to the pickup ion driving is only at the smallest scale.

For the case of the shear effects, if the shear driving is at the correlation length scale then the effect is 0 [12]. In this scenario, we assume that we can ignore the correlation length source terms

$$\left.\frac{\mathrm{d}\lambda_\pm}{\mathrm{d}t}\right|_S = 0 \tag{3.70}$$

$$\left.\frac{\mathrm{d}\lambda_D}{\mathrm{d}t}\right|_S = 0 \tag{3.71}$$

Written in terms of the correlation integrals

$$\left.\frac{\mathrm{d}L_\pm}{\mathrm{d}t}\right|_S = \lambda_\pm \left.\frac{\mathrm{d}Z_\pm^2}{\mathrm{d}t}\right|_S \tag{3.72}$$

$$\left.\frac{\mathrm{d}L_D}{\mathrm{d}t}\right|_S = 0 \tag{3.73}$$

3.3.2 Maintain Length Scale Conservation Laws

Even though the sources affect different length-scales, in order to keep $Z_\pm^{a_\pm}\lambda_\pm = const$, where $a_\pm = 2\beta_\pm/\alpha_\pm$, there must be an effective negative source term in the $\lambda_\pm$ equations. Using $\frac{\mathrm{d}(Z_\pm^{a_\pm}\lambda_\pm)}{\mathrm{d}t} = 0$ yields

$$\left.\frac{\mathrm{d}\lambda_\pm}{\mathrm{d}t}\right|_S = -\frac{a_\pm}{2}\frac{\lambda_\pm}{Z_\pm^2}\left.\frac{\mathrm{d}Z_\pm^2}{\mathrm{d}t}\right|_S = -\frac{a_\pm}{2}\frac{\lambda_\pm}{Z_\pm^2}\left(S_\pm^{sh} + S^{PID}\right) \tag{3.74}$$

$$\left.\frac{\mathrm{d}\lambda_D}{\mathrm{d}t}\right|_S = 0 \tag{3.75}$$

Written in terms of the integrated correlation functions we have

$$\left.\frac{\mathrm{d}L_\pm}{\mathrm{d}t}\right|_S = \left(1 - \frac{a_\pm}{2}\right)\lambda_\pm \left.\frac{\mathrm{d}Z_\pm^2}{\mathrm{d}t}\right|_S = \left(1 - \frac{a_\pm}{2}\right)\lambda_\pm \left(S_\pm^{sh} + S^{PID}\right) \tag{3.76}$$

$$\left.\frac{\mathrm{d}L_D}{\mathrm{d}t}\right|_S = 0 \tag{3.77}$$

3.3.3 Constant Area Under the Curve

The last choice is a specific condition of maintaining the conservation laws, where $a_\pm = 2$. This choice relies on the argument that we want the area under the correlation integrals to remain constant, thus

$$\left.\frac{\mathrm{d}L_\pm}{\mathrm{d}t}\right|_S = 0 \tag{3.78}$$

$$\left.\frac{\mathrm{d}L_D}{\mathrm{d}t}\right|_S = 0 \tag{3.79}$$

3.4 Temperature Models

The last piece of the solar wind model is an equation for the temperature evolution. If we assume that the plasma is expanding radially with uniform velocity (in addition to the conservation of mass), then the density falls off according to $\rho = \rho_0 \left(R_0/r\right)^2$. As the volume of the spherically expanding plasma increases, the temperature falls off as the internal energy decreases. This process can be called adiabatic cooling and is represented by the following equation

$$PV^\gamma = const \tag{3.80}$$

where P is the pressure, V is the volume and γ is the appropriate adiabatic index. In the solar wind, the adiabatic index is $\gamma = 5/3$. The temperature evolution equation can be written as

$$\frac{\mathrm{d}T}{\mathrm{d}r} = -2(\gamma - 1)\frac{T}{r} = -\frac{4}{3}\frac{T}{r} \tag{3.81}$$

As the dissipation of the turbulence is thought to be responsible for the heating that is observed in the solar wind [51, 52, 28], the temperature increases proportional to the rate of decrease/transfer of energy in the nonlinear terms representing the energy cascade. The temperature equation is modified to the form (modified from the Breech et al. [13] model (section E.2))

$$\frac{\mathrm{d}T}{\mathrm{d}r} = -\frac{4}{3}\frac{T}{r} + \frac{1}{3}\frac{m_p}{k_B}\left(-\left.\frac{\mathrm{d}Z_+^2}{\mathrm{d}t}\right|_{NL} - \left.\frac{\mathrm{d}Z_-^2}{\mathrm{d}t}\right|_{NL}\right) \tag{3.82}$$

The first term stays the same as the adiabatic temperature case, but now, a second term is added to associate the effect of the transition of energy into temperature through the energy cascade. The nonlinear transfer terms are negative because they need to associate with the increase in the temperature. The proton mass m_p and Boltzmann constant k_B ensure that the second term has the correct units (in Kelvin/distance). For this model, we are assuming that the energy difference does not effect the temperature

The Adhikari et al. [1] model uses a slightly different modification to the temperature (section E.1)

$$\frac{\mathrm{d}T}{\mathrm{d}r} = -\frac{4}{3}\frac{T}{r} + \frac{1}{9}\frac{m_p}{k_B}\alpha\left(\frac{Z_+^2 Z_-}{\lambda_+} + \frac{Z_-^2 Z_+}{\lambda_-} + D\left(\frac{Z_-}{\lambda_+} + \frac{Z_+}{\lambda_-}\right)\right) \tag{3.83}$$

The first notable difference is that Adhikari et al. adds in the nonlinear term for the energy difference, implying that the energy difference also has an energy cascade that transitions into temperature at the smallest scales. The second difference is the neglect of the Kármán-Taylor constants ($\alpha_\pm$, α_D) from the nonlinear terms in the energy equations. The energy cascade implies that the rate of the cascade is the rate that the energy dissipates into temperature, and therefore the rate at which the temperature increases. There is a parameter in the second term α, but that is set as $\alpha = 1$ in Adhikari et al. [1], whereas $\alpha_\pm = 2$ and $\alpha_D = 1$.

The two modified temperature equations provided do not explicitly include the increases in temperature due to the source terms (section 3.3). Since the sources increase the energy, the result is that there is more energy in the cascade, so an increase in temperature through the coupling to the nonlinear terms is seen.

Chapter 4

Data Analysis

In this chapter we compile some MHD simulation data that will be discussed here and referenced in later sections. We also look at observational data which provides our initial conditions and showcases the quantitative behaviour we should expect from our models.

4.1 Simulation Data Analysis

This section contains data obtained from a set of simulations that were run. The simulations were run as a two dimensional MHD simulation using a resolution of 4096 by 4096 over various σ_c starting conditions. The viscosity ν and resistivity η were set equal, at 0.0003. The mean background magnetic field was chosen to be $B_0 = 0$, this is due to the fact that the simulations are in two dimensions only. To mimic the more realistic two dimensional isotropic turbulence (rather than three dimensional isotropic turbulence), the background magnetic field must be normal to the turbulent plane. Running a two dimensional MHD simulation is great for saving compute time and simplifying analysis, but might fail to capture the true nature of the turbulence, particularly any wave effects that propagate parallel to the mean magnetic fields. In these plots produced from values calculated with the simulation, values taken early in the simulation ($t \approx 0 \rightarrow 0.5$) are not indicative of the result as the turbulence needs to 'boot-up' from the initial conditions given.

4.1.1 Correlation Length Relations

For the purposes of simplified models (*e.g.,* Breech et al. [13]), looking at how the correlation lengths evolve over time is helpful. With the correlation lengths defined as the correlation integrals divided by the energy

$$\lambda_\pm = \frac{L_\pm}{Z_\pm^2} \tag{4.1}$$

$$\lambda_D = \frac{L_D}{D} \tag{4.2}$$

we can obtain λ_+/λ_-, λ_+/λ_D and λ_-/λ_D. Figure 4.1 shows these correlation length fractions from the 2D MHD simulations. We would expect, as $\sigma_c \to 0$ the correlation lengths converge, this would allow us to approximate outer-heliosphere models as having a low σ_c value and one correlation length $\lambda_+ \approx \lambda_- \approx \lambda_D$. This expectation is met in the simulation, Figure 4.1 shows at $\sigma_c = 0$, λ_+/λ_D and λ_-/λ_D is approximately 1.2. As σ_c increases, λ_-/λ_D increases and λ_+/λ_- decreases. λ_+/λ_D only decreases a small amount to 0.7 as $\sigma_c \to 1$. λ_+/λ_- is approximately 0.9 at $\sigma_c = 0$ and decreases towards 0 as $\sigma_c \to 1$, this is expected as $Z_-^2 \to 0$ as $\sigma_c \to 1$ so $\lambda_- = L_-/Z_-^2$ gets very large. These values show that we can assume one correlation length at low σ_c values.

4.1.2 Energy Estimation

The total energy of the solar wind can be expressed in two ways, through the kinetic and magnetic energies (E_u, E_b respectively) or through the backward and forward propagating Elsässer energies (E_+, E_- respectively)

$$E_T = \frac{1}{4}\left(Z_+^2 + Z_-^2\right) = \frac{1}{2}\left(E_+ + E_-\right) \tag{4.3}$$

$$= \frac{1}{2}\left(u^2 + b^2\right) = E_u + E_b \tag{4.4}$$

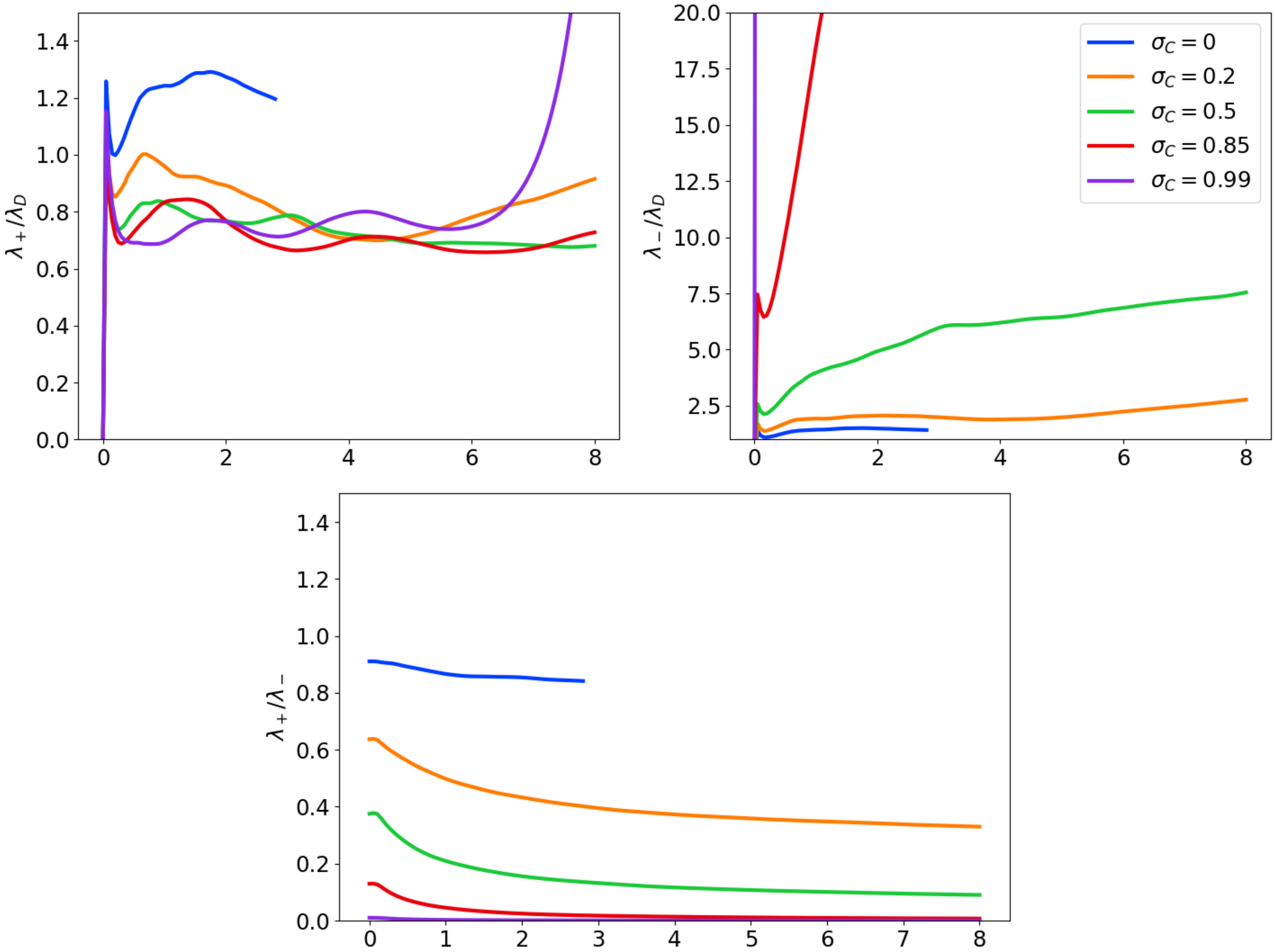

Figure 4.1: Plots of the similarities between the correlation lengths from the 2D MHD simulations with various runs representing different initial σ_c conditions.

We can describe the rate of change of the kinetic and magnetic energies in terms of the proportion of the rate of change of the total energy

$$\frac{\mathrm{d}E_u}{\mathrm{d}t} = \gamma_u \frac{\mathrm{d}E_T}{\mathrm{d}t} \tag{4.5}$$

$$\frac{\mathrm{d}E_b}{\mathrm{d}t} = \gamma_b \frac{\mathrm{d}E_T}{\mathrm{d}t} \tag{4.6}$$

where γ_u, γ_b is the proportion of change of the total energy for the kinetic and magnetic energies respectively. Since $E_T = E_u + E_b$, we must have $\gamma_b = 1 - \gamma_u$ and $0 \leq \gamma_u \leq 1$. We also know that we have an exact expression for the conservation of kinetic energy

$$\frac{1}{2}\frac{\mathrm{d}}{\mathrm{d}t}\left\langle \boldsymbol{u}_i \boldsymbol{u}_i \right\rangle = -\frac{1}{2}\nu \left\langle \Sigma_{ij} \left(\partial_i \boldsymbol{u}_j + \partial_j \boldsymbol{u}_i\right)^2 \right\rangle = -\nu \left\langle |\boldsymbol{\omega}|^2 \right\rangle \tag{4.7}$$

where the vorticity is the curl of the velocity $\boldsymbol{\omega} = \nabla \times \boldsymbol{u}$. Similarly, the conservation of magnetic energy is

$$\frac{1}{2}\frac{\mathrm{d}}{\mathrm{d}t}\left\langle \boldsymbol{b}_i \boldsymbol{b}_i \right\rangle = -\eta \left\langle |\boldsymbol{j}|^2 \right\rangle \tag{4.8}$$

where the current is the curl of the magnetic field $\boldsymbol{j} = \nabla \times \boldsymbol{b}$. The quantities for the viscosity ν, resistivity η, enstrophy ω^2 and the squared current j^2 are known from the simulation. Therefore, we can obtain expressions for the accuracy of the phenomenological energy containing range dissipation (calculated via the Elsässer variables) versus the true dissipation. With the rate of change of the total energy

$$\frac{\mathrm{d}E_T}{\mathrm{d}t} = \frac{1}{4}\left(\alpha_+ \frac{Z_+^2 Z_-}{\lambda_+} + \alpha_- \frac{Z_-^2 Z_+}{\lambda_-}\right) \tag{4.9}$$

and the rate of changes of the kinetic and magnetic energies ($\frac{\mathrm{d}E_u}{\mathrm{d}t}, \frac{\mathrm{d}E_b}{\mathrm{d}t}$) calculated via finite differences from the simulation data. The proportions of the rate of energy changes (γ_u, γ_b) for the inertial range total energy are

$$\gamma_u = -4\frac{\mathrm{d}E_u}{\mathrm{d}t}\left(\alpha_+ \frac{Z_+^2 Z_-}{\lambda_+} + \alpha_- \frac{Z_-^2 Z_+}{\lambda_-}\right)^{-1} \tag{4.10}$$

$$\gamma_b = -4\frac{\mathrm{d}E_b}{\mathrm{d}t}\left(\alpha_+ \frac{Z_+^2 Z_-}{\lambda_+} + \alpha_- \frac{Z_-^2 Z_+}{\lambda_-}\right)^{-1} \tag{4.11}$$

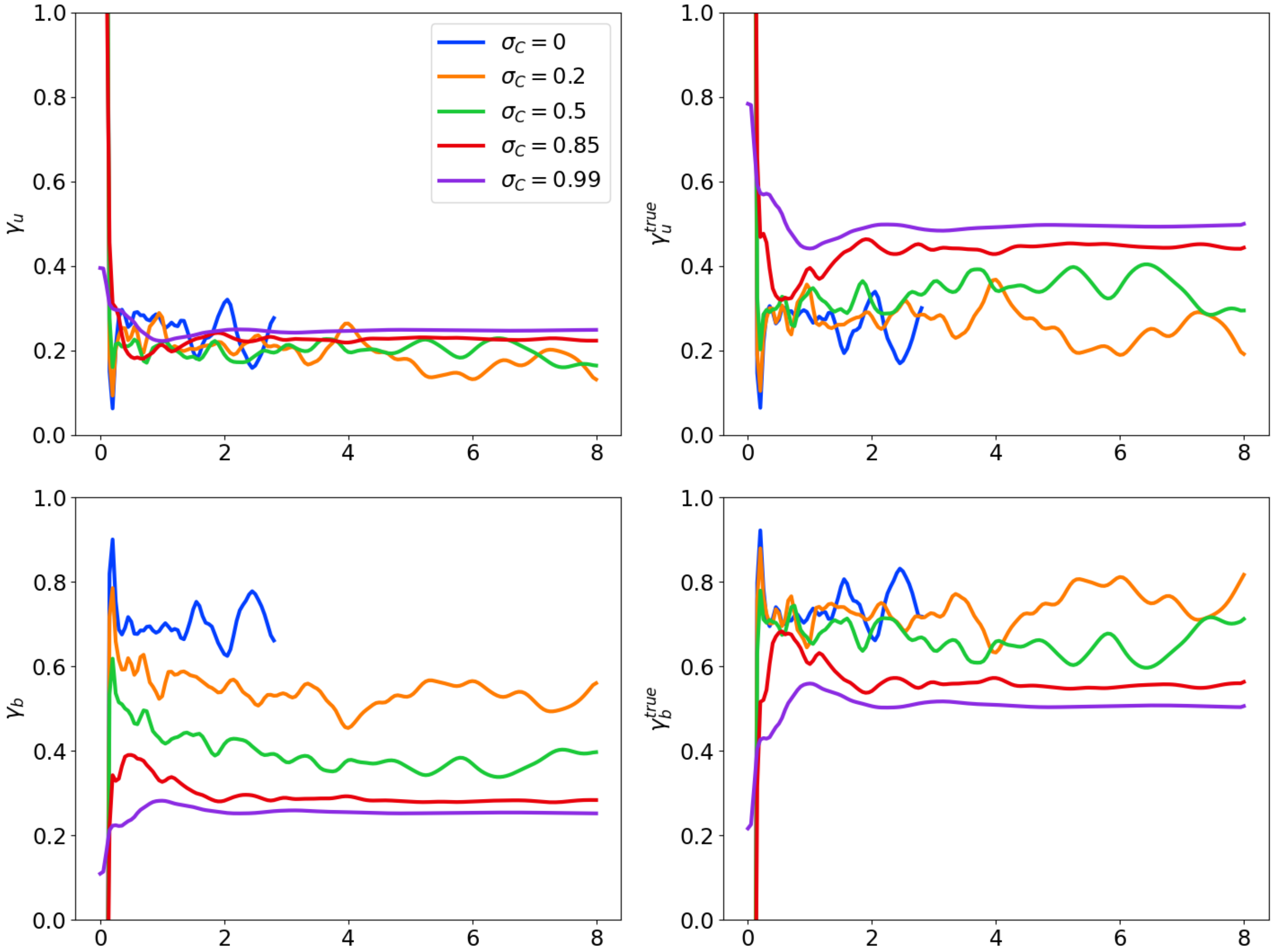

Figure 4.2: Plots of the proportions of change for the kinetic and magnetic energy for the nonlinear phenomenologies γ_u, γ_b and the true decay $\gamma_u^{true}, \gamma_b^{true}$ from the 2D MHD simulation data over time with several runs of varying initial σ_c values.

and the true simulation proportions of the rate of energy changes are

$$\gamma_u^{true} = -4\frac{\mathrm{d}E_u}{\mathrm{d}t}\left(\nu\frac{\omega^2}{2} + \eta\frac{j^2}{2}\right)^{-1} \tag{4.12}$$

$$\gamma_b^{true} = -4\frac{\mathrm{d}E_b}{\mathrm{d}t}\left(\nu\frac{\omega^2}{2} + \eta\frac{j^2}{2}\right)^{-1} \tag{4.13}$$

Figure 4.2 plots the true and phenomenological proportions of change (γ_u, γ_b) for the kinetic and magnetic energies from the various 2D MHD simulation. Straight away, the phenomenological models γ_u, γ_b do not suggest a conservation of energy $\gamma_b \neq 1 - \gamma_u$. γ_u maintains a value around 0.2 for all σ_c initial conditions, whereas γ_b is almost 0.8 for $\sigma_c = 0$ but decreases as σ_c increases, ending roughly equal to γ_u at $\sigma_c = 0.99$. The true proportions of change (γ_u^{true}, γ_b^{true}) shows the expected behaviour; energy is conserved $\gamma_b^{true} = 1 - \gamma_u^{true}$. At the low σ_c values (0, 0.2 and 0.5), γ_b^{true} is approximately 0.8 and γ_u^{true} is approximately 0.2. Towards the higher σ_c values, the proportion of rate of change of the kinetic energy increases towards 0.5 and γ_b^{true} decreases to 0.5, $\gamma_u^{true} \approx \gamma_b^{true}$. As the phenomenological model does not meet the expected results ($\gamma_{u,b} \neq \gamma_{u,b}^{true}$), it implies that the energy containing range model for the energy cascade (in the 2D MHD simulation) does not properly model the dissipation.

4.1.3 Nonlinear Parameter Estimation

With the simulation data, we can calculate the Kármán-Taylor nonlinear $\alpha_\pm$ and $\beta_\pm$ parameters, by taking the finite difference of the respective variable and dividing by the phenomenological term to get the parameter. Using $Z_\pm^2$ Model A,

$$\alpha_\pm = -\frac{\mathrm{d}Z_\pm^2}{\mathrm{d}t}\left(\frac{\lambda_\pm}{Z_\pm^2 Z_\mp}\right) \tag{4.14}$$

With two nonlinear equation models for $\lambda_\pm$ (Model A, Model B) we can obtain the following two parameters

$$\beta_\pm^A = \frac{\mathrm{d}\lambda_\pm}{\mathrm{d}t}\left(Z_\pm^2 Z_\mp\right)^{-1/3} \tag{4.15}$$

$$\beta_\pm^B = \frac{\mathrm{d}\lambda_\pm}{\mathrm{d}t}\left(\frac{1}{Z_\mp}\right) \tag{4.16}$$

Figure 4.3 shows the Kármán-Taylor "constants" $\alpha_\pm$, $\beta_\pm^{A,B}$ calculated from the 2D MHD simulation. As discussed in subsection 4.1.1, $Z_-^2 \to 0$ as $\sigma_c \to 1$ so α_- and $\beta_-^{A,B}$ get very large. α_+ is approximately constant for $\sigma_c = 0, 0.2, 0.5, 0.85$ with values around 0.1. At $\sigma_c = 0.99$, α_+ increases linearly over the duration of the simulation to 0.8. α_- is not constrained at the higher σ_c values, but at $\sigma_c = 0$ α_- has the same value as α_+ (which is expected). Even at $\sigma_c = 0.2$, α_- increases to 0.5 during the simulation.β_+^A is roughly constant (although it is less stable than $\alpha_\pm$) and ranging from 0.04 at $\sigma_c = 0$ to 0.01 at $\sigma_c = 0.85$. On

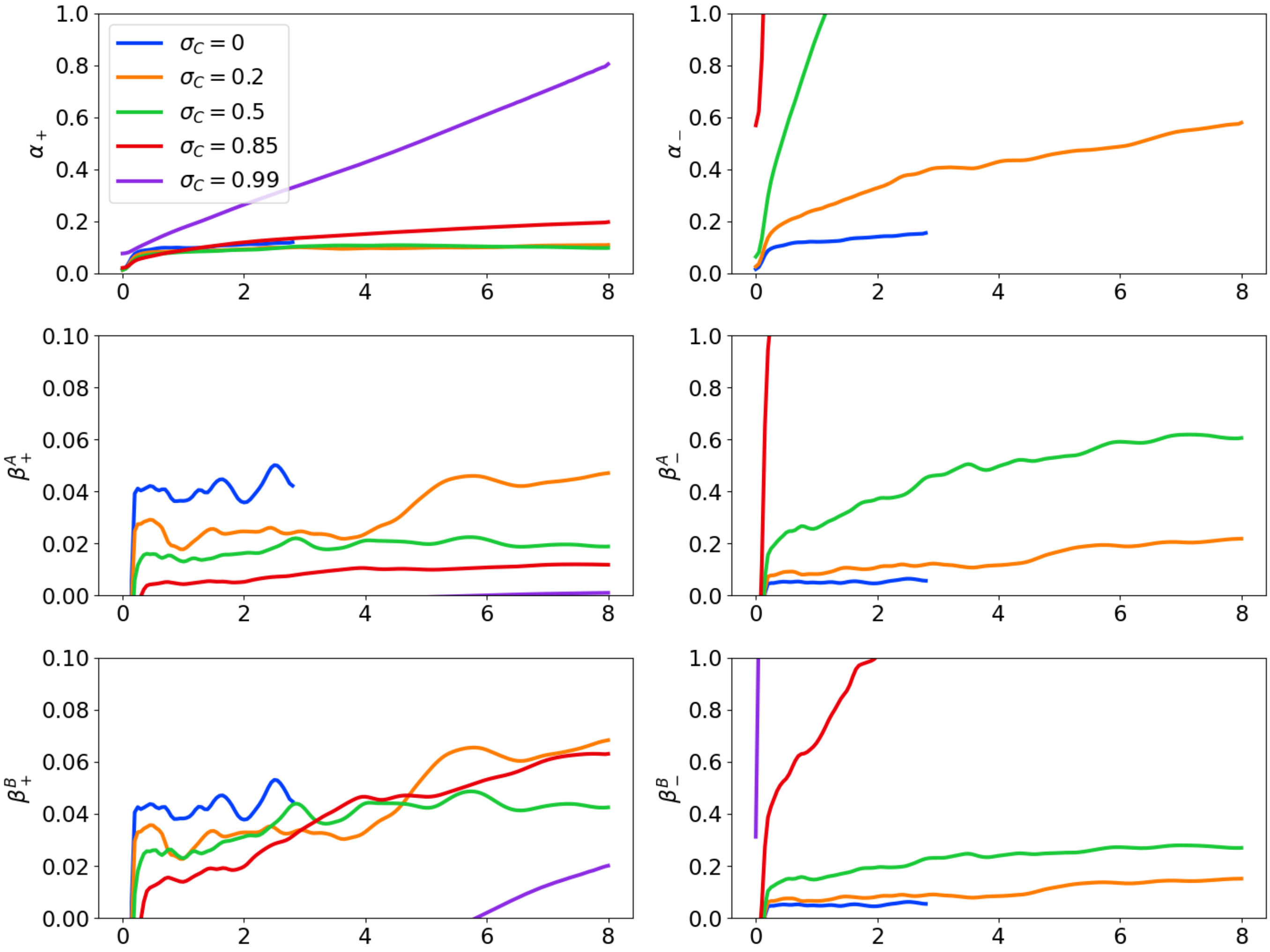

Figure 4.3: Plots of the nonlinear Kármán-Taylor constants ($\alpha_\pm$, $\beta^{A,B}_\pm$) from the 2D MHD simulations using various σ_c starting conditions.

the other hand, β^B_+ linearly increases during the simulation ending at values of 0.06 for $\sigma_c = 0.2, 0.85$ and 0.04 for $\sigma_c = 0.5$. Converse to $\beta^{A,B}_+$, β^A_- linearly increases more than β^B_+ over the course of the simulations. For both $\beta^{A,B}_-$, the value is increasing too quickly at high σ_c values (≥ 0.85). β^B_- has values 0.1 for $\sigma_c = 0, 0.2$ and 0.2 for $\sigma_c = 0.5$ and with β^A_+ increasing, it still maintains values around 0.1 for $\sigma_c = 0, 0.2$ but rises to 0.6 for $\sigma_c = 0.5$.

β_+ shows favourable behaviour when using $\lambda_\pm$ Model A; β^A_+ shows constant behaviour compared to β^B_+ across the different σ_c simulation runs. However, β_- shows favourable behaviour using $\lambda_\pm$ Model B; β^B_- shows constant behaviour compared to β^A_+ across the different σ_c simulation runs.

4.1.4 Conservation Constant

As an extension to the parameter estimation (subsection 4.1.3), we can estimate the parameters associated with the conservation laws mentioned in subsection 3.2.3. Using $Z^2_\pm$ Model A and $\lambda_\pm$ Model A, the conservation law values are

$$Z_\pm^{a^A_\pm}\lambda_\pm = C^A_\pm \tag{4.17}$$

with the powers

$$a^A_+ = \left(\frac{2\beta^B_+}{\alpha^B_+}\right)\left(\frac{1+\sigma_c}{1-\sigma_c}\right)^{1/3} \tag{4.18}$$

$$a^A_- = \left(\frac{2\beta^B_-}{\alpha^B_-}\right)\left(\frac{1-\sigma_c}{\sigma_c+1}\right)^{1/3} \tag{4.19}$$

Using $Z^2_\pm$ Model A and $\lambda_\pm$ Model B, the conservation law values are

$$Z_\pm^{a^B_\pm}\lambda_\pm = C^B_\pm \tag{4.20}$$

where

$$a^B_\pm = \frac{2\beta^B_\pm}{\alpha^B_\pm} \tag{4.21}$$

Figure 4.4 shows the conservation law powers for the two different $\lambda_\pm$ nonlinear models (using the same nonlinear $Z^2_\pm$ model) $a^{A,B}_\pm$ from the 2D MHD simulations. These powers are calculated from the parameters (subsection 4.1.3) and multiplied according to the equations stated above. Figure 4.5 shows the constants $C^{A,B}_\pm$ calculated from the $a^{A,B}_\pm$, $Z^2_\pm$ and $\lambda_\pm$ values derived from the 2D MHD simulations. You may note that, both Figure 4.4 and Figure 4.5 show the same values for both models $a^A_\pm = a^B_\pm$ (therefore, $C^A_\pm = C^B_\pm$). This is expected, as the difference associated with the parameters $\beta^A_\pm$ and $\beta^B_\pm$ caused by the difference in the nonlinear models is the inverse of the σ_c correction factor in $a^A_\pm$. If the function $f(x)$ defines taking the finite differences of the variable

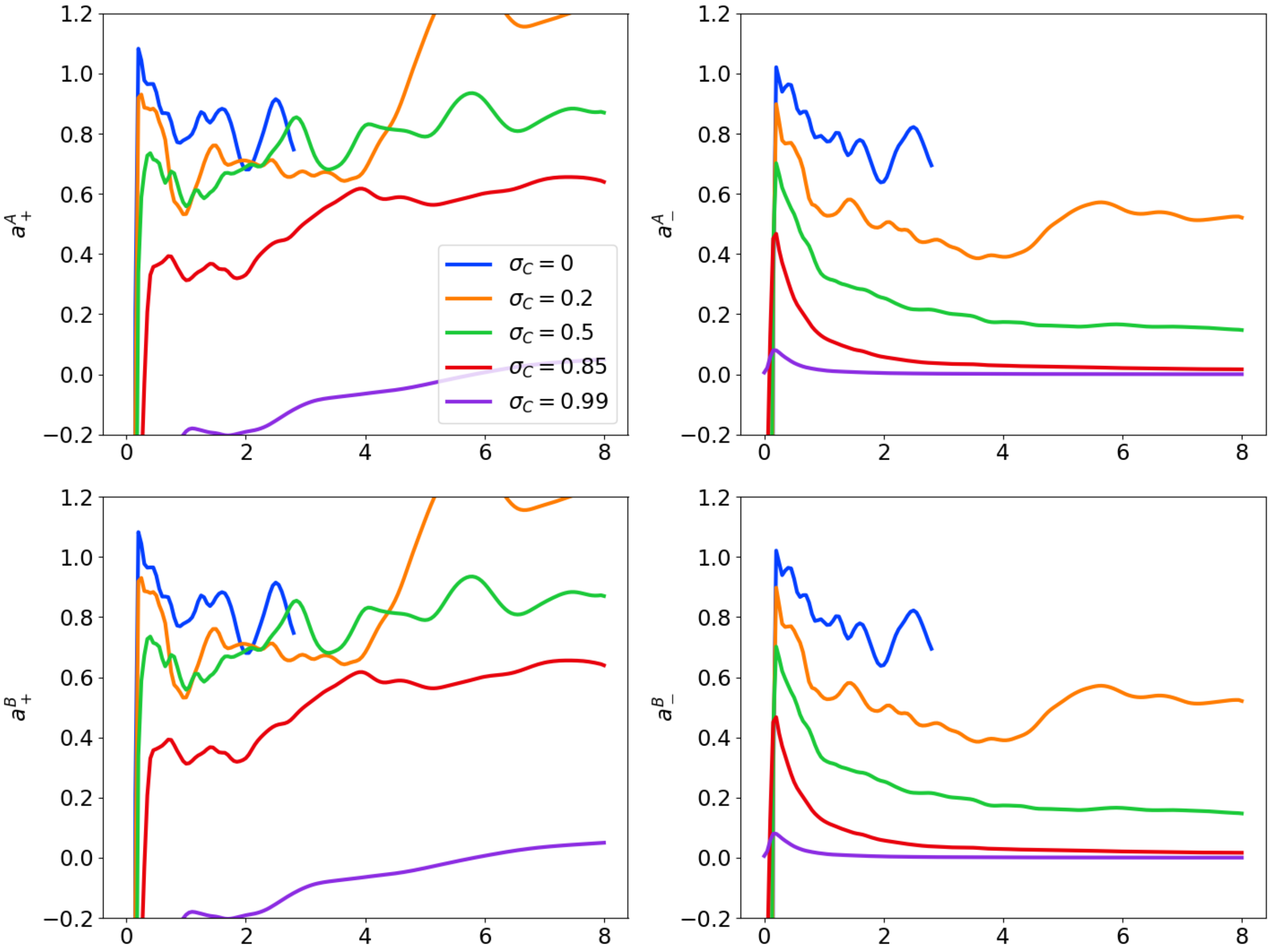

Figure 4.4: Plots of the conservation law powers $a_\pm^{A,B}$ from the 2D MHD simulation data over time with several runs of varying initial σ_c values.

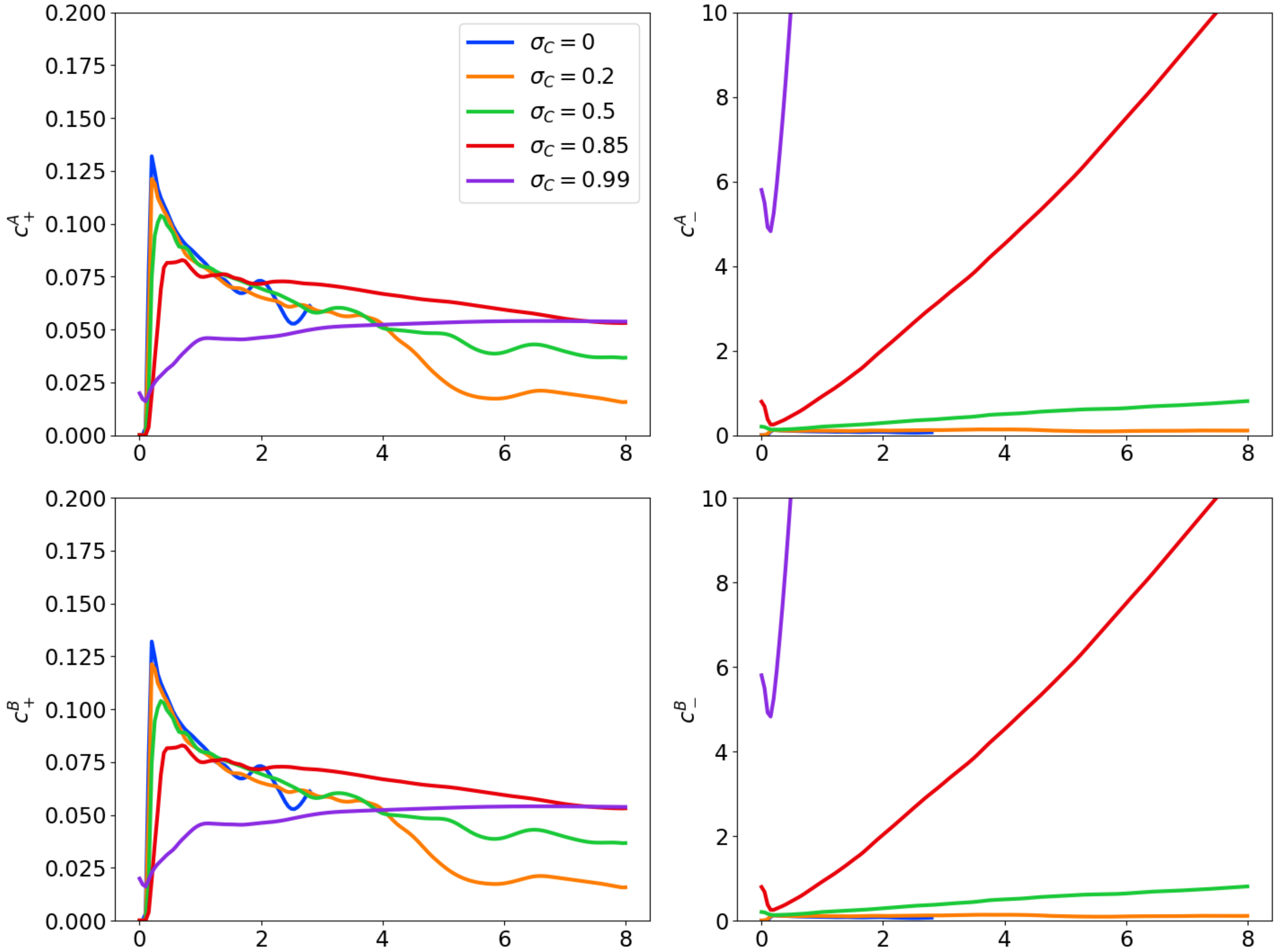

Figure 4.5: Plots of the conservation law constants $C_{\pm}^{A,B}$ from the 2D MHD simulation data over time with several runs of varying initial σ_c values.

x to estimate the rate of change, the conservation powers are calculated as

$$\alpha_{\pm}^{A,B} = \alpha_{\pm} = \frac{f(Z_{\pm}^2)\lambda_{\pm}}{Z_{\pm}^2 Z_{\mp}} \tag{4.22}$$

$$\beta_{\pm}^{A} = \frac{f(\lambda_{\pm})}{(Z_{\pm}^2 Z_{\mp})^{1/3}} \tag{4.23}$$

$$\beta_{\pm}^{B} = \frac{f(\lambda_{\pm})}{Z_{\mp}} \tag{4.24}$$

For example, equating the '+' conservation powers

$$a_{+}^{A} = a_{+}^{B} \tag{4.25}$$

$$\implies \frac{2\beta_{+}^{A}}{\alpha_{+}}\left(\frac{-\sigma_c - 1}{\sigma_c - 1}\right)^{1/3} = \frac{2\beta_{+}^{B}}{\alpha_{+}} \tag{4.26}$$

$$\implies \beta_{+}^{A}\left(\frac{-\sigma_c - 1}{\sigma_c - 1}\right)^{1/3} = \beta_{+}^{B} \tag{4.27}$$

$$\implies \frac{f(\lambda_{+})}{(Z_{+}^2 Z_{-})^{1/3}}\left(\frac{-\sigma_c - 1}{\sigma_c - 1}\right)^{1/3} = \frac{f(\lambda_{+})}{Z_{-}} \tag{4.28}$$

$$\implies \frac{Z_{-}}{(Z_{+}^2 Z_{-})^{1/3}}\left(\frac{-\sigma_c - 1}{\sigma_c - 1}\right)^{1/3} = 1 \tag{4.29}$$

$$\implies \frac{Z_{-}^2}{Z_{+}^2}\left(\frac{1 + \sigma_c}{1 - \sigma_c}\right) = 1 \tag{4.30}$$

which is true, as $Z_{-}^2/Z_{+}^2 = (\sigma_c - 1)/(-\sigma_c - 1)$.

Figure 4.5 shows that the *constants* $C_{\pm}^{A,B}$ aren't entirely constant. Although it could be argued that $C_{+}^{A,B}$ is relatively constant at all σ_c values and $C_{-}^{A,B}$ is roughly constant at $\sigma_c = 0, 0.2$. At $\sigma_c = 0.5, 0.85, 0.99$, the conservation constant $C_{-}^{A,B}$ is increasing over time in the simulation. The large values in $C_{-}^{A,B}$ is due to the large values found in Z_{-}^2 and λ_{-}, as the conservation power $a_{-}^{A,B}$ is relatively constant over the simulation time (Figure 4.5). Both $a_{\pm}^{A,B}$ decrease with increasing σ_c values and are approximately equal for $\sigma_c = 0, 0.2$.

4.2 Satellite Data

This section discusses observational data kindly given to us by Adhikari et al. [1] plotted in Figures 4.6 to 4.9. The data from Adhikari et al. [1] comes as two datasets, one for the inner heliosphere from the Helios 2 and Ulysses spacecraft from 0.29 AU to 5 AU and another for the outer heliosphere from the Voyager 2 spacecraft ranging from 1 AU to 75 AU.

Figure 4.6 shows the proton temperature for the Voyager 2 data [53] and the adiabatic cooling model (section 3.4). Clearly, there is a big difference between the adiabatic cooling model and the voyager 2 data. Past 1 AU, the Voyager 2 data shows an increase in temperature (compared to the adiabatic profile) that slowly decreases until around 20 AU. The increase in temperature observed is a strong indicator and attributed to turbulence being present in the solar wind [51]. The energy from the MHD turbulent fluctuations eventually dissipates and shows up as increased temperature resulting in the different temperature profile seen. Past 20 AU (in the outer heliosphere), there is another (rather sharp) increase in the observed temperature that is evidence of the interstellar pickup ions [29, 53] increasing the energy of the solar wind.

Figure 4.7 shows the Voyager 2 data [1] of the radial velocity and the density. The radial velocity shows that there are fluctuations in the speed over distance (really, time section 2.2). The slowest observed radial velocity is around 300 km/s whereas the fastest speeds reach over 650 km/s. The assumed $U_r = 400$ km/s matches nicely with the slower wind speeds seen, faster wind speeds will be captured by the shear driving turbulence term section 2.5. The second plot shows the log-log plot of the density showing around 10 particles per cubic centimetre at 1 AU and 0.001 particles per cubic centimetre at 75 AU. The model of spherical expansion of the density (obtained from the conservation of mass and the constant, radial velocity) $\rho = \rho_0 \left(R_0/r\right)^2$ matches nicely to the observed data.

Figure 4.8 shows the observational data of the backward Z_+^2 and forward Z_-^2 energies (per unit mass) and the normalized energy difference and cross helicity. Z_+^2 has an initial value of $13,515$ (km/s)^2 per unit mass. The backwards Elsässer energy decreases to a minimum of 9.99 (km/s)^2 per unit mass at 21 AU. Z_-^2 has an initial value of 753 (km/s)^2 per unit mass and decreases towards towards a similar minimum value of 8.02 (km/s)^2 per unit mass as Z_+^2 at 21

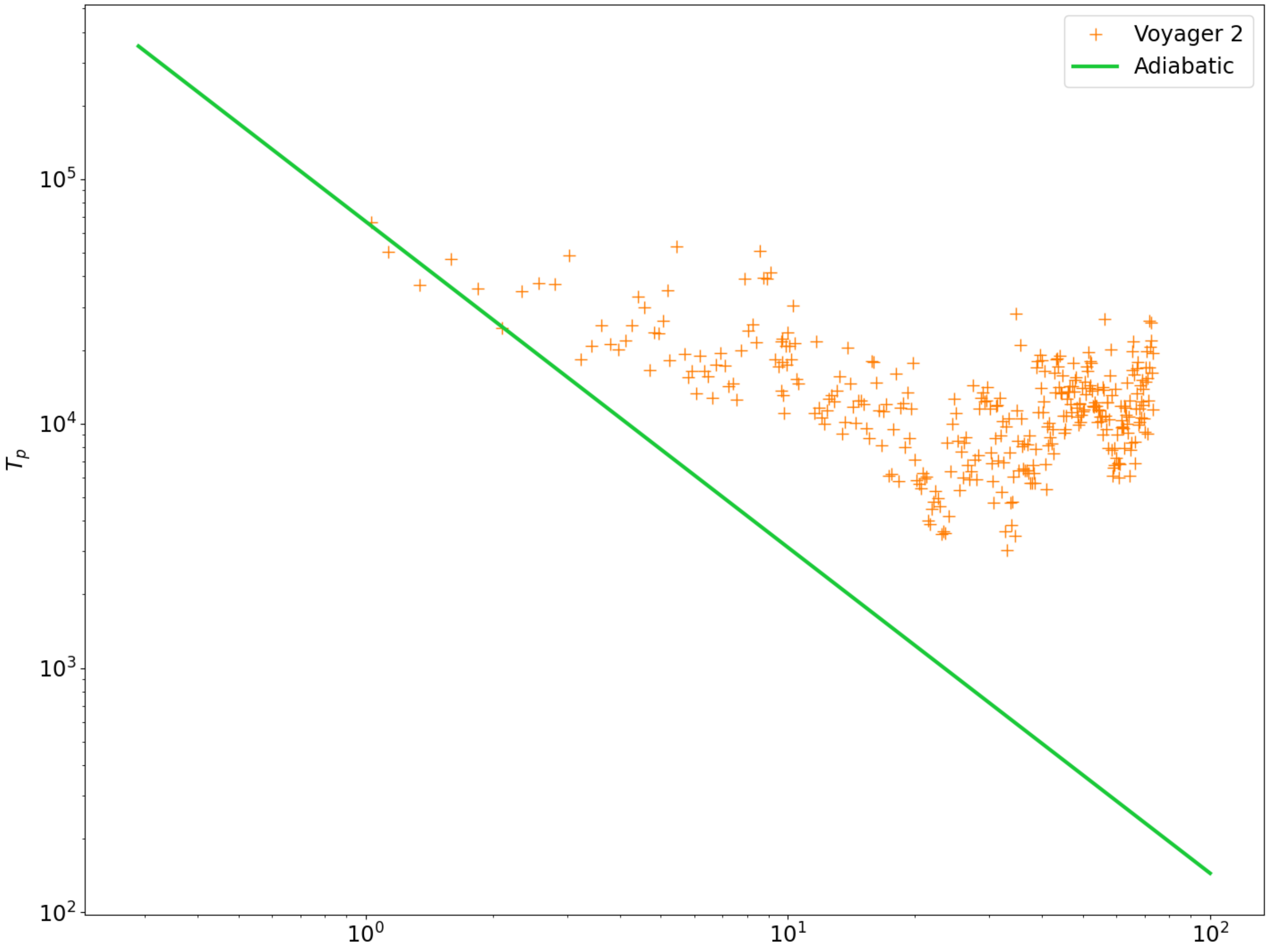

Figure 4.6: Proton temperature (in Kelvin) versus radial distance (in AU). Plotted is the Voyager 2 data (orange plus) and the adiabatic temperature model (green).

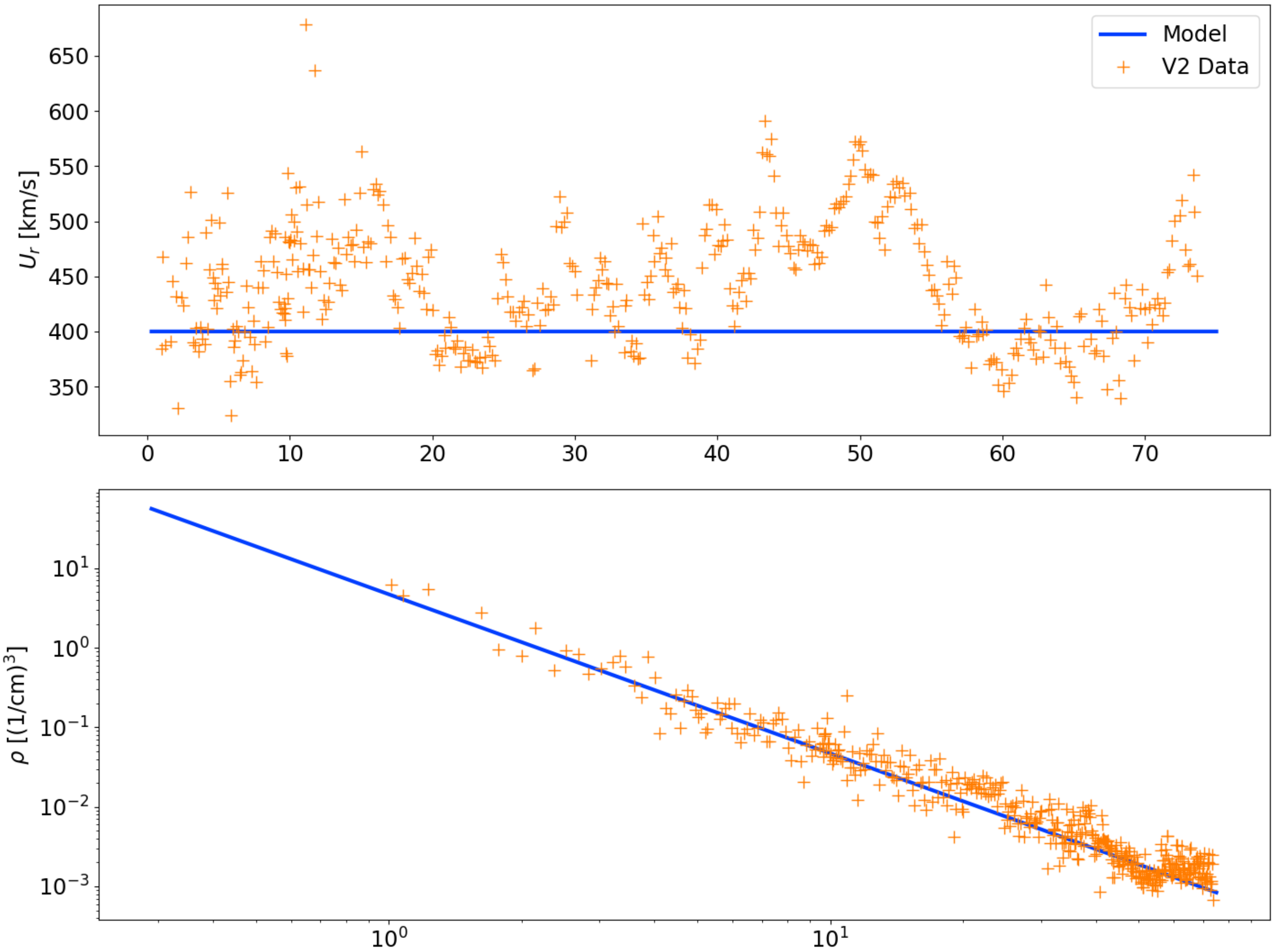

Figure 4.7: Graphs of satellite observations (orange) and the models (blue) of the radial velocity and the density. The observations are obtained from Voyager 2 (orange) ranging from 1 AU to 75 AU (courtesy of Adhikari et al. [1]). The radial velocity model shows the assumed constant radial velocity $U_r = 400$ km/s. The density model shows the assumed $\rho = \rho_0(R_0/r)^2$.

AU. Past 21 AU, we see the effects of the interstellar pickup ions, increasing the energy of Z_+^2 and Z_-^2. Observational data shows, for the normalized energy difference σ_D, an equality of the kinetic and magnetic energies at 0.29 AU. As the radial distance increases, σ_D decreases (to around -0.75) indicating that there is more magnetic energy in the solar wind. From the Voyager 2 data, σ_D increases past 10 AU back towards 0. Other observational studies tend to show that $\sigma_D \approx -1/3$ [46]. In the Helios 2/Ulysses data from 0.29 to 5 AU, the normalized cross helicity σ_c has an initial value of 0.894, then increases towards zero. This shows that in the early heliosphere, the Elsässer energy strongly favours the backward propagating modes. Then, towards 5 AU the forward and backward modes start to become more equal. The Voyager 2 data from 1 to 75 AU supports this observation, σ_c is centered around zero meaning that in the outer heliosphere the two Elsässer energy quantities are roughly equal.

Figure 4.9 shows the observational data of the backward λ_+, forward λ_- and energy difference λ_D correlation lengths. Starting with the Helios2/Ulysses dataset, λ_+ has an initial value of 0.00143 AU, λ_- has an initial value of 0.000779 AU and λ_D has an initial value of 0.0204 AU. λ_D decreases over 0.29 to 5 AU to a value of 0.997 AU whereas λ_+ and λ_- increase to values of 2.279 and 2.375 AU respectively. The value of 7.887 AU for λ_- at 4.610 AU is assumed to be an outlier. The Voyager 2 correlation length observational data is more difficult to analyse as it varies greatly from measurement to measurement and covers several orders of magnitude. The Voyager 2 data for λ_+ and λ_- seems to agree with the Helios2/Ulysses datasets where they overlap (to within some degree of variability) from 1 to 5 AU as most of the data lies within 10^6 and 10^7 kilometres. From the Voyager 2 dataset, the outlier point from the Helios2/Ulysses dataset could be considered less of an outlier. Past 5 AU, one might approximate λ_+ and λ_- as relatively constant. The majority of the λ_D data for both the datasets lie within 5×10^5 and 10^7 kilometres. However, not visible on the plot, λ_D has two negative values in

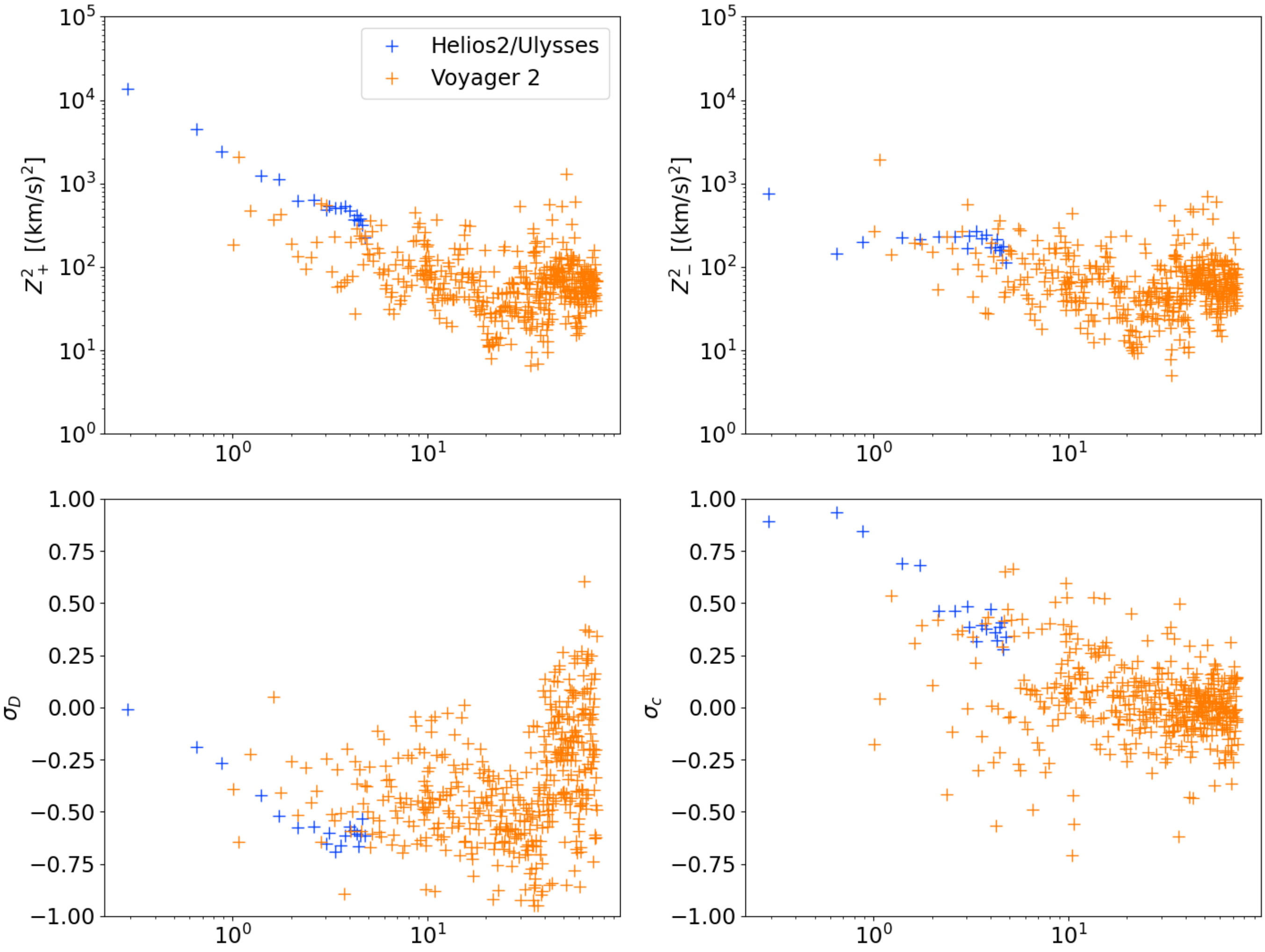

Figure 4.8: Graphs of satellite observations of the energy of the backward Z_+^2 and forward Z_-^2 propagating modes and the normalized energy difference σ_D and cross helicity σ_c. The observations from Helios 2 and Ulysses (blue) are from 0.29 to 5 AU and the observations from Voyager 2 (orange) are from 1 AU to 75 AU. The observational data is courtesy of Adhikari et al. [1].

Parameter	Initial Value
Z^2_{+0}	$13,515$ km^2/s^2
Z^2_{-0}	753 km^2/s^2
D_0	-57.07 km^2/s^2
T_0	3.5×10^5 K
λ_{+0}	0.00143 AU
λ_{-0}	0.000779 AU
λ_{D0}	0.0204 AU

Table 4.1: Initial conditions at 0.29 AU based off the Helios 2 dataset

the Voyager 2 dataset. At 5.140 AU $\lambda_D = -11.636 \times 10^6$ kilometres and at 9.202 AU $\lambda_D = -4.359 \times 10^6$ kilometres.

Keeping to the Helios 2 observed data, Table 4.1 shows the initial conditions (at $r = r_0 = 0.29$ AU) that will be used commonly in the next two sections.

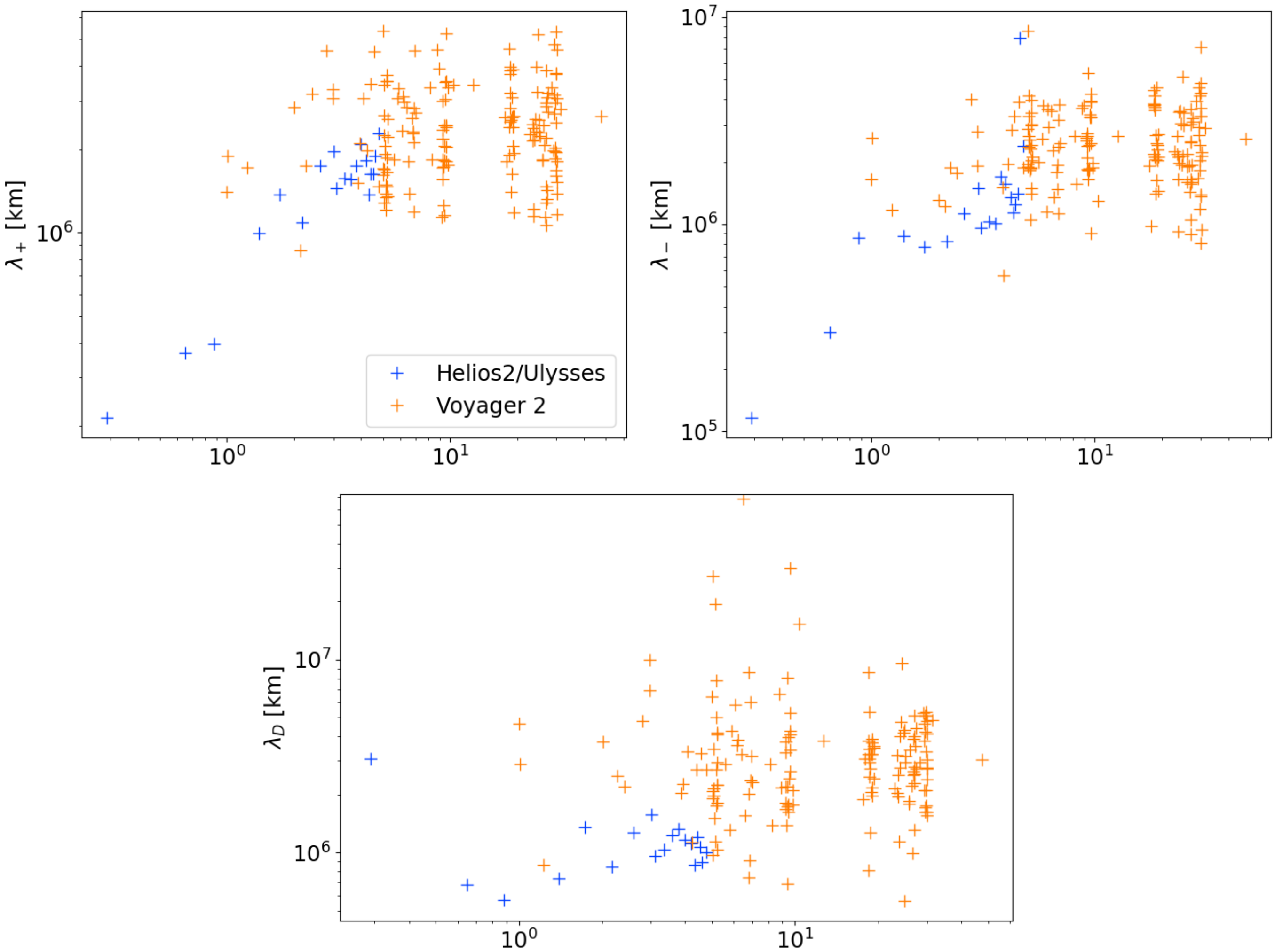

Figure 4.9: Graphs of satellite observations (in kilometres) for the backward λ_+, forward λ_- and energy difference λ_D correlation length fluctuations. The observations from Helios 2 and Ulysses (blue) are from 0.29 to 5 AU and the observations from Voyager 2 (orange) are from 1 AU to 75 AU. The observational data is courtesy of Adhikari et al. [1].

Chapter 5

Analytic Solutions

In this section, we will be taking the steady state equations mentioned in Appendix D with the additional assumption that $V_A/U \ll 1$

$$\frac{\mathrm{d}Z_\pm^2}{\mathrm{d}r} = -\frac{Z_\pm^2}{r} - M^\pm \frac{D}{r} + \frac{1}{U} N_\pm + \frac{1}{U} S_\pm \tag{5.1}$$

$$\frac{\mathrm{d}D}{\mathrm{d}r} = -\frac{D}{r} - \frac{1}{2}\frac{1}{r}\left(M^+ Z_-^2 + M^- Z_+^2\right) + \frac{1}{U} N_D + \frac{1}{U} S_D \tag{5.2}$$

$$\frac{\mathrm{d}L_\pm}{\mathrm{d}r} = -\frac{L_\pm}{r} - M_L^\pm \frac{L_D}{r} + \frac{1}{U} N_\pm^L + \frac{1}{U} S_\pm^L \tag{5.3}$$

$$\frac{\mathrm{d}L_D}{\mathrm{d}r} = -\frac{L_D}{r} - \frac{1}{2}\frac{1}{r}\left(M_L^+ L_- + M_L^- L_+\right) + \frac{1}{U} N_D^L + \frac{1}{U} S_D^L \tag{5.4}$$

The M terms are the mixing terms that depend on the symmetry of the turbulence. For the 2 dimensional case, the term of order U depends on the winding angle Ψ between the radial direction and the magnetic field direction and therefore depends on the radial distance. For 3D isotropic turbulence $M = 1/3$, $M_L = 0$ and for 2D isotropic turbulence $M \propto \cos^2\Psi$, $M_L \propto 2\cos^2\Psi - 1$. For the analytical solutions we will be assuming that all the mixing terms M are constant, which corresponds to choosing the winding angle. In these cases, $M^+ = M^- = M = \mathit{const}$ and $M_L^+ = M_L^- = M_L = \mathit{const}$. In this section we will also compare the solutions obtained to analytical solutions of the Adhikari et al. [1] equations made with the same small order V_A/U assumption.

5.1 Linear Equations

In this section we will assume that the nonlinear terms of the coupled equations are zero ($N = 0$). Likewise, we will assume that there is no turbulence source driving terms ($S = 0$).

5.1.1 Zero Energy Difference ($D = 0, L_D = 0$)

Starting with the simplest case, we will additionally assume that there is no energy difference terms $L_D = 0$, $D = 0$.

$$\frac{\mathrm{d}Z_\pm^2}{\mathrm{d}r} + \frac{Z_\pm^2}{r} = 0 \tag{5.5}$$

$$\implies \frac{Z_\pm^2}{Z_{\pm 0}^2} = \frac{r_0}{r} \tag{5.6}$$

$$\frac{\mathrm{d}L_\pm}{\mathrm{d}r} + \frac{L_\pm}{r} = 0 \tag{5.7}$$

$$\implies \frac{L_\pm}{L_{\pm 0}} = \frac{r_0}{r} \tag{5.8}$$

This also implies that the correlation lengths are constant $\lambda_\pm = \lambda_{\pm 0}$. By using $L_\pm = \lambda_\pm Z_\pm^2$,

$$L_\pm = Z_\pm^2 \lambda_\pm = \frac{r_0 L_{\pm 0}}{r} = \frac{r_0 Z_{\pm 0}^2 \lambda_{\pm 0}}{r} \tag{5.9}$$

$$\implies \frac{r_0 Z_{\pm 0}^2}{r} \lambda_\pm = \frac{r_0 Z_{\pm 0}^2 \lambda_{\pm 0}}{r} \tag{5.10}$$

$$\implies \lambda_\pm = \lambda_{\pm 0} \tag{5.11}$$

5.1.1.1 Adhikari et al. Equation

In this reduced form, the Adhikari et al. models are the same, providing the same result.

5.1.1.2 Discussion

The zero energy difference model is plotted in Figure 5.1 and Figure 5.2 (blue) and shows the simple r^{-1} decay model. Figure 5.3 shows the constant correlation length (blue).

5.1.2 Constant Energy Difference

Assuming the energy difference is constant $D = D_0$, and the corresponding correlation integral is constant $L_D = L_{D0}$, we obtain the following evolution equations

$$\frac{\mathrm{d}Z_\pm^2}{\mathrm{d}r} + \frac{Z_\pm^2}{r} + M\frac{D_0}{r} = 0 \tag{5.12}$$

$$\frac{\mathrm{d}L_\pm}{\mathrm{d}r} + \frac{L_\pm}{r} + M_L\frac{L_{D0}}{r} = 0 \tag{5.13}$$

The equations can be solved using an integrating factor $\mu = r$, giving the following results

$$Z_\pm^2 = -MD_0 + MD_0\frac{r_0}{r} + Z_{\pm 0}^2\frac{r_0}{r} \tag{5.14}$$

$$L_\pm = -M_L L_{D0} + M_L L_{D0}\frac{r_0}{r} + L_{\pm 0}\frac{r_0}{r} \tag{5.15}$$

5.1.2.1 Adhikari et al. Equation

We can obtain the Adhikari et al. [1] model by setting $M = 1$ and $M_L = 1/2$

$$Z_\pm^2 = -D_0 + D_0\frac{r_0}{r} + Z_{\pm 0}^2\frac{r_0}{r} \tag{5.16}$$

$$L_\pm = -\frac{1}{2}L_{D0} + \frac{1}{2}L_{D0}\frac{r_0}{r} + L_{\pm 0}\frac{r_0}{r} \tag{5.17}$$

5.1.2.2 Discussion

The constant energy difference models are also plotted as four models in Figures 5.1 to 5.3. The first three models are plotted due to the different choices of the constant mixing term parameters; the three dimensional isotropic model $M = 1/3$, $M_L = 0$ in orange, the two dimensional isotropic turbulence model with a 0° winding angle resulting in $M = 1$, $M_L = 1$ plotted in green and the two dimensional isotropic turbulence model in red with 45° winding angle resulting in $M = 1/2$, $M_L = 0$. The last model is the Adhikari et al. [1] model in purple which corresponds to the choice of $M = 1$, $M_L = 1/2$.

Figure 5.1 shows the models decreasing in energy over radial distance. The energy Z_+^2 for the constant energy difference models starts to flatten out in between 1 and 10 AU, and becomes mostly constant at 100 AU with the larger

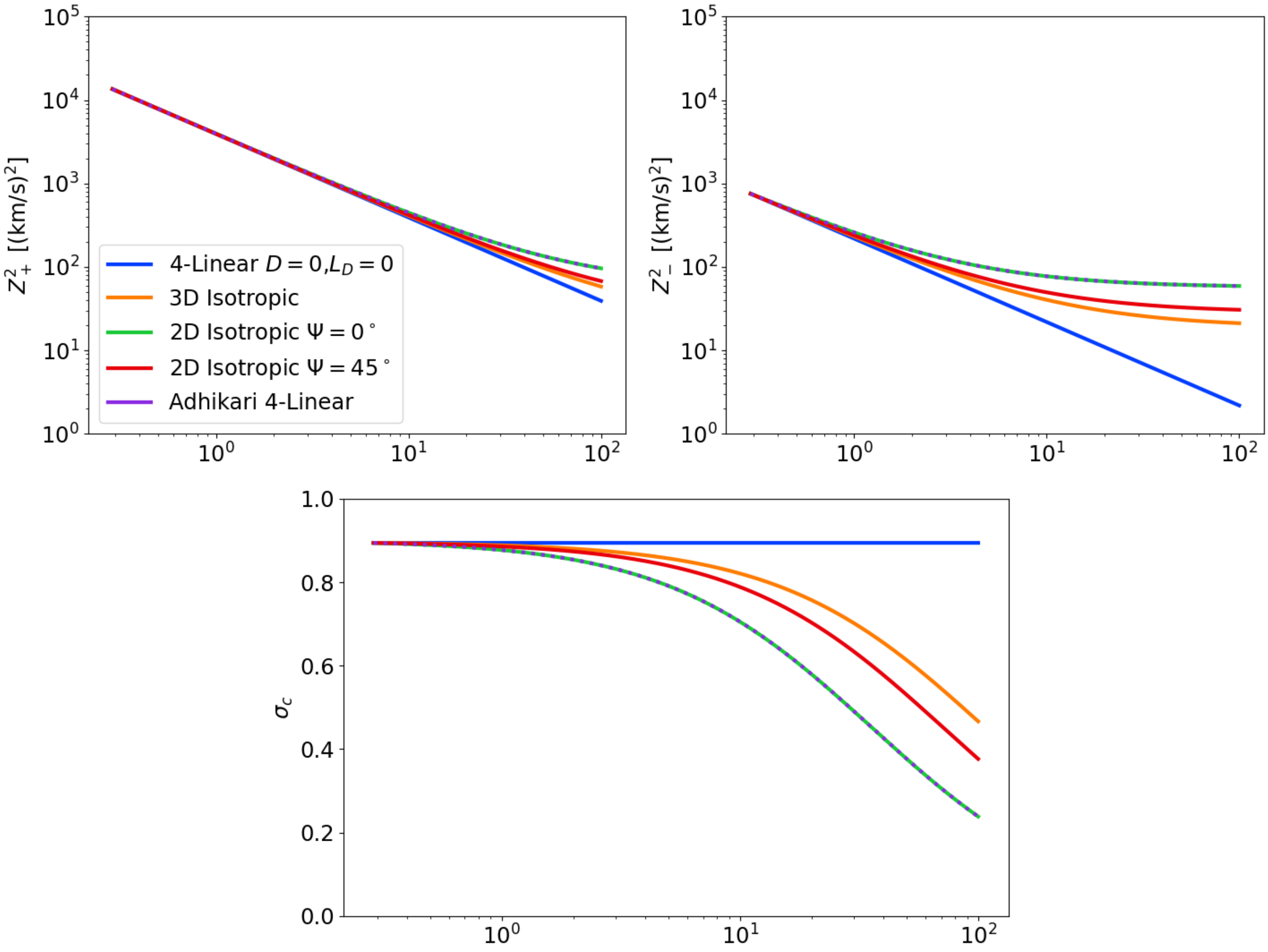

Figure 5.1: Plots of the backward and forward energies and the normalized cross helicity over radial distance to 100 AU. Plotted is the exact solution to the 4-equation models with no energy difference (blue), under 3D isotropic turbulence (orange), under 2D isotropic turbulence with assumed winding angle of 0° (green), under 2D isotropic turbulence with the winding angle 45° (red) and the 4 equation Adhikari et al. model (purple). In these plots, the green and purple lines are equal.

mixing parameter choices resulting in larger final energy. Z_-^2 follows the zero energy difference model r^{-1} decay rate until 20 AU where the constant energy difference models start to flatten out with the larger mixing parameter choices resulting in larger energy final energy. The cross helicity shows the models with the larger mixing parameters (Adhikari and $\Psi = 45°$ models) converge towards an equipartition of the Elsässer energies quicker than models with smaller mixing parameters ($\Psi = 0°$ and 3D isotropic models).

Figure 5.2 shows the 0° winding angle and the Adhikari et al. [1] model maintaining larger correlation integral values due to the larger choices of the correlation integral mixing term M_L, L_+ flattens out at 10 AU and L_- increases slightly from the initial value, but is mostly constant after 1 AU. The models with $M_L = 0$ (3D isotropic turbulence, $\Psi = 45°$) follow the r^{-1} decay rate.

The correlation lengths Figure 5.3 for the $\Psi = 45°$ and 3D isotropic turbulence models decrease from the initial value, this follows from their correlation length r^{-1} decay rate and the eventually constant energies with $\lambda_\pm = L_\pm/Z_\pm^2$. Conversely, the Adhikari and $\Psi = 0°$ show an increase in correlation length over radial distance.

5.1.3 Linear 6 Equation Model

To solve the 6 equation model, we have 2 sets of 3-coupled linear ordinary differential equations. The 2 sets of equations have the same form

$$\frac{\mathrm{d}\boldsymbol{x}(t)}{\mathrm{d}t} = \frac{1}{t}\boldsymbol{M}\boldsymbol{x}(t) \tag{5.18}$$

where $\boldsymbol{M}$ is the coefficient matrix for the system. Solving this system is simple as we get solutions of the form

$$\boldsymbol{x}(t) = c_1\boldsymbol{v}_1\left(\frac{t}{t_0}\right)^{\omega_1} + c_2\boldsymbol{v}_2\left(\frac{t}{t_0}\right)^{\omega_2} + c_3\boldsymbol{v}_3\left(\frac{t}{t_0}\right)^{\omega_3} \tag{5.19}$$

where $\boldsymbol{v}_1, \boldsymbol{v}_2$, and $\boldsymbol{v}_3$ are the eigenvectors of the system and ω_1, ω_2, and ω_3 are the corresponding eigenvalues of the system. c_1, c_2, and c_3 are constants consisting of the initial conditions $\boldsymbol{x}(t_0) = \boldsymbol{x}$. The system of equations for the

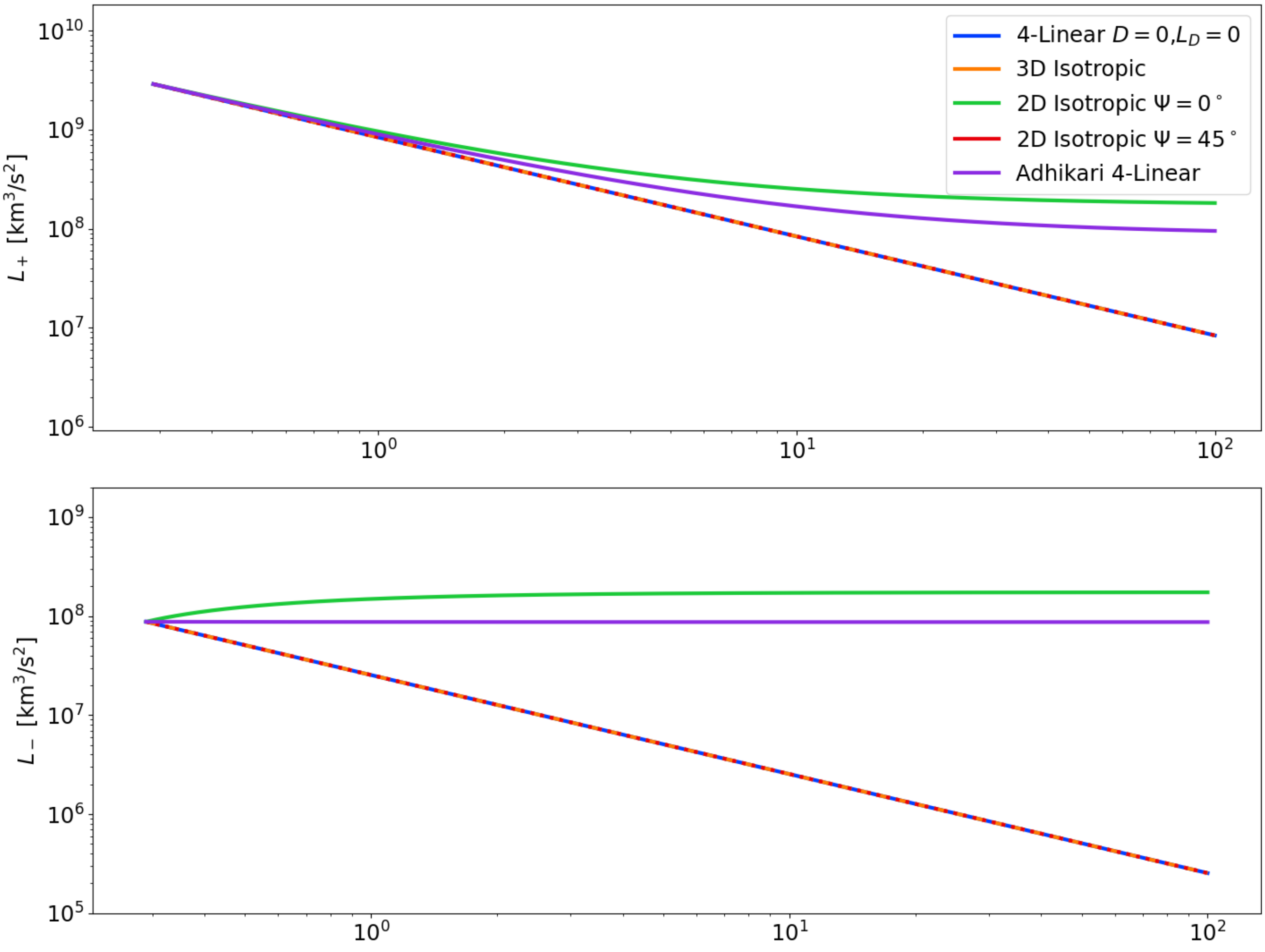

Figure 5.2: Plots of the backward and forward correlation integrals over radial distance to 100 AU. Plotted is the exact solution to the 4-equation models with no energy difference (blue), under 3D isotropic turbulence (orange), under 2D isotropic turbulence with assumed winding angle of 0° (green), under 2D isotropic turbulence with the winding angle 45° (red) and the 4 equation Adhikari et al. model (purple). In these plots, the blue, red and orange plots lines are equal.

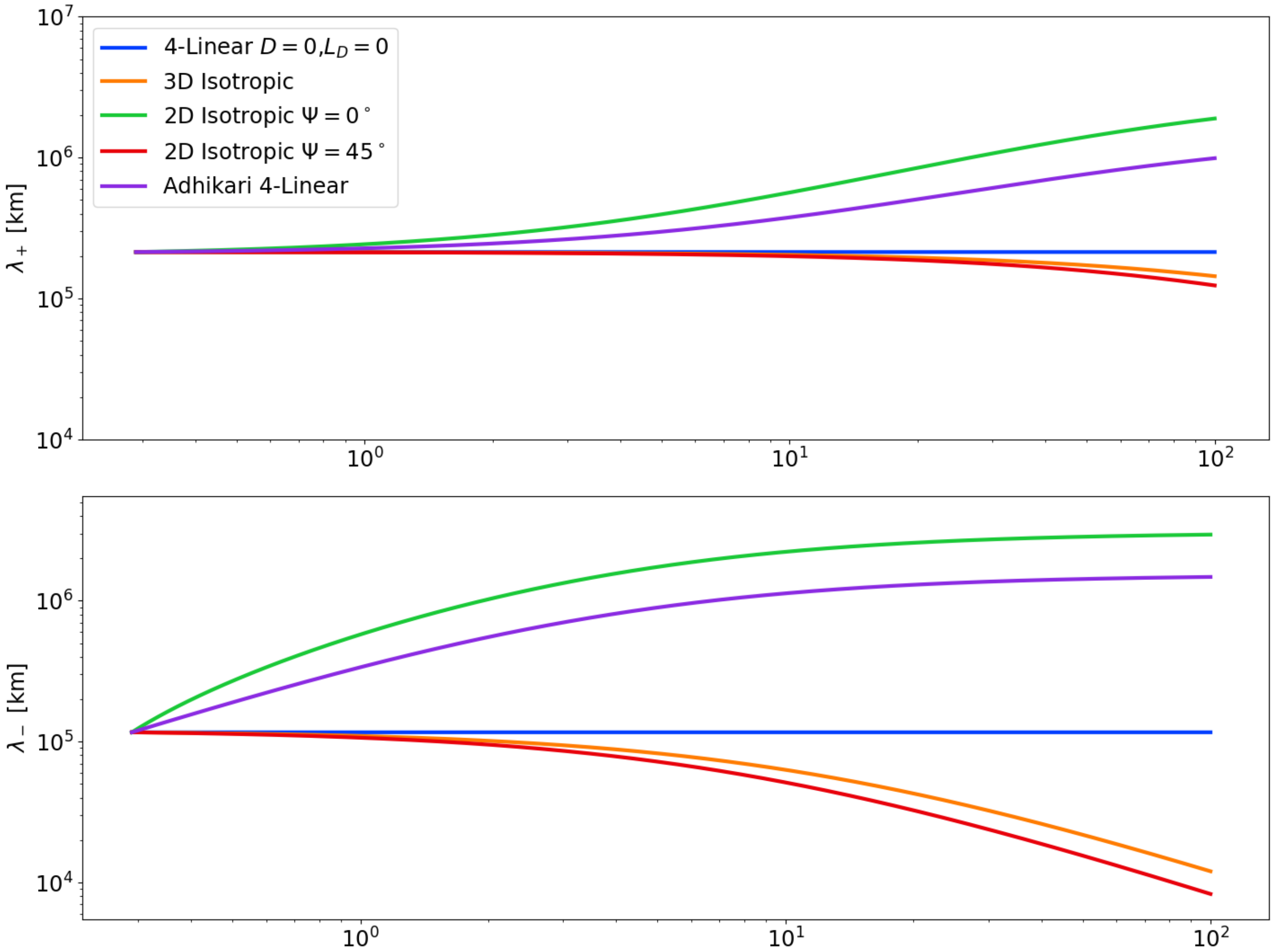

Figure 5.3: Plots of the backward and forward correlation lengths over radial distance to 100 AU. Plotted is the exact solution to the 4-equation models with no energy difference (blue), under 3D isotropic turbulence (orange), under 2D isotropic turbulence with assumed winding angle of 0° (green), under 2D isotropic turbulence with the winding angle 45° (red) and the 4 equation Adhikari et al. model (purple).

Elsässer variables for the linear system of ordinary differential equations are the following

$$\frac{\mathrm{d}Z_{\pm}^2}{\mathrm{d}r} = -\frac{Z_{\pm}^2}{r} - M\frac{D}{r} \tag{5.20}$$

$$\frac{\mathrm{d}D}{\mathrm{d}r} = -\frac{1}{2}M\frac{Z_{+}^2}{r} - \frac{1}{2}M\frac{Z_{-}^2}{r} - \frac{D}{r} \tag{5.21}$$

$$\frac{\mathrm{d}L_{\pm}}{\mathrm{d}r} = -\frac{L_{\pm}}{r} - M_L\frac{L_D}{r} \tag{5.22}$$

$$\frac{\mathrm{d}L_D}{\mathrm{d}r} = -\frac{1}{2}M_L\frac{L_+}{r} - \frac{1}{2}M_L\frac{L_-}{r} - \frac{L_D}{r} \tag{5.23}$$

converting Z_+^2, Z_-^2, and D to matrix form, we get

$$\begin{bmatrix} \frac{\mathrm{d}Z_+^2}{\mathrm{d}r} \\ \frac{\mathrm{d}Z_-^2}{\mathrm{d}r} \\ \frac{\mathrm{d}D}{\mathrm{d}r} \end{bmatrix} = -\frac{1}{r}\begin{bmatrix} 1 & 0 & M \\ 0 & 1 & M \\ \frac{1}{2}M & \frac{1}{2}M & 1 \end{bmatrix}\begin{bmatrix} Z_+^2 \\ Z_-^2 \\ D \end{bmatrix} \tag{5.24}$$

which admits eigenvalues $\omega_1 = -1$, $\omega_2 = M-1$, $\omega_3 = -M-1$ with eigenvectors $\boldsymbol{v}_1 = \begin{bmatrix} -1 \\ 1 \\ 0 \end{bmatrix}$, $\boldsymbol{v}_2 = \begin{bmatrix} -1 \\ -1 \\ 1 \end{bmatrix}$, $\boldsymbol{v}_3 = \begin{bmatrix} 1 \\ 1 \\ 1 \end{bmatrix}$. The solution to the system is the following

$$\begin{bmatrix} Z_+^2 \\ Z_-^2 \\ D \end{bmatrix} = c_1\boldsymbol{v}_1\left(\frac{r}{r_0}\right)^{\omega_1} + c_2\boldsymbol{v}_2\left(\frac{r}{r_0}\right)^{\omega_2} + c_3\boldsymbol{v}_3\left(\frac{r}{r_0}\right)^{\omega_3} \tag{5.25}$$

Setting $r = r_0$, $Z_+^2(r_0) = Z_{+0}^2$, $Z_-^2(r_0) = Z_{-0}^2$, $D(r_0) = D_0$ we can find the constants

$$c_1 = \frac{1}{2}\left(Z_{-0}^2 - Z_{+0}^2\right) \tag{5.26}$$

$$c_2 = \frac{1}{4}\left(2D_0 - Z_{-0}^2 - Z_{+0}^2\right) \tag{5.27}$$

$$c_3 = \frac{1}{4}\left(2D_0 + Z_{+0}^2 + Z_{-0}^2\right) \tag{5.28}$$

Similarly, the correlation integrals have the same form as the energy equations and so the same result $\omega_1^L = -1$, $\omega_2^L = M_L - 1$, $\omega_3^L = -M_L - 1$. Setting $r = r_0$,

$L_+(r_0) = L_{+0}$, $L_-(r_0) = L_{-0}$, $L_D(r_0) = L_{D0}$ we can find the constants

$$c_1^L = \frac{1}{2}\left(L_{-0} - L_{+0}\right) \tag{5.29}$$

$$c_2^L = \frac{1}{4}\left(2L_{D0} - L_{-0} - L_{+0}\right) \tag{5.30}$$

$$c_3^L = \frac{1}{4}\left(2L_{D0} + L_{+0} + L_{-0}\right) \tag{5.31}$$

for the linear solution

$$\begin{bmatrix} L_+ \\ L_- \\ L_D \end{bmatrix} = c_1^L \boldsymbol{v}_1 \left(\frac{r}{r_0}\right)^{\omega_1^L} + c_2^L \boldsymbol{v}_2 \left(\frac{r}{r_0}\right)^{\omega_2^L} + c_3^L \boldsymbol{v}_3 \left(\frac{r}{r_0}\right)^{\omega_3^L} \tag{5.32}$$

As far as we are aware these solutions have not been presented in the literature.

5.1.3.1 Adhikari et al. Equation

We can obtain the Adhikari et al. [1] model by settings $M = 1$

$$\frac{\mathrm{d}Z_\pm^2}{\mathrm{d}r} + \frac{Z_\pm^2}{r} + \frac{D}{r} = 0 \tag{5.33}$$

$$\frac{\mathrm{d}D}{\mathrm{d}r} + \frac{1}{2}\frac{Z_+^2}{r} + \frac{1}{2}\frac{Z_-^2}{r} + \frac{D}{r} = 0 \tag{5.34}$$

This gives eigenvalues of $\omega_1 = -1$, $\omega_2 = 0$, $\omega_3 = -2$ with the same constants c_1, c_2, and c_3. The system for the Adhikari et al. model of correlation integrals is the transpose of our system with $M_L = 1$

$$\begin{bmatrix} \frac{\mathrm{d}L_+}{\mathrm{d}r} \\ \frac{\mathrm{d}L_-}{\mathrm{d}r} \\ \frac{\mathrm{d}L_D}{\mathrm{d}r} \end{bmatrix} = -\frac{1}{r}\begin{bmatrix} 1 & 0 & \frac{1}{2} \\ 0 & 1 & \frac{1}{2} \\ 1 & 1 & 1 \end{bmatrix}\begin{bmatrix} L_+ \\ L_- \\ L_D \end{bmatrix} \tag{5.35}$$

The eigenvalues of the correlation integral system of equations are $\omega_1 = -1$, $\omega_2 = 0$, $\omega_3 = -2$ with the same constants c_1^L, c_2^L, and c_3^L.

5.1.3.2 Discussion

The linear six equation models are plotted in Figures 5.4 and 5.5 showing the Adhikari six equation linear model (red) and our six equation linear models under different isotropy conditions (blue, orange and green). All the equations

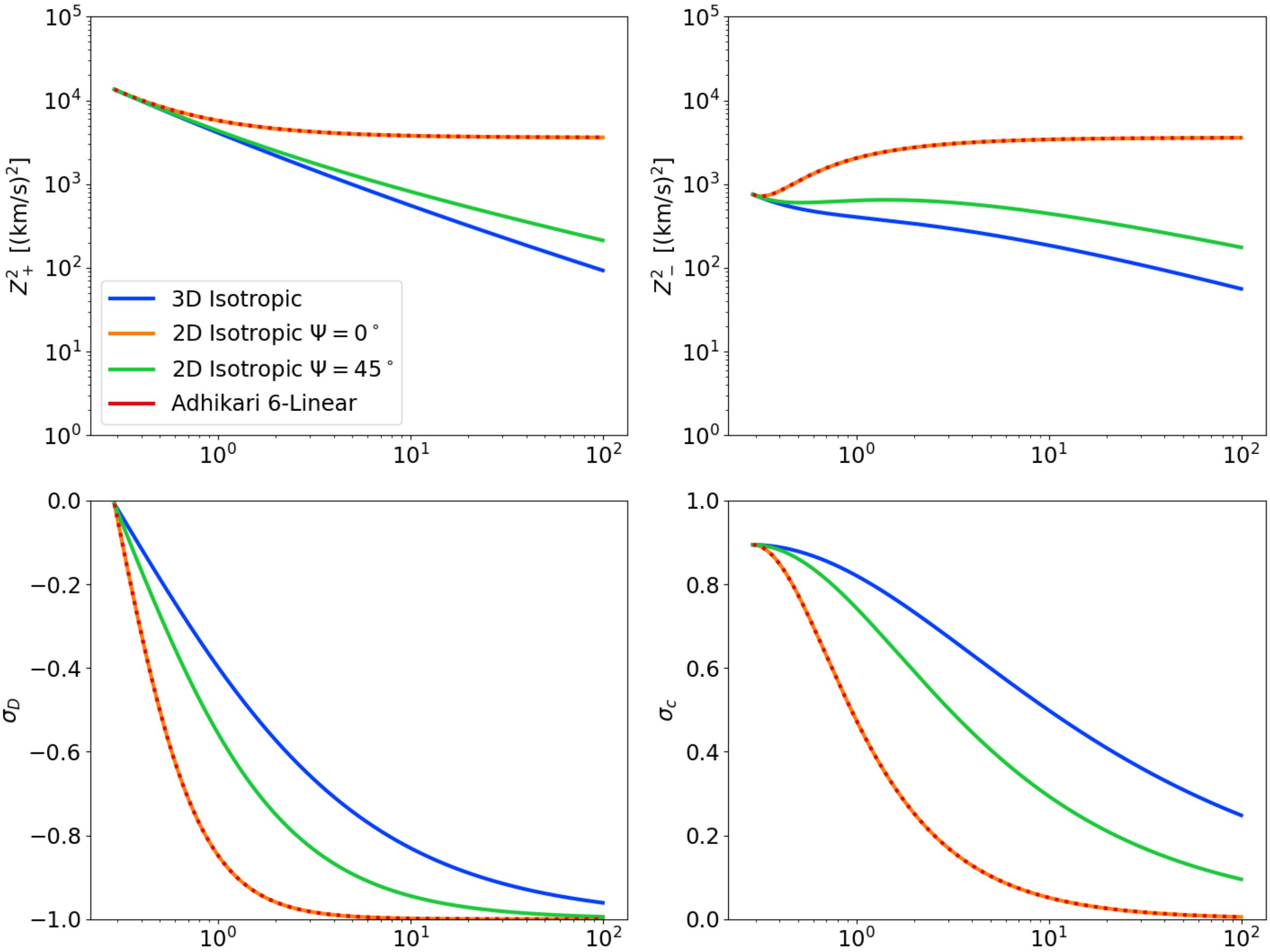

Figure 5.4: Plots of the backward and forward energies, the normalized energy difference and the normalized cross helicity over radial distance to 100 AU. Plotted is the exact solutions to the 6-equation models under 3D isotropic turbulence (blue), 2D isotropic turbulence with 0° winding angle (orange), 2D isotropic turbulence with 45° winding angle (green) and the Adhikari et al. model (red). In these plots the red and orange equations are equal.

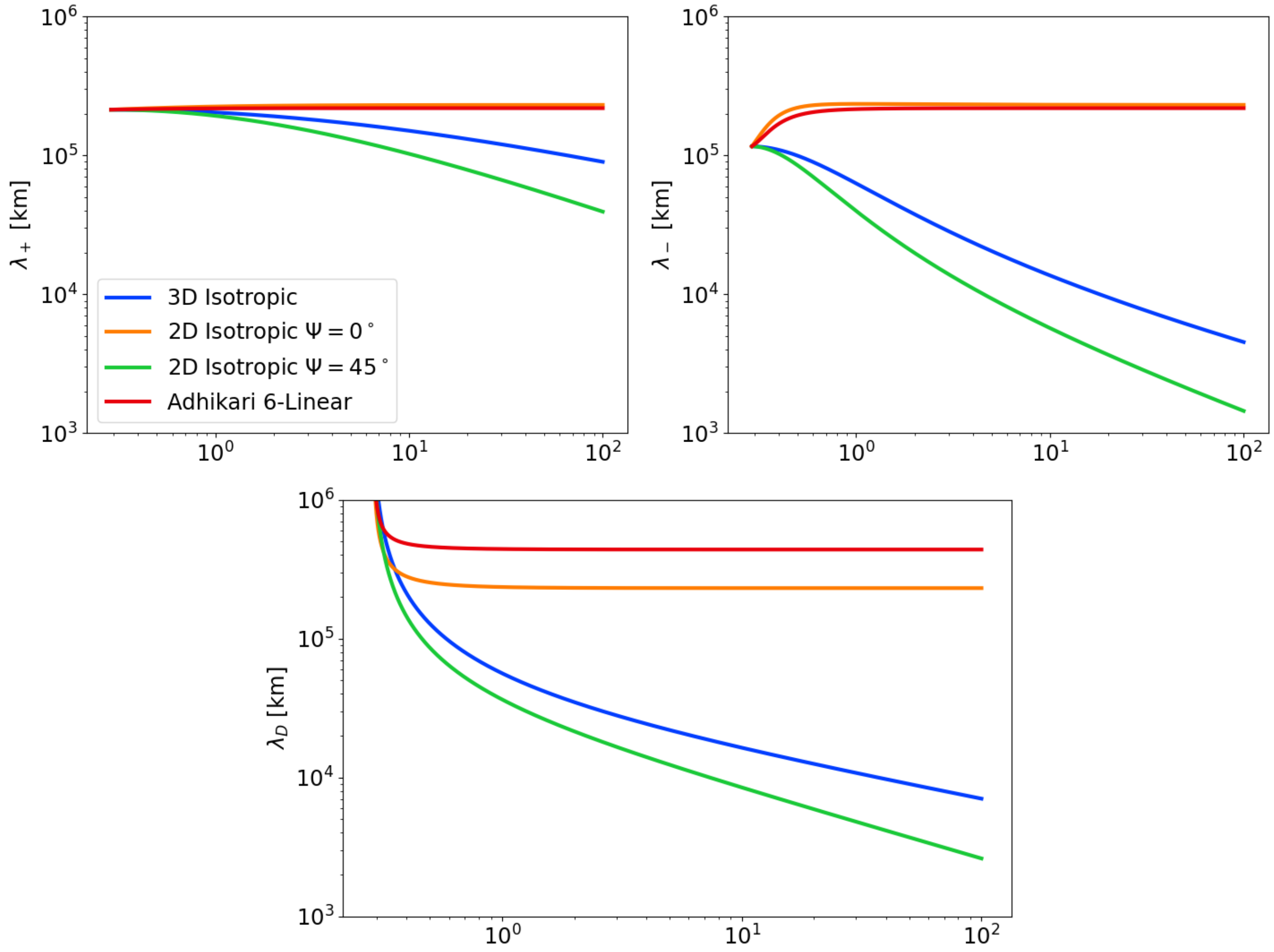

Figure 5.5: Plots of the backward and forward correlation lengths and the correlation length for the energy difference over radial distance to 100 AU. Plotted is the exact solutions to the 6-equation models under 3D isotropic turbulence (blue), 2D isotropic turbulence with 0° winding angle (orange), 2D isotropic turbulence with 45° winding angle (green) and the Adhikari et al. model (red).

depicted show a significant decrease in the normalized energy difference σ_D from 0 to -1. As we would like σ_D to reach an equilibrium at $-1/3$ (section 4.2) we clearly need the nonlinear term to push σ_D back towards 0. As it stands, the linear-six equation models have a vast amount of excess magnetic energy. The normalized cross helicity σ_c shows expected behaviour of reaching 0 in the outer heliosphere, implying that the Elsässer energies are becoming equalized, this is also seen in the Z_+^2 and Z_-^2 plots. Z_+^2 is roughly equal to Z_-^2 after 10 AU. In Figure 5.4, the Adhikari (red) and 2D isotropic turbulence with a 0° winding angle (orange) are equivalent. These two models have an increasing Z_-^2 that reaches a steady state within 2 AU. Likewise, the Adhikari and $\Psi = 0°$ models reach a steady state for Z_+^2 around 2 AU after decreasing from the initial value. The 3D isotropic turbulence (blue) and $\Psi = 45°$ (green) linear models show both the energies $Z_\pm^2$ decreasing over the radial distance. In Figure 5.5, the Adhikari and $\psi = 45°$ linear models (red and orange respectively) show a constant, steady state for all of the correlation lengths λ_+, λ_- and λ_D after 2 AU whereas the 3D isotropic and $\Psi = 45°$ linear models (blue and green respectively), show the length scales decreasing over the radial distance.

5.2 Nonlinear Equations

In this section, we will try to obtain solutions with non-zero nonlinear terms. We will still be assuming that there is no turbulent source driving terms ($S = 0$).

5.2.1 Single Length-scale λ

Matthaeus et al. [36] provide a steady state solution for the following set of equations

$$\frac{\mathrm{d}Z^2}{\mathrm{d}r} + \frac{A}{r}Z^2 = -\alpha\frac{Z^3}{\lambda} \tag{5.36}$$

$$\frac{\mathrm{d}\lambda}{\mathrm{d}r} + \frac{C}{r}\lambda = \beta Z \tag{5.37}$$

These equations have been obtained by assuming that there is only one length scale $\lambda_\pm = \lambda$ and energy scale $Z_\pm^2 = Z^2$. It is also assumed that $\lambda_D = 0$ and with $\sigma_D = const$, $D = \sigma_D Z^2$. The nonlinear pieces are the direct analogy to the HD Kármán-Taylor style phenomenologies ($\lambda_\pm$ Model B, $Z_\pm^2$ Model A). The following is the solution for a general α and β rather than the specific case of $\alpha = 2\beta = 1$ that Matthaeus et al. provide

$$\frac{Z^2}{Z_0^2} = \left(\frac{r_0}{r}\right)^A \left[\frac{\alpha+2\beta}{2}\frac{D}{Q}\left(\left(\frac{r}{r_0}\right)^Q - 1\right) + 1\right]^{-4\beta/(\alpha+2\beta)} \tag{5.38}$$

$$\frac{\lambda}{\lambda_0} = \left(\frac{r_0}{r}\right)^C \left[\frac{\alpha+2\beta}{2}\frac{D}{Q}\left(\left(\frac{r}{r_0}\right)^Q - 1\right) + 1\right]^{2\beta/(\alpha+2\beta)} \tag{5.39}$$

The terms A and C relate to the isotropy assumption (Appendix C, Appendix D) and $Q = 1 + C - \frac{1}{2}A$ and $D = \frac{Z_0}{U}\frac{r_0}{\lambda_0}$. The model proposed here could be viewed as a model for the outer heliosphere where $\sigma_D \approx -1/3$ and $\sigma_c \approx 0$.

5.2.2 Two Length-scales $\lambda_\pm$

Without the one length and energy scale assumption and keeping to the same Kármán-Taylor style phenomenologies ($\lambda_\pm$ Model B, $Z_\pm^2$ Model A), the equations for $Z_\pm^2$ and $L_\pm = \lambda_\pm Z_\pm^2$ are the following

$$\frac{\mathrm{d}Z_\pm^2}{\mathrm{d}r} + A\frac{Z_\pm^2}{r} + B\frac{Z_\mp^2}{r} = -\frac{\alpha_\pm}{U}\frac{Z_\pm^4 Z_\mp}{L_\pm} \tag{5.40}$$

$$\frac{\mathrm{d}L_\pm}{\mathrm{d}r} + C\frac{L_\pm}{r} + D\frac{L_\mp}{r} = \frac{1}{U}(\beta_\pm - \alpha_\pm)Z_\pm^2 Z_\mp \tag{5.41}$$

We have still maintained $D = \sigma_D Z^2$ with $Z^2 = \frac{1}{2}\left(Z_+^2 + Z_-^2\right)$ and $L_D = \sigma_D L$ with $L = \frac{1}{2}(L_+ + L_-)$. Therefore the mixing terms result in the general parameters $A = 1 + \frac{1}{2}M\sigma_D$, $B = \frac{1}{2}M\sigma_D$, $C = 1 + \frac{1}{2}M_L\sigma_D$ and $D = \frac{1}{2}M_L\sigma_D$ for constant mixing terms M and M_L. By assuming $\alpha_\pm = \alpha$, $\beta_\pm = \beta$ and $A = C = 1$ and also removing the symmetric '$\mp$' transport couplings $B = D = 0$ which corresponds to choosing $\frac{1}{2}M\sigma_D = 0$ and $\frac{1}{2}M_L\sigma_D = 0$, we get

$$\frac{\mathrm{d}Z_\pm^2}{\mathrm{d}r} + \frac{Z_\pm^2}{r} = -\frac{\alpha}{U}\frac{Z_\pm^4 Z_\mp}{L_\pm} \tag{5.42}$$

$$\frac{\mathrm{d}L_\pm}{\mathrm{d}r} + \frac{L_\pm}{r} = \frac{1}{U}(\beta - \alpha)Z_\pm^2 Z_\mp \tag{5.43}$$

We will start by simplify the $Z_\pm^2$ equation, using $\omega_\pm = Z_\pm^2$

$$\implies \frac{\mathrm{d}\omega_\pm}{\mathrm{d}r} + \frac{\omega}{r} = -\frac{\alpha}{U}\frac{\omega_\pm^2 \omega_\mp^{1/2}}{L_\pm} \tag{5.44}$$

This is a Bournoulli differential equation [44], by making the next substitution $\Omega_\pm = \omega_\pm^{1-n}$, where $n = 2$ is the highest power in the nonlinear term (meaning $\Omega_\pm = \omega_\pm^{-1} = Z_\pm^{-2}$). By dividing by the highest power $\omega_\pm^2$ and using $\frac{\mathrm{d}\Omega_\pm}{\mathrm{d}r} = -\omega_\pm^{-2}\frac{\mathrm{d}\omega_\pm}{\mathrm{d}r}$ we obtain

$$\frac{\mathrm{d}\Omega_\pm}{\mathrm{d}r} - \frac{\Omega_\pm}{r} = \frac{\alpha}{U}\frac{\Omega_\mp^{-1/2}}{L_\pm} \tag{5.45}$$

$$\frac{\mathrm{d}L_\pm}{\mathrm{d}r} + \frac{L_\pm}{r} = \frac{1}{U}\left(\beta - \alpha\right)\Omega_\pm^{-1}\Omega_\mp^{-1/2} \tag{5.46}$$

Using an integrating factor of $\frac{1}{r}$ for $\Omega_\pm$ and r for $L_\pm$ we can simplify both evolution equations

$$\frac{\mathrm{d}(\frac{1}{r}\Omega_\pm)}{\mathrm{d}r} = -\frac{\alpha}{U}\frac{1}{r}\frac{\Omega_\mp^{-1/2}}{L_\pm} \tag{5.47}$$

$$\frac{\mathrm{d}(rL_\pm)}{\mathrm{d}r} = r\frac{1}{U}(\beta - \alpha)\Omega_\pm^{-1}\Omega_\mp^{-1/2} \tag{5.48}$$

Now, we are able to divide the two differential equations, to cancel out the dependence on $\Omega_\mp$ and then solve for $\frac{1}{r}\Omega_\pm$ and $rL_\pm$

$$\implies \frac{\mathrm{d}(\frac{1}{r}\Omega_\pm)}{\mathrm{d}(rL_\pm)} = \frac{\alpha}{\beta - \alpha}\frac{\frac{1}{r}\Omega_\pm}{rL_\pm} \tag{5.49}$$

$$\implies \frac{\Omega_\pm}{\Omega_{\pm 0}} = \left(\frac{r}{r_0}\right)^{\frac{\beta}{\beta-\alpha}}\left(\frac{L_\pm}{L_{\pm 0}}\right)^{\frac{\alpha}{\beta-\alpha}} \tag{5.50}$$

$$\implies \frac{Z_\pm^2}{Z_{\pm 0}^2} = \left(\frac{r}{r_0}\right)^{-\frac{\beta}{\beta-\alpha}}\left(\frac{L_\pm}{L_{\pm 0}}\right)^{-\frac{\alpha}{\beta-\alpha}} \tag{5.51}$$

Plugging our values for $Z_\pm^2$ Equation 5.51 in terms of $L_\pm$ into Equation 5.48

$$\frac{\mathrm{d}(rL_\pm)}{\mathrm{d}r} = \frac{1}{r_0}\frac{\beta - \alpha}{U}\left(Z_{\pm 0}^2\left(\frac{r}{r_0}\right)^{-\frac{\beta}{\beta-\alpha}-1}\left(\frac{L_\pm}{L_{\pm 0}}\right)^{-\frac{\alpha}{\beta-\alpha}}\right)\left(Z_{\mp 0}^2\left(\frac{r}{r_0}\right)^{-\frac{\beta}{\beta-\alpha}}\left(\frac{L_\mp}{L_{\mp 0}}\right)^{-\frac{\alpha}{\beta-\alpha}}\right)^{1/2} \tag{5.52}$$

$$= \frac{1}{r_0}\frac{\beta - \alpha}{U}\left(Z_{\pm 0}^2 Z_{\mp 0}\right)\left(\frac{r}{r_0}\right)^{-\frac{3}{2}\frac{\beta}{\beta-\alpha}-1}\left(\frac{rL_\pm}{L_{\pm 0}}\right)^{-\frac{\alpha}{\beta-\alpha}}\left(\frac{rL_\mp}{L_{\mp 0}}\right)^{-\frac{1}{2}\frac{\alpha}{\beta-\alpha}} \tag{5.53}$$

and then using the chain rule $\frac{\mathrm{d}(rL_+)}{\mathrm{d}r}\frac{\mathrm{d}r}{\mathrm{d}(rL_-)} = \frac{\mathrm{d}(rL_+)}{\mathrm{d}(rL_-)}$, we can start to find solutions for L_+ in terms of L_- and r

$$\frac{\mathrm{d}(rL_+)}{\mathrm{d}(rL_-)} = \left(\frac{Z_{+0}}{Z_{-0}}\right)\left(\frac{rL_+}{L_{+0}}\right)^{-\frac{1}{2}\frac{\alpha}{\beta-\alpha}}\left(\frac{rL_-}{L_{-0}}\right)^{\frac{1}{2}\frac{\alpha}{\beta-\alpha}} \tag{5.54}$$

$$\implies \int (rL_+)^{\frac{1}{2}\frac{\alpha}{\beta-\alpha}}\,\mathrm{d}\,(rL_+) = c_1^+ c_2^+ \int (rL_-)^{\frac{1}{2}\frac{\alpha}{\beta-\alpha}}\,\mathrm{d}\,(rL_-) \tag{5.55}$$

For notational simplicity we have switched to the following short hand $c_1^\pm = \left(\frac{Z_{\pm 0}}{Z_{\mp 0}}\right)^a$ and $c_2^\pm = \left(\frac{L_{\pm 0}}{L_{\mp 0}}\right)^a$, where the power a is arbitrary and not the equal in all of $c_1^\pm$ and $c_2^\pm$. For example, in Equation 5.55, c_2^+ has $a = \frac{1}{2}\frac{\alpha}{\beta-\alpha}$ but will still be recorded as c_2^+.

At this point we need to pay close attention to the α and β parameters for $rL_\pm$. For $\alpha = \beta$, Equation 5.55 becomes undefined, so from this point onwards we require $\alpha \neq \beta$. If we follow [36] (as restated in subsection 5.2.1) and choose $\alpha = 1, \beta = 1/2$ ($\frac{1}{2}\frac{\alpha}{\beta-\alpha} = -1$), we get a power law solution that depends on the initial conditions (really, the only requirement is $\beta = \alpha/2$)

$$\int (rL_+)^{-1}\,\mathrm{d}\,(rL_+) = c_1^+ c_2^+ \int (rL_-)^{-1}\,\mathrm{d}\,(rL_-) \tag{5.56}$$

$$\implies \ln\left(\frac{rL_+}{r_0 L_{+0}}\right) = c_1^+ c_2^+ \ln\left(\frac{rL_-}{r_0 L_{-0}}\right) \tag{5.57}$$

$$\implies \frac{rL_\pm}{r_0 L_{\pm 0}} = \left(\frac{rL_\mp}{r_0 L_{\mp 0}}\right)^{c_1^\pm c_2^\pm} \tag{5.58}$$

If we want $\frac{1}{2}\frac{\alpha}{\beta-\alpha} = m$ for $m \geq 0$, we get $\beta = \alpha\frac{1+2m}{2m}$. If $m = 0$ then $\alpha = 0$ and $m = 1/2$ implies $\beta = 0$. Otherwise, $\beta > \alpha$ which results in an increasing Reynold's number which is nonphysical for unforced, decaying turbulence [36], this solution is the following

$$\int (rL_+)^m\,\mathrm{d}\,(rL_+) = c_1^+ c_2^+ \int (rL_-)^m\,\mathrm{d}\,(rL_-) \tag{5.59}$$

$$\implies \frac{(rL_+)^{m+1} - (r_0 L_{+0})^{m+1}}{m+1} = c_1^+ c_2^+ \frac{(rL_-)^{m+1} - (r_0 L_{-0})^{m+1}}{m+1} \tag{5.60}$$

$$\implies (rL_\pm)^{m+1} = c_1^\pm c_2^\pm \left((rL_\mp)^{m+1} - (r_0 L_{\mp 0})^{m+1}\right) + (r_0 L_{\pm 0})^{m+1} \tag{5.61}$$

If we want a physically constrained solution, then we require $\frac{1}{2}\frac{\alpha}{\beta-\alpha} = -n$ for

$n > 1$ which implies that $\beta = \alpha\frac{2n-1}{2n}$ therefore $\alpha > \beta$

$$\int (rL_+)^{-n}\,\mathrm{d}\,(rL_+) = c_1^+ c_2^- \int (rL_-)^{-n}\,\mathrm{d}\,(rL_-) \tag{5.62}$$

$$\implies (rL_\pm)^{1-n} = c_1^\pm c_2^\pm \left((rL_\mp)^{1-n} - (r_0 L_{\mp 0})^{1-n}\right) + (r_0 L_{\pm 0})^{1-n} \tag{5.63}$$

With Equations (5.58), (5.61) and (5.63) as solutions for Equation 5.55, providing an expression for $L_\pm$ in terms of $L_\mp$ and r we can substitute the formulae back into Equation 5.53. Starting with Equation 5.61,

$$\frac{\mathrm{d}(rL_\pm)}{\mathrm{d}r} = \frac{\alpha}{2mU}\frac{c_3^\pm}{r_0}\left(\frac{r}{r_0}\right)^{-\frac{3}{2}-3m} (rL_\pm)^{-2m} \tag{5.64}$$

$$\times \left[c_1^\mp c_2^\mp \left((rL_\pm)^{m+1} - (r_0 L_{\pm 0})^{m+1}\right) + \left(r_0 L_{\mp 0}^{m+1}\right)\right]^{-m/(m+1)} \tag{5.65}$$

where, once again we are simplifying the notation with $c_3^\pm = \left(Z_{\pm 0}^2 Z_{\mp 0}\right)^a$. Equation 5.65 is an equation of the form

$$\int x^{2m}\left(B(x^{m+1} + C) + D\right)^{\frac{m}{m+1}}\,\mathrm{d}x = A\int r^{-5/2+3m}\mathrm{d}r \tag{5.66}$$

Unfortunately, we cannot obtain a solution for $L_\pm$ as forms for the right hand side of Equation 5.66 give solutions containing hypergeometric functions. Using Equation 5.63 will yield the same equation form as Equation 5.66 but with $m = -n$.

The one solvable case is found by using Equation 5.58 (*i.e.,* $2\beta = \alpha$)

$$\frac{\mathrm{d}(rL_\pm)}{\mathrm{d}r} = \frac{-\alpha}{2U}\frac{c_3^\pm}{r_0}\left(\frac{r}{r_0}\right)^{1/2}\left(\frac{rL_\pm}{L_{\pm 0}}\right)^2\left(\frac{rL_\mp}{L_{\mp 0}}\right) \tag{5.67}$$

$$\implies \frac{\mathrm{d}(rL_\pm)}{\mathrm{d}r} = \frac{-\alpha}{2U}\frac{c_3^\pm}{r_0}\frac{1}{L_{\pm 0}^2 L_{\mp 0}}\left(\frac{r}{r_0}\right)^{1/2}(rL_\pm)^2(rL_\mp) \tag{5.68}$$

$$\implies \frac{\mathrm{d}(rL_\pm)}{\mathrm{d}r} = \frac{-\alpha}{2U}\frac{c_3^\pm}{L_{\pm 0}^{c_1^\mp c_2^\pm + 2}}\frac{1}{r_0^{c_1^\mp c_2^\pm + 3/2}} r^{1/2}(rL_\pm)^{c_1^\mp c_2^\pm + 2} \tag{5.69}$$

$$\implies \int (rL_\pm)^{-c_1^\mp c_2^\pm - 2}\,\mathrm{d}(rL_\pm) = \frac{-\alpha}{2U}\frac{c_3^\pm}{L_{\pm 0}^{c_1^\mp c_2^\pm + 2}}\frac{1}{r_0^{c_1^\mp c_2^\pm + 3/2}}\int r^{1/2}\mathrm{d}r \tag{5.70}$$

$$\implies \frac{1}{-c_1^\mp c_2^\pm - 1}\left[(rL_\pm)^{-c_1^\mp c_2^\pm - 1} - (r_0 L_{\pm 0})^{-c_1^\mp c_2^\pm - 1}\right] = \frac{-\alpha}{2U}\frac{c_3^\pm}{L_{\pm 0}^{c_1^\mp c_2^\pm + 2}}\frac{1}{r_0^{c_1^\mp c_2^\pm + 3/2}}\frac{2}{3}\left[r^{3/2} - r_0^{3/2}\right] \tag{5.71}$$

$$\implies \frac{L_\pm}{L_{\pm 0}} = \frac{r_0}{r}\left\{\frac{\alpha}{3}\left(c_1^\mp c_2^\pm + 1\right)\frac{c_3^\pm r_0}{L_{\pm 0}U}\left[\left(\frac{r}{r_0}\right)^{3/2} - 1\right] + 1\right\}^{-\frac{1}{c_1^\mp c_2^\pm + 1}} \tag{5.72}$$

This gives us an equation for $L_\pm$ only dependent on r. Continuing to use $\beta = \alpha/2$ and using Equation 5.72 with Equation 5.51 we get the equation for $Z_\pm^2$ depending on r

$$\frac{Z_\pm^2}{Z_{\pm 0}^2} = \frac{r}{r_0}\left(\frac{L_\pm}{L_{\pm 0}}\right)^2 \tag{5.73}$$

$$\implies \frac{Z_\pm^2}{Z_{\pm 0}^2} = \frac{r_0}{r}\left\{\frac{\alpha}{3}\left(c_1^\mp c_2^\pm + 1\right)\frac{c_3^\pm r_0}{L_{\pm 0} U}\left[\left(\frac{r}{r_0}\right)^{3/2} - 1\right] + 1\right\}^{-\frac{2}{c_1^\mp c_2^\pm + 1}} \tag{5.74}$$

These solutions also do not appear to have been published elsewhere.

5.2.3 Discussion

Figure 5.6 shows the plots of the analytical solutions to the nonlinear models. The two scale model in blue uses Equation 5.74 and Equation 5.72 with the initial conditions in Table 4.1 and with $\alpha = 2\beta = 0.2$ chosen from the simulation data (subsection 4.1.3). We see that this solution decreases Z_+^2 to the order of 10^1 and Z_-^2 to the order of 10^{-7}. Correspondingly, the correlation length λ_+ stays within the order of 10^6 and λ_- increases to the order of 10^9. The values seen in this analytical solution do not agree with the observational data as λ_- and Z_-^2 are much larger and smaller respectively than the observational data shows by a factor of 10^3 and 10^9 respectively. Whilst λ_+ and Z_+^2 stay within the bounds of the observational data.

The single scale model has been plotted with various winding angles $\Psi = 0°$ (orange), $\Psi = 45°$ (green) and $\Psi = 90°$ (red) with the assumed energy difference correlation integral $L_D = \sigma_D L$ and the same α and β parameters as the two scale model in Figure 5.6. The various iterations show similar behaviour, with the smaller winding angles showing a larger energy and larger correlation length. The single scale models show the correlation length λ of the order $10^6 - 10^7$ which matches observational data. However, the energy Z^2 decays to the order of 10^{-2} which is much smaller than observational data shows. The single scale models show stronger energy decay than the two scale Z_+^2 energy, but weaker than the two scale Z_-^2 energy. Likewise, the single scale models shows greater growth of the correlation length than the two scale λ_+ length, but weaker than λ_-.

These two nonlinear analytical models do not match the expected behaviour in the solar wind. The single scale model more closely relates to the observed solar wind values compared to the two scale model, this is due to the two scale model being more restricted in requiring the lack of the mixing terms and the power law of the two scale model depending on the initial conditions. Note that These models are rather incomplete as they do not contain the source terms and the energy difference. To get some more robust solutions, we will need to obtain numerical solutions.

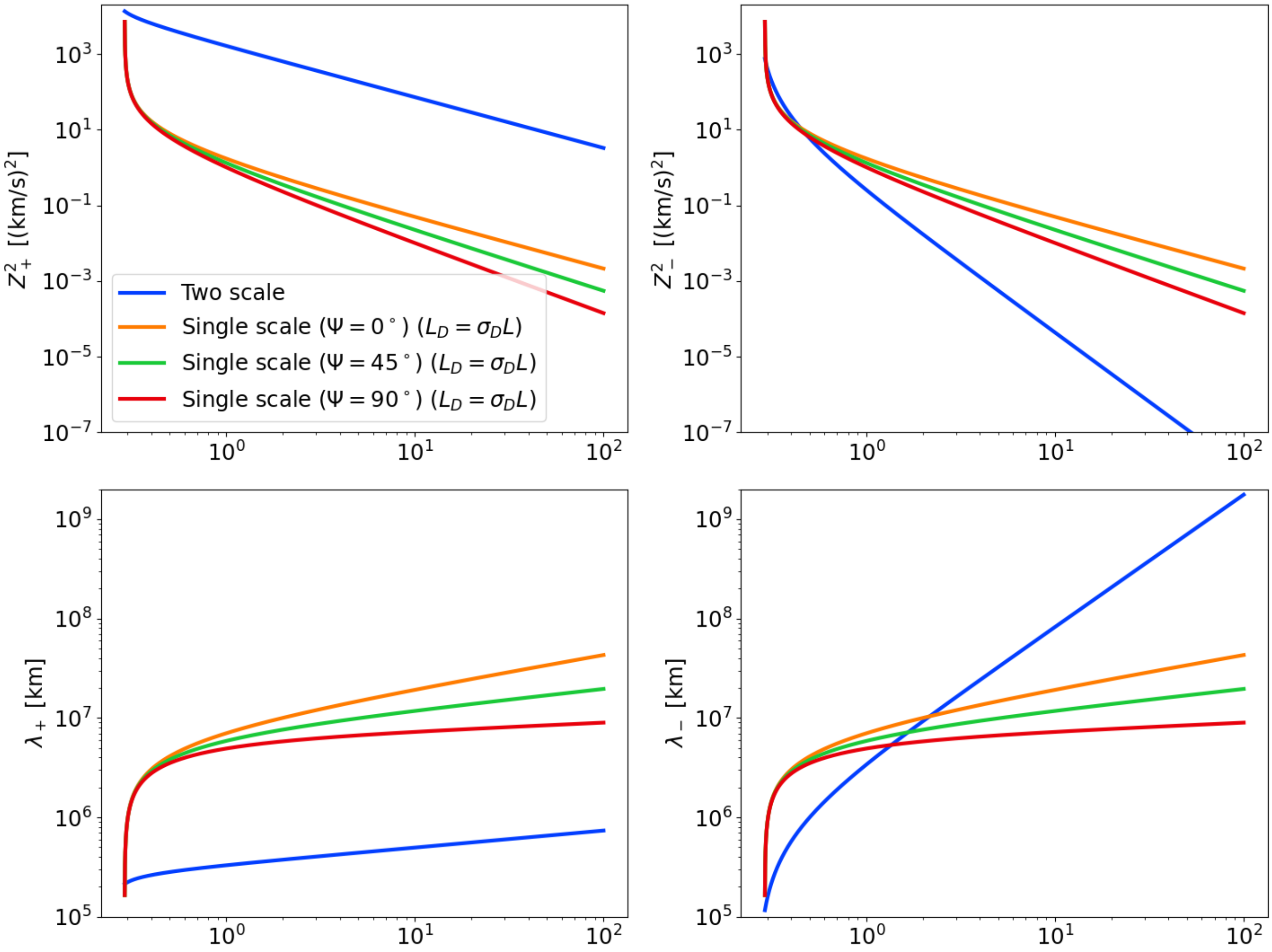

Figure 5.6: Plots of the Elsässer energies $Z_\pm^2$ and their corresponding correlation lengths $\lambda_\pm$ for the two-scale, nonlinear, analytical model (blue) up to 100 AU. The single scale, nonlinear, analytical model (orange) is plotted with a 45° winding angle and assuming $Z_\pm^2 = Z^2$ and $\lambda_\pm = \lambda$.

Chapter 6

Numerical Solutions

In this section, we will be numerically solving the steady state equations (subsection 3.1.1, section 3.4, and Appendix D) using the two dimensional isotropic mixing terms, with the different nonlinear models proposed in section 3.2 and the source terms in section 3.3; these obtain new results. For ease, we restate the steady state equations below

$$\frac{\mathrm{d}Z_\pm^2}{\mathrm{d}r} = -\frac{U \pm V_{Ar}}{U \mp V_{Ar}}\frac{Z_\pm^2}{r} - \frac{1}{U \mp V_{Ar}}M^\pm D + \frac{1}{U \mp V_{Ar}}N_\pm + \frac{1}{U \mp V_{Ar}}S_\pm \tag{6.1}$$

$$\frac{\mathrm{d}D}{\mathrm{d}r} = -\frac{D}{r} - \frac{1}{2}\frac{1}{U}\left(M^+ Z_-^2 + M^- Z_+^2\right) + \frac{1}{U}N_D + \frac{1}{U}S_D \tag{6.2}$$

$$\frac{\mathrm{d}L_\pm}{\mathrm{d}r} = -\frac{U \pm V_{Ar}}{U \mp V_{Ar}}\frac{L_\pm}{r} - \frac{1}{U \mp V_{Ar}}M_L^\pm \frac{L_D}{r} + \frac{1}{U \mp V_{Ar}}N_\pm^L + \frac{1}{U \mp V_{Ar}}S_\pm^L \tag{6.3}$$

$$\frac{\mathrm{d}L_D}{\mathrm{d}r} = -\frac{L_D}{r} - \frac{1}{2}\frac{1}{U}\left(M_L^- L_+ + M_L^+ L_-\right) + \frac{1}{U}N_D^L + \frac{1}{U}S_D^L \tag{6.4}$$

$$\frac{\mathrm{d}T}{\mathrm{d}r} = -\frac{4}{3}\frac{T}{r} + \frac{1}{3}\frac{m_p}{k_B}\left(-\left.\frac{\mathrm{d}Z_+^2}{\mathrm{d}t}\right|_{NL} - \left.\frac{\mathrm{d}Z_-^2}{\mathrm{d}t}\right|_{NL}\right) \tag{6.5}$$

where the 2 dimensional mixing terms are

$$M_{2D}^\pm = \frac{1}{r}\left[U\cos^2\Psi \pm V_{Ar}\left(3\cos^2\Psi - 2\right) \pm V_{Ar0}\left(\frac{\Omega R_0}{U}\right)\left(1 - \frac{3R_0}{2r}\right)\sin\theta\sin 2\Psi\right] \tag{6.6}$$

$$M_{2D,L}^\pm = \frac{1}{r}\left[U\left(2\cos^2\Psi - 1\right) \pm V_{Ar}\left(6\cos^2\Psi - 5\right) \pm V_{Ar0}\left(\frac{\Omega R_0}{U}\right)\left(\frac{3R_0}{2r} - 1\right)\sin\theta\sin 2\Psi\right] \tag{6.7}$$

We will frequently refer to the normalized cross helicity σ_c and the normalized energy difference σ_D; they can be calculated as follows

$$\sigma_c = \frac{Z_+^2 - Z_-^2}{Z_+^2 + Z_-^2} \tag{6.8}$$

$$\sigma_D = \frac{2D}{Z_+^2 + Z_-^2} \tag{6.9}$$

The numerical solutions are obtained by using an explicit Runge-Kutta method of order 5(4) (RK45) via the Python3 package `scipy.integrate.solve_ivp` [18, 50, 58] with the initial values as stated in Table 4.1. The numerical solutions will be found by integrating from an inner boundary $r = 0.29$AU up to $r = 75$ AU. We include the large-scale magnetic field V_A that we neglected in the analytical solutions with the initial value $V_{A0} = 400$ km/s at the Alfvén critical radius, taken to be $R_0 \approx 0.047$ AU (10 solar radii). We also choose $\theta = \pi/2$ (the ecliptic plane) and $\Omega = 2.9 \times 10^{-6}$ rad/s as the angular speed of the Sun. The source term parameters have been fixed at $C_{sh} = 0.5$ and $f_D = 0.25$.

6.1 Parameter Optimization

Each of the nonlinear models proposed have free parameters ($\alpha_{\pm,D}$, $\beta_{\pm,D}$ etc.). These parameters play an important role in the energy cascade process. We have gathered an idea of the value of these parameters from the simulation analysis (subsection 4.1.3) and the relationships between $\alpha_\pm$ and $\beta_\pm$ depending on the model chosen (subsection 3.2.3). However, we have also spoken about how some of the parameters seem to depend on the normalized cross helicity σ_c. In the observed solar wind behaviour, we see that σ_c starts at 0.894 and then tends to 0, this means that the choice of a *constant* parameter will not properly represent the mathematical description of the σ_c dependent parameters over the entire solution.

We employ some parameter optimization techniques to optimize the nonlinear parameters such that the equations fit to the observational data. To do this, we used the Python3 package `lmfit` [40], which is a helpful wrapper for `scipy.optimize` [58]. Due to the coupled, nonlinear nature of the equations being optimized, local minimizers, like least squares do not behave well. We call a simulated annealing package from `scipy.optimize.dual_annealing` [61] through `lmfit` to find the global minimum.

We will be using the parameter optimization with the quantitative results from the simulation (subsection 4.1.3) to help identify appropriate models for the solar wind and its parameters. Some of the models we have proposed in section 3.2 do not behave physically no matter what we have tried to find a viable parameter solution. These cases have most often been discarded without a word, but some will be noted in later parts of this section due to the physical implications of the failed models.

Unless otherwise specified, all optimized parameters will be constrained to the range 0.01 to 1.4 and where parameters have a symmetric form *e.g.,* $\alpha_\pm$, if the value is stated without specifying the subscript then the two parameters have been constrained to be equal *e.g.,* $\alpha = \alpha_+ = \alpha_-$.

6.2 Nonlinear Models

In this section, we introduce models in batches that follow similar functions or goals. We start with introducing the nonlinear models for $Z_\pm^2$ and D by assuming a constant area under the curve of the correlation tensors. This allows us to examine the different models proposed for the energy difference in isolation. Next, we will introduce models for L_D while including some of the better models for D. We then move on to introducing the models for $L_\pm$ such that all of the variables have non-zero nonlinear models. Lastly, we attempt to introduce a different assumption for the source driving for the correlation lengths and examine the different behaviour in that scenario.

Model Name	$\frac{\mathrm{d}Z^2_\pm}{\mathrm{d}t}\Big\rvert_{NL}$	$\frac{\mathrm{d}D}{\mathrm{d}t}\Big\rvert_{NL}$	$\frac{\mathrm{d}L_\pm}{\mathrm{d}t}\Big\rvert_{NL}$	$\frac{\mathrm{d}L_D}{\mathrm{d}t}\Big\rvert_{NL}$
A	$-\alpha_\pm \frac{Z^2_\pm Z_\mp}{\lambda_\pm}$	$-\alpha_D \frac{D}{\tau^D_A} + \alpha_{D,2}\left(\frac{\mathrm{d}Z^2_+}{\mathrm{d}t}\Big\rvert_{NL} + \frac{\mathrm{d}Z^2_-}{\mathrm{d}t}\Big\rvert_{NL}\right)$	0	0
B	$-\alpha_\pm \frac{Z^2_\pm Z_\mp}{\lambda_\pm}$	$-\alpha_D \frac{D}{\tau^D_A} - \alpha_{D,2}\frac{u^2}{\tau^*}$	0	0
C	$-\alpha_\pm \frac{Z^2_\pm Z_\mp}{\lambda_\pm}$	$-\alpha_D D\left(\frac{Z_+}{\lambda_-} + \frac{Z_-}{\lambda_+}\right)$	0	0

Table 6.1: Table of the nonlinear models with the assumption of conserving the area under the correlation tensors. Models A_λ and B_λ (not shown) employ λ instead of λ_D in τ^D_A

6.2.1 Conserved Correlation Integral Models

The solutions presented here revolve around the constant area under the curve of the correlation tensors, so that we assume the nonlinear terms for the correlation integrals are zero ($\frac{\mathrm{d}L_\pm}{\mathrm{d}t}\big|_{NL} = 0$ and $\frac{\mathrm{d}L_D}{\mathrm{d}t}\big|_{NL} = 0$) and the source terms are zero ($\frac{\mathrm{d}L_\pm}{\mathrm{d}t}\big|_{S} = 0$ and $\frac{\mathrm{d}L_D}{\mathrm{d}t}\big|_{S} = 0$). With the same Elsässer energy models ($Z^2_\pm$ Model A) and source driving terms for the energy (section 3.3), we will iterate over the different proposed energy difference models according to Table 6.1. With a conserved $L_\pm$, and $\lambda_\pm = \frac{L_\pm}{Z^2_\pm}$, the evolution equation for the Elsässer correlation lengths follows as

$$(U \mp V_{Ar})\frac{\mathrm{d}\lambda_\pm}{\mathrm{d}r} = -M^\pm_L \frac{1}{Z^2_\pm}\frac{L_D}{r} + M^\pm D\frac{\lambda_\pm}{Z^2_\pm} + \alpha_\pm Z_\mp - \frac{\lambda_\pm}{Z^2_\pm}S_\pm \tag{6.10}$$

We see that the nonlinear term for $\lambda_\pm$ is equivalent to Equation Model B but with $\beta_\pm = \alpha_\pm$

$$\frac{\mathrm{d}\lambda_\pm}{\mathrm{d}t}\bigg|_{NL} = \beta_\pm Z_\mp \tag{6.11}$$

(Recall in accord with our assumption of $\frac{\mathrm{d}L_\pm}{\mathrm{d}t}\big|_{NL} = 0$ in this section, the general choice of the current $L_\pm$ nonlinear models is $\frac{\mathrm{d}L_\pm}{\mathrm{d}t}\big|_{NL} = (\beta_\pm - \alpha_\pm)Z^2_\pm Z_\mp$)

Solving the models in Table 6.1 yields the green L curves; Figure 6.1 (see Equation 6.3). L_+ shows a relatively steady decrease in the size from its initial position down to 3×10^7 km^2/s^2. L_D starts off negative, and then becomes positive after 5 AU but stays relatively small reaching a maximum size of 4×10^8 km^2/s^2 at 0.5 AU and ending at 2.7×10^7 km^2/s^2 at 75 AU. L_- shows quite different behaviour compared to the other two correlation lengths,

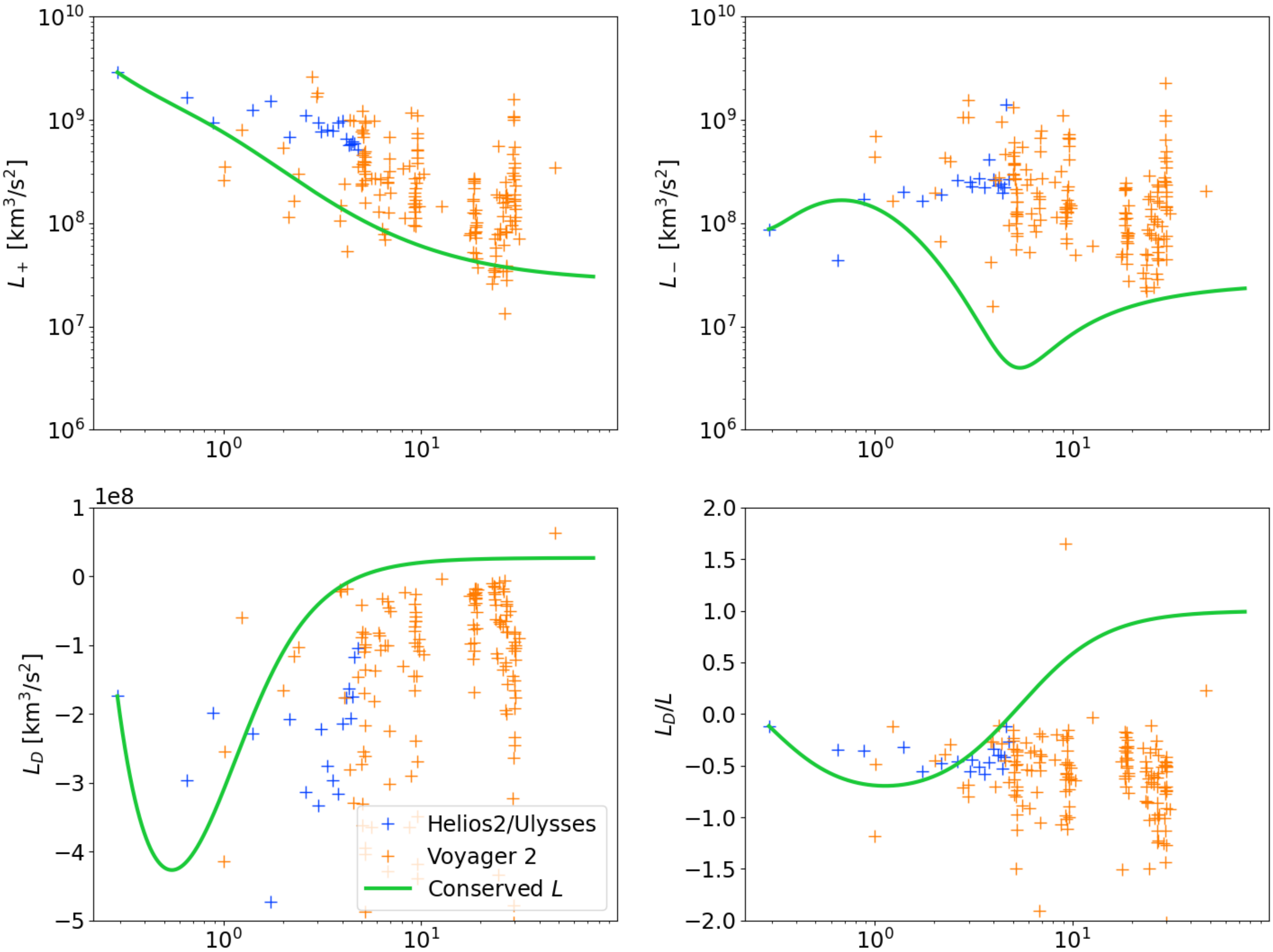

Figure 6.1: Plot of the models in Table 6.1 showing the correlation integrals over radial distance in AU.

it increases from its initial value to around 1.6×10^8 km^2/s^2 at 1 AU and then decreases significantly to 4×10^6 km^2/s^2 at 1 AU and then increases once again to 2.3×10^7 km^2/s^2 at 75 AU.

The behaviour of L_- is caused by the interaction of the mixing and transport terms with L_D. Before 1 AU, the L_- mixing term $(-\frac{1}{U+V_{Ar}} M_L^- L_D)$ is positive and larger in magnitude than the negative transport term $(-\frac{U-V_{Ar}}{U+V_{Ar}} \frac{L_-}{r})$ resulting in an overall increase. At 1 AU, the mixing term becomes negative resulting in an overall decrease. As L_D becomes positive, the L_- mixing term, once again becomes positive which results in the final increase for L_-.

When L_D changes sign (*i.e.,* goes through zero), the Alfvén timescale (as used in D Model A and D Model B) becomes undefined if the associated correlation length is λ_D since $1/\tau_A^D = \frac{V_A}{\lambda} = \frac{V_A D}{L_D}$. To address this undesirable feature we revise Model A and Model B in Table 6.1 such that the Alfvén timescales in the energy difference terms relies on the correlation length $\lambda = \frac{L_+ + L_-}{Z_+^2 + Z_-^2}$ denoted as model Model A_λ and Model B_λ.

When L_D becomes positive, we have two choices in our modelling, either, we aim to keep $\sigma_D \approx -1/3$ according to observational data which will result in λ_D becoming negative and correspond with more magnetic than kinetic energy, or, we let D become positive in an attempt to constrain $\lambda_D > 0$ but will result in $\lambda_D = L_D/D$ becoming undefined at the cross over point. If we maintain the first choice, the major concern is the seemingly nonphysical interpretation of a variable with units in negative km. However, this can be understood if we go back to the velocity and magnetic field interpretation: $L_D = L_u - L_b > 0$ corresponds to the velocity correlation integral becoming greater than the magnetic correlation integral; $D = u^2 - b^2 < 0$ corresponds to a larger magnetic energy than kinetic, therefore $\lambda_D = \frac{L_u - L_b}{u^2 - b^2} < 0$ is perfectly reasonable but not ideal (and there exists points in the observational data that support $\lambda_D < 0$). If we wish to maintain $\lambda_D > 0$, then we require both $D < 0$ and $L_D < 0$ which cannot be captured by the current choice of L_D model.

Figure 6.2 and Figure 6.3 plot the energies and the correlation lengths re-

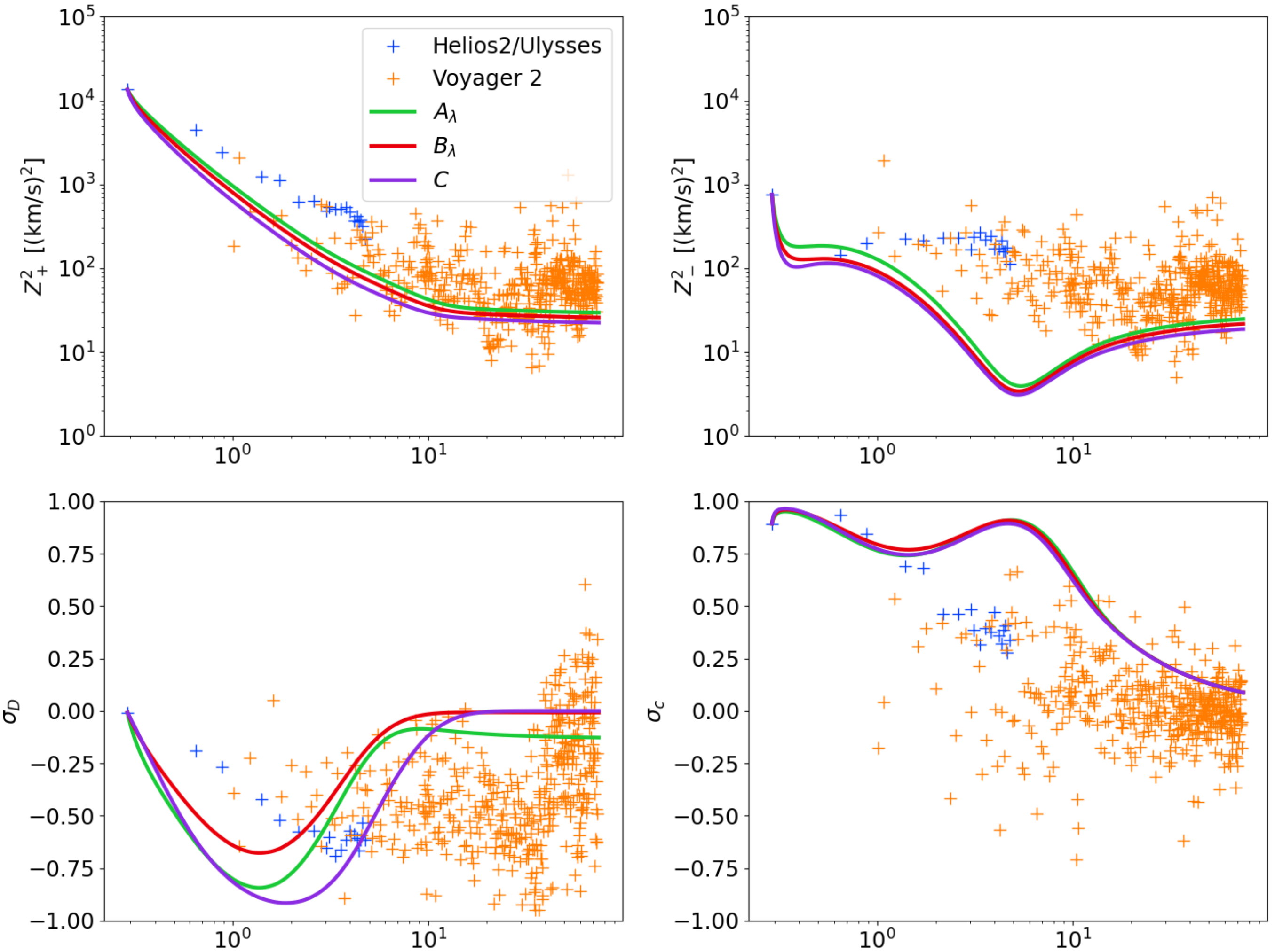

Figure 6.2: Plot of the models in Table 6.1 with Table 6.2 parameters showing the energies over radial distance in AU.

Model Name	$\alpha_\pm$	α_D	$\alpha_{D,2}$
A_λ	0.25	0.125	0.125
B_λ	0.35	0.125	0.125
C	0.5	0.125	N/A

Table 6.2: Table of the parameters used for the nonlinear models with the assumption of conserving the area under the correlation tensors.

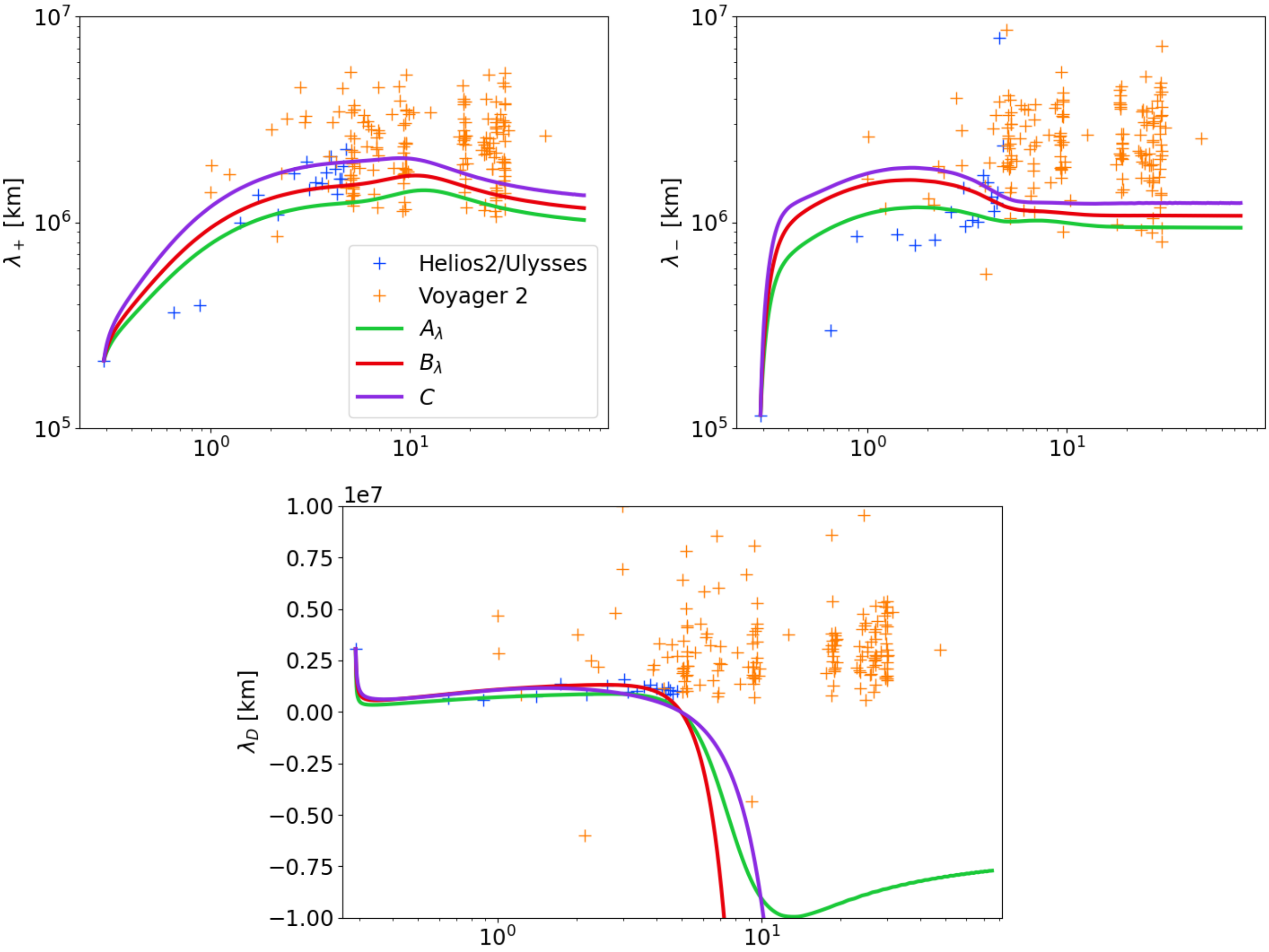

Figure 6.3: Plot of the models in Table 6.1 with Table 6.2 parameters showing the correlation lengths over radial distance in AU.

spectively for the models used in Table 6.1 using the parameters in Table 6.2; Model A_λ (green), Model B_λ (red) and Model C (purple). These three models show almost the same quantitative behaviour and do not significantly change by using different parameter values. Their parameters have been chosen manually to highlight some aspects of the models. The plots for $Z_\pm^2$ and $\lambda_\pm$ show a small difference caused primarily by the choices of the α constant for the $Z_\pm^2$ nonlinear terms. The wobbliness in Z_-^2 is caused by the changes in the dominant term, within 0.3 AU; the negative nonlinear term dominates until the positive mixing term equalizes with it until 1 AU. Then, the negative nonlinear term becomes dominant again as the mixing term gets smaller (as D starts to tend toward zero), until 8 AU when the pickup ion driving turns on. At small radial distances (before 0.5 AU), the negative mixing term and the large nonlinear term (caused by the early, large decays of $Z_\pm^2$) cause D to rapidly decrease. After 0.5 AU, the nonlinear term becomes positive (as L_D is negative and the large $Z_\pm^2$ decays have abated) causing D to increase until 10 AU when the pickup ions driving turns on. Model A_λ allows for σ_D to decrease at a slow rate after 10 AU due to the pickup ions affecting the second nonlinear term more than the other models. When σ_D tends towards 0, $\lambda_D = L_D/D$ becomes large, hence the large decay as seen for Model B_λ and Model C (L_D is positive). Since Model A_λ does not approach 0 like the other two models, λ_D grows in magnitude, but maintains the appropriate size to the observed data (but opposite in sign).

Figure 6.4 plots the proton temperature associated with the models in Table 6.1. We see that all of the models obtain similar plots; displaying an increase in temperature (compared to the adiabatic cooling profile) due to the turbulent dissipation before 10 AU, then dramatically increasing in temperature as the pickup ions add energy to the turbulent fluctuations.

Summary. The models in this section display some correct quantitative behaviour; $\lambda_\pm$ are within the expected ranges and are approximately equal at large distances. The temperatures show increased temperature compared to

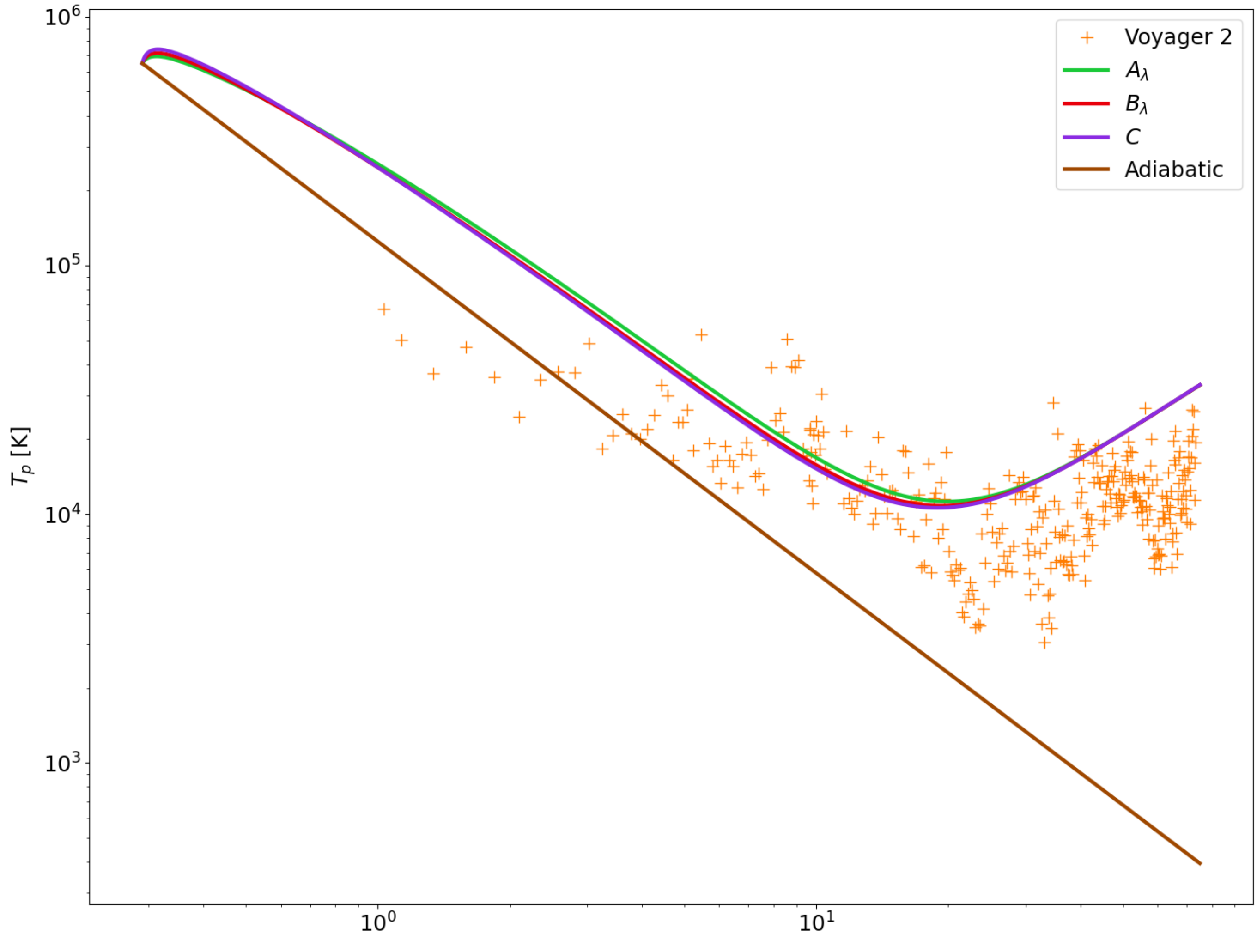

Figure 6.4: Plot of the proton temperature associated with the models in Table 6.1 over radial distance in AU.

the adiabatic expansion and displays the additional increase once the pickup ions turn on. The downsides of these models is the Z_-^2 energy displays values too small primarily due to the dominant mixing term. The energy difference that plays into this mixing term is too large in the early heliosphere and σ_D approaches 0 in the outer heliosphere as the pickup ions turn on. The significant problem lies in constraining L_D and λ_D. The nonlinear D models show similar behaviour despite the different forms of A_λ/B_λ and C; A_λ and B_λ suggest an equipartition of the opposing Alfvén effect and a spectral cascade whereas model C assumes D evolves over the Elsässer turnover time.

6.3 L_D Nonlinear Models

We have seen what happens when we maintain the conservation of L_D and $L_\pm$. Let us introduce models in Table 6.3 for the nonlinear L_D terms in an attempt to constrain the behaviour of L_D and λ_D by keeping L_D negative and preventing σ_D from approaching 0. This is when the complexity starts to increase as any changes made to the evolution of L_D will propagate into $L_\pm$ via the mixing terms which will propagate into $Z_\pm^2$ via the nonlinear terms. Likewise, changes of L_D will propagate into D via Alfvén timescale or, in the case of Model C, through the nonlinear term via the Elsässer energies and correlation lengths.

Since the behaviour of σ_D is similar for each of the models discussed in Table 6.1, we will focus mainly on D Model A and D Model C. The models now containing an L_D nonlinear term are displayed in Table 6.3. Model D (which uses L_D Model A) is constructed via nonlinear modelling of the following form for $L_D = L_u - L_b$. Model E and Model F correspond to the simpler L_D nonlinear evolution model, essentially decay of an Alfvén timescale. The subscripts that will be depicted with these models indicates the choices of the correlation lengths chosen for the Alfvén timescale. Due to the ambiguity in the Alfvén timescale correlation length for some arbitrary model X, we can choose $1/\tau_A^D = \frac{V_A D}{L_D} = \frac{V_A}{\lambda_D}$ depicted as Model X_{λ_D}, $1/\tau_A^D = \frac{V_A\left(Z_+^2+Z_-^2\right)}{L_+ + L_-} = \frac{V_A}{\lambda}$ depicted as Model X_λ and $1/\tau_A^D = V_A\left|\frac{D}{L_D}\right| = \frac{V_A}{|\lambda_D|}$ depicted as Model $X_{|\lambda_D|}$. Models with two subscripts $X_{x,y}$ indicate the choice for the correlation length for the Alfvén timescale for the energy difference D and the correlation integral L_D respectively.

Figures 6.5 to 6.8 plot the models in Table 6.3 with the parameters in Table 6.4. The parameters in model D_λ have been found by the parameter optimizer. There might be a better set of parameters that exist for that model D_λ but, due to the limitations of the optimization technique, the complexity of the model and the large amount of parameters, we will only offer this one solution here.

Figure 6.5 plots the correlation integrals of the evaluated models. The first thing to note is the difference in the behaviour of the same model with different Alfvén timescale assumptions. Model $E_{|\lambda_D|,\lambda_D}$ (red) results in all the correlation integrals unboundedly increasing, whereas Model $E_{\lambda,\lambda}$ (purple) enters a power law decay for $L_\pm$ after 10 AU as L_D approaches 0 and turns off the mixing term. Despite our best efforts Model D_{λ_D} (green) is the only model to keep L_D negative, L_D quickly approaches 0 resulting in power law decays for $L_\pm$ over most of the radial range. For Model F_λ (pink), L_D becomes positive around 1 AU and then decreases towards 0 which also produces power law solutions for $L_\pm$. On the other hand, F_{λ_D} (brown) keeps $L_\pm$ constant after 3 AU and within the bounds of the observational data. L_D becomes positive after 1 AU but then flattens out, becoming constant after 5 AU on the order of 10^8 km^2/s^2. Model F_{λ_D} behaves well in the outer heliosphere (barring the positive L_D), showing the correlation integrals become equivalent $L_+ \approx L_- \approx L_D$.

Figure 6.6 shows the energies of the evaluated models. Model D_{λ_D} (green) has a small α parameter for the nonlinear $Z_\pm^2$ term which results in a small decay rate. The larger $Z_\pm^2$ terms result in a smaller σ_D at early radial distances. Model D_{λ_D} results in a larger normalized cross helicity $\sigma_c \approx 0.75$ which does

Model Name	$\frac{\mathrm{d}Z_\pm^2}{\mathrm{d}t}\Big\vert_{NL}$	$\frac{\mathrm{d}D}{\mathrm{d}t}\Big\vert_{NL}$	$\frac{\mathrm{d}L_\pm}{\mathrm{d}t}\Big\vert_{NL}$	$\frac{\mathrm{d}L_D}{\mathrm{d}t}\Big\vert_{NL}$
D	$-\alpha_\pm \frac{Z_\pm^2 Z_\mp}{\lambda_\pm}$	$-\alpha_D \frac{D}{\tau_A^D} + \alpha_{D,2}\left(\frac{\mathrm{d}Z_\pm^2}{\mathrm{d}t}\Big\vert_{NL} + \frac{\mathrm{d}Z_\pm^2}{\mathrm{d}t}\Big\vert_{NL}\right)$	0	$(\beta_u - \alpha_u)u^2 - (\beta_b - \alpha_b)ub^2$
E	$-\alpha_\pm \frac{Z_\pm^2 Z_\mp}{\lambda_\pm}$	$-\alpha_D \frac{D}{\tau_A^D} + \alpha_{D,2}\left(\frac{\mathrm{d}Z_\pm^2}{\mathrm{d}t}\Big\vert_{NL} + \frac{\mathrm{d}Z_\pm^2}{\mathrm{d}t}\Big\vert_{NL}\right)$	0	$-\beta_D \frac{L_D}{\tau_A^D}$
F	$-\alpha_\pm \frac{Z_\pm^2 Z_\mp}{\lambda_\pm}$	$-\alpha_D D\left(\frac{Z_+}{\lambda_-} + \frac{Z_-}{\lambda_+}\right)$	0	$-\beta_D \frac{L_D}{\tau_A^D}$

Table 6.3: Table of the nonlinear models iterating over some of the models for L_D with the assumption of conserving $L_\pm$

Model Name	$\alpha_\pm$	α_u	α_b	α_D	$\alpha_{D,2}$	β_D	β_u	β_b
D_λ	0.0187	0.9595	0.9058	0.3399	0.5515	N/A	0.3679	0.3321
$E_{\vert\lambda_D\vert,\lambda_D}$	0.4	N/A	N/A	0.25	0.125	0.125	N/A	N/A
$E_{\lambda,\lambda}$	0.4	N/A	N/A	0.25	0.125	0.125	N/A	N/A
F_{λ_D}	0.4	N/A	N/A	0.25	N/A	0.125	N/A	N/A
F_λ	0.4	N/A	N/A	0.5	N/A	0.25	N/A	N/A

Table 6.4: Table of parameters for models listed in Table 6.3 with model D_λ parameters found by the parameter optimization technique.

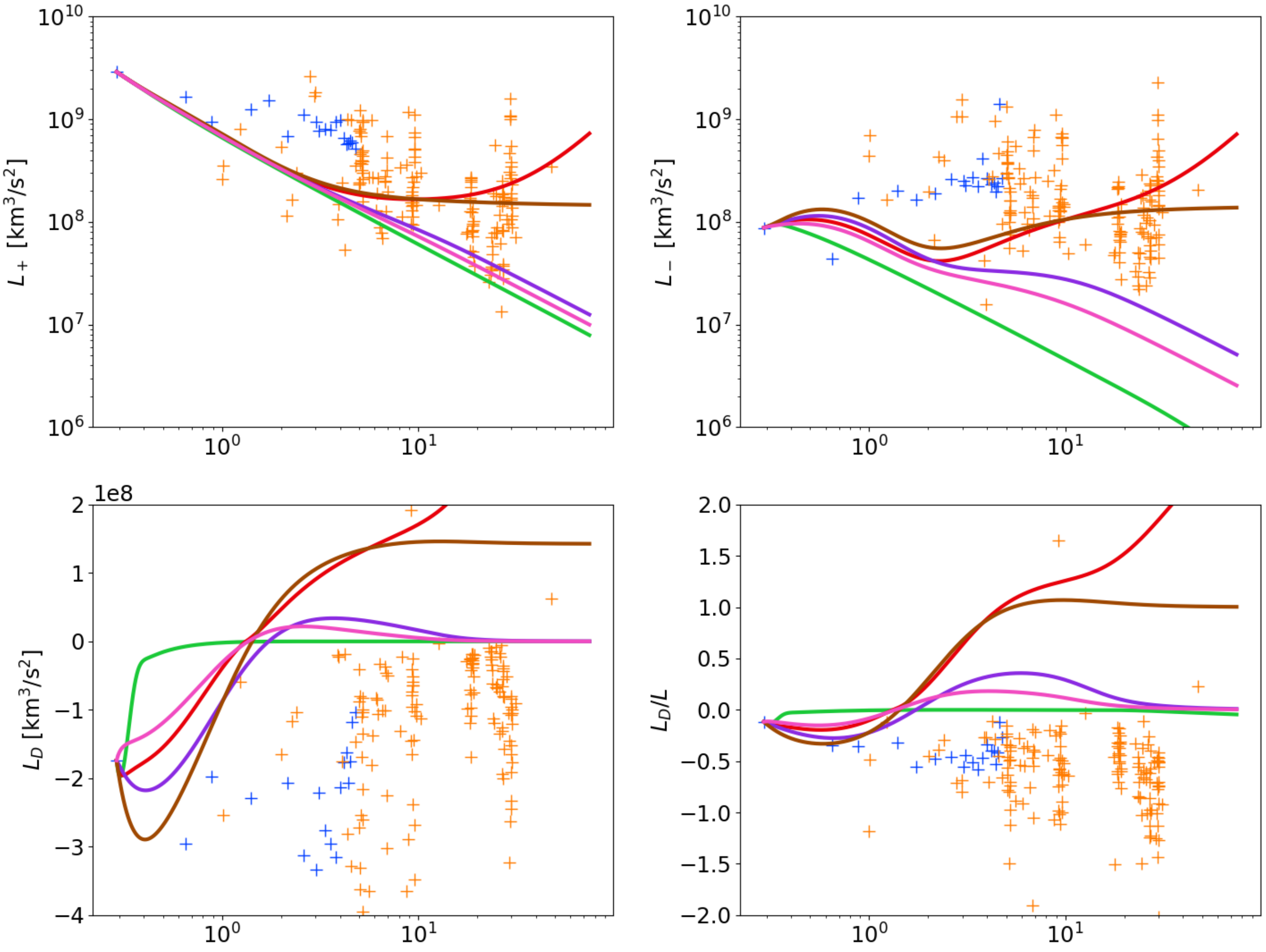

Figure 6.5: Plot of the models in Table 6.3 with Table 6.4 parameters showing the correlation integrals over radial distance to 75 AU.

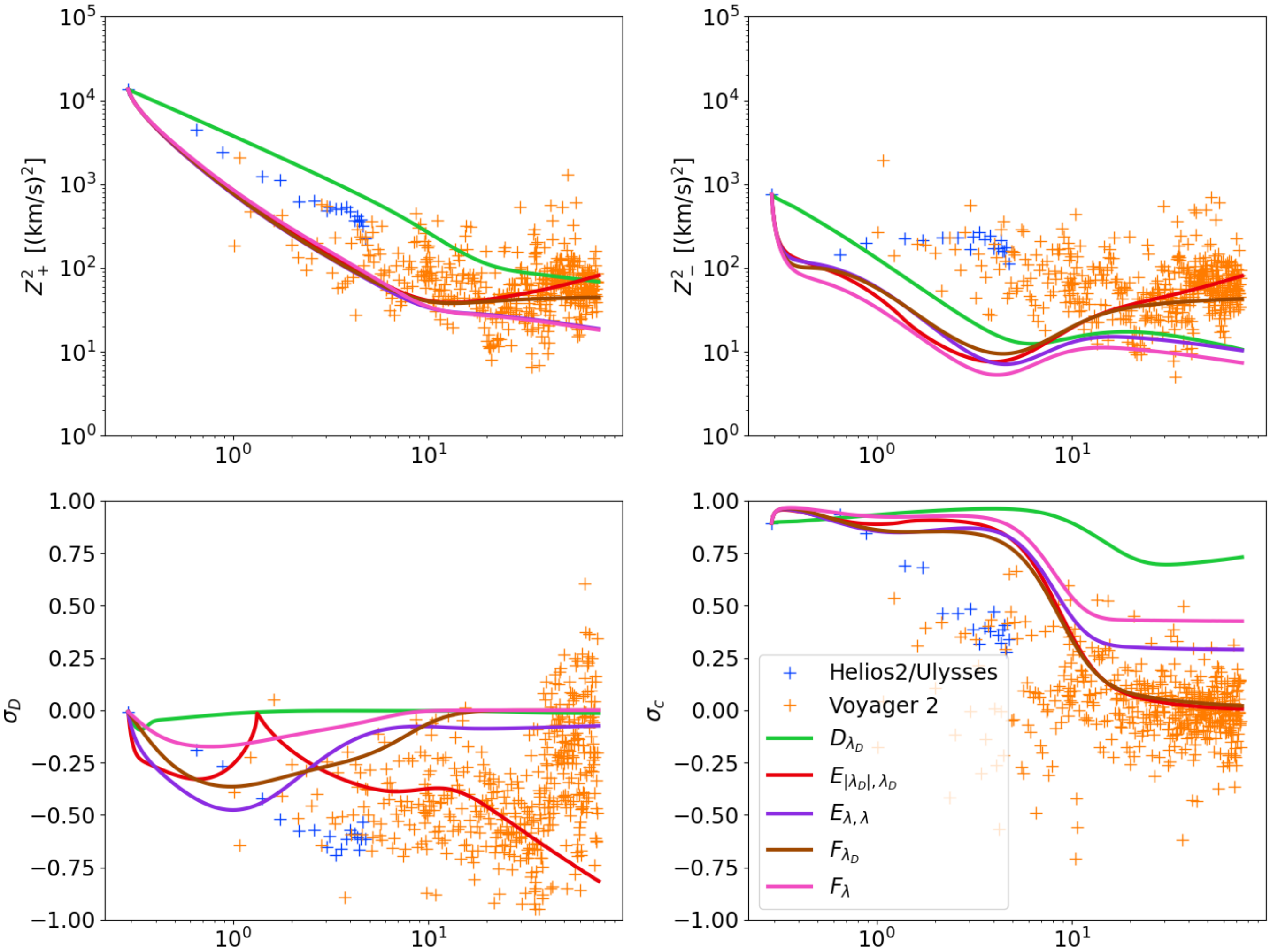

Figure 6.6: Plot of the models in Table 6.3 with Table 6.4 parameters showing the energies over radial distance to 75 AU.

not match observational data. Model $E_{\lambda,\lambda}$ (purple) maintains similar $Z_{\pm}^2$ values to the remaining models, only resulting in a final σ_c value of 0.25. σ_D does not converge towards 0, instead maintaining a value around -0.125 after 10 AU. This solution ends with decreasing energy values. The other E model, Model $E_{|\lambda_D|,\lambda_D}$ (red) results in increasing energy values after the pickup ions turn on and $\sigma_c \approx 0$ after 10 AU. However, due to the absolute value in the Alfvén timescale for the energy difference nonlinear term, an abrupt turning point occurs after 1 AU corresponding to L_D changing sign (as it crosses 0 and the nonlinear piece becomes undefined). The absolute value then constrains σ_D to stay negative, reaching an equilibrium at $\sigma_D \approx -1/3$ until the pickup ions get strong enough and decrease σ_D even further. Model F_λ (pink) keeps σ_D small, not even reaching -0.25 at 1 AU, and then converges to 0 before 10 AU. Model F_λ results in decreasing $Z_{\pm}^2$ energies and a large σ_c value of 0.4. Finally, Model F_{λ_D} also keeps σ_D small and converges to 0 after 10 AU. At large distances, the Elsässer energies converge to an approximately equal value ($\sigma_c \approx 0$) and stay constant. σ_D does not become undefined as L_D changes sign, as the energy difference nonlinear model (D Model C) does not contain an Alfvén timescale.

Figure 6.7 shows the correlation lengths for the models used in Table 6.3. Model D_{λ_D} (green) is the only model that maintains a positive λ_D value (albeit, relatively zero). Due to the small Elsässer nonlinear parameter α and next to no mixing, there is minimal growth in the $\lambda_\pm$ correlation lengths that dips below 10^5 km in the outer heliosphere. Model $E_{|\lambda_D|,\lambda}$ (red) displays unbounded, increasing $\lambda_\pm$ values in the outer heliosphere and a λ_D that surpasses -3×10^7 km and is still decreasing at 75 AU. Model $E_{\lambda,\lambda}$ (purple) displays decreasing $\lambda_\pm$ after the pickup ions turn on. Model $E_{\lambda,\lambda}$'s λ_D displays significantly different behaviour than the others seen so far, as D approaches 0 and L_D changes sign, λ_D decreases to the order of -1.25×10^7 km which is still within the range of the largest negative observational data point. λ_D then starts increasing as the pickup ions turn on and approaches 0 (from the negative side). Model F_{λ_D} (brown) also shows λ_D vanishing as σ_D approaches 0, but $\lambda_\pm$ decrease at a

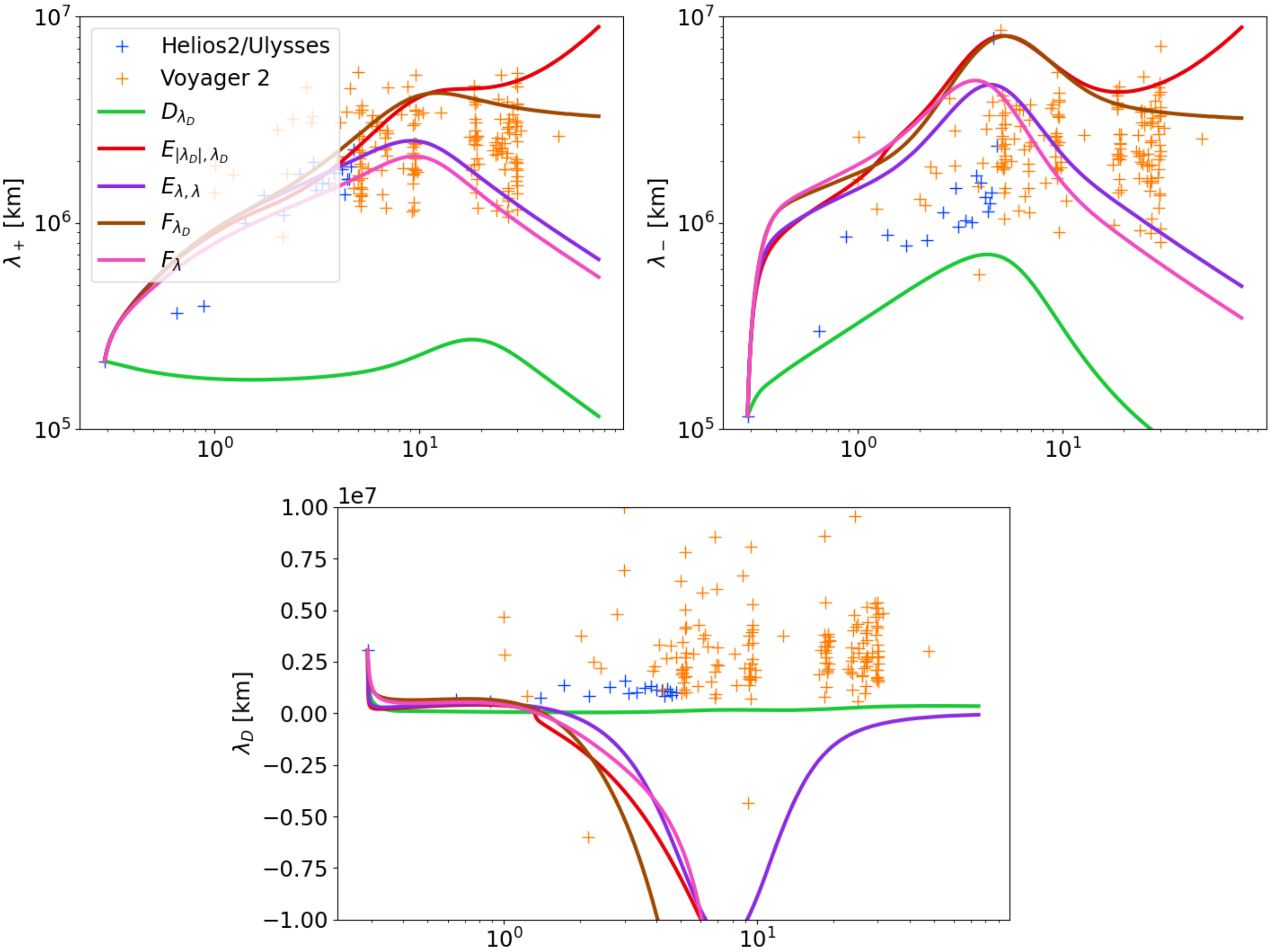

Figure 6.7: Plot of the models in Table 6.3 with Table 6.4 parameters showing the correlation lengths over radial distance to 75 AU.

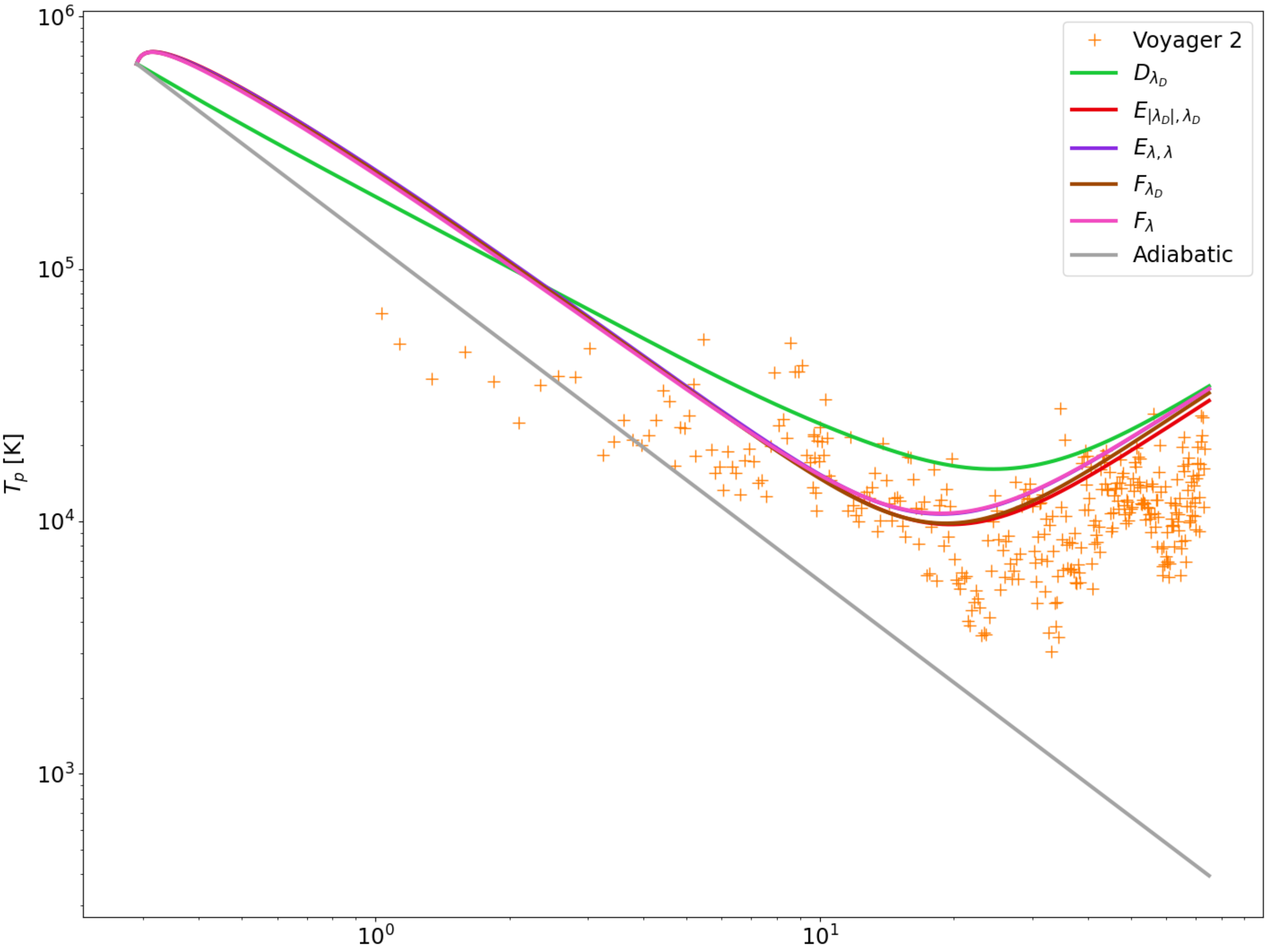

Figure 6.8: Radial temperature profiles for models listed in Table 6.3 with Table 6.4 parameters up to 75 AU.

smaller rate than the other decreasing models and have equivalent values. The Elsässer correlation lengths ($\lambda_\pm$) in Model F_λ (pink) follows the same trend as Model $E_{\lambda,\lambda}$ and maintains equivalent values. λ_D vanishes as D approaches 0.

Figure 6.8 shows that all of the models listed in Table 6.3 still display the pickup ion driving increase in the proton temperature that matches the observed values. Model D_{λ_D} (green) is the only one that displays a distinct curve at early distances due to the small α parameter choice. This model still maintains appropriate temperature values but is on the higher end of the observed data range and results in a larger temperature after 2 AU than the other models that have the steep increase at the start of the solution that drops off after 2 AU until the pickup ions turn on.

Summary. Unfortunately, we have not been able to find reasonable solutions that constrain L_D (and λ_D). Models using L_D Model A (Model D_λ) show promise at being able to keep L_D negative and close to 0 but have been difficult to find solutions for. We have been able to get nice behaviour out of Model F_{λ_D}; the energy difference evolves over the total energy turnover time and L_D evolves over the Alfvén timescale. F_{λ_D} still cannot capture the expected σ_D behaviour and Z_-^2 lies under the observational data points. We have shown a variety of models that capture different $L_\pm$ behaviour through just the addition of the L_D nonlinear term.

6.4 $L_\pm$ Nonlinear Models

Now, we shall examine the effects of applying nonlinear models to $L_\pm$, we test combinations of models from previous sections with the addition of $\lambda_\pm$ Model A and Model B converted to $L_\pm$ via $\frac{\mathrm{d}L_\pm}{\mathrm{d}t}\big|_{NL} = Z_\pm^2\frac{\mathrm{d}\lambda_\pm}{\mathrm{d}t}\big|_{NL} + \lambda_\pm\frac{\mathrm{d}Z_\pm^2}{\mathrm{d}t}\big|_{NL}$. We present some of the best performing models we could find in Table 6.5 and use the parameters found by the parameter optimization technique (Table 6.6). As before, the subscript in the model name determines the correlation length chosen for the Alfvén timescale. A superscript; for example X^y, is used to indicate the same model with a different set of parameter solutions.

Figure 6.9 displays the temperature of the models obtained from in Table 6.5 using the parameters in Table 6.6. As with the previous cases, there is not much difference between the models; the models still show the heating of the plasma and an increase in the temperature after 10 AU due to the pickup ions. Model H_λ (purple) has the smallest increase at the start and the affect of the pickup ions is only visible after 40 AU with a shallower slope. Model I (brown) is the other extreme, having the largest temperature increase at the start followed by a steeper decay. Once the pickup ions turn on, Model I is the second to display its effects and has one of the steepest increases.

Model Name	$\frac{\mathrm{d}Z_\pm^2}{\mathrm{d}t}\Big\rvert_{NL}$	$\frac{\mathrm{d}D}{\mathrm{d}t}\Big\rvert_{NL}$	$\frac{\mathrm{d}L_\pm}{\mathrm{d}t}\Big\rvert_{NL}$	$\frac{\mathrm{d}L_D}{\mathrm{d}t}\Big\rvert_{NL}$
G	$-\alpha_\pm \frac{Z_\pm^2 Z_\mp}{\lambda_\pm}$	$-\alpha_D \frac{D}{\tau_A^D} + \alpha_{D,2}\left(\frac{\mathrm{d}Z_\pm^2}{\mathrm{d}t}\Big\rvert_{NL} + \frac{\mathrm{d}Z_\pm^2}{\mathrm{d}t}\Big\rvert_{NL}\right)$	$(\beta_\pm - \alpha_\pm)Z_\pm^2 Z_\mp$	$(\beta_u - \alpha_u)u^2 - (\beta_b - \alpha_b)ub^2$
H	$-\alpha_\pm \frac{Z_\pm^2 Z_\mp}{\lambda_\pm}$	$-\alpha_D \frac{D}{\tau_A^D} + \alpha_{D,2}\left(\frac{\mathrm{d}Z_\pm^2}{\mathrm{d}t}\Big\rvert_{NL} + \frac{\mathrm{d}Z_\pm^2}{\mathrm{d}t}\Big\rvert_{NL}\right)$	$\beta_\pm Z_\pm^2 (Z_\pm^2 Z_\mp)^{1/3} - \alpha_\pm Z_\pm^2 Z_\mp$	0
I	$-\alpha_\pm \frac{Z_\pm^2 Z_\mp}{\lambda_\pm}$	$-\alpha_D D\left(\frac{Z_+}{\lambda_-} + \frac{Z_-}{\lambda_+}\right)$	$(\beta_\pm - \alpha_\pm)Z_\pm^2 Z_\mp$	0
J	$-\alpha_\pm \frac{Z_\pm^2 Z_\mp}{\lambda_\pm}$	$-\alpha_D D\left(\frac{Z_+}{\lambda_-} + \frac{Z_-}{\lambda_+}\right)$	$(\beta_\pm - \alpha_\pm)Z_\pm^2 Z_\mp$	$-\beta_D \frac{L_D}{\tau_A^D}$
K	$-\alpha_\pm \frac{Z_\pm^2 Z_\mp}{\lambda_\pm}$	$-\alpha_D \frac{D}{\tau_A^D} + \alpha_{D,2}\left(\frac{\mathrm{d}Z_\pm^2}{\mathrm{d}t}\Big\rvert_{NL} + \frac{\mathrm{d}Z_\pm^2}{\mathrm{d}t}\Big\rvert_{NL}\right)$	$(\beta_\pm - \alpha_\pm)Z_\pm^2 Z_\mp$	$-\beta_D \frac{L_D}{\tau_A^D}$

Table 6.5: Table of the nonlinear models, iterating over some models for D, $L_\pm$, and L_D

Model Name	α_+	α_-	α_u	α_b	α_D	$\alpha_{D,2}$	β_+	β_-	β_u	β_b	β_D
G_λ^1	0.3670	0.3670	1.0795	0.3733	0.2496	0.1	0.8658	0.8658	0.3330	0.9780	N/A
G_λ^2	0.1240	0.1240	1.0610	0.7190	0.2854	0.4445	0.1586	0.1586	0.4820	0.2554	N/A
H_λ	0.1669	0.1669	N/A	N/A	0.3143	0.5698	0.9595	0.9595	N/A	N/A	N/A
I	0.7909	0.2644	N/A	N/A	0.11	N/A	0.9040	1.3951	N/A	N/A	N/A
$J_{\lambda_D}^1$	0.1734	0.1734	N/A	N/A	0.0108	N/A	0.4829	0.4829	N/A	N/A	0.0176
$J_{\lambda_D}^2$	0.2028	0.2028	N/A	N/A	0.0255	N/A	0.1014	0.1014	N/A	N/A	0.0586
$K_{\lambda,\lambda}$	0.5388	0.5388	N/A	N/A	0.7926	N/A	1.4	1.4	N/A	N/A	1.0954

Table 6.6: Table of the parameters found by the parameter optimization technique for models listed in Table 6.5

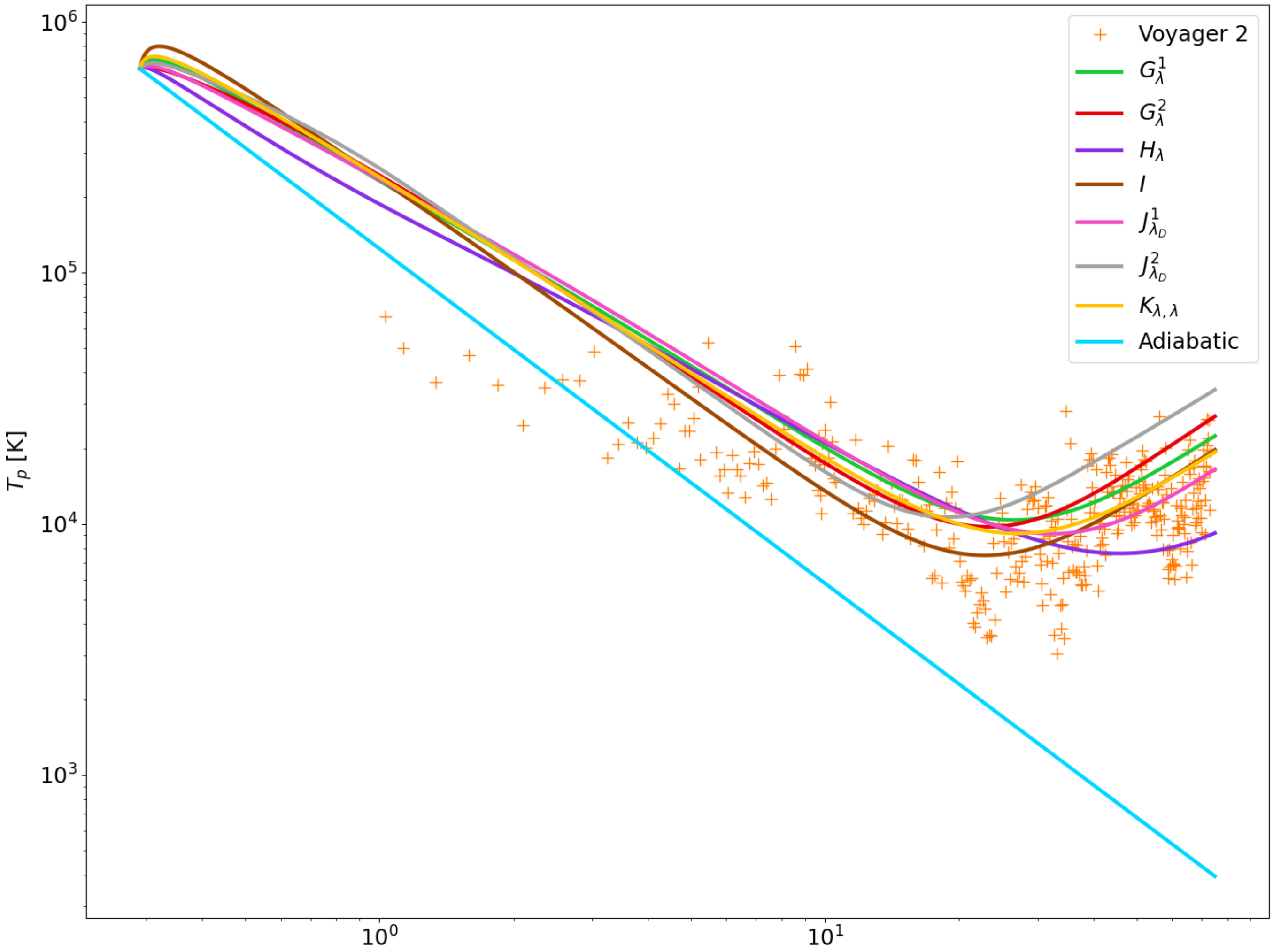

Figure 6.9: Radial temperature profiles associated with the models listed in Table 6.5 with Table 6.6 parameters up to 75 AU.

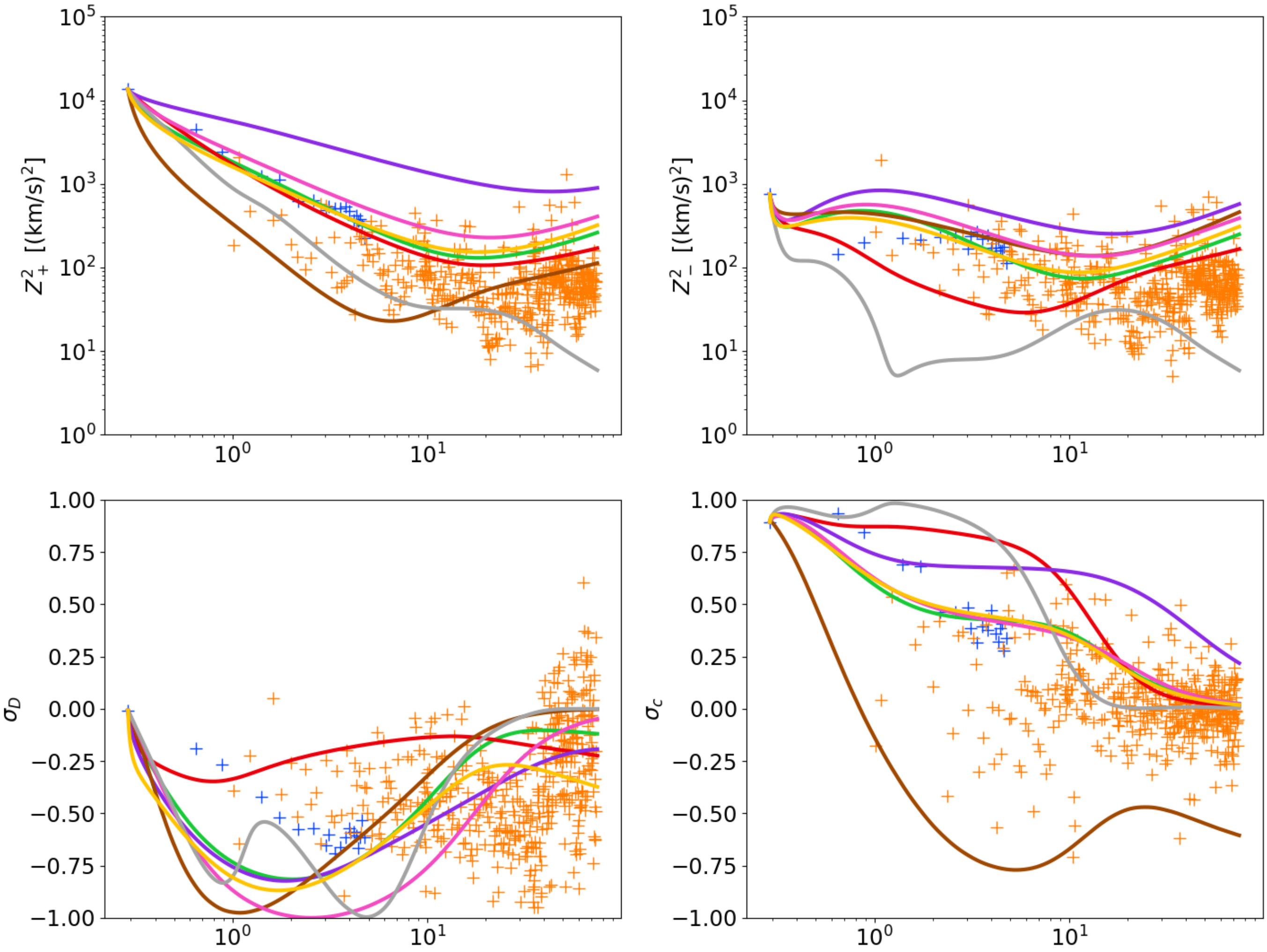

Figure 6.10: Plot of the models in Table 6.5 with Table 6.6 parameters showing the energies over radial distance to 75 AU.

Figure 6.10 plots the energies of the models in Table 6.5 using the parameters in Table 6.6 (refer to Figure 6.9 for the key). Model G_λ^1 (green) and G_λ^2 (red) have similar profiles for Z_+^2. Their profiles for Z_-^2 are significantly different as seen in the σ_c plot. Model G_λ^1 has $\sigma_c \approx 0.75$ until 6 AU when σ_c starts to converge towards 0, whereas G_λ^2 has $\sigma_c < 0.5$. Despite the smaller $\alpha_\pm$ parameter in Model G_λ^2, Model G_λ^1 has the larger energy values. This is due to the difference between the $\alpha_\pm$ and $\beta_\pm$ values, Model G_λ^1 has positive nonlinear Elsässer correlation integral terms $\beta_\pm - \alpha_\pm = 0.4988$ which results in growth in $L_\pm$ (and larger $L_\pm$ values) which, in turn results in a smaller nonlinear term for $Z_\pm^2$. G_λ^1 and G_λ^2 display positive nonlinear terms until the pickup ions turn on; the Alfvén effect is larger than the spectral transfer from $Z_\pm^2$. G_λ^2 has a large (positive) nonlinear term which results in an total increase in D in the early heliosphere whereas G_λ^1 displays a total decrease in D due to its smaller nonlinear term and large (negative) mixing term. The net result is G_λ^1 reaches its minimum value $\sigma_D \approx -0.81$ at 2 AU and G_λ^2 reaches its minimum value $\sigma_D \approx -0.35$ at 0.75 AU. After the pickup ions turn on G_λ^1's σ_D becomes larger than G_λ^2 and reaches $\sigma_D \approx -0.1$ at 75 AU and shows a slow rate of decrease. G_λ^2 reaches $\sigma_D \approx -0.22$ at 75 AU and shows a fast rate of decrease.

Model $J_{\lambda_D}^1$ (pink) has been chosen such that $\beta_\pm > \alpha_\pm$ whereas Model $J_{\lambda_D}^2$ (grey) keeps a more appropriate $\alpha_\pm \geq 2\beta_\pm$. The evolution of the energies of $J_{\lambda_D}^1$ is similar to entirely different models like G_λ^1 (green) and Model $K_{\lambda,\lambda}$ (yellow). $J_{\lambda_D}^2$ displays a distinct wobbly behaviour, particularly for Z_-^2 and σ_D. At the start of the run, Z_-^2 decreases due to the large nonlinear term then the Z_-^2 terms cancel out at 0.4 AU. After 0.4 AU, Z_-^2 decreases again due to the sum of the nonlinear and transport term being larger than the mixing term until 1 AU. After 1 AU L_D becomes positive and causes L_- to grow (through the mixing term) which causes the nonlinear term in Z_-^2 to decrease, now the mixing term is larger than the nonlinear and transport terms which results in an increasing Z_-^2 until the pickup ions turn on. The wobbly behaviour in σ_D is caused entirely by following the abrupt changes to the energies and the correlation lengths. $J^2_{\lambda_D}$ depicts decaying $Z^2_\pm$ after the pickup ions after 20 AU due to the decreasing correlation integrals. The decay of the energies even after the pickup ions is unexpected and due to the decrease in the correlation lengths through the negative nonlinear term ($\alpha_\pm > \beta_\pm$) which is caused by feedback from increasing the energy before 20 AU. At 20 AU, the decrease in the correlation integrals is stronger than the increase due to the pickup ions, resulting in the decreasing energies.

Model I (brown) displays the consequences of choosing $\alpha_+ \neq \alpha_-$. From the larger α_+ value, Z^2_+ decays quickly and Z^2_- decays slowly. σ_c becomes negative after 1 AU as now, there is more energy contribution from Z^2_-. σ_D decays quickly, reaching -0.975 at 1 AU before entering linear growth back towards zero. Model H_λ (purple) shows the slowest decay in the energies due to the small nonlinear term (as the correlation integrals are large); the energies are large and mostly outside of the range of observational data. Model $K_{\lambda,\lambda}$ (yellow) shows slightly large Z^2_+ and Z^2_- values but is still within the range of some data points. σ_D initially decreases to -0.78 after 1 AU but then increase back up to -0.22 at 2 AU. After 2 AU, σ_D decreases, finishing with a decreasing trend at the appropriate value of -0.33 at 75 AU.

Figure 6.11 plots the correlation integrals $L_\pm$ and L_D and the ratio between L_D and $L = \frac{1}{2}\left(L_+ + L_-\right)$ of the models in Table 6.5 using the parameters in Table 6.4. As discussed with the energies, Model $J^2_{\lambda_D}$ (grey) displays wobbly behaviour due the nonlinear feedback from the energies and changes in the sign of L_D around 1 AU influencing the sign of the mixing terms. As $L_\pm$ decreases, L_D becomes twice as large (and greater) than $L_\pm$ which is amplified after 10 AU and $L_\pm$ start decreasing significantly despite $J^2_{\lambda_D}$ having the smallest L_D. The model using $\lambda_\pm$ Model A; Model H_λ (purple) displays growth of $L_\pm$, becoming larger than the other models. This model is the only one that we could find that uses $\lambda_\pm$ Model A but the parameters the optimizer found use a large disparity between $\alpha_\pm$ and $\beta_\pm$ which is the reason for the large growth of $L_\pm$. Since L_D nonlinear term is zero for H_λ, L_D is driven purely by the mixing

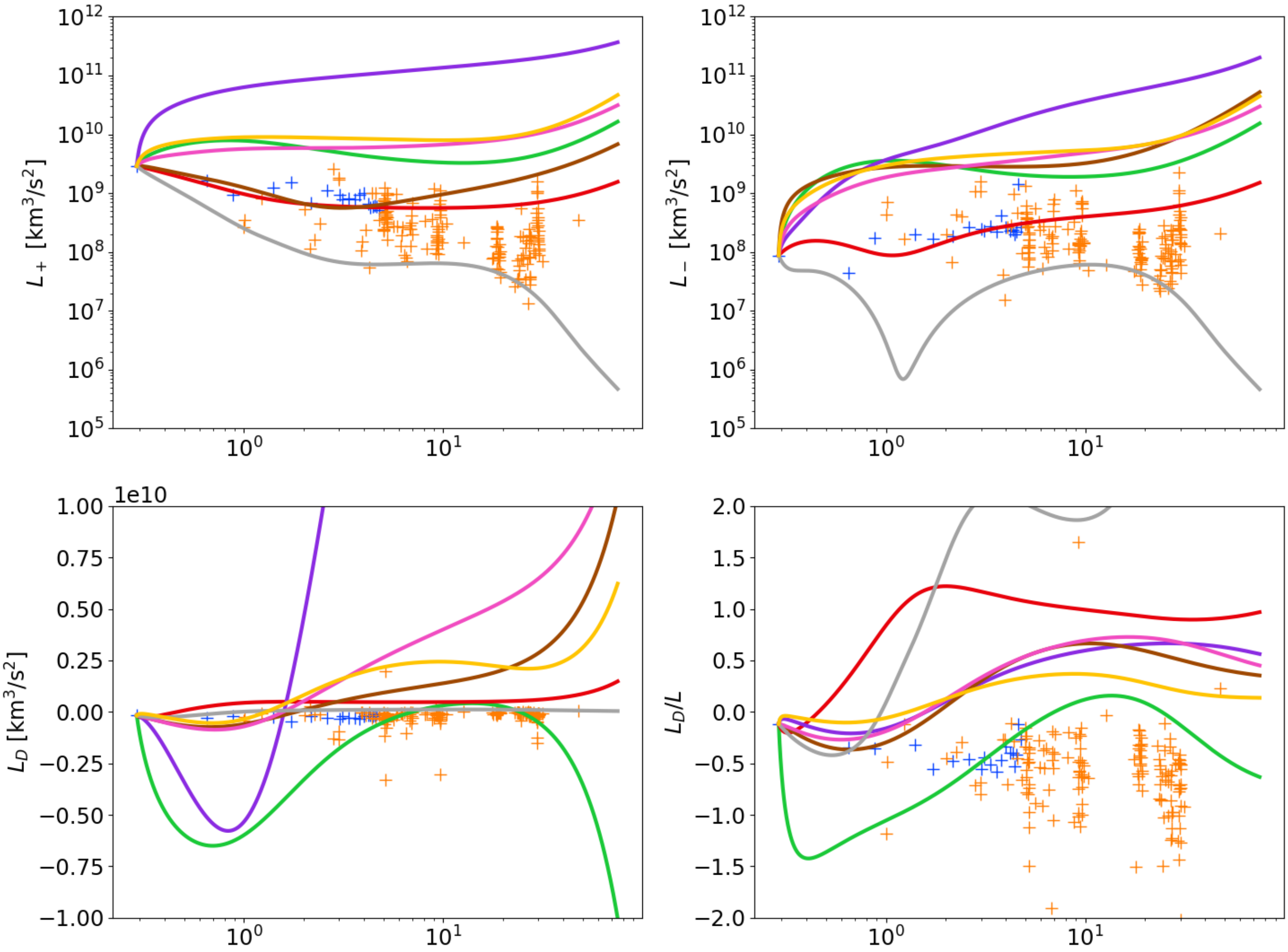

Figure 6.11: Plot of the models in Table 6.5 with Table 6.6 parameters showing the correlation integrals over radial distance to 75 AU.

and transport terms. L_D decreases to less than -5×10^9 km^3/s^2 around 1 AU before growing significantly and changing sign. L_D settles to roughly half of the average of the Elsässer correlation lengths.

Model I (brown) has similar $\beta_\pm$ values ($\beta_+ \approx \beta_-$), so the large disparity between α_+ and α_- causes L_+ to decrease whilst L_- has one of the largest growths. In Model $K_{\lambda,\lambda}$, L_D becomes positive after 1 AU and stays positive because of the strong mixing terms as $L_\pm$ are large. After 30 AU, L_D rapidly increases due to the mixing terms as $L_\pm$ are growing from the pickup ions through the nonlinear terms. Despite the rapid growth of L_D, L_D/L decreases as the pickup ions increase the energy of the system. Model $J^1_{\lambda_D}$ (pink) follows a similar trend to $K_{\lambda,\lambda}$.

Model G^1_λ (green) is the only model to keep L_D negative with the exception of the distances between 7 and 24 AU. Before 0.7 AU, L_D has negative growth until the transport term is larger than the nonlinear term resulting in L_D turning and approaching zero and eventually becoming positive. As the pickup ions turn on; increasing u^2 and b^2 equally, the (negative) nonlinear term becomes larger and pushes L_D back to being negative. Model G^2_λ (red) displays the most reasonable evolution of $L_\pm$ and L_D out of the models presented in this section and remarkably different behaviour from the same model with different parameters (G^1_λ). $L_\pm$ stay within the bounds of the observational data; slowly increasing due to the pickup ions after 1 AU. L_D becomes positive at 0.45 AU and becomes proportional to L after 1 AU.

Figure 6.12 shows all the models in Table 6.5 have stable, increasing Elsässer correlation lengths with the exception of Model $J^2_{\lambda_D}$ (grey). This is caused by the addition of the $L_\pm$ nonlinear which implies a nonlinear term for $\lambda_\pm$; both $\lambda_\pm$ Model A and Model B increase the correlation length. Model G^1_λ (green) maintains positive λ_D until 7 AU when L_D becomes positive. After 30 AU, λ_D undergoes an unbounded increase, surpassing the order of 1×10^8 km^3/s^2. Model G^2_λ and $K_{\lambda,\lambda}$ decrease λ_D as D gets smaller but stays defined and of the order of -5×10^8 km^3/s^2. The remaining models become undefined as $D \to 0$.

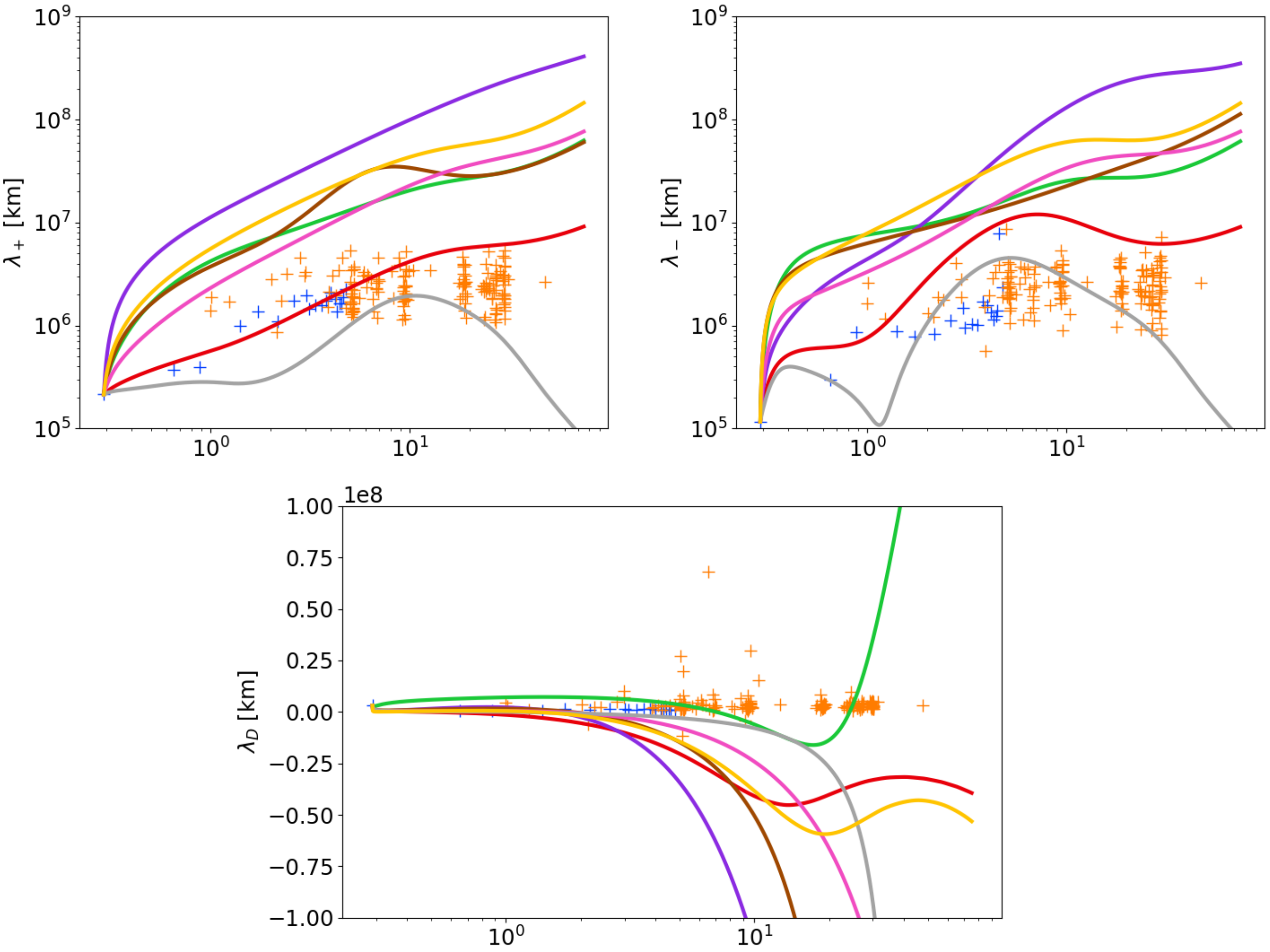

Figure 6.12: Plot of the models in Table 6.5 with Table 6.6 parameters showing the correlation lengths over radial distance to 75 AU.

Summary. With the addition of $L_\pm$ nonlinear models, we have been able to show models that achieve a non-zero equilibrium between the kinetic and magnetic energies ($\sigma_D < 0$). At the cost of large and increasing $L_\pm$, $Z_\pm^2$ have become closer to their observed Helios 2/Ulysses and Voyager 2 observational data. We have still not been able to constrain L_D; once again, Model G_λ^1 (using L_D Model A) does the best job at keeping $L_b > L_u$ but gets large before 1 AU and gains unconstrained decay in the outer heliosphere. Model $K_{\lambda,\lambda}$ does the best at following the observed energy values, $\sigma_D \approx -1/3$ is achieved in the outer heliosphere and $Z_\pm^2$ seem to follow the observational trends. Valid models using $\lambda_\pm$ Model A have been difficult to find, it is easier to use Model B despite the potential for the inconsistency when one of the fields turns off. $J_{\lambda_D}^1$ is the only model that follows the appropriate parameter relation suggested by [36]; $\alpha_\pm \geq \beta_\pm$, or more specifically $\alpha_\pm \geq 2\beta_\pm$ as $\alpha_\pm \approx \beta_\pm$ obtains the conserved correlation integral equations ($L_\pm$ Model 0).

6.5 Source Models

In section 3.3 we discussed turbulence source driving in the solar wind and introduced the assumptions that can be applied to the correlation lengths. So far, we have been maintaining $\frac{\mathrm{d}L_\pm}{\mathrm{d}t}\big|_S = 0$; in this section we will assume that the changes to the correlation lengths through the turbulence driving will be zero. In other words, the turbulence source driving occurs at scales greater than (in the case of the pickup ions) and equal to (in the case of the shear driving) the correlation lengths $\lambda_\pm$. Using $L_\pm = \lambda_\pm Z_\pm^2$ and $\frac{\mathrm{d}\lambda_\pm}{\mathrm{d}t}\big|_S = 0$, the source term for the correlation integral is

$$\left.\frac{\mathrm{d}L_\pm}{\mathrm{d}t}\right|_S = \lambda_\pm \left.\frac{\mathrm{d}Z_\pm^2}{\mathrm{d}t}\right|_S \tag{6.12}$$

Therefore, the correlation integrals also increase due to the source driving effects. In this section, we have re-run the numerical solutions for some of the models (using their same parameters) from previous sections using the new source driving assumption. Model D_{λ_D} (Tables 6.3 and 6.4) is the only model to become undefined when the new assumption is applied; in this case, the energy difference becomes undefined as L_D becomes positive, driven by larger energies. The energies increase, relative to the conserved source driving model due to the increase in $\lambda_{\pm}$ that causes the Elsässer energies (negative) nonlinear term to become smaller.

Figure 6.13 shows the temperatures for some models picked from previous sections; there is no significant difference in the behaviour of the temperature. Figure 6.14 shows the strong increase in the energies as the pickup ions turn on. Lastly, Figure 6.15 shows the increases in the correlation integrals due to the pickup ion driving.

By assuming no source terms are applied to the Elsässer correlation lengths, we see large growth in the correlation integrals and lengths and even larger growth in the energies as the pickup ions turn on. This is in opposition to the observational data that seems to depict a decreasing trend in the $L_{\pm}$ and $\lambda_{\pm}$ after the pickup ions turn on.

6.6 Optimized Adhikari et al. Model

For comparison purposes, we have also implemented the Adhikari et al. [1] model and obtained optimized parameters for it. In the Adhikari et al. [1] model (see section E.1) the parameters they have chosen are larger than what would be expected. $\alpha_{\pm} = \beta_{\pm} = 2$ is much larger than simulation results quantitatively show (subsection 4.1.3 and [5]) and the shear parameter $C_{sh} = 7.35$ which is much larger than the 0.5 to 1.5 range recommendation from [12, 13, 37].

Applying the parameter optimization to our implementation of the Adhikari et al. [1] model for α, α_D and C_{sh} results in the new parameter values found in Table 6.7. Now, $\alpha = 0.44$ and the shear parameter C_{sh} is now 0.725 (rather than 7.35), which fits inside the 0.5 to 1.5 range recommendation. Interestingly, using the new parameters to plot the energies in Figure E.1 and the

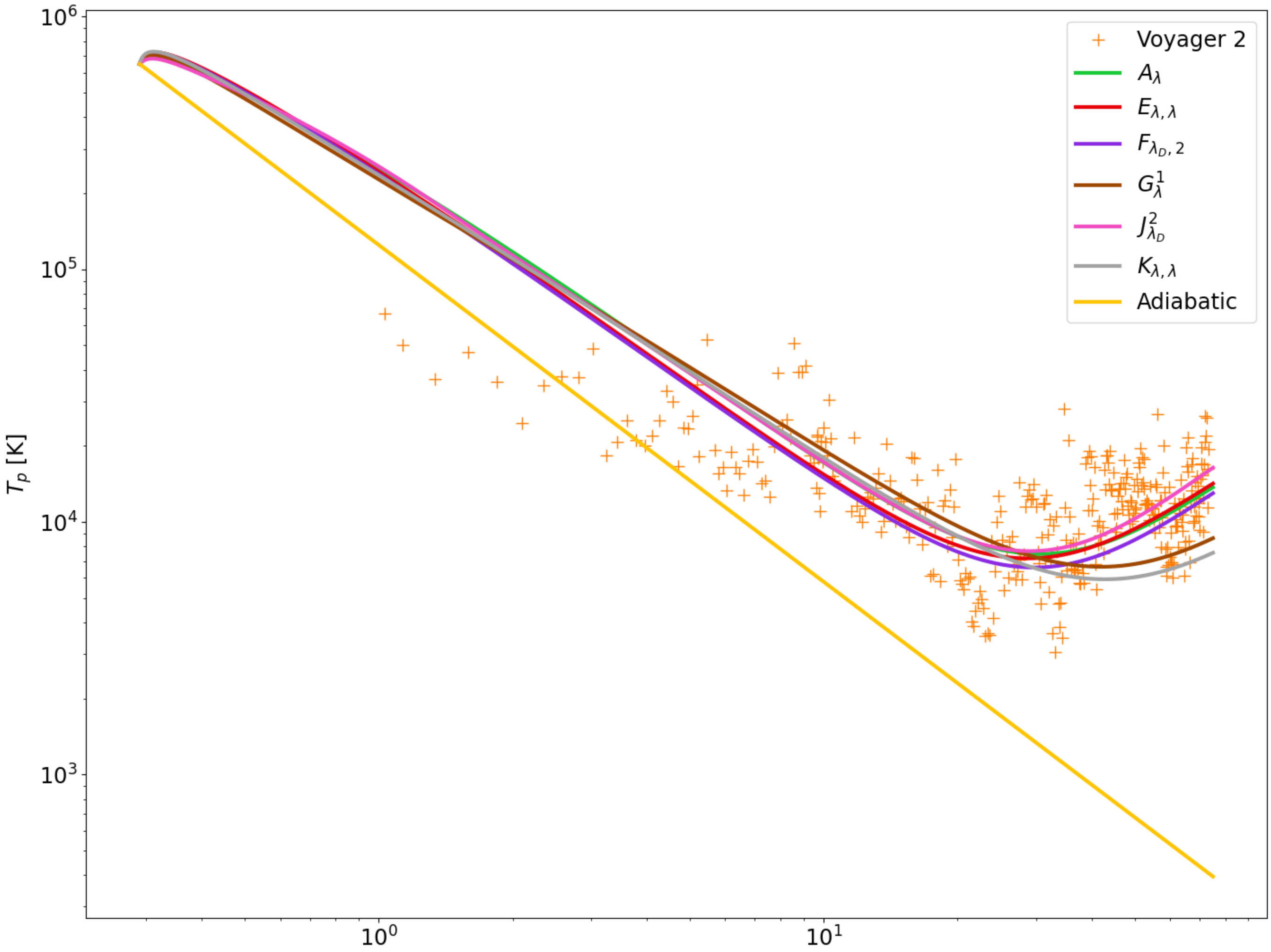

Figure 6.13: Plot of the some models in Tables 6.1, 6.3 and 6.5 with parameters Tables 6.2, 6.4 and 6.6 showing the temperature over radial distance to 75 AU using the zero inertial scale source driving assumption.

Parameters	Values
α	0.440
α_D	0.250
C_{sh}	0.725

Table 6.7: Minimized parameters to fit the observational data for the Adhikari et al. [1] transport model

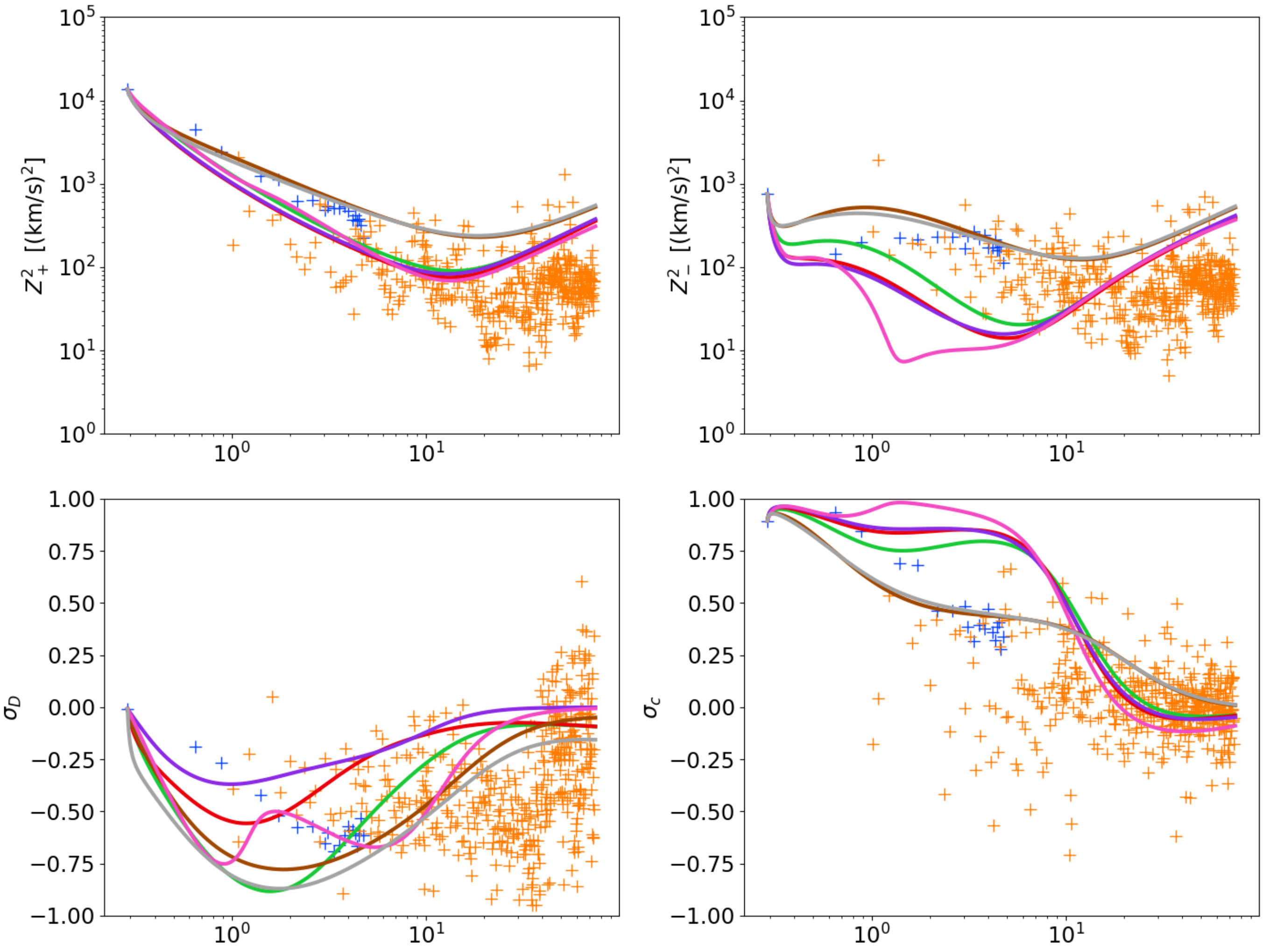

Figure 6.14: Plot of the some models in Tables 6.1, 6.3 and 6.5 with parameters Tables 6.2, 6.4 and 6.6 showing the energies over radial distance to 75 AU using the zero inertial scale source driving assumption.

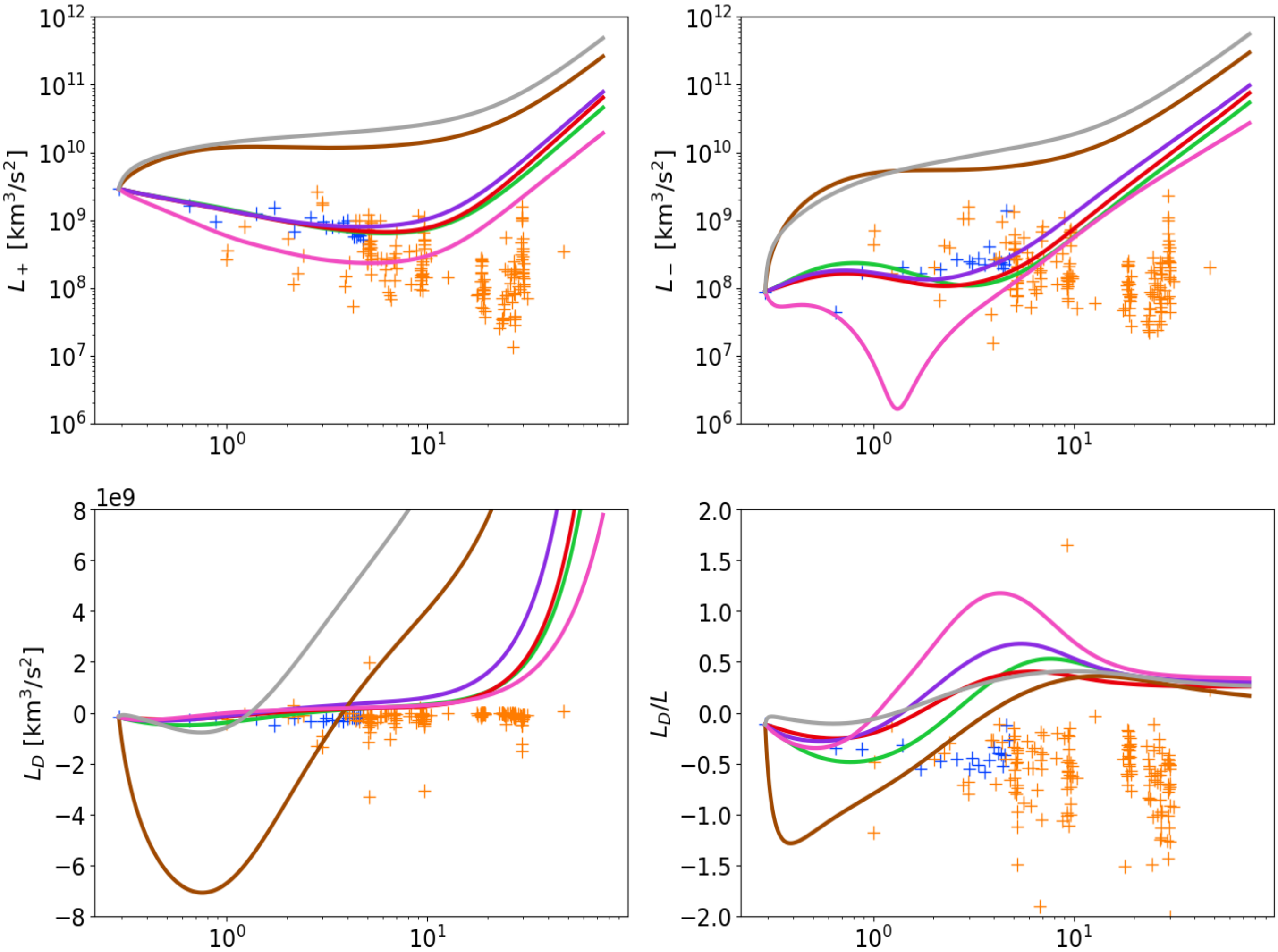

Figure 6.15: Plot of the some models in Tables 6.1, 6.3 and 6.5 with parameters Tables 6.2, 6.4 and 6.6 showing the correlation integrals over radial distance to 75 AU using the zero inertial scale source driving assumption.

correlation lengths in Figure E.2 (in purple) shows minimal difference between the parameters originally proposed by [1]. The only noticeable difference lies in the correlation lengths $\lambda_\pm$; after 10 AU they start to decrease in size rather than continue with an upward trend and the normalized energy difference does not become positive, meaning there is no spike in λ_D, which is a physically appealing situation.

6.7 Discussion

In this chapter, we have provided numerical solutions to numerous models introduced in chapter 3. In some cases, we could not find physical solutions for these models; this does not mean that we can discard those models entirely and that their assumption are bad. The parameter optimizing technique has limitations due to the stability of finding numerical solutions, particularly when optimizing for the highly coupled, nonlinear terms. Some nonlinear models might still be able to fit the observational behaviour but require more precise parameter choices that the parameter optimizer fails to grasp.

By increasing the complexity of the models by adding more nonlinear terms, we still could *not* capture good behaviour from L_D and, in most cases, σ_D. Most models could follow the general trend of the Elsässer energies and their correlation lengths but there is a large amount of variability available between the models and between the same models with different parameter choices. In general, $\lambda_\pm$ Model B behaves behaves better than $\lambda_\pm$ Model A. Also, L_D Model A is the only model we could find that could keep L_D negative, but doing so adds more complexity to the system via the four additional parameters. We also find that assuming a net zero effect to the correlation lengths by the turbulence driving does *not* produce reasonable results.

Comparing our results to the Adhikari et al. [1] model (section E.1) and the Breech et al. [13] model (section E.2), each model has downsides. The Adhikari et al. [1] models matches closely with the observational Elsässer energies, but

σ_D approaches 0 in the outer heliosphere. The correlation lengths grow slightly larger than the observational data after 10 AU and λ_D is showing as continuously increasing after 10 AU which does not match the observational data. Lastly, L_D decreases and becomes constant after 1 AU whereas observational and simulation data predicts L_D to hang around 0. The lack of the gradient mixing terms in the Adhikari et al. [1] model is difficult to justify. As some of our models have shown, the mixing terms provide a lot of complexity to the overall outcome of the model. As for the simplified, three equation Breech et al. [13] model, $Z_\pm^2$ doesn't display behaviour much worse than some of our models and the single correlation length used matches the data very nicely. Both Adhikari et al. [1] and Breech et al. [13] models are showing to match the temperature data much like our own. The sudden spike in temperature at the start of the solutions can be ameliorated by increasing the initial temperature value.

Chapter 7

Conclusions

In this thesis, we have introduced the MHD approximation for the solar wind and considered the modelling of the transport of fluctuations in the solar wind velocity and magnetic fields. We have discussed the turbulence characteristics of MHD fluids and why it becomes so complicated. Our modelling reflects this complexity, as there are a large number of potential candidates to describe the nonlinear evolution of the correlation and cross correlation quantities. We have also provided simulation and observational data to justify and validate our models. Next, we have examined analytical solutions that work more as validations for specific numerical solution cases than as physical solutions describing the solar wind. Lastly, we examined an array of models using various combinations of the nonlinear terms and found adequate agreement with some of the models (although requiring specific parameter choices), with concessions made with regards to L_D and λ_D. The exact recommendations of the nonlinear models will depend on the desired simplicity of the system.

7.1 Future Research Directions

Compared to Breech et al. [13], our model is more complicated but, we still assume time-independence and strictly radial dependence. Like Breech et al. [13], we could extend our model to include varying solar latitudes. We have also only included the shear/shock and pickup ion sources, there are many more turbulent source driving terms to include [25]. Lastly, to improve our models we could include scales for perpendicular and parallel turbulence evolution, although this would drastically complicate things even more.

It would be prudent, in future work to obtain better data. The Voyager 2 data has been difficult to work with; the extreme variability has made it difficult to judge behaviour, particularly with the correlation lengths and σ_D. The relatively slow moving spacecraft means that as the radial distance increases, time has passed; we ignore this fact with our steady-state assumption. Over the course of the Voyager 2 mission, several solar cycles have occurred which directly influences the speed of the solar wind [57]. Voyager 2 also has had flybys with Jupiter, Saturn, Uranus and Neptune lasting up to a month each; the Adhikari et al. data removes the flyby periods because the planetary magnetospheres influence the solar wind. After Neptune (approximately 30 AU), Voyager 2 entered a declining trajectory from the ecliptic plane. Ulysses' solar orbit has been over and under the poles and shown that the solar wind speed increases away from the Sun's equator [38]. In future, including new measurements from the Parker Solar Probe [56] could help improve the models and allow us to decrease the initial radial distance.

In order to make a stronger conclusion for model validity, we will need to analyse more observational data along with more simulation results.

References

[1] L. Adhikari, G. P. Zank, R. Bruno, D. Telloni, P. Hunana, A. Dosch, R. Marino, and Q. Hu. The transport of low-frequency turbulence in astrophysical flows. ii. solutions for the super-alfvénic solar wind. *The Astrophysical Journal*, 805(1):63, 2015.

[2] L. Adhikari, G. P. Zank, and L.-L. Zhao. A solar coronal hole and fast solar wind turbulence model and first-orbit Parker Solar Probe (PSP) observations. *Astrophys. J.*, 901(2):102, 2020. doi: 10.3847/1538-4357/abb132.

[3] L. Adhikari, G. Zank, L. Zhao, D. Telloni, T. Horbury, H. O'Brien, V. Evans, V. Angelini, C. Owen, P. Louarn, et al. Evolution of anisotropic turbulence in the fast and slow solar wind: Theory and solar orbiter measurements. *Astronomy and Astrophysics*, 2021.

[4] L. Adhikari, G. P. Zank, and L. Zhao. The transport and evolution of mhd turbulence throughout the heliosphere: Models and observations. *Fluids*, 6(10):368, 2021.

[5] R. Bandyopadhyay, W. H. Matthaeus, S. Oughton, and M. Wan. Evolution of similarity lengths in anisotropic magnetohydrodynamic turbulence. *J. Fluid Mech.*, 876:5–18, 2019. doi: 10.1017/jfm.2019.513.

[6] R. Bandyopadhyay, M. L. Goldstein, B. A. Maruca, W. H. Matthaeus, T. N. Parashar, D. Ruffolo, R. Chhiber, A. Usmanov, A. Chasapis, R. Qudsi, S. D. Bale, J. W. Bonnell, T. D. d. Wit, K. Goetz, P. R.

Harvey, R. J. MacDowall, D. M. Malaspina, M. Pulupa, J. C. Kasper, K. E. Korreck, A. W. Case, M. Stevens, P. Whittlesey, D. Larson, R. Livi, K. G. Klein, M. Velli, and N. Raouafi. Enhanced energy transfer rate in solar wind turbulence observed near the sun from Parker Solar Probe. *Astrophys. J. Suppl. Ser*, 246:48, 2020. doi: 10.3847/1538-4365/ab5dae.

[7] G. K. Batchelor. The theory of axisymmetric turbulence. *Proc. Roy. Soc. Lond. A*, 186:480, 1946.

[8] G. K. Batchelor. *The Theory of Homogeneous Turbulence*. Cambridge University Press, Cambridge, UK, 1970.

[9] J. W. Belcher and L. Davis Jr. Large-amplitude Alfvénwaves in the interplanetary medium, 2. *J. Geophys. Res.*, 76:3534–3563, 1971. doi: 10.1029/JA076i016p03534.

[10] J. W. Bieber, W. Wanner, and W. H. Matthaeus. Dominant two-dimensional solar wind turbulence with implications for cosmic ray transport. *J. Geophys. Res.*, 101:2511–2522, 1996. doi: 10.1029/95JA02588.

[11] J. Brandt and J. Hardorp. Ionic comet tails and the direction of the solar wind. *Astronomy and Astrophysics*, 5:322, 1970.

[12] B. Breech, W. H. Matthaeus, J. Minnie, S. Oughton, S. Parhi, J. W. Bieber, and B. Bavassano. Radial evolution of cross helicity in high-latitude solar wind. *Geophys. Res. Lett.*, 32:L06103, 2005. doi: 10.1029/2004GL022321.

[13] B. Breech, W. H. Matthaeus, J. Minnie, J. Bieber, S. Oughton, C. W. Smith, and P. Isenberg. Turbulence transport throughout the heliosphere. *Journal of Geophysical Research: Space Physics*, 113(A8), 2008.

[14] P. J. Coleman. Turbulence, viscosity, and dissipation in the solar wind plasma. *Astrophys. J.*, 153:371–388, 1968. doi: 10.1086/149674.

[15] S. Dasso, L. J. Milano, W. H. Matthaeus, and C. W. Smith. Anisotropy in fast and slow solar wind fluctuations. *Astrophys. J.*, 635:L181–L184, 2005. doi: 10.1086/499559.

[16] T. de Kármán and L. Howarth. On the statistical theory of isotropic turbulence. *Proc. Roy. Soc. London Ser. A*, 164:192–215, 1938. doi: 10.1098/rspa.1938.0013.

[17] C. DeForest, W. Matthaeus, T. Howard, and D. Rice. Turbulence in the solar wind measured with comet tail test particles. *The Astrophysical Journal*, 812(2):108, 2015.

[18] J. R. Dormand and P. J. Prince. A family of embedded runge-kutta formulae. *Journal of computational and applied mathematics*, 6(1):19–26, 1980.

[19] A. Dosch, L. Adhikari, and G. Zank. The transport of low-frequency turbulence in astrophysical flows: Correlation lengths. In *AIP Conference Proceedings*, volume 1539, pages 155–158. American Institute of Physics, 2013.

[20] H. L. Dryden. A review of the statistical theory of turbulence. *Quart. Appl. Math.*, 1:7, 1943.

[21] W. M. Elsasser. The hydromagnetic equations. *Phys. Rev.*, 79:183, 1950.

[22] U. Frisch. *Turbulence.* Cambridge University Press, Cambridge, UK, 1995.

[23] J. T. Gosling. Magnetic reconnection in the solar wind. *Space Sci. Rev.*, page 13, 2011. doi: 10.1007/s11214-011-9747-2.

[24] J. T. Gosling, R. M. Skoug, D. J. McComas, and C. W. Smith. Direct evidence for magnetic reconnection in the solar wind near 1 AU. *J. Geophys. Res.*, 110:A01107, 2005. doi: 10.1029/2004JA010809.

[25] J. V. Hollweg. Waves and instabilities in the solar wind. *Rev. Geophys. Space Phys.*, 13:263–289, 1975.

[26] M. Hossain, P. C. Gray, D. H. Pontius Jr, W. H. Matthaeus, and S. Oughton. Phenomenology for the decay of energy-containing eddies in homogeneous mhd turbulence. *Physics of Fluids*, 7(11):2886–2904, 1995.

[27] A. Hundhausen and J. Gosling. Solar wind structure at large heliocentric distances: An interpretation of pioneer 10 observations. *Journal of Geophysical Research*, 81(7):1436–1440, 1976.

[28] P. A. Isenberg, C. W. Smith, and W. H. Matthaeus. Turbulent heating of the distant solar wind by interstellar pickup protons. *Astrophys. J.*, 592: 564–573, 2003. doi: 10.1086/375584.

[29] P. A. Isenberg, C. W. Smith, and W. H. Matthaeus. Turbulent heating of the distant solar wind by interstellar pickup protons. *The Astrophysical Journal*, 592(1):564, 2003.

[30] M. G. Kivelson, M. G. Kivelson, and C. T. Russell. *Introduction to space physics*. Cambridge university press, 1995.

[31] A. N. Kolmogorov. Local structure of turbulence in an incompressible viscous fluid at very high Reynolds numbers. *Dokl. Akad. Nauk SSSR*, 30:301–305, 1941. doi: 10.1098/rspa.1991.0075. [Reprinted in Proc. R. Soc. London, Ser. A **434**, 9–13 (1991)].

[32] A. N. Kolmogorov. On degeneration of isotropic turbulence in an incompressible viscous liquid. *C.R. Acad. Sci. U.R.S.S.*, 31:538–540, 1941.

[33] A. N. Kolmogorov. Dissipation of energy in the locally isotropic turbulence. *C.R. Acad. Sci. U.R.S.S.*, 32:16, 1941. doi: 10.1098/rspa.1991.0076. [Reprinted in Proc. R. Soc. London, Ser. A **434**, 15–17 (1991)].

[34] W. H. Matthaeus, M. L. Goldstein, and D. A. Roberts. Evidence for the presence of quasi-two-dimensional nearly incompressible fluctuations in

the solar wind. *J. Geophys. Res.*, 95:20 673–20 683, 1990. doi: 10.1029/JA095iA12p20673.

[35] W. H. Matthaeus, S. Oughton, D. H. Pontius Jr, and Y. Zhou. Evolution of energy-containing turbulent eddies in the solar wind. *Journal of Geophysical Research: Space Physics*, 99(A10):19267–19287, 1994.

[36] W. H. Matthaeus, G. P. Zank, and S. Oughton. Phenomenology of hydromagnetic turbulence in a uniformly expanding medium. *Journal of plasma physics*, 1996.

[37] W. H. Matthaeus, J. Minnie, B. Breech, S. Parhi, J. W. Bieber, and S. Oughton. Transport of cross helicity and the radial evolution of Alfvénicity in the solar wind. *Geophys. Res. Lett.*, 31:L12803, 2004. doi: 10.1029/2004GL019645.

[38] D. McComas, S. Bame, B. Barraclough, W. Feldman, H. Funsten, J. Gosling, P. Riley, R. Skoug, A. Balogh, R. Forsyth, et al. Ulysses' return to the slow solar wind. *Geophysical Research Letters*, 25(1):1–4, 1998.

[39] NASA. The heliosphere, 2017. URL `https://www.nasa.gov/mission_pages/sunearth/science/Heliosphere.html`.

[40] M. Newville, T. Stensitzki, D. B. Allen, and A. Ingargiola. LMFIT: Non-Linear Least-Square Minimization and Curve-Fitting for Python, Sept. 2014. URL `https://doi.org/10.5281/zenodo.11813`.

[41] K. T. Osman and T. S. Horbury. Multispacecraft measurement of anisotropic correlation functions in solar wind turbulence. *Astrophys. J.*, 654:L103–L106, 2007.

[42] K. T. Osman and T. S. Horbury. Quantitative estimates of the slab and 2-d power in solar wind turbulence using multispacecraft data. *J. Geophys. Res.*, 114:A06103, 2009. doi: 10.1029/2008JA014036.

[43] S. Oughton, W. H. Matthaeus, C. W. Smith, B. Breech, and P. A. Isenberg. Transport of solar wind fluctuations: A two-component model. *J. Geophys. Res.*, 116:A08105, 2011. doi: 10.1029/2010JA016365.

[44] A. E. Parker. Who solved the bernoulli differential equation and how did they do it? *The College Mathematics Journal*, 44(2):89–97, 2013.

[45] E. N. Parker. Dynamics of the interplanetary gas and magnetic fields. *The Astrophysical Journal*, 128:664, 1958.

[46] S. Perri and A. Balogh. Differences in solar wind cross-helicity and residual energy during the last two solar minima. *Geophys. Res. Lett.*, 37:L17102, 2010. doi: 10.1029/2010GL044570.

[47] M. Rees and G. Reid. The aurora, the radiation belt and the solar wind: a unifying hypothesis. *Nature*, 184(4685):539–540, 1959.

[48] D. A. Roberts, L. W. Klein, M. L. Goldstein, and W. H. Matthaeus. The nature and evolution of magnetohydrodynamic fluctuations in the solar wind: Voyager observations. *J. Geophys. Res.*, 92:11 021–11 040, 1987. doi: 10.1029/JA092iA10p11021.

[49] D. A. Roberts, M. L. Goldstein, L. W. Klein, and W. H. Matthaeus. Origin and evolution of fluctuations in the solar wind: Helios observations and Helios-Voyager comparisons. *J. Geophys. Res.*, 92:12 023–12 035, 1987. doi: 10.1029/JA092iA11p12023.

[50] L. F. Shampine. Some practical runge-kutta formulas. *Mathematics of computation*, 46(173):135–150, 1986.

[51] C. W. Smith, W. H. Matthaeus, G. P. Zank, N. F. Ness, S. Oughton, and J. D. Richardson. Heating of the low-latitude solar wind by dissipation of turbulent magnetic fluctuations. *J. Geophys. Res.*, 106:8253–8272, 2001.

[52] C. W. Smith, P. A. Isenberg, W. H. Matthaeus, and J. D. Richardson.

Turbulent heating of the solar wind by newborn interstellar pickup protons. *Astrophys. J.*, 638:508–517, 2006.

[53] C. W. Smith, P. A. Isenberg, W. H. Matthaeus, and J. D. Richardson. Turbulent heating of the solar wind by newborn interstellar pickup protons. *The Astrophysical Journal*, 638(1):508, 2006.

[54] G. I. Taylor. Statistical theory of turbulence. Parts 1–4. *Proc. Roy. Soc. Lond. A*, 151:421–444, 1935. doi: 10.1098/rspa.1935.0158.

[55] G. I. Taylor. The spectrum of turbulence. *Proc. Roy. Soc. Lond. A*, 164: 476–490, 1938. doi: 10.1098/rspa.1938.0032.

[56] D. Telloni, L. Sorriso-Valvo, L. D. Woodham, O. Panasenco, M. Velli, F. Carbone, G. P. Zank, R. Bruno, D. Perrone, M. Nakanotani, C. Shi, R. D'Amicis, R. De Marco, V. K. Jagarlamudi, K. Steinvall, R. Marino, L. Adhikari, L. Zhao, H. Liang, A. Tenerani, R. Laker, T. S. Horbury, S. D. Bale, M. Pulupa, D. M. Malaspina, R. J. MacDowall, K. Goetz, T. Dudok de Wit, P. R. Harvey, J. C. Kasper, K. E. Korreck, D. Larson, A. W. Case, M. L. Stevens, P. Whittlesey, R. Livi, C. J. Owen, S. Livi, P. Louarn, E. Antonucci, M. Romoli, H. O'Brien, V. Evans, and V. Angelini. Evolution of solar wind turbulence from 0.1 to 1 au during the first Parker Solar Probe–Solar Orbiter radial alignment. *Astrophys. J. Lett.*, 912(2):L21, 2021. doi: 10.3847/2041-8213/abf7d1.

[57] M. Tokumaru, M. Kojima, and K. Fujiki. Solar cycle evolution of the solar wind speed distribution from 1985 to 2008. *Journal of Geophysical Research: Space Physics*, 115(A4), 2010.

[58] P. Virtanen, R. Gommers, T. E. Oliphant, M. Haberland, T. Reddy, D. Cournapeau, E. Burovski, P. Peterson, W. Weckesser, J. Bright, S. J. van der Walt, M. Brett, J. Wilson, K. J. Millman, N. Mayorov, A. R. J. Nelson, E. Jones, R. Kern, E. Larson, C. J. Carey, İ. Polat, Y. Feng, E. W.

Moore, J. VanderPlas, D. Laxalde, J. Perktold, R. Cimrman, I. Henriksen, E. A. Quintero, C. R. Harris, A. M. Archibald, A. H. Ribeiro, F. Pedregosa, P. van Mulbregt, and SciPy 1.0 Contributors. SciPy 1.0: Fundamental Algorithms for Scientific Computing in Python. *Nature Methods*, 17:261–272, 2020. doi: 10.1038/s41592-019-0686-2.

[59] Y. C. Whang. Shock interactions in the outer heliosphere. *Space Sci. Rev.*, 57:339–388, 1991.

[60] Wikipedia. The energy cascade, 2017. URL `https://commons.wikimedia.org/wiki/File:Schematic-illustration-of-the-energy-spectrum-of-turbulent-velocity-cascade.png`.

[61] Y. Xiang, S. Gubian, B. Suomela, and J. Hoeng. Generalized simulated annealing for global optimization: the gensa package. *R J.*, 5(1):13, 2013.

[62] G. P. Zank. *Transport Processes in Space Physics and Astrophysics*, volume 877 of *Lecture Notes in Physics*. Springer, New York, 2014. doi: 10.1007/978-1-4614-8480-6.

[63] G. P. Zank, W. H. Matthaeus, and C. W. Smith. Evolution of turbulent magnetic fluctuation power with heliocentric distance. *J. Geophys. Res.*, 101:17 093–17 107, 1996. doi: 10.1029/96JA01275.

[64] G. P. Zank, A. Dosch, P. Hunana, V. Florinski, W. H. Matthaeus, and G. M. Webb. The transport of low-frequency turbulence in astrophysical flows. I. Governing equations. *Astrophys. J.*, 745:35, 2012. doi: 10.1088/0004-637X/745/1/35.

[65] L.-L. Zhao, G. Zank, L. Adhikari, M. Nakanotani, D. Telloni, and F. Carbone. Spectral features in field-aligned solar wind turbulence from parker solar probe observations. *The Astrophysical Journal*, 898(2):113, 2020.

[66] Y. Zhou and W. H. Matthaeus. Transport and turbulence modeling of solar wind fluctuations. *J. Geophys. Res.*, 95:10 291, 1990.

Appendix A

The Fluctuating Evolution Equations

The dynamics of the solar wind can be approximated mathematically using a compressible, one-fluid, MHD approximation. The MHD equations are the following, stating with the equation representing the conservation of mass,

$$\frac{\partial \rho}{\partial \mathrm{t}} + \nabla \cdot (\boldsymbol{V} \rho) = 0 \tag{A.1}$$

and an equation of motion,

$$\rho \left(\frac{\partial \boldsymbol{V}}{\partial \mathrm{t}} + \boldsymbol{V} \cdot \nabla \boldsymbol{V} \right) = -\nabla p + \frac{1}{c} \boldsymbol{J} \times \boldsymbol{B} + \boldsymbol{D} \tag{A.2}$$

where ρ is the mass density of the fluid, $\boldsymbol{V}$ is the fluid velocity, p is the fluid pressure, $\boldsymbol{J}$ is the electric current density, $\boldsymbol{B}$ is the magnetic field and $\boldsymbol{D}$ is a viscous dissipation term, usually including $\nu \nabla^2 \boldsymbol{V}$ where ν is the kinematic viscosity. All fields represented in the equations are functions of the three dimensional space $(\boldsymbol{x})$ and time (t). Maxwell's equations describing the electromagnetic fields in a vacuum are assumed and written as the following (in

Gaussian units),

$$\nabla \cdot \boldsymbol{E} = 4\pi\rho_e \tag{A.3}$$

$$\nabla \cdot \boldsymbol{B} = 0 \tag{A.4}$$

$$\nabla \times \boldsymbol{E} = -\frac{1}{c}\frac{\partial \boldsymbol{B}}{\partial \mathrm{t}} \tag{A.5}$$

$$\nabla \times \boldsymbol{B} = \frac{1}{c}\left(4\pi \boldsymbol{J} + \frac{\partial \boldsymbol{E}}{\partial \mathrm{t}}\right) \tag{A.6}$$

where $\boldsymbol{E}$ is the electric field strength, ρ_e is the electric charge density and c is the speed of light. Assuming Ohm's Law, where the conductor is moving at the fluid velocity $\boldsymbol{V}$, the electric current density is

$$\boldsymbol{J} = \sigma\left(\boldsymbol{E} + \frac{1}{c}\boldsymbol{V} \times \boldsymbol{B}\right) \tag{A.7}$$

where σ is the conductivity. The electric field $\boldsymbol{E}$ can be solved for from Equation A.7, hence removed from the Equations (A.3) to (A.6) and (A.7). The result is an induction equation (from Equation A.5) for the MHD approximation,

$$\frac{\partial \boldsymbol{B}}{\partial \mathrm{t}} = \nabla\times(\boldsymbol{V} \times \boldsymbol{B}) + \boldsymbol{D'} \tag{A.8}$$

where $\boldsymbol{D'}$ is the Ohmic dissipation term proportional to $\frac{1}{\sigma}\nabla^2\boldsymbol{B}$. The cross product terms in Equation A.2 and Equation A.8 can be simplified as follows

$$\nabla \times (\boldsymbol{V} \times \boldsymbol{B}) = \boldsymbol{B} \cdot \nabla\boldsymbol{V} + \boldsymbol{V}(\nabla \cdot \boldsymbol{B}) - \boldsymbol{V} \cdot \nabla\boldsymbol{B} - \boldsymbol{B}(\nabla \cdot \boldsymbol{V}) \tag{A.9}$$

$$= \boldsymbol{B} \cdot \nabla\boldsymbol{V} - \boldsymbol{V} \cdot \nabla\boldsymbol{B} - \boldsymbol{B}(\nabla \cdot \boldsymbol{V}) \tag{A.10}$$

$$\frac{1}{c}\boldsymbol{J} \times \boldsymbol{B} = \frac{1}{c}\frac{c}{4\pi}(\nabla \times \boldsymbol{B}) \times \boldsymbol{B} = \frac{1}{4\pi}(\boldsymbol{B} \cdot \nabla\boldsymbol{B} - \nabla(\frac{B^2}{2})) \tag{A.11}$$

The second term $\frac{1}{8\pi}\nabla B^2$ in Equation A.11 can be interpreted as a pressure gradient force. Now, with the total pressure term $p^T = p + \frac{B^2}{8\pi}$, Equation A.2 and Equation A.8 can be rewritten

$$\frac{\partial \boldsymbol{V}}{\partial \mathrm{t}} + \boldsymbol{V} \cdot \nabla\boldsymbol{V} - \frac{1}{4\pi\rho}\boldsymbol{B} \cdot \nabla\boldsymbol{B} = -\frac{1}{\rho}\nabla p^T \tag{A.12}$$

$$\frac{\partial \boldsymbol{B}}{\partial \mathrm{t}} + \boldsymbol{V} \cdot \nabla\boldsymbol{B} - \boldsymbol{B} \cdot \nabla\boldsymbol{V} = -\boldsymbol{B}\nabla \cdot \boldsymbol{V} \tag{A.13}$$

Equations (A.12) and (A.13) and the conservation of mass (Equation A.1) form the basis of the MHD approximation of the solar wind.

Following a derivation from Zhou and Matthaeus [66], we will apply a two scale decomposition for the vector fields to obtain evolution equations for the large-scale, slowly varying components and the fluctuating turbulence. We will separate the fluid velocity field $\boldsymbol{V} = \boldsymbol{U} + \boldsymbol{u}$ into the mean flow $\boldsymbol{U}$ and a fluctuating component $\boldsymbol{u}$ with $\langle \boldsymbol{V} \rangle = \boldsymbol{U}$ and $\langle \boldsymbol{u} \rangle = 0$. Likewise, we will separate the magnetic field $\boldsymbol{B} = \boldsymbol{B}_0 + \boldsymbol{b}$ into its mean flow $\boldsymbol{B}_0$ and a fluctuating component $\boldsymbol{b}$ with $\langle \boldsymbol{B} \rangle = \boldsymbol{B}_0$. Likewise, the density and pressures will be separated into mean and fluctuating components $\rho = \rho_0 + \delta\rho$, $p^T = p_0^T + \delta p^T$. The mean components can be described as the large-scale fields with the fluctuating part representing the small-scale field. Averaging Equation A.12 and Equation A.13,

$$\frac{\partial \boldsymbol{U}}{\partial \mathrm{t}} + (\boldsymbol{U} \cdot \nabla \boldsymbol{U} + \langle \boldsymbol{u} \cdot \nabla \boldsymbol{u} \rangle) - \frac{1}{4\pi\rho} (\boldsymbol{B}_0 \cdot \nabla \boldsymbol{B}_0 + \langle \boldsymbol{b} \cdot \nabla \boldsymbol{b} \rangle) = -\nabla p_0^T \quad \text{(A.14)}$$

$$\frac{\partial \boldsymbol{B}_0}{\partial \mathrm{t}} + \boldsymbol{U} \cdot \nabla \boldsymbol{B}_0 + \langle \boldsymbol{u} \cdot \nabla \boldsymbol{b} \rangle - (\boldsymbol{B}_0 \cdot \nabla \boldsymbol{U} + \langle \boldsymbol{b} \cdot \nabla \boldsymbol{u} \rangle) \quad \text{(A.15)}$$

$$= -(\boldsymbol{B}_0 \nabla \cdot \boldsymbol{U} + \langle \boldsymbol{b} \nabla \cdot \boldsymbol{u} \rangle) \quad \text{(A.16)}$$

Averaging the conservation of mass

$$\nabla \cdot (\boldsymbol{U}\rho) = 0 \quad \text{(A.17)}$$

Subtracting the averaged equations Equation A.14 and Equation A.16 from Equation A.12 and Equation A.13, we get the transport equations for the fluctuating velocity and magnetic fields.

$$\frac{\partial \boldsymbol{u}}{\partial \mathrm{t}} + \boldsymbol{U} \cdot \nabla \boldsymbol{u} + \boldsymbol{u} \cdot \nabla \boldsymbol{U} - \frac{1}{4\pi\rho} (\boldsymbol{B}_0 \cdot \nabla \boldsymbol{b} + \boldsymbol{b} \cdot \nabla \boldsymbol{B}_0) = -\frac{1}{\rho} \nabla \delta p^T + \boldsymbol{N}^\nu \quad \text{(A.18)}$$

$$\frac{\partial \boldsymbol{b}}{\partial \mathrm{t}} + \boldsymbol{U} \cdot \nabla \boldsymbol{b} + \boldsymbol{u} \cdot \nabla \boldsymbol{B}_0 - \boldsymbol{B}_0 \cdot \nabla \boldsymbol{u} - \boldsymbol{b} \cdot \nabla \boldsymbol{U} = -\boldsymbol{b} \nabla \cdot \boldsymbol{U} - \boldsymbol{B}_0 \nabla \cdot \boldsymbol{u} + \boldsymbol{N}^b \quad \text{(A.19)}$$

Likewise, we get the following for the conservation of mass

$$\nabla \cdot (\boldsymbol{u}\rho) = 0 \quad \text{(A.20)}$$

We could begin manipulating Equation A.18 and Equation A.19, but it is favourable to use the Elsässer representation [21]

$$\boldsymbol{z}_{\pm} = \boldsymbol{u} \pm \frac{\boldsymbol{b}}{\sqrt{4\pi\rho}} = \boldsymbol{u} \pm \boldsymbol{v}_A \tag{A.21}$$

where $\boldsymbol{v}_A$ is the fluctuating magnetic field called an Alfvén speed in Gaussian speed units, therefore $\boldsymbol{z}_{\pm}$ is also in speed units. We will also define the large-scale magnetic field as an Alfvén speed $\boldsymbol{V}_A = \boldsymbol{B}_0/\sqrt{4\pi\rho}$. In order to form the Elsässer fluctuation equations, we will use the conservation of mass to remove the gradient of the density

$$\nabla \cdot (\rho \boldsymbol{U}) = 0 \tag{A.22}$$

$$\implies \rho \nabla \cdot \boldsymbol{U} + \boldsymbol{U} \cdot \nabla \rho = 0 \tag{A.23}$$

$$\implies \boldsymbol{U} \cdot \nabla \rho = -\rho \nabla \cdot \boldsymbol{U} \tag{A.24}$$

$$\implies \frac{\boldsymbol{U}}{\rho} \cdot \nabla \rho = -\nabla \cdot \boldsymbol{U} \tag{A.25}$$

we can also remove the density gradient by replacing it with divergences of the large-scale flows as follows

$$\boldsymbol{B}_0 \cdot \nabla \frac{1}{\sqrt{4\pi\rho}} = \nabla \cdot \boldsymbol{V}_A + \frac{1}{\sqrt{4\pi\rho}} \nabla \cdot \boldsymbol{B}_0 = \nabla \cdot \boldsymbol{V}_A \tag{A.26}$$

$$\boldsymbol{U} \cdot \nabla \frac{1}{\sqrt{4\pi\rho}} = -\boldsymbol{U} \cdot \left(\frac{1}{2\rho} \frac{1}{\sqrt{4\pi\rho}} \nabla \rho \right) = -\frac{1}{2} \frac{1}{\sqrt{4\pi\rho}} \frac{\boldsymbol{U}}{\rho} \cdot \nabla \rho = \frac{1}{2} \frac{1}{\sqrt{4\pi\rho}} \nabla \cdot \boldsymbol{U} \tag{A.27}$$

$$\frac{1}{(\sqrt{4\pi\rho})^2} \boldsymbol{B}_0 \cdot \nabla \boldsymbol{b} = \boldsymbol{V}_A \cdot \nabla \boldsymbol{v}_A + \frac{1}{\sqrt{4\pi\rho}} \boldsymbol{B}_0 \cdot \left(\boldsymbol{b} \nabla \frac{1}{\sqrt{4\pi\rho}} \right) = \boldsymbol{V}_A \cdot \nabla \boldsymbol{v}_A + \boldsymbol{v}_A \left(\nabla \cdot \boldsymbol{V}_A \right) \tag{A.28}$$

We can derive the transport equations for the fluctuating Elsässer variables by summing (for $\boldsymbol{z}_+$) or subtracting ($\boldsymbol{z}_-$) Equation A.19 from Equation A.18

$$\begin{aligned} &\frac{\partial \boldsymbol{u}}{\partial \mathrm{t}} \pm \frac{1}{\sqrt{4\pi\rho}} \frac{\partial \boldsymbol{b}}{\partial \mathrm{t}} + \boldsymbol{U} \cdot \nabla \boldsymbol{u} \pm \frac{1}{\sqrt{4\pi\rho}} \boldsymbol{U} \cdot \nabla \boldsymbol{b} + \boldsymbol{u} \cdot \nabla \boldsymbol{U} \mp \frac{1}{\sqrt{4\pi\rho}} \boldsymbol{b} \cdot \nabla \boldsymbol{U} \\ &\mp \frac{1}{\sqrt{4\pi\rho}} \boldsymbol{B_0} \cdot \nabla \boldsymbol{u} - \frac{1}{(\sqrt{4\pi\rho})^2} \boldsymbol{B_0} \cdot \nabla \boldsymbol{b} \pm \frac{1}{\sqrt{4\pi\rho}} \boldsymbol{u} \cdot \nabla \boldsymbol{B_0} - \frac{1}{(\sqrt{4\pi\rho})^2} \boldsymbol{b} \cdot \nabla \boldsymbol{B_0} \\ &= -\frac{1}{\rho} \nabla p^T + \boldsymbol{N} \mp \frac{1}{\sqrt{4\pi\rho}} \left(\nabla \cdot \boldsymbol{U} \right) \boldsymbol{b} \mp \frac{1}{\sqrt{4\pi\rho}} \left(\nabla \cdot \boldsymbol{u} \right) \boldsymbol{B}_0 \pm \frac{1}{\sqrt{4\pi\rho}} \boldsymbol{N}^{\Omega} \end{aligned} \tag{A.29}$$

$$\frac{\partial \boldsymbol{u}}{\partial \mathrm{t}} \pm \frac{\partial \boldsymbol{v}_A}{\partial \mathrm{t}} + \boldsymbol{U} \cdot \nabla \boldsymbol{u} \pm \left(\boldsymbol{U} \cdot \nabla \boldsymbol{v}_{\boldsymbol{A}} - \frac{1}{2} \boldsymbol{v}_A \left(\nabla \cdot \boldsymbol{U} \right) \right) + \boldsymbol{u} \cdot \nabla \boldsymbol{U} \mp \boldsymbol{v}_{\boldsymbol{A}} \cdot \nabla \boldsymbol{U} \mp \boldsymbol{V}_{\boldsymbol{A}} \cdot \nabla \boldsymbol{u}$$
$$- \left(\boldsymbol{V}_{\boldsymbol{A}} \cdot \nabla \boldsymbol{v}_{\boldsymbol{A}} + \boldsymbol{v}_A \nabla \cdot \boldsymbol{V}_A \right) \pm \frac{1}{\sqrt{4\pi\rho}} \boldsymbol{u} \cdot \nabla \boldsymbol{B}_{\boldsymbol{0}} - \frac{1}{\sqrt{4\pi\rho}} \boldsymbol{v}_A \cdot \nabla \boldsymbol{B}_0 \pm \left(\nabla \cdot \boldsymbol{U} \right) \boldsymbol{v}_A \pm \left(\nabla \cdot \boldsymbol{u} \right) \boldsymbol{V}_A$$
$$= -\frac{1}{\rho} \nabla p^T + \boldsymbol{N} \pm \frac{1}{\sqrt{4\pi\rho}} \boldsymbol{N}^{\Omega} \tag{A.30}$$

$$\frac{\partial (\boldsymbol{u} \pm \boldsymbol{v}_A)}{\partial \mathrm{t}} + \boldsymbol{U} \cdot \nabla (\boldsymbol{u} \pm \boldsymbol{v}_A) + (\boldsymbol{u} \mp \boldsymbol{v}_A) \cdot \nabla \boldsymbol{U} \mp \boldsymbol{V}_A \cdot \nabla \left(\boldsymbol{u} \pm \boldsymbol{v}_A \right) \pm \boldsymbol{v}_A \nabla \cdot \boldsymbol{V}_A$$
$$\pm \frac{1}{\sqrt{4\pi\rho}} \left(\boldsymbol{u} \mp \boldsymbol{v}_A \right) \cdot \nabla \boldsymbol{B}_0 \pm \left(\boldsymbol{v}_A - \frac{1}{2} \boldsymbol{v}_A \right) \left(\nabla \cdot \boldsymbol{U} \right) \pm \left(\nabla \cdot \boldsymbol{u} \right) \boldsymbol{V}_A$$
$$= -\frac{1}{\rho} \nabla p^T + \boldsymbol{N} \pm \frac{1}{\sqrt{4\pi\rho}} \boldsymbol{N}^{\Omega} \tag{A.31}$$

$$\frac{\partial \boldsymbol{z}^{\pm}}{\partial \mathrm{t}} + \boldsymbol{U} \cdot \nabla \boldsymbol{z}^{\pm} + \boldsymbol{z}^{\mp} \cdot \nabla \boldsymbol{U} \mp \boldsymbol{V}_A \cdot \nabla \boldsymbol{z}^{\pm}$$
$$\pm \frac{1}{\sqrt{4\pi\rho}} \boldsymbol{z}^{\mp} \cdot \nabla \boldsymbol{B}_0 \pm \frac{1}{2} \boldsymbol{v}_A (\nabla \cdot \boldsymbol{U}) + \boldsymbol{v}_A \nabla \cdot \boldsymbol{V}_A \pm (\nabla \cdot \boldsymbol{u}) \boldsymbol{V}_A$$
$$= -\frac{1}{\rho} \nabla p^T + \boldsymbol{N}_{\pm} \tag{A.32}$$

$$\frac{\partial \boldsymbol{z}^{\pm}}{\partial \mathrm{t}} + \boldsymbol{U} \cdot \nabla \boldsymbol{z}^{\pm} + \boldsymbol{z}^{\mp} \cdot \nabla \boldsymbol{U} \mp \boldsymbol{V}_A \cdot \nabla \boldsymbol{z}^{\pm} \pm \frac{1}{\sqrt{4\pi\rho}} \boldsymbol{z}^{\mp} \cdot \nabla \boldsymbol{B}_0$$
$$+ \frac{\boldsymbol{z}^{\pm} - \boldsymbol{z}^{\mp}}{2} \left(\nabla \cdot \frac{\boldsymbol{U}}{2} \right) \pm \frac{\boldsymbol{z}^{\pm} - \boldsymbol{z}^{\mp}}{2} \nabla \cdot \boldsymbol{V}_A \pm \left(\nabla \cdot \boldsymbol{u} \right) \boldsymbol{V}_A$$
$$= -\frac{1}{\rho} \nabla p^T + \boldsymbol{N}_{\pm} \tag{A.33}$$

$$\frac{\partial \boldsymbol{z}^{\pm}}{\partial \mathrm{t}} + \left(\boldsymbol{U} \mp \boldsymbol{V}_A \right) \cdot \nabla \boldsymbol{z}^{\pm} + \boldsymbol{z}^{\mp} \cdot \left(\nabla \boldsymbol{U} \pm \frac{1}{\sqrt{4\pi\rho}} \nabla \boldsymbol{B}_0 \right) + \frac{\boldsymbol{z}^{\pm} - \boldsymbol{z}^{\mp}}{2} \nabla \cdot \left(\frac{\boldsymbol{U}}{2} \pm \boldsymbol{V}_A \right)$$
$$\pm \left(\nabla \cdot \boldsymbol{u} \right) \boldsymbol{V}_A = -\frac{1}{\rho} \nabla p^T + \boldsymbol{N}_{\pm} \tag{A.34}$$

using $\nabla \cdot \boldsymbol{u} = 0$ (*i.e.,* incompressible fluctuations), we are finally left with the following equations which describe the evolution of the fluctuating MHD fields through the use of the Elsässer variables which represent Alfvén waves propagating anti-parallel (+) and parallel (−) to the magnetic fields along with more general fluctuations

$$\frac{\partial \boldsymbol{z}^{\pm}}{\partial \mathrm{t}} + \left(\boldsymbol{U} \mp \boldsymbol{V}_A \right) \cdot \nabla \boldsymbol{z}^{\pm} + \boldsymbol{z}^{\mp} \cdot \left(\nabla \boldsymbol{U} \pm \frac{1}{\sqrt{4\pi\rho}} \nabla \boldsymbol{B}_0 \right) + \frac{\boldsymbol{z}^{\pm} - \boldsymbol{z}^{\mp}}{2} \nabla \cdot \left(\frac{\boldsymbol{U}}{2} \pm \boldsymbol{V}_A \right)$$
$$= -\frac{1}{\rho} \nabla p^T + \boldsymbol{N}_{\pm} \tag{A.35}$$

Appendix B

Correlations

Continuing with the Zhou and Matthaeus [66] derivation started in Appendix A, we will be using the equation derived in Appendix A; Equation A.35 and constructing correlation functions that describe the statistical features of the fluctuating MHD turbulence in the solar wind.

The Elsässer field variables $\boldsymbol{z}^{\pm}$ takes space $\boldsymbol{x}$ and time t as parameters $\boldsymbol{z}^{\pm}(\boldsymbol{x}, t) = \boldsymbol{z}^{\pm}$. By varying the spatial coordinate by some distance $\boldsymbol{w}$, the Elsässer field can be taken with relative lag $\boldsymbol{z}^{\pm}(\boldsymbol{x} + \boldsymbol{w}, t) = \boldsymbol{z}^{\pm\prime}$ with which we can define a correlation tensor by ensemble averaging

$$\boldsymbol{H}_{ij}^{\pm} = \left\langle \boldsymbol{z}_i^{\pm} \boldsymbol{z}_j^{\pm\prime} \right\rangle \tag{B.1}$$

We can also define a cross correlation tensor of the Elsässer fields

$$\boldsymbol{\Lambda}_{ij}^{\pm} = \left\langle \boldsymbol{z}_i^{\pm} \boldsymbol{z}_j^{\mp\prime} \right\rangle \tag{B.2}$$

This chapter will derive the evolution equations of the correlation and cross correlation tensors which will form our model for the transport of the solar wind.

B.1 Evolution of the Correlations

With our fluctuating Elsässer variable MHD equation Equation A.35,

$$\begin{aligned}\frac{\partial \boldsymbol{z}^{\pm}}{\partial \mathrm{t}} + (\boldsymbol{U} \mp \boldsymbol{V}_{A}) \cdot \nabla \boldsymbol{z}^{\pm} + \boldsymbol{z}^{\mp} \cdot \left(\nabla \boldsymbol{U} \pm \frac{1}{\sqrt{4\pi\rho}} \nabla \boldsymbol{B}_{0}\right) + \frac{\boldsymbol{z}^{\pm} - \boldsymbol{z}^{\mp}}{2} \nabla \cdot \left(\frac{\boldsymbol{U}}{2} \pm \boldsymbol{V}_{A}\right) \\ = -\frac{1}{\rho} \nabla p^{T} + \boldsymbol{N}_{\pm}\end{aligned} \tag{B.3}$$

we will multiply the $\boldsymbol{z}_i^{\pm}$ component equation by the $\boldsymbol{z}_j^{\pm\prime}$ component, and take the $\boldsymbol{z}_j^{\pm\prime}$ component equation and multiply it by the $\boldsymbol{z}_i^{\pm}$ component to get the following two equations

$$\begin{aligned}\boldsymbol{z}_j^{\pm\prime} \frac{\partial \boldsymbol{z}_i^{\pm}}{\partial \mathrm{t}} + \boldsymbol{z}_j^{\pm\prime} \left(\boldsymbol{U}_k \mp \boldsymbol{V}_{A,k}\right) \nabla_k \boldsymbol{z}_i^{\pm} + \boldsymbol{z}_j^{\pm\prime} \boldsymbol{z}_k^{\mp} \left(\nabla_k \boldsymbol{U}_i \pm \frac{1}{\sqrt{4\pi\rho}} \nabla_k \boldsymbol{B}_{0,i}\right) \\ + \boldsymbol{z}_j^{\pm\prime} \frac{\boldsymbol{z}_i^{\pm} - \boldsymbol{z}_i^{\mp}}{2} \nabla_k \left(\frac{\boldsymbol{U}_k}{2} \pm \boldsymbol{V}_{A,k}\right) = -\boldsymbol{z}_j^{\pm\prime} \frac{1}{\rho} \nabla_i p^{T} + \boldsymbol{z}_j^{\pm\prime} \boldsymbol{N}_i^{\pm}\end{aligned} \tag{B.4}$$

$$\begin{aligned}\boldsymbol{z}_i^{\pm} \frac{\partial \boldsymbol{z}_j^{\pm\prime}}{\partial \mathrm{t}} + \boldsymbol{z}_i^{\pm} \left(\boldsymbol{U}_k \mp \boldsymbol{V}_{A,k}\right) \nabla_k \boldsymbol{z}_j^{\pm\prime} + \boldsymbol{z}_i^{\pm} \boldsymbol{z}_k^{\mp\prime} \left(\nabla_k \boldsymbol{U}_j \pm \frac{1}{\sqrt{4\pi\rho}} \nabla_k \boldsymbol{B}_{0,j}\right) \\ + \boldsymbol{z}_i^{\pm} \frac{\boldsymbol{z}_j^{\pm\prime} - \boldsymbol{z}_j^{\mp\prime}}{2} \nabla_k \left(\frac{\boldsymbol{U}_k}{2} \pm \boldsymbol{V}_{A,k}\right) = -\boldsymbol{z}_i^{\pm} \frac{1}{\rho} \nabla_j p^{T} + \boldsymbol{z}_i^{\pm} \boldsymbol{N}_j^{\pm}\end{aligned} \tag{B.5}$$

Sum Equation B.4 and Equation B.5 and use the product rule

$$\begin{aligned}\frac{\partial \left(\boldsymbol{z}_i^{\pm} \boldsymbol{z}_j^{\pm\prime}\right)}{\partial \mathrm{t}} + \left(\boldsymbol{U}_k \mp \boldsymbol{V}_{A,k}\right) \nabla_k \left(\boldsymbol{z}_i^{\pm} \boldsymbol{z}_j^{\pm\prime}\right) \\ + \boldsymbol{z}_j^{\pm\prime} \boldsymbol{z}_k^{\mp} \left(\nabla_k \boldsymbol{U}_i \pm \frac{1}{\sqrt{4\pi\rho}} \nabla_k \boldsymbol{B}_{0,i}\right) + \boldsymbol{z}_i^{\pm} \boldsymbol{z}_k^{\mp\prime} \left(\nabla_k \boldsymbol{U}_j \pm \frac{1}{\sqrt{4\pi\rho}} \nabla_k \boldsymbol{B}_{0,j}\right) \\ + \frac{\boldsymbol{z}_i^{\pm} \boldsymbol{z}_j^{\pm\prime} - \boldsymbol{z}_i^{\mp} \boldsymbol{z}_j^{\pm\prime}}{2} \nabla_k \left(\frac{\boldsymbol{U}_k}{2} \pm \boldsymbol{V}_{A,k}\right) + \frac{\boldsymbol{z}_i^{\pm} \boldsymbol{z}_j^{\pm\prime} - \boldsymbol{z}_i^{\pm} \boldsymbol{z}_j^{\mp\prime}}{2} \nabla_k \left(\frac{\boldsymbol{U}_k}{2} \pm \boldsymbol{V}_{A,k}\right) \\ = -\boldsymbol{z}_j^{\pm\prime} \frac{1}{\rho} \nabla_i p^{T} - \boldsymbol{z}_i^{\pm} \frac{1}{\rho} \nabla_j p^{T} + \boldsymbol{z}_j^{\pm\prime} \boldsymbol{N}_i^{\pm} + \boldsymbol{z}_i^{\pm} \boldsymbol{N}_j^{\pm}\end{aligned} \tag{B.6}$$

$$\begin{aligned}\frac{\partial \left(\boldsymbol{z}_i^{\pm} \boldsymbol{z}_j^{\pm\prime}\right)}{\partial \mathrm{t}} + \left(\boldsymbol{U}_k \mp \boldsymbol{V}_{A,k}\right) \nabla_k \left(\boldsymbol{z}_i^{\pm} \boldsymbol{z}_j^{\pm\prime}\right) \\ + \boldsymbol{z}_j^{\pm\prime} \boldsymbol{z}_k^{\mp} \left(\nabla_k \boldsymbol{U}_i \pm \frac{1}{\sqrt{4\pi\rho}} \nabla_k \boldsymbol{B}_{0,i}\right) + \boldsymbol{z}_i^{\pm} \boldsymbol{z}_k^{\mp\prime} \left(\nabla_k \boldsymbol{U}_j \pm \frac{1}{\sqrt{4\pi\rho}} \nabla_k \boldsymbol{B}_{0,j}\right) \\ + \boldsymbol{z}_i^{\pm} \boldsymbol{z}_j^{\pm\prime} \nabla_k \left(\frac{\boldsymbol{U}_k}{2} \pm \boldsymbol{V}_{A,k}\right) - \frac{1}{2} \left(\boldsymbol{z}_i^{\pm} \boldsymbol{z}_j^{\mp\prime} + \boldsymbol{z}_i^{\mp} \boldsymbol{z}_j^{\pm\prime}\right) \nabla_k \left(\frac{\boldsymbol{U}_k}{2} \pm \boldsymbol{V}_{A,k}\right) \\ = -\boldsymbol{z}_j^{\pm\prime} \frac{1}{\rho} \nabla_i p^{T} - \boldsymbol{z}_i^{\pm} \frac{1}{\rho} \nabla_j p^{T} + \boldsymbol{z}_j^{\pm\prime} \boldsymbol{N}_i^{\pm} + \boldsymbol{z}_i^{\pm} \boldsymbol{N}_j^{\pm}\end{aligned} \tag{B.7}$$

Now apply an ensemble average

$$\begin{aligned}
&\frac{\partial \left\langle \boldsymbol{z}_i^{\pm} \boldsymbol{z}_j^{\pm\prime} \right\rangle}{\partial \mathrm{t}} + \left(\boldsymbol{U}_k \mp \boldsymbol{V}_{A,k}\right) \nabla_k \left\langle \boldsymbol{z}_i^{\pm} \boldsymbol{z}_j^{\pm\prime} \right\rangle \\
&+ \left\langle \boldsymbol{z}_j^{\pm\prime} \boldsymbol{z}_k^{\mp} \right\rangle \left(\nabla_k \boldsymbol{U}_i \pm \frac{1}{\sqrt{4\pi\rho}} \nabla_k \boldsymbol{B}_{0,i}\right) + \left\langle \boldsymbol{z}_i^{\pm} \boldsymbol{z}_k^{\mp\prime} \right\rangle \left(\nabla_k \boldsymbol{U}_j \pm \frac{1}{\sqrt{4\pi\rho}} \nabla_k \boldsymbol{B}_{0,j}\right) \\
&+ \left\langle \boldsymbol{z}_i^{\pm} \boldsymbol{z}_j^{\pm\prime} \right\rangle \nabla_k \left(\frac{\boldsymbol{U}_k}{2} \pm \boldsymbol{V}_{A,k}\right) - \frac{1}{2} \left(\left\langle \boldsymbol{z}_i^{\pm} \boldsymbol{z}_j^{\mp\prime} \right\rangle + \left\langle \boldsymbol{z}_i^{\mp} \boldsymbol{z}_j^{\pm\prime} \right\rangle\right) \nabla_k \left(\frac{\boldsymbol{U}_k}{2} \pm \boldsymbol{V}_{A,k}\right) \\
&= \left\langle \boldsymbol{z}_j^{\pm\prime} \boldsymbol{N}_i^{\pm} + \boldsymbol{z}_i^{\pm} \boldsymbol{N}_j^{\pm} \right\rangle \qquad \text{(B.8)}
\end{aligned}$$

The following is the equation in the correlation tensor form as defined at the start of this appendix

$$\begin{aligned}
&\frac{\partial \boldsymbol{H}_{ij}^{\pm}}{\partial \mathrm{t}} + \left(\boldsymbol{U}_k \mp \boldsymbol{V}_{A,k}\right) \nabla_k \boldsymbol{H}_{ij}^{\pm} + \boldsymbol{H}_{ij}^{\pm} \nabla_k \left(\frac{\boldsymbol{U}_k}{2} + \boldsymbol{V}_{A,k}\right) \\
&+ \boldsymbol{\Lambda}_{kj}^{\mp} \left(\nabla_k \boldsymbol{U}_i \pm \frac{1}{\sqrt{4\pi\rho}} \nabla_k \boldsymbol{B}_{0,i}\right) + \boldsymbol{\Lambda}_{ik}^{\pm} \left(\nabla_k \boldsymbol{U}_j \pm \frac{1}{\sqrt{4\pi\rho}} \nabla_k \boldsymbol{B}_{0,j}\right) \\
&- \frac{1}{2} \left(\boldsymbol{\Lambda}_{ij}^{\pm} + \boldsymbol{\Lambda}_{ij}^{\mp}\right) \nabla_k \left(\frac{\boldsymbol{U}_k}{2} \pm \boldsymbol{V}_{A,k}\right) = \boldsymbol{N}_{ij}^{\pm} \qquad \text{(B.9)}
\end{aligned}$$

Taking the trace $i = j$, we get

$$\frac{\partial \boldsymbol{H}_{ii}^{\pm}}{\partial \mathrm{t}} + \left(\boldsymbol{U}_k \mp \boldsymbol{V}_{A,k}\right) \nabla_k \boldsymbol{H}_{ii}^{\pm} + \boldsymbol{H}_{ii}^{\pm} \nabla_k \left(\frac{\boldsymbol{U}_k}{2} + \boldsymbol{V}_{A,k}\right) + \boldsymbol{\Pi}_{ii}^{\pm} = \boldsymbol{N}_{ii}^{\pm} \qquad \text{(B.10)}$$

where

$$\begin{aligned}
\boldsymbol{\Pi}_{ii}^{\pm} = &\boldsymbol{\Lambda}_{ki}^{\mp} \left(\nabla_k \boldsymbol{U}_i \pm \frac{1}{\sqrt{4\pi\rho}} \nabla_k \boldsymbol{B}_{0,i}\right) + \boldsymbol{\Lambda}_{ik}^{\pm} \left(\nabla_k \boldsymbol{U}_i \pm \frac{1}{\sqrt{4\pi\rho}} \nabla_k \boldsymbol{B}_{0,i}\right) \qquad \text{(B.11)} \\
&- \frac{1}{2} \left(\boldsymbol{\Lambda}_{ii}^{\pm} + \boldsymbol{\Lambda}_{ii}^{\mp}\right) \nabla_k \left(\frac{\boldsymbol{U}_k}{2} \pm \boldsymbol{V}_{A,k}\right)
\end{aligned}$$

Equation B.11 of the correlation evolution equation (Equation B.10) defines the mixing operations that couples the inward and outward fluctuations to the cross correlation of the two fields. The term $\boldsymbol{N}^{\pm}$, is the nonlinear coupling that serves to dissipate the energy into the observed heating of the solar wind.

B.2 Evolution of the Cross Correlations

To obtain a complete solution of the transport equations, we will need to obtain an evolution equation for the cross correlation function $\boldsymbol{\Lambda}_{ij}$. In a similar fashion to section B.1, we will form the cross correlation by multiplying the $\boldsymbol{z}_i^{+}$

component equation by the $\boldsymbol{z}_j^{-\prime}$ component, and the $\boldsymbol{z}_j^{-\prime}$ component equation and multiplying it by the $\boldsymbol{z}_i^{+}$ component. Summing the two equations and then ensemble averaging yields

$$\begin{aligned}
&\frac{\partial \left\langle \boldsymbol{z}_i^+ \boldsymbol{z}_j^{-\prime} \right\rangle}{\partial \mathrm{t}} + \boldsymbol{U}_k \nabla_k \left\langle \boldsymbol{z}_i^+ \boldsymbol{z}_j^{-\prime} \right\rangle + \left\langle \boldsymbol{z}_i^+ \boldsymbol{V}_{A,k} \nabla_k \boldsymbol{z}_j^{-\prime} - \boldsymbol{z}_j^{-\prime} \boldsymbol{V}_{A,k} \nabla_k \boldsymbol{z}_i^+ \right\rangle + \left\langle \boldsymbol{z}_i^+ \boldsymbol{z}_j^{-\prime} \right\rangle \nabla_k \frac{\boldsymbol{U}_k}{2} \\
&\quad + \left\langle \boldsymbol{z}_k^- \boldsymbol{z}_j^{-\prime} \right\rangle \left(\nabla_k \boldsymbol{U}_i + \frac{1}{\sqrt{4\pi\rho}} \nabla_k \boldsymbol{B}_{0,i} \right) + \left\langle \boldsymbol{z}_i^+ \boldsymbol{z}_k^{+\prime} \right\rangle \left(\nabla_k \boldsymbol{U}_j - \frac{1}{\sqrt{4\pi\rho}} \nabla_k \boldsymbol{B}_{0,j} \right) \\
&\qquad - \frac{1}{2} \left\langle \boldsymbol{z}_i^+ \boldsymbol{z}_j^{+\prime} \right\rangle \nabla_k \left(\frac{\boldsymbol{U}_k}{2} - \boldsymbol{V}_{A,k} \right) - \frac{1}{2} \left\langle \boldsymbol{z}_i^- \boldsymbol{z}_j^{-\prime} \right\rangle \nabla_k \left(\frac{\boldsymbol{U}_k}{2} + \boldsymbol{V}_{A,k} \right) \\
&\qquad\qquad = \left\langle \boldsymbol{z}_j^{-\prime} \boldsymbol{N}_i^+ + \boldsymbol{z}_i^+ \boldsymbol{N}_j^- \right\rangle \qquad \text{(B.12)}
\end{aligned}$$

The third term requires a bit more work to simplify, by taking out the $\boldsymbol{V}_A$ term out of the averaging the following steps produce a term that consists of the dot product between the large scale Alfvén speed $\boldsymbol{V}_A$ and the gradient of the cross-correlation function $\boldsymbol{\Lambda}_{ij}^+$ with respect to the correlation lag $\boldsymbol{w}$

$$\left\langle \boldsymbol{z}_i^+ \nabla_k \boldsymbol{z}_j^{-\prime} - \boldsymbol{z}_j^{-\prime} \nabla_k \boldsymbol{z}_i^+ \right\rangle = \left\langle \boldsymbol{z}_i^+(\boldsymbol{x}) \nabla_k \boldsymbol{z}_j^-(\boldsymbol{x}+\boldsymbol{w}) - \boldsymbol{z}_j^-(\boldsymbol{x}+\boldsymbol{w}) \nabla_k \boldsymbol{z}_i^+(\boldsymbol{x}) \right\rangle \qquad \text{(B.13)}$$

by translation invariance, we can let $\boldsymbol{x} \rightarrow \boldsymbol{x} - \boldsymbol{w}$ for the second term only,

$$= \left\langle \boldsymbol{z}_i^+(\boldsymbol{x}) \nabla_k \boldsymbol{z}_j^-(\boldsymbol{x}+\boldsymbol{w}) - \boldsymbol{z}_j^-(\boldsymbol{x}) \nabla_k \boldsymbol{z}_i^+(\boldsymbol{x}-\boldsymbol{w}) \right\rangle \qquad \text{(B.14)}$$

$$= \left\langle \boldsymbol{z}_i^+(\boldsymbol{x}) \nabla_k \boldsymbol{z}_j^-(\boldsymbol{x}_+) - \boldsymbol{z}_j^-(\boldsymbol{x}) \nabla_k \boldsymbol{z}_i^+(\boldsymbol{x}_-) \right\rangle \qquad \text{(B.15)}$$

for ease, $\boldsymbol{x}_\pm = \boldsymbol{x} \pm \boldsymbol{w}$. The gradient term can be expressed as the following from the chain rule

$$\nabla_k f(\boldsymbol{x}_\pm) = \frac{\partial f(\boldsymbol{x}_\pm)}{\partial \boldsymbol{x}_\pm} = \pm \frac{\partial f(\boldsymbol{x}_\pm)}{\partial \boldsymbol{w}} = \frac{\partial f(\boldsymbol{x}_\pm)}{\partial \boldsymbol{x}} \qquad \text{(B.16)}$$

using the product rule and invoking homogeneity in the last step $\boldsymbol{\Lambda}_{ij}^+(\boldsymbol{w}) = \boldsymbol{\Lambda}_{ji}^-(-\boldsymbol{w})$, the derivative with respect to the offset $\boldsymbol{w}$ can be simplified

$$\left\langle \boldsymbol{z}_i^+(\boldsymbol{x}) \frac{\partial \boldsymbol{z}_j^-(\boldsymbol{x}_+)}{\partial \boldsymbol{w}} + \boldsymbol{z}_j^-(\boldsymbol{x}) \frac{\partial \boldsymbol{z}_i^+(\boldsymbol{x}_-)}{\partial \boldsymbol{w}} \right\rangle \qquad \text{(B.17)}$$

$$= \left\langle \frac{\partial (\boldsymbol{z}_i^+(\boldsymbol{x}) \boldsymbol{z}_j^-(\boldsymbol{x}_+))}{\partial \boldsymbol{w}} - \boldsymbol{z}_j^-(\boldsymbol{x}_+) \frac{\partial \boldsymbol{z}_i^+(\boldsymbol{x})}{\partial \boldsymbol{w}} + \frac{\partial (\boldsymbol{z}_j^-(\boldsymbol{x}) \boldsymbol{z}_i^+(\boldsymbol{x}_-))}{\partial \boldsymbol{w}} - \boldsymbol{z}_i^+(\boldsymbol{x}_-) \frac{\partial \boldsymbol{z}_j^-(\boldsymbol{x})}{\partial \boldsymbol{w}} \right\rangle \qquad \text{(B.18)}$$

$$= \frac{\partial \boldsymbol{\Lambda}_{ij}^+(\boldsymbol{w})}{\partial \boldsymbol{w}} + \frac{\partial \boldsymbol{\Lambda}_{ji}^-(-\boldsymbol{w})}{\partial \boldsymbol{w}} = 2 \frac{\partial \boldsymbol{\Lambda}_{ij}^+(\boldsymbol{w})}{\partial \boldsymbol{w}} = 2 \nabla_{\boldsymbol{w},k} \boldsymbol{\Lambda}_{ij}^+(\boldsymbol{w}) \qquad \text{(B.19)}$$

Now, the evolution equation for the cross correlations is the following

$$\begin{aligned}&\frac{\partial \boldsymbol{\Lambda}^{+}_{ij}}{\partial \mathrm{t}} + \boldsymbol{U}_k \nabla_k \boldsymbol{\Lambda}^{+}_{ij} + 2\boldsymbol{V}_{A,k} \nabla_{\boldsymbol{w},k} \boldsymbol{\Lambda}^{+}_{ij} + \boldsymbol{\Lambda}^{+}_{ij} \nabla_k \frac{\boldsymbol{U}_k}{2} \\ &+\boldsymbol{H}^{-}_{kj} \left(\nabla_k \boldsymbol{U}_i + \frac{1}{\sqrt{4\pi\rho}} \nabla_k \boldsymbol{B}_{0,i} \right) + \boldsymbol{H}^{+}_{ik} \left(\nabla_k \boldsymbol{U}_j - \frac{1}{\sqrt{4\pi\rho}} \nabla_k \boldsymbol{B}_{0,j} \right) \\ &-\frac{1}{2} \boldsymbol{H}^{-}_{ij} \nabla_k \left(\frac{\boldsymbol{U}_k}{2} + \boldsymbol{V}_{A,k} \right) - \frac{1}{2} \boldsymbol{H}^{+}_{ij} \nabla_k \left(\frac{\boldsymbol{U}_k}{2} - \boldsymbol{V}_{A,k} \right) = \boldsymbol{N}^{D}_{ij} \end{aligned} \qquad \text{(B.20)}$$

Taking the trace $i = j$, we get

$$\frac{\partial \boldsymbol{\Lambda}^{+}_{ii}}{\partial \mathrm{t}} + \boldsymbol{U}_k \nabla_k \boldsymbol{\Lambda}^{+}_{ii} + 2\boldsymbol{V}_{A,k} \nabla_{\boldsymbol{w},k} \boldsymbol{\Lambda}^{+}_{ii} + \boldsymbol{\Lambda}^{+}_{ii} \nabla_k \frac{\boldsymbol{U}_k}{2} + \boldsymbol{\Sigma}^{+}_{ii} + \boldsymbol{\Sigma}^{-}_{ii} = \boldsymbol{N}^{D}_{ii} \qquad \text{(B.21)}$$

where

$$\boldsymbol{\Sigma}^{\pm}_{ii} = -\frac{1}{2} \boldsymbol{H}^{\pm}_{ii} \nabla_k \left(\frac{\boldsymbol{U}_k}{2} \mp \boldsymbol{V}_{A,k} \right) + \boldsymbol{H}^{\pm}_{ki} \left(\nabla_k \boldsymbol{U}_i \mp \frac{1}{\sqrt{4\pi\rho}} \nabla_k \boldsymbol{B}_{0,i} \right) \qquad \text{(B.22)}$$

To get the equation for $\boldsymbol{\Lambda}^{-}_{ii}(w)$, simply apply the homogeneous property $\boldsymbol{\Lambda}^{+}_{ij}(\boldsymbol{w}) = \boldsymbol{\Lambda}^{-}_{ji}(-\boldsymbol{w})$. We can see that the $\boldsymbol{\Sigma}^{\pm}$ terms form the 'mixing' terms in the cross correlation equation that provides couplings to the inward and outward fluctuation correlations and depends on the gradients of the large-scale background fields. The term $\boldsymbol{N}^{D}_{ii}$ is the nonlinear coupling and provides the effect responsible for the generation of small scales from large ones and the dissipation of the energy. The only term that is not analogous to the correlation equation (Equation B.10) is the gradient term with respect to the small scale separation parameter $\boldsymbol{w}$ ($\nabla_{\boldsymbol{w},k} \boldsymbol{\Lambda}^{+}_{ij}$) which arises due to the defining the turbulence as *locally* isotropic and depends on whether the fluctuations are parallel or normal to the mean magnetic field.

Appendix C

Isotropic Turbulence

In a statistical sense, it is useful to simplify the correlation tensors by determining (or assuming) symmetry properties of the turbulent fields. We will examine two main symmetry conditions suggested from Batchelor [8]; isotropic and axisymmetric turbulence. Batchelor [8] introduces the symmetric properties of the correlation functions in regards to the tensor of the fluctuating velocity, most relevant to this thesis is the second order correlation tensor $\boldsymbol{Q}^u_{ij}(\boldsymbol{w}) = \langle \boldsymbol{u}_i(\boldsymbol{x})\boldsymbol{u}_j(\boldsymbol{x}+\boldsymbol{w})\rangle$. As stated in Zhou and Matthaeus [66], we are interested in the cross helicity H_C and the total incompressible energy per unit mass $E = E_u + E_b$ with the kinetic and magnetic energy contributions E_u, E_b respectively. In homogeneous turbulence, these quantities can be expressed as the ensemble averages $E = \frac{1}{2}\left\langle \boldsymbol{u}\cdot\boldsymbol{u} + \boldsymbol{v}_A\cdot\boldsymbol{v}_A\right\rangle$ and $H_C = \frac{1}{2}\left\langle \boldsymbol{u}\cdot\boldsymbol{v}_A\right\rangle$. Now it is easier to see that by defining the following correlation tensors

$$\boldsymbol{Q}^u_{ij}(\boldsymbol{w}) = \langle \boldsymbol{u}_i(\boldsymbol{x})\boldsymbol{u}_j(\boldsymbol{x}+\boldsymbol{w})\rangle \tag{C.1}$$

$$\boldsymbol{Q}^b_{ij}(\boldsymbol{w}) = \frac{1}{4\pi\rho}\langle \boldsymbol{b}_i(\boldsymbol{x})\boldsymbol{b}_j(\boldsymbol{x}+\boldsymbol{w})\rangle \tag{C.2}$$

we can retrieve the total energy $E = \frac{1}{2}\left[\boldsymbol{Q}^u_{ii}(\boldsymbol{w}=0) + \boldsymbol{Q}^b_{ii}(\boldsymbol{w}=0)\right]$. We can also retrieve the cross helicity with the following correlation tensor

$$\boldsymbol{Q}^{ub,\pm}_{ij}(\boldsymbol{w}) = \frac{1}{2\sqrt{4\pi\rho}}\langle \boldsymbol{u}_i(\boldsymbol{x})\boldsymbol{b}_j(\boldsymbol{x}+\boldsymbol{w}) \pm \boldsymbol{b}_i(\boldsymbol{x})\boldsymbol{u}_j(\boldsymbol{x}+\boldsymbol{w})\rangle \tag{C.3}$$

via $H_C = \frac{1}{2}\boldsymbol{Q}^{ub,+}(\boldsymbol{w}=0)$. Now, the correlation tensors introduced in Appendix B; with which we have calculated evolution equations for, can be defined in terms of the correlation Equations (C.1) to (C.3)

$$\boldsymbol{H}^{\pm}_{ij} = \left\langle \boldsymbol{z}^{\pm}_i \boldsymbol{z}^{\pm\prime}_j \right\rangle = \boldsymbol{Q}^u_{ij} + \boldsymbol{Q}^b_{ij} \pm 2\boldsymbol{Q}^{ub,+}_{ij} \tag{C.4}$$

$$\boldsymbol{\Lambda}^+_{ij} + \boldsymbol{\Lambda}^-_{ji} = \left\langle \boldsymbol{z}^+_i \boldsymbol{z}^{-\prime}_j + \boldsymbol{z}^-_j \boldsymbol{z}^{+\prime}_i \right\rangle = \boldsymbol{Q}^u_{ij} - \boldsymbol{Q}^b_{ij} + \boldsymbol{Q}^u_{ji} - \boldsymbol{Q}^b_{ji} \mp 2\left(\boldsymbol{Q}^{ub,-}_{ij} - \boldsymbol{Q}^{ub,-}_{ji}\right) \tag{C.5}$$

C.1 3D Isotropic Turbulence

Isotropic turbulence is the assumption that the products of the velocity components, and their derivatives are invariant under rotations and reflections of a coordinate system moving with the fluid. In this section, we will work with the velocity correlation tensor $\boldsymbol{Q}_{ij} = \boldsymbol{Q}^u_{ij}$, however, the results will generalize to the tensors Equations (C.1) to (C.3) and therefore Equations (C.4) and (C.5). The following is the form of the correlation function under isotropic symmetries [8]

$$\boldsymbol{Q}^{iso}_{ij}(w) = F(w)\boldsymbol{w}_i\boldsymbol{w}_j + G(w)\boldsymbol{\delta}_{ij} \tag{C.6}$$

The functions $F(w), G(w)$ are arbitrary scalar functions of $w = (\boldsymbol{w}_i\boldsymbol{w}_i)^{1/2}$ and time t (but we will ignore the dependence on time). In an isotropic system, there is no dependence on the preferred direction. In order to satisfy the incompressibility ($\nabla \cdot \boldsymbol{u} = 0$),

$$\frac{\partial \boldsymbol{Q}_{ij}(\boldsymbol{w})}{\partial \boldsymbol{w}_i} = \frac{\partial \boldsymbol{Q}_{ij}(\boldsymbol{w})}{\partial \boldsymbol{w}_j} = 0 \tag{C.7}$$

we require,

$$\frac{\partial \boldsymbol{Q}_{ij}(\boldsymbol{w})}{\partial \boldsymbol{w}_i} = \frac{\partial}{\partial \boldsymbol{w}_i}\left[F(w)\hat{\boldsymbol{w}}_i\hat{\boldsymbol{w}}_j\right] + \frac{\partial}{\partial \boldsymbol{w}_i}\left[G(w)\boldsymbol{\delta}_{ij}\right] \tag{C.8}$$

$$= \frac{\partial}{\partial \boldsymbol{w}_i}\left[F(w)\boldsymbol{w}_i\boldsymbol{w}_j\right] + \frac{\partial}{\partial \boldsymbol{w}_j}\left[G(w)\right] \tag{C.9}$$

$$= F(w)\boldsymbol{w}_j\frac{\partial \boldsymbol{w}_i}{\partial \boldsymbol{w}_i} + F(w)\boldsymbol{w}_i\frac{\partial \boldsymbol{w}_j}{\partial \boldsymbol{w}_i} + \boldsymbol{w}_i\boldsymbol{w}_j\frac{\partial F(w)}{\partial \boldsymbol{w}_i} + \frac{\partial G(w)}{\partial w}\frac{\partial w}{\partial \boldsymbol{w}_j} \tag{C.10}$$

$$= 3F(w)\boldsymbol{w}_j + F(w)\boldsymbol{w}_i\boldsymbol{\delta}_{ij} + \frac{\boldsymbol{w}_i\boldsymbol{w}_i}{w}\boldsymbol{w}_j\frac{\partial F(w)}{\partial w} + \frac{\boldsymbol{w}_j}{w}\frac{\partial G(w)}{\partial w} \tag{C.11}$$

$$= \boldsymbol{w}_j\left[4F(w) + w\frac{\partial F(w)}{\partial w} + \frac{1}{w}\frac{\partial G(w)}{\partial w}\right] \tag{C.12}$$

$$= 0 \tag{C.13}$$

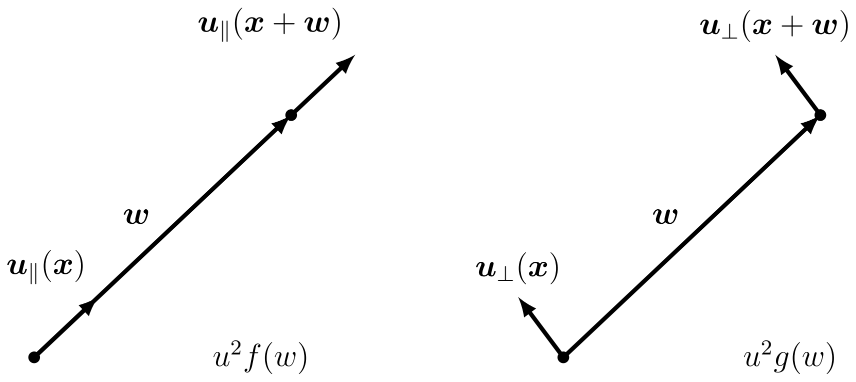

Figure C.1: Longitudinal and lateral velocity correlations

therefore, for all values of w

$$4F(w) + w\frac{\partial F(w)}{\partial w} + \frac{1}{w}\frac{\partial G(w)}{\partial w} = 0 \tag{C.14}$$

We shall introduce a pair of coefficient functions $f(w)$ and $g(w)$ defined by

$$u_{\|}^2 f(w) = \left\langle \boldsymbol{u}_{\|}\boldsymbol{u}_{\|}' \right\rangle \tag{C.15}$$

$$u_{\perp}^2 g(w) = \left\langle \boldsymbol{u}_{\perp}\boldsymbol{u}_{\perp}' \right\rangle \tag{C.16}$$

that use the parallel $\boldsymbol{u}_{\|}$ and perpendicular $\boldsymbol{u}_{\perp}$ velocity components relative to the vector separation/lag $\hat{\boldsymbol{w}}$. Figure C.1 shows the longitudinal velocity correlation $f(w)$ and the lateral velocity correlation $g(w)$. From now on, we will assume that the separation vector $\hat{\boldsymbol{w}}$ is in the 1 direction only, therefore the parallel velocity component is $\boldsymbol{u}_{\|} = \boldsymbol{u}_1$ and the longitudinal velocity component is $\boldsymbol{u}_{\perp} = \boldsymbol{u}_2$. The coefficient functions f and g can be related to the correlation tensor (and the F and G functions)

$$\boldsymbol{Q}_{11}(w) = \left\langle \boldsymbol{u}_{\|}(x,0,0)\boldsymbol{u}_{\|}(x+w,0,0) \right\rangle = F(w)\boldsymbol{w}_1\boldsymbol{w}_1 + G(w)\boldsymbol{\delta}_{11} \tag{C.17}$$

$$= w^2 F(w) + G(w) = u_{\|}^2 f(w) \tag{C.18}$$

$$\boldsymbol{Q}_{22}(w) = \left\langle \boldsymbol{u}_{\perp}(x,0,0)\boldsymbol{u}_{\perp}(x+w,0,0) \right\rangle = F(w)\boldsymbol{w}_2\boldsymbol{w}_2 + G(w)\boldsymbol{\delta}_{22} = u_{\perp}^2 g(w) \tag{C.19}$$

Now, Equation C.6 and Equation C.14 become

$$\boldsymbol{Q}_{ij}(\boldsymbol{w}) = u^2\left((f-g)\frac{\boldsymbol{w}_i\boldsymbol{w}_j}{w^2} + g\boldsymbol{\delta}_{ij}\right) \tag{C.20}$$

and

$$g(w) = f(w) + \frac{1}{2} w \frac{\partial f(w)}{\partial w} \tag{C.21}$$

Evaluating the correlation tensor with zero separation $\hat{\boldsymbol{w}} = 0$ to obtain the kinetic energy $\boldsymbol{Q}_{ij}(0) = E_u$, we get the following result

$$\boldsymbol{Q}_{ij}(0) = u^2 \boldsymbol{\delta}_{ij} \overset{\text{trace}}{=} 3u^2 \tag{C.22}$$

since $f(0) = g(0) = 1$. Integrating the correlation tensor over the separation vector in a single direction, with $\ell_f = \int_0^\infty f(w)\mathrm{d}w$ and $\ell_g = \int_0^\infty g(w)\mathrm{d}w$

$$\int_0^\infty \boldsymbol{Q}_{ij}(w)\mathrm{d}w = u^2 \lambda_f \left(\hat{\boldsymbol{w}}_i \hat{\boldsymbol{w}}_j + \boldsymbol{\delta}_{ij}\right) \overset{\text{trace}}{=} 4u^2 \ell_f = 4L_f \tag{C.23}$$

where $L_f = \int_0^\infty \boldsymbol{Q}_{11}(w)\mathrm{d}w$. Scaling the trace of the results, the following is the simplification of the energy tensors of the Elsässer variables and the energy difference for isotropic symmetries

$$\boldsymbol{H}_{ij}^{\pm}(0) = \frac{Z_\pm^2}{3} \boldsymbol{\delta}_{ij} \tag{C.24}$$

$$\frac{1}{2}\left(\boldsymbol{\Lambda}_{ij}^{+}(0) + \boldsymbol{\Lambda}_{ji}^{-}(0)\right) = \frac{D}{3} \boldsymbol{\delta}_{ij} \tag{C.25}$$

and the correlation integral tensors

$$\int_0^\infty \boldsymbol{H}_{ij}^{\pm}(w)\mathrm{d}w = \frac{L_\pm}{4}\left(\hat{\boldsymbol{w}}_i \hat{\boldsymbol{w}}_j + \boldsymbol{\delta}_{ij}\right) \tag{C.26}$$

$$\int_0^\infty \frac{1}{2}\left(\boldsymbol{\Lambda}_{ij}^{+}(w) + \boldsymbol{\Lambda}_{ji}^{-}(w)\right)\mathrm{d}w = \frac{L_D}{4}\left(\hat{\boldsymbol{w}}_i \hat{\boldsymbol{w}}_j + \boldsymbol{\delta}_{ij}\right) \tag{C.27}$$

C.2 2D Isotropic Turbulence (Axisymmetric)

Axisymmetric turbulence follows from isotropic turbulence with the stricter requirement of invariance under rotations about a fixed axis parallel to $\boldsymbol{n}$. In the specific case of the solar wind, the axisymmetric axis $\hat{\boldsymbol{n}}$ is interpreted to be parallel to the mean magnetic field $\boldsymbol{B}_0$. In which case, a two-dimensional plane exists perpendicular to the mean magnetic field that contains the isotropic turbulent fluctuations. The following is the form for the axisymmetric second order correlation function

$$\boldsymbol{Q}_{ij}^{axi}(w^2, w_n) = A(w^2, w_n)\boldsymbol{w}_i\boldsymbol{w}_j + B(w^2, w_n)\hat{\boldsymbol{n}}_i\hat{\boldsymbol{n}}_j + C(w^2, w_n)\boldsymbol{\delta}_{ij} + D(w^2, w_n)\boldsymbol{w}_i\hat{\boldsymbol{n}}_j + E(w^2, w_n)\hat{\boldsymbol{n}}_i\boldsymbol{w}_j \tag{C.28}$$

The functions A, B, C, D, and E are arbitrary functions of $w^2 = \boldsymbol{w}\cdot\boldsymbol{w}$, $w_n = \boldsymbol{w}\cdot\hat{\boldsymbol{n}}$ and time t (once again we will ignore the time dependence). By making note of the following relation [7]

$$\frac{\partial}{\partial \boldsymbol{w}_i} = \frac{\partial w}{\partial \boldsymbol{w}_i}\frac{\partial}{\partial w} + \frac{\partial n}{\partial \boldsymbol{w}_i}\frac{\partial}{\partial w_n} = \frac{\boldsymbol{w}_i}{w}\frac{\partial}{\partial w} + \left(\frac{\hat{\boldsymbol{n}}_i}{w} - \frac{w_n \boldsymbol{w}_i}{w^2}\right)\frac{\partial}{\partial w_n} \tag{C.29}$$

and following in a similar fashion to the 3D case, the incompressibility condition requires that

$$\frac{\partial \boldsymbol{Q}_{ij}}{\partial \boldsymbol{w}_i} = \boldsymbol{w}_j\left(4A + w\frac{\partial A}{\partial w} + \frac{1}{w}\frac{\partial C}{\partial w} - \frac{w_n}{w^2}\frac{\partial C}{\partial w_n} + w_n\frac{\partial E}{\partial w} + \frac{1-w_n^2}{w}\frac{\partial E}{\partial w_n}\right) + \hat{\boldsymbol{n}}_j\left(\frac{1}{w}\frac{\partial C}{\partial w_n} + n\frac{\partial B}{\partial w} + \frac{1-w_n^2}{w}\frac{\partial C}{\partial w_n} + 3D + w\frac{\partial D}{\partial w} + E\right) = 0 \tag{C.30}$$

which implies that

$$4A + w\frac{\partial A}{\partial w} + \frac{1}{w}\frac{\partial C}{\partial w} - \frac{w_n}{w^2}\frac{\partial C}{\partial w_n} + w_n\frac{\partial E}{\partial w} + \frac{1-w_n^2}{w}\frac{\partial E}{\partial w_n} = 0 \tag{C.31}$$

$$\frac{1}{w}\frac{\partial C}{\partial w_n} + n\frac{\partial B}{\partial w} + \frac{1-w_n^2}{w}\frac{\partial C}{\partial w_n} + 3D + w\frac{\partial D}{\partial w} + E = 0 \tag{C.32}$$

Obviously, calculating the relations of the scalar functions A, B, C, D, and E is more involved than the three dimensional case, we will refer to Batchelor [7] and Matthaeus et al. [35]. Starting with taking the correlation tensor at zero separation $w = 0$

$$\boldsymbol{Q}_{ij}(0) = B(0)\boldsymbol{\delta}_{ij} + C(0)\boldsymbol{n}_i\boldsymbol{n}_j \tag{C.33}$$

from the relations for $B(0)$ and $C(0)$ [7, 35], it follows that the axisymmetric energy tensor can be simplified to

$$\boldsymbol{Q}_{ij}(0) = \frac{u^2}{2}\left(\boldsymbol{\delta}_{ij} - \hat{\boldsymbol{n}}_i\hat{\boldsymbol{n}}_j\right) \tag{C.34}$$

For our purposes,

$$\boldsymbol{H}_{ij}^{\pm}(0) = \frac{Z_{\pm}^2}{2}\left(\boldsymbol{\delta}_{ij} - \hat{\boldsymbol{n}}_i\hat{\boldsymbol{n}}_j\right) \tag{C.35}$$

$$\frac{1}{2}\left(\boldsymbol{\Lambda}_{ij}^{+}(0) + \boldsymbol{\Lambda}_{ij}^{-}(0)\right) = \frac{D}{2}\left(\boldsymbol{\delta}_{ij} - \hat{\boldsymbol{n}}_i\hat{\boldsymbol{n}}_j\right) \tag{C.36}$$

Likewise, integrating the correlation tensors nets

$$\int_0^\infty \boldsymbol{H}_{ij}^{\pm}(w)\mathrm{d}w = L_{\pm}\hat{\boldsymbol{e}}_i\hat{\boldsymbol{e}}_j \tag{C.37}$$

$$\int_0^\infty \frac{1}{2}\left(\boldsymbol{\Lambda}_{ij}^{+}(w) + \boldsymbol{\Lambda}_{ij}^{-}(w)\right)\mathrm{d}w = L_D\hat{\boldsymbol{e}}_i\hat{\boldsymbol{e}}_j \tag{C.38}$$

where $\boldsymbol{w} = w\hat{\boldsymbol{e}}$ where $\hat{\boldsymbol{e}}$ is a unitvector such that $\hat{\boldsymbol{e}} \cdot \hat{\boldsymbol{n}} = 0$.

Appendix D

6 Equation Model Derivation

Here we use results from the earlier appendices to assemble the six equation model for the two fluctuation symmetry cases considered (isotropic and axisymmetric). Many of these results are available in Matthaeus et al. [35], although we often provide more details here. With the correlation evolution equations from Appendix B along with the symmetry assumptions from Appendix C we can obtain evolution equations for the energies, written in terms of the Elsässer variables by evaluating the correlation tensor evolution Equations (B.10) and (B.21) at zero separation ($w = 0$),

$$Z_{\pm}^2 = \boldsymbol{H}_{ii}^{\pm}(0) \tag{D.1}$$

$$D = \frac{1}{2}\left(\boldsymbol{\Lambda}_{ii}^{+}(0) + \boldsymbol{\Lambda}_{ii}^{-}(0)\right) \tag{D.2}$$

For simplicity, it is easier to define a symmetric energy difference correlation tensor as follows [35, 36]

$$\boldsymbol{R}_{ij}^{Ds}(w) = \frac{1}{2}\left(\boldsymbol{\Lambda}_{ij}^{+}(w) + \boldsymbol{\Lambda}_{ji}^{-}(w)\right) \tag{D.3}$$

which gives $\boldsymbol{R}_{ii}^{Ds}(0) = D$. We can obtain the evolution equations for the correlation integral scales by integrating the correlation tensor evolution Equations (B.10) and (B.21) from distances $w = 0$ to $w = \infty$, and introducing the lag-integrated correlation functions (we will refer to as L's or correlation integrals)

$$L_\pm = \int_0^\infty \boldsymbol{H}_{ii}^\pm(w)\mathrm{d}w \tag{D.4}$$

$$L_D = \int_0^\infty \boldsymbol{R}_{ij}^{Ds}(w)\mathrm{d}w \tag{D.5}$$

To obtain the correlation length scales, divide the correlation integral scales by the appropriate "energies" to obtain distance units,

$$\lambda_\pm = \frac{L_\pm}{Z_\pm^2} \tag{D.6}$$

$$\lambda_D = \frac{L_D}{D} \tag{D.7}$$

The following are the three evolution equations representing the energy of the backward fluctuations Z_+^2, forward fluctuations Z_-^2 and the energy difference D

$$\frac{\partial Z_\pm^2}{\partial \mathrm{t}} + (\boldsymbol{U} \mp \boldsymbol{V}_A)\cdot\nabla Z_\pm^2 + Z_\pm^2\nabla\cdot\left(\frac{\boldsymbol{U}}{2} \pm \boldsymbol{V}_A\right) + M^\pm D = N_\pm + S_\pm \tag{D.8}$$

$$\frac{\partial D}{\partial \mathrm{t}} + \boldsymbol{U}\cdot\nabla D + D\nabla\cdot\frac{\boldsymbol{U}}{2} + \frac{1}{2}\left(M^+ Z_-^2 + M^- Z_+^2\right) = N_D + S_D \tag{D.9}$$

The terms $N_{\pm/D}$ and $S_{\pm/D}$ represent the nonlinear terms and the sources respectively. The mixing terms $M^\pm$ will be derived in section D.3. The following are the evolution equations for the lag-integrated correlation functions backward fluctuations L_+, forward fluctuations L_- and the the energy difference L_D,

$$\frac{\partial L_\pm}{\partial \mathrm{t}} + (\boldsymbol{U} \mp \boldsymbol{V}_A)\cdot\nabla L_\pm + L_\pm\nabla\cdot\left(\frac{\boldsymbol{U}}{2} \pm \boldsymbol{V}_A\right) + \int_0^\infty \boldsymbol{\Pi}_{ii}\mathrm{d}w = N_\pm^L + S_\pm^L \tag{D.10}$$

$$\begin{aligned}&\frac{\partial L_D}{\partial \mathrm{t}} + \boldsymbol{U}\cdot\nabla L_D - 2\hat{\boldsymbol{w}}\cdot\boldsymbol{V}_A D + L_D\nabla\cdot\frac{\boldsymbol{U}}{2}\\ &+\frac{1}{2}\left(\int_0^\infty \boldsymbol{\Sigma}_{ii}^+(w)\mathrm{d}w + \int_0^\infty \boldsymbol{\Sigma}_{ii}^-(w)\mathrm{d}w\right) = N_D^L + S_D^L\end{aligned} \tag{D.11}$$

Like the energy equations, the terms $N_{\pm/D}^L$ and $S_{\pm/D}^L$ represent the nonlinear terms and the source terms respectively. The mixing terms for the L evolution equations $\int_0^\infty \boldsymbol{\Pi}_{ii}^\pm\mathrm{d}w$ and $\int_0^\infty \boldsymbol{\Sigma}_{ii}^\pm\mathrm{d}w$ will be calculated in section D.4. Appendix D.5 converts the above evolution equations and the mixing terms into steady-state, radial evolution equations.

D.1 Gradient and Divergence of the Mean Flow

Assuming the uniformly spherical expansion of the solar wind with a constant mean speed U, $\boldsymbol{U}$ in spherical polar coordinates is

$$\boldsymbol{U} = U\hat{\boldsymbol{r}} \tag{D.12}$$

We will take the gradient in spherical coordinates, which is the following

$$\begin{aligned}
\nabla\boldsymbol{U} &= \nabla_{sph}(U\hat{\boldsymbol{r}}) && \text{(D.13)}\\
&= U(\hat{\boldsymbol{r}}\frac{\partial}{\partial \mathrm{r}} + \hat{\boldsymbol{\theta}}\frac{1}{r}\frac{\partial}{\partial\theta} + \hat{\boldsymbol{\phi}}\frac{1}{r\sin\theta}\frac{\partial}{\partial\phi})(\hat{\boldsymbol{r}}) && \text{(D.14)}\\
&= U(\hat{\boldsymbol{r}}\frac{\partial\hat{\boldsymbol{r}}}{\partial \mathrm{r}} + \hat{\boldsymbol{\theta}}\frac{1}{r}\frac{\partial\hat{\boldsymbol{r}}}{\partial\theta} + \hat{\boldsymbol{\phi}}\frac{1}{r\sin\theta}\frac{\partial\hat{\boldsymbol{r}}}{\partial\phi}) && \text{(D.15)}\\
&= U(\hat{\boldsymbol{\theta}}\hat{\boldsymbol{\theta}}\frac{1}{r} + \hat{\boldsymbol{\phi}}\hat{\boldsymbol{\phi}}\frac{\sin\theta}{r\sin\theta}) && \text{(D.16)}\\
&= \frac{U}{r}\begin{bmatrix} 0 & 0 & 0\\ 0 & 1 & 0\\ 0 & 0 & 1\end{bmatrix} && \text{(D.17)}
\end{aligned}$$

The divergence of the mean flow is

$$\nabla\cdot\frac{\boldsymbol{U}}{2} = \frac{1}{r^2}\frac{\partial(\frac{U}{2}r^2)}{\partial \mathrm{r}} = \frac{U}{r} \tag{D.18}$$

D.2 Gradient and Divergence of the Parker Spiral

The sun's large scale magnetic field can be modelled as the Parker Spiral, expressed in spherical polar coordinates as [45]

$$B_r(r,\theta,\phi) = B(\theta,\phi_0)\left(\frac{R_0}{r}\right)^2 \tag{D.19}$$

$$B_\theta(r,\theta,\phi) = 0 \tag{D.20}$$

$$B_\phi(r,\theta,\phi) = B(\theta,\phi_0)\left(\frac{\Omega R_0}{U}\right)\left(\frac{r}{R_0}-1\right)\left(\frac{R_0}{r}\right)^2\sin\theta \tag{D.21}$$

with $B(\theta,\phi_0) = B_0$ and R_0 is the Alfvén critical radius, approximately 10 solar radii. With the following notation simplification for $f = B_{0r}$ (the radial component) and $g = B_{0\phi}$ (the azimuthal component), we will now calculate the gradient of the Parker Spiral in spherical polar coordinates.

$$\nabla_{sph}\boldsymbol{B}_0 = \left(\hat{\boldsymbol{r}}\frac{\partial}{\partial \mathrm{r}} + \frac{1}{r}\hat{\boldsymbol{\theta}}\frac{\partial}{\partial \theta} + \frac{1}{r\sin\theta}\hat{\boldsymbol{\phi}}\frac{\partial}{\partial \phi}\right)\left(f\hat{\boldsymbol{r}} + g\hat{\boldsymbol{\phi}}\right) \tag{D.22}$$

$$= \hat{\boldsymbol{r}}\hat{\boldsymbol{r}}\frac{\partial f}{\partial \mathrm{r}} + \hat{\boldsymbol{r}}f\frac{\partial \hat{\boldsymbol{r}}}{\partial \mathrm{r}} + \frac{1}{r}\frac{\partial f}{\partial \theta} + \frac{1}{r}\hat{\boldsymbol{\theta}}f\frac{\partial \hat{\boldsymbol{r}}}{\partial \theta} + \frac{1}{r\sin\theta}\hat{\boldsymbol{\phi}}\hat{\boldsymbol{r}}\frac{\partial f}{\partial \phi} + \frac{1}{r\sin\theta}\hat{\boldsymbol{\phi}}f\frac{\partial \hat{\boldsymbol{r}}}{\partial \phi}$$

$$+\hat{\boldsymbol{r}}\hat{\boldsymbol{\phi}}\frac{\partial g}{\partial \mathrm{r}} + \hat{\boldsymbol{r}}g\frac{\partial \hat{\boldsymbol{\phi}}}{\partial \mathrm{r}} + \frac{1}{r}\hat{\boldsymbol{\theta}}\hat{\boldsymbol{\phi}}\frac{\partial g}{\partial \theta} + \frac{1}{r}\hat{\boldsymbol{\theta}}g\frac{\partial \hat{\boldsymbol{\phi}}}{\partial \theta} + \frac{1}{r\sin\theta}\hat{\boldsymbol{\phi}}\hat{\boldsymbol{\phi}}\frac{\partial g}{\partial \phi} + \frac{1}{r\sin\theta}\hat{\boldsymbol{\phi}}g\frac{\partial \hat{\boldsymbol{\phi}}}{\partial \phi} \tag{D.23}$$

$$= \hat{\boldsymbol{r}}\hat{\boldsymbol{r}}\frac{\partial f}{\partial \mathrm{r}} + 0 + \frac{1}{r}\frac{\partial f}{\partial \theta} + \frac{1}{r}\hat{\boldsymbol{\theta}}\hat{\boldsymbol{\theta}}f + \frac{1}{r\sin\theta}\hat{\boldsymbol{\phi}}\hat{\boldsymbol{r}}\frac{\partial f}{\partial \phi} + \frac{1}{r}\hat{\boldsymbol{\phi}}\hat{\boldsymbol{\phi}}f$$

$$+\hat{\boldsymbol{r}}\hat{\boldsymbol{\phi}}\frac{\partial g}{\partial \mathrm{r}} + 0 + \frac{1}{r}\hat{\boldsymbol{\theta}}\hat{\boldsymbol{\phi}}\frac{\partial g}{\partial \theta} + 0 + \frac{1}{r\sin\theta}\hat{\boldsymbol{\phi}}\hat{\boldsymbol{\phi}}\frac{\partial g}{\partial \phi} + \frac{1}{r\sin\theta}\hat{\boldsymbol{\phi}}g\left(-\cos\theta\hat{\boldsymbol{\theta}} - \sin\theta\hat{\boldsymbol{r}}\right) \tag{D.24}$$

$$= \begin{bmatrix} \frac{\partial f}{\partial \mathrm{r}} & 0 & 0 \\ \frac{1}{r}\frac{\partial f}{\partial \theta} & \frac{1}{r}f & 0 \\ \frac{1}{r\sin\theta}\frac{\partial f}{\partial \phi} & 0 & \frac{1}{r}f \end{bmatrix} + \begin{bmatrix} 0 & 0 & \frac{\partial g}{\partial \mathrm{r}} \\ 0 & 0 & \frac{1}{r}\frac{\partial g}{\partial \theta} \\ -\frac{1}{r}g & -\frac{1}{r}\cot\theta g & \frac{1}{r\sin\theta}\frac{\partial g}{\partial \phi} \end{bmatrix} \tag{D.25}$$

calculating the derivatives of f and g,

$$\frac{\partial f}{\partial \mathrm{r}} = -\frac{2}{r}f \tag{D.26}$$

$$\frac{\partial f}{\partial \theta} = f' = \frac{\partial B(\theta, \phi_0)}{\partial \theta}\left(\frac{R_0}{r}\right)^2 \tag{D.27}$$

$$\frac{\partial f}{\partial \phi} = 0 \tag{D.28}$$

$$\frac{\partial g}{\partial \mathrm{r}} = \frac{1}{r}\left(\frac{2R_0 - r}{r - R_0}\right)g \tag{D.29}$$

$$\frac{\partial g}{\partial \theta} = g' = \frac{\partial B(\theta, \phi_0)}{\partial \theta}\left(\frac{\Omega R_0}{U}\right)\left(1 - \frac{R_0}{r}\right)\left(\frac{R_0}{r}\right)\sin\theta + f\left(\frac{\Omega R_0}{U}\right)\left(\frac{r}{R_0} - 1\right)\cos\theta \tag{D.30}$$

$$\frac{\partial g}{\partial \phi} = 0 \tag{D.31}$$

Therefore, in a more useful form,

$$\nabla_{sph}\boldsymbol{B}_0 = \begin{bmatrix} -2 & 0 & 0 \\ f'/f & 1 & 0 \\ 0 & 0 & 1 \end{bmatrix}\frac{f}{r} + \begin{bmatrix} 0 & 0 & \frac{2R_0 - r}{r - R_0} \\ 0 & 0 & g'/g \\ -1 & -\cot\theta & 0 \end{bmatrix}\frac{g}{r} \tag{D.32}$$

Using the continuity equation and the constant mean flow, $\rho U r^2 = \rho_0 U_0 R_0^2 \implies \rho = \rho_0\left(R_0/r\right)^2$. The radial component of the mean magnetic field as an Alfvén velocity can be written as

$$V_{Ar} = \frac{1}{\sqrt{4\pi\rho}} B_{0r} = \frac{B_0}{\sqrt{4\pi\rho}} \left(\frac{R_0}{r}\right)^2 \tag{D.33}$$

$$= \frac{B_0}{\sqrt{4\pi\rho_0}} \left(\frac{R_0}{r}\right) \tag{D.34}$$

$$= V_{Ar0} \left(\frac{R_0}{r}\right) \tag{D.35}$$

Likewise, the azimuthal component as an Alfvén speed is

$$V_{A\phi} = \frac{1}{\sqrt{4\pi\rho}} B_{0\phi} = \frac{B_0}{\sqrt{4\pi\rho}} \left(\frac{R_0}{r}\right)^2 \left(\frac{\Omega R_0}{U}\right) \left(\frac{r}{R_0} - 1\right) \sin\theta \tag{D.36}$$

$$= \frac{B_0}{\sqrt{4\pi\rho_0}} \left(\frac{R_0}{r}\right) \left(\frac{\Omega R_0}{U}\right) \left(\frac{r}{R_0} - 1\right) \sin\theta \tag{D.37}$$

$$= V_{Ar0} \left(\frac{\Omega R_0}{U}\right) \left(1 - \frac{R_0}{r}\right) \sin\theta \tag{D.38}$$

The divergence of the Alfvén speed associated with the Parker Spiral is therefore

$$\nabla \cdot \boldsymbol{V}_A = \frac{1}{r^2} \frac{\partial (V_{Ar0}(R_0/r) r^2)}{\partial \mathrm{r}} + \frac{1}{r\sin\theta} \frac{\partial (V_{A\theta} \sin\theta)}{\partial\theta} + \frac{1}{r\sin\theta} \frac{\partial V_{A\phi}}{\partial\phi} = \frac{V_{Ar}}{r} \tag{D.39}$$

D.3 Calculating the Energy Mixing Tensor

The energy mixing tensor is given by $\boldsymbol{\Pi}^{\pm}_{ii}(w)$ evaluated with zero lag $w = 0$,

$$\boldsymbol{\Pi}^{\pm}_{ii}(w=0) \equiv -\nabla_j \left(\frac{\boldsymbol{U}_j}{2} \pm \boldsymbol{V}_{A,j}\right) \boldsymbol{R}^{Ds}_{ii}(w=0) + 2\left(\nabla_i \boldsymbol{U}_j \pm \frac{1}{\sqrt{4\pi\rho}} \nabla_i \boldsymbol{B}_{0,j}\right) \boldsymbol{R}^{Ds}_{ij}(w=0) \tag{D.40}$$

the symmetric energy-difference correlation tensor $\boldsymbol{R}^{Ds}_{ij}(w)$ value at $w = 0$ depends on the symmetries of the fluctuations. We consider two cases: 3D isotropic and 2D isotropic (axisymmetric).

D.3.1 3D Isotropic Turbulence

Assuming the turbulent fluctuations are isotropic in three dimensions, $\boldsymbol{R}^{Ds}_{ij}(0) = \frac{D}{3}\boldsymbol{\delta}_{ij}$, therefore the mixing term is,

$$\boldsymbol{\Pi}^{\pm}_{ii}(0) = -\nabla_j \left(\frac{\boldsymbol{U}_j}{2} \pm \boldsymbol{V}_{A,j}\right) \frac{D}{3}\boldsymbol{\delta}_{ii} + 2\left(\nabla_i \boldsymbol{U}_j \pm \frac{1}{\sqrt{4\pi\rho}} \nabla_i \boldsymbol{B}_{0,j}\right) \frac{D}{3}\boldsymbol{\delta}_{ij} \tag{D.41}$$

Separating out the gradient terms contracted with the delta function, the gradient of the large-scale flow (as calculated in section D.1) contracted with the delta function is

$$\nabla_i \boldsymbol{U}_j \boldsymbol{\delta}_{ij} = \frac{U}{r} Tr\left\{ \begin{bmatrix} 0 & 0 & 0 \\ 0 & 1 & 0 \\ 0 & 0 & 1 \end{bmatrix} \begin{bmatrix} 1 & 0 & 0 \\ 0 & 1 & 0 \\ 0 & 0 & 1 \end{bmatrix} \right\} \overset{\text{trace}}{=} 2\frac{U}{r} \tag{D.42}$$

and the trace of the gradient of the background magnetic field (calculated in section D.2) times the delta function is zero,

$$\begin{aligned} &\frac{1}{\sqrt{4\pi\rho}} \nabla_i \boldsymbol{B}_{0,j} \boldsymbol{\delta}_{ij} \\ = Tr&\left\{ \left(\begin{bmatrix} -2 & 0 & 0 \\ V'_{Ar}/V_{Ar} & 1 & 0 \\ 0 & 0 & 1 \end{bmatrix} \frac{V_{Ar}}{r} + \begin{bmatrix} 0 & 0 & \frac{2R_0 - r}{r - R_0} \\ 0 & 0 & V'_{A\phi}/V_{A\phi} \\ -1 & -\cot\theta & 0 \end{bmatrix} \frac{V_{A\phi}}{r} \right) \begin{bmatrix} 1 & 0 & 0 \\ 0 & 1 & 0 \\ 0 & 0 & 1 \end{bmatrix} \right\} \\ &\overset{\text{trace}}{=} 0 \end{aligned} \tag{D.43}$$

The divergence terms are

$$-\nabla_j \left(\frac{\boldsymbol{U}_j}{2} \pm \boldsymbol{V}_{A,j} \right) \frac{D}{3} \boldsymbol{\delta}_{ii} = -\frac{1}{r} \left(U \pm V_{Ar} \right) D \tag{D.44}$$

We can now write down the three dimensional isotropic mixing tensor $M^{\pm}_{3D}$,

$$\boldsymbol{\Pi}^{\pm}_{ii}(0) \overset{\text{trace}}{=} -\frac{1}{r} \left(U \pm V_{Ar} \right) D + \frac{4}{3} \frac{U}{r} D \tag{D.45}$$

$$= \frac{1}{r} \left(\frac{U}{3} \mp V_{Ar} \right) D = M^{\pm}_{3D} D \tag{D.46}$$

D.3.2 2D Isotropic Turbulence

Assuming the turbulent fluctuations are isotropic in a two dimensional plane that is normal to the large-scale background magnetic field $\boldsymbol{B}_0$, the energy difference correlation tensor is $\boldsymbol{R}^{Ds}_{ij}(0) = \frac{D}{2} \left(\boldsymbol{\delta}_{ij} - \hat{\boldsymbol{B}}_{0,i} \hat{\boldsymbol{B}}_{0,j} \right)$ (Appendix C). Here we assume that the $\hat{\boldsymbol{x}}$-axis is aligned on the background magnetic field, $\hat{\boldsymbol{B}}_0 \parallel \hat{\boldsymbol{x}}$, and the radial direction is in the $(\hat{\boldsymbol{x}}, \hat{\boldsymbol{z}})$ plane; the turbulence fluctuations are perpendicular to $\hat{\boldsymbol{B}}_0$ (Figure D.1). Since the gradients of the

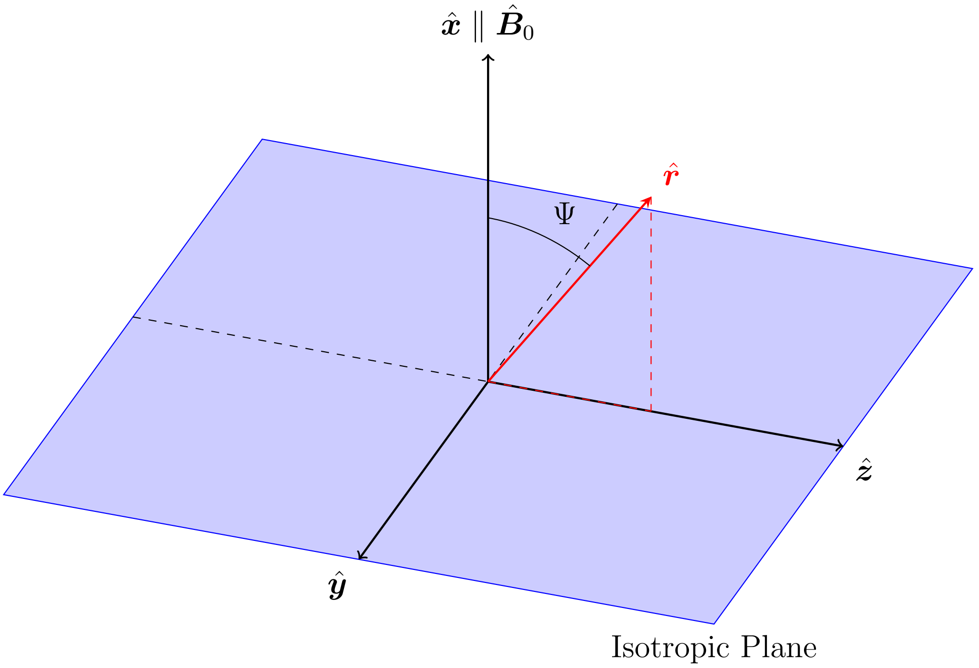

Figure D.1: Two dimensional isotropic (axisymmetric) turbulence where the Cartesian coordinate system $(\hat{\boldsymbol{x}}, \hat{\boldsymbol{y}}, \hat{\boldsymbol{z}})$ is chosen, such that the radial and magnetic field plane (r, B_0) lie in the $(\hat{\boldsymbol{x}}, \hat{\boldsymbol{z}})$ plane, with the $\hat{\boldsymbol{x}}$-axis aligning with the background magnetic field (the field-aligned coordinate system).

large-scale magnetic field and the mean velocity are easily expressed in spherical polar coordinates, we need to map from a field-aligned coordinate system $(\hat{\boldsymbol{x}}, \hat{\boldsymbol{y}}, \hat{\boldsymbol{z}})$ to a radially aligned coordinate system $(\hat{\boldsymbol{x}}', \hat{\boldsymbol{y}}', \hat{\boldsymbol{z}}')$ locally aligned with $(\hat{\boldsymbol{r}}, \hat{\boldsymbol{\theta}}, \hat{\boldsymbol{\phi}})$. This mapping is given by applying a rotation about the $\hat{\boldsymbol{y}}$-axis $\boldsymbol{\Theta}_y$ *clockwise* by the winding angle Ψ between the mean magnetic field $\hat{\boldsymbol{B}}_0$ and the radial direction $\hat{\boldsymbol{r}}$ (Figure D.2)

$$\hat{\boldsymbol{B}}_0' = \boldsymbol{\Theta}_y(\Psi)\hat{\boldsymbol{B}}_0 = \cos\Psi\hat{\boldsymbol{r}} - \sin\Psi\hat{\boldsymbol{\phi}} \tag{D.47}$$

Please note, the winding angle Ψ must be the negative of the angle between $\hat{\boldsymbol{B}}_0$ and $\hat{\boldsymbol{r}}$ as the correct rotation direction about the $\hat{\boldsymbol{y}}$-axis is clockwise. Therefore, $\Psi = -\cos^{-1}\left(\hat{\boldsymbol{B}}_0 \cdot \hat{\boldsymbol{r}}\right)$. Now, the energy difference correlation tensor is $\boldsymbol{R}_{ij}^{Ds}(0) = \frac{D}{2}\left(\boldsymbol{\delta}_{ij} - \hat{\boldsymbol{B}}_{0,i}'\hat{\boldsymbol{B}}_{0,j}'\right)$ leading to the following mixing tensor

$$\begin{aligned}\boldsymbol{\Pi}_{ii}^{\pm}(0) = &-\nabla_j\left(\frac{\boldsymbol{U}_j}{2} \pm \boldsymbol{V}_{A,j}\right)\frac{D}{2}\left(\boldsymbol{\delta}_{ii} - \hat{\boldsymbol{B}}_{0,i}'\hat{\boldsymbol{B}}_{0,i}'\right)\\ &+2\left(\nabla_i\boldsymbol{U}_j \pm \frac{1}{\sqrt{4\pi\rho}}\nabla_i\boldsymbol{B}_{0,j}\right)\frac{D}{2}\left(\boldsymbol{\delta}_{ij} - \hat{\boldsymbol{B}}_{0,i}'\hat{\boldsymbol{B}}_{0,j}'\right)\end{aligned} \tag{D.48}$$

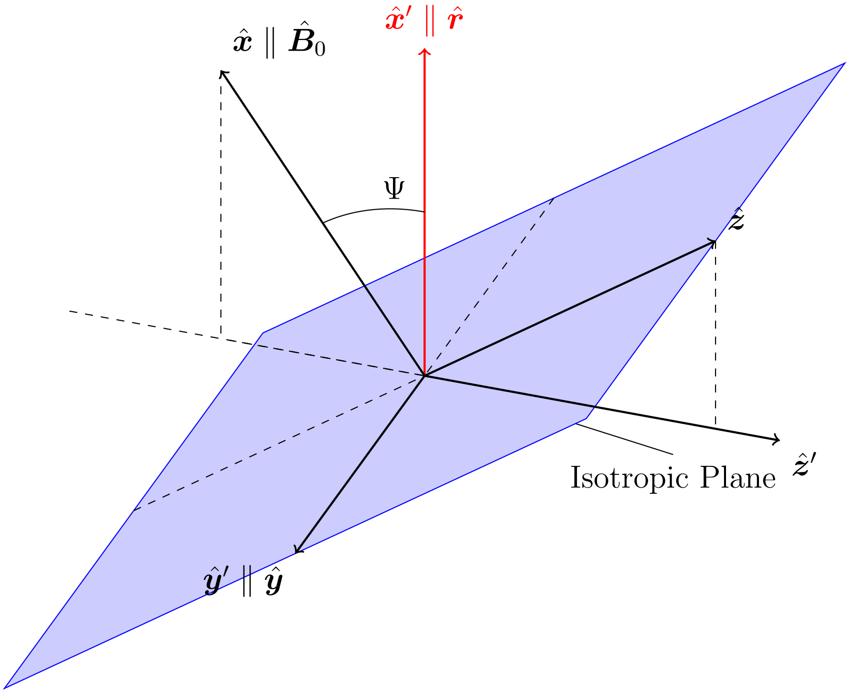

Figure D.2: Two dimensional isotropic (axisymmetric) turbulence where the Cartesian coordinate system $(\hat{\boldsymbol{x}}, \hat{\boldsymbol{y}}, \hat{\boldsymbol{z}})$ is chosen, such that the radial and magnetic field plane (r, B_0) lie in the $(\hat{\boldsymbol{x}}, \hat{\boldsymbol{z}})$ plane. The Cartesian coordinate system is rotated about the $\hat{\boldsymbol{y}}$-axis by the winding angle Ψ (clockwise) to obtain a new radially aligned coordinate system $(\hat{\boldsymbol{x}}', \hat{\boldsymbol{y}}', \hat{\boldsymbol{z}}')$ such that the $\hat{\boldsymbol{x}}'$-axis aligns with the radial direction $\hat{\boldsymbol{r}}$.

The divergence terms are the same as the 3D isotropic turbulence case

$$-\nabla_i \left(\frac{\boldsymbol{U}_i}{2} \pm \boldsymbol{V}_{A,i} \right) \frac{D}{2} \left(\boldsymbol{\delta}_{ii} - \hat{\boldsymbol{B}}'_{0,i} \hat{\boldsymbol{B}}'_{0,i} \right) = -\frac{1}{r} \left(U \pm V_{Ar} \right) D \tag{D.49}$$

the term with the gradient of the mean flow is

$$\nabla_i \boldsymbol{U}_j (\boldsymbol{\delta}_{ij} - \hat{\boldsymbol{B}}'_{0,i} \hat{\boldsymbol{B}}'_{0,j}) D = \frac{U}{r} Tr \left\{ \begin{bmatrix} 0 & 0 & 0 \\ 0 & 1 & 0 \\ 0 & 0 & 1 \end{bmatrix} \begin{bmatrix} 1 - \cos^2 \Psi & 0 & \sin \Psi \cos \Psi \\ 0 & 1 & 0 \\ \sin \Psi \cos \Psi & 0 & 1 - \sin^2 \Psi \end{bmatrix} \right\} D \tag{D.50}$$

$$= \frac{U}{r} Tr \left\{ \begin{bmatrix} 0 & 0 & 0 \\ 0 & 1 & 0 \\ 0 & 0 & 1 - \sin^2 \Psi \end{bmatrix} \right\} D \tag{D.51}$$

$$\overset{\text{trace}}{=} \frac{U}{r} \left(1 + 1 - \sin^2 \Psi \right) D = \frac{U}{r} \left(1 + \cos^2 \Psi \right) D \tag{D.52}$$

and the term with the gradient of the mean magnetic field is

$$
\begin{aligned}
&\frac{1}{\sqrt{4\pi\rho}}\nabla_i \boldsymbol{B}_{0,j}\left(\boldsymbol{\delta}_{ij} - \hat{\boldsymbol{B}}'_{0,i}\hat{\boldsymbol{B}}'_{0,j}\right) D \qquad \text{(D.53)} \\
&= Tr\Bigg\{\left(\begin{bmatrix} -2 & 0 & 0 \\ V'_{Ar}/V_{Ar} & 1 & 0 \\ 0 & 0 & 1 \end{bmatrix}\frac{V_{Ar}}{r} + \begin{bmatrix} 0 & 0 & \frac{2R_0-r}{r-R_0} \\ 0 & 0 & V'_{A\phi}/V_{A\phi} \\ -1 & -\cot\theta & 0 \end{bmatrix}\frac{V_{A\phi}}{r}\right) \\
&\quad \times \begin{bmatrix} 1-\cos^2\Psi & 0 & \sin\Psi\cos\Psi \\ 0 & 1 & 0 \\ \sin\Psi\cos\Psi & 0 & 1-\sin^2\Psi \end{bmatrix} D\Bigg\} \qquad \text{(D.54)} \\
&= Tr\Bigg\{\begin{bmatrix} -2\left(1-\cos^2\Psi\right) & 0 & -2\sin\Psi\cos\Psi \\ \frac{V'_{Ar}}{V_{Ar}}\left(1-\cos^2\Psi\right) & 1 & \frac{V'_{Ar}}{V_{Ar}}\sin\Psi\cos\Psi \\ \sin\Psi\cos\Psi & 0 & 1-\sin^2\Psi \end{bmatrix}\frac{V_{Ar}}{r}D \\
&+ \begin{bmatrix} \frac{2R_0-r}{r-R_0}\sin\Psi\cos\Psi & 0 & \frac{2R_0-r}{r-R_0}\left(1-\sin^2\Psi\right) \\ V'_{A\phi}/V_{A\phi}\sin\Psi\cos\Psi & 0 & V'_{A\phi}/V_{A\phi}\left(1-\sin^2\Psi\right) \\ -\left(1-\cos^2\Psi\right) & -\cot\theta & -\sin\Psi\cos\Psi \end{bmatrix}\frac{V_{A\phi}}{r}D\Bigg\} \qquad \text{(D.55)} \\
&\overset{\text{trace}}{=} \left(-2\left(1-\cos^2\Psi\right) + 1 + \left(1-\sin^2\Psi\right)\right)\frac{V_{Ar}}{r}D \\
&\quad + \left(\frac{2R_0-r}{r-R_0}\sin\Psi\cos\Psi - \sin\Psi\cos\Psi\right)\frac{V_{A\phi}}{r}D \qquad \text{(D.56)} \\
&= \frac{1}{r}\left(V_{Ar}\left(3\cos^2\Psi - 1\right) + V_{Ar0}\left(\frac{\Omega R_0}{U}\right)\left(1-\frac{3R_0}{2r}\right)\sin\theta\sin 2\Psi\right) D \qquad \text{(D.57)}
\end{aligned}
$$

putting all the pieces together, we get the two dimensional mixing tensor $M_{2D}^{\pm}$

$$
\boldsymbol{\Pi}_{ii}^{\pm}(0) \overset{\text{trace}}{=} \frac{1}{r}\left(U\cos^2\Psi \pm V_{Ar}\left(3\cos^2\Psi - 2\right) \pm V_{Ar0}\left(\frac{\Omega R_0}{U}\right)\left(1-\frac{3R_0}{2r}\right)\sin\theta\sin 2\Psi\right) D \qquad \text{(D.58)}
$$

$$
= M_{2D}^{\pm} D \qquad \text{(D.59)}
$$

D.4 Calculation of the Correlation Integral Mixing Tensor

To construct the mixing terms for the correlation integral equations, we need to integrate $\boldsymbol{\Pi}^{\pm}$ and $\boldsymbol{\Sigma}^{\pm}$. Due to this integration step, there is a choice that needs to be made for the integration direction as we are integrating with respect to the lag/separation w in the correlation tensors. After integration, we can follow steps similar to the calculation of the energy mixing tensors where the integration of the correlation tensor is proportional to $\boldsymbol{\delta}_{ij} + \hat{\boldsymbol{w}}_i\hat{\boldsymbol{w}}_j$ for 3D isotropic turbulence and $\hat{\boldsymbol{w}}_i\hat{\boldsymbol{w}}_j$ for 2D isotropic turbulence (Appendix C). The mixing term for the $L_\pm$ equations is the following

$$\boldsymbol{\Pi}^{\pm}_{ii}(w) \equiv -\nabla_j \left(\frac{\boldsymbol{U}_j}{2} \pm \boldsymbol{V}_{A,j}\right) \boldsymbol{R}^{Ds}_{ii}(w) + 2\left(\nabla_i \boldsymbol{U}_j \pm \frac{1}{\sqrt{4\pi\rho}}\nabla_i \boldsymbol{B}_{0,j}\right) \boldsymbol{R}^{Ds}_{ij}(w) \tag{D.60}$$

and the mixing term for the energy difference correlation equation is the following

$$\boldsymbol{\Sigma}^{\pm}_{ii}(w) = -\nabla_j \left(\frac{\boldsymbol{U}_j}{2} \mp \boldsymbol{V}_{A,j}\right) \boldsymbol{H}^{\pm}_{ii}(w) + 2\left(\nabla_i \boldsymbol{U}_j \mp \frac{1}{\sqrt{4\pi\rho}}\nabla_i \boldsymbol{B}_{0,j}\right) \boldsymbol{H}^{\pm}_{ij}(w) \tag{D.61}$$

D.4.1 3D Isotropic Turbulence

Assuming three-dimensional isotropic turbulence, the integrals of the correlation tensors can be written as

$$\int_0^\infty \boldsymbol{R}^{Ds}_{ij}(w)\mathrm{d}w = \frac{L_D}{4}\left(\boldsymbol{\delta}_{ij} + \hat{\boldsymbol{w}}_i\hat{\boldsymbol{w}}_j\right) \tag{D.62}$$

$$\int_0^\infty \boldsymbol{H}^{\pm}_{ij}(w)\mathrm{d}w = \frac{L_\pm}{4}\left(\boldsymbol{\delta}_{ij} + \hat{\boldsymbol{w}}_i\hat{\boldsymbol{w}}_j\right) \tag{D.63}$$

Calculating the divergence term for $\int_0^\infty \boldsymbol{\Pi}^{\pm}_{ii}(w)\mathrm{d}w$ is the following

$$-\nabla_i \left(\frac{\boldsymbol{U}_i}{2} \pm \boldsymbol{V}_{A,i}\right) \int_0^\infty \boldsymbol{R}^{Ds}_{ii}(w)\mathrm{d}w = -\frac{1}{r}\left(U \pm V_{Ar}\right)\frac{L_D}{4}\left(\boldsymbol{\delta}_{ii} + \hat{\boldsymbol{w}}_i\hat{\boldsymbol{w}}_i\right) \tag{D.64}$$

$$\overset{\text{trace}}{=} -\frac{L_D}{r}\left(U \pm V_{Ar}\right) \tag{D.65}$$

Likewise, the divergence term for $\int_0^\infty \boldsymbol{\Sigma}^{\pm}_{ii}(w)\mathrm{d}w$ is the following

$$-\nabla_j \left(\frac{\boldsymbol{U}_j}{2} \mp \boldsymbol{V}_{A,j}\right) \int_0^\infty \boldsymbol{H}^{\pm}_{ii}(w)\mathrm{d}w = -\frac{1}{r}\left(U \mp V_{Ar}\right)\frac{L_\pm}{4}\left(\boldsymbol{\delta}_{ii} + \hat{\boldsymbol{w}}_i\hat{\boldsymbol{w}}_i\right) \tag{D.66}$$

$$\overset{\text{trace}}{=} -\frac{L_\pm}{r}\left(U \mp V_{Ar}\right) \tag{D.67}$$

Calculating the gradient terms is more difficult as we need to choose the integration directions. There are two main choices for 3D isotropic turbulence, the first is choosing the integration unit vector $\hat{\boldsymbol{w}}$ to be along the radial direction $\hat{\boldsymbol{w}} = \hat{\boldsymbol{r}}$. The other choice is for the integration unit vector to be normal to the radial direction $\hat{\boldsymbol{w}} \cdot \hat{\boldsymbol{r}} = 0$. We will be primarily focusing on integrating with lag in the radial direction $\hat{\boldsymbol{w}} = \hat{\boldsymbol{r}} = \begin{bmatrix} 1 & 0 & 0 \end{bmatrix}$ (section 2.2). We find that the mean velocity gradient term for $\int_0^\infty \boldsymbol{\Pi}_{ii}(w)\mathrm{d}w$ cancels out with the divergence term and evaluates as the following

$$2\nabla_i \boldsymbol{U}_j \int_0^\infty \boldsymbol{R}_{ij}^{Ds}(w)\mathrm{d}w = 2\frac{U}{r} Tr\left\{ \begin{bmatrix} 0 & 0 & 0 \\ 0 & 1 & 0 \\ 0 & 0 & 1 \end{bmatrix} \frac{L_D}{4} \left(\boldsymbol{\delta}_{ij} + \hat{\boldsymbol{w}}_i \hat{\boldsymbol{w}}_j \right) \right\} \tag{D.68}$$

$$= \frac{U}{r}\frac{L_D}{2} Tr\left\{ \begin{bmatrix} 0 & 0 & 0 \\ 0 & 1 & 0 \\ 0 & 0 & 1 \end{bmatrix} \begin{bmatrix} 2 & 0 & 0 \\ 0 & 1 & 0 \\ 0 & 0 & 1 \end{bmatrix} \right\} \tag{D.69}$$

$$= \frac{U}{r}\frac{L_D}{2} Tr\left\{ \begin{bmatrix} 0 & 0 & 0 \\ 0 & 1 & 0 \\ 0 & 0 & 1 \end{bmatrix} \right\} \tag{D.70}$$

$$\overset{\text{trace}}{=} \frac{L_D}{r} U \tag{D.71}$$

Similarly, for $\int_0^\infty \boldsymbol{\Sigma}_{ii}^{\pm}(w)\mathrm{d}w$

$$2\nabla_i \boldsymbol{U}_j \int_0^\infty \boldsymbol{H}_{ij}^{\pm}(w)\mathrm{d}w \overset{\text{trace}}{=} \frac{L_{\pm}}{r} U \tag{D.72}$$

Now, calculating the mean magnetic field term for $\int_0^\infty \mathbf{\Pi}_{ii}(w)\mathrm{d}w$

$$2\frac{1}{\sqrt{4\pi\rho}}\nabla_i \boldsymbol{B}_{0,j}\int_0^\infty \boldsymbol{R}_{ij}^{Ds}\mathrm{d}w \tag{D.73}$$

$$= \frac{L_D}{2}Tr\Bigg\{\left(\begin{bmatrix} -2 & 0 & 0 \\ V'_{Ar}/V_{Ar} & 1 & 0 \\ 0 & 0 & 1 \end{bmatrix}\frac{V_{Ar}}{r} + \begin{bmatrix} 0 & 0 & \frac{2R_0-r}{r-R_0} \\ 0 & 0 & V'_{A\phi}/V_{A\phi} \\ -1 & -\cot\theta & 0 \end{bmatrix}\frac{V_{A\phi}}{r}\right)\begin{bmatrix} 2 & 0 & 0 \\ 0 & 1 & 0 \\ 0 & 0 & 1 \end{bmatrix}\Bigg\} \tag{D.74}$$

$$= \frac{L_D}{2}Tr\Bigg\{\left(\begin{bmatrix} -4 & 0 & 0 \\ 2V'_{Ar}/V_{Ar} & 1 & 0 \\ 0 & 0 & 1 \end{bmatrix}\frac{V_{Ar}}{r} + \begin{bmatrix} 0 & 0 & \frac{2R_0-r}{r-R_0} \\ 0 & 0 & V'_{A\phi}/V_{A\phi} \\ -2 & -\cot\theta & 0 \end{bmatrix}\frac{V_{A\phi}}{r}\right)\Bigg\} \tag{D.75}$$

$$\overset{\text{trace}}{=} -\frac{L_D}{r}V_{Ar} \tag{D.76}$$

and there is no difference for the $\int_0^\infty \mathbf{\Sigma}_{ii}^{\pm}(w)\mathrm{d}w$

$$2\frac{1}{\sqrt{4\pi\rho}}\nabla_i \boldsymbol{B}_{0,j}\int_0^\infty \boldsymbol{H}_{ij}^{\pm}\mathrm{d}w \overset{\text{trace}}{=} -\frac{L_\pm}{r}V_{Ar} \tag{D.77}$$

Therefore, the correlation integral $L_\pm$ mixing tensor evaluated in the radial direction and assuming three dimensional isotropic turbulence is

$$\int_0^\infty \mathbf{\Pi}_{ii}^{\pm}\mathrm{d}w = -\frac{L_D}{r}\left(U \pm V_{Ar}\right) + \frac{L_D}{r}\left(U \mp V_{Ar}\right) = \mp 2\frac{L_D}{r}V_{Ar} \tag{D.78}$$

and the correlation integral L_D mixing tensor is

$$\int_0^\infty \mathbf{\Sigma}_{ii}^{\pm}\mathrm{d}w = -\frac{L_\pm}{r}\left(U \mp V_{Ar}\right) + \frac{L_\pm}{r}\left(U \pm V_{Ar}\right) = \pm 2\frac{L_\pm}{r}V_{Ar} \tag{D.79}$$

D.4.2 2D Isotropic Turbulence

Assuming the turbulent fluctuations are isotropic in two dimensions, the integrals of the correlation tensors can be written as the following

$$\int_0^\infty \boldsymbol{R}_{ij}^{Ds}(w)\mathrm{d}w = L_D\hat{\boldsymbol{w}}_i\hat{\boldsymbol{w}}_j \tag{D.80}$$

$$\int_0^\infty \boldsymbol{H}_{ij}^{\pm}(w)\mathrm{d}w = L_\pm\hat{\boldsymbol{w}}_i\hat{\boldsymbol{w}}_j \tag{D.81}$$

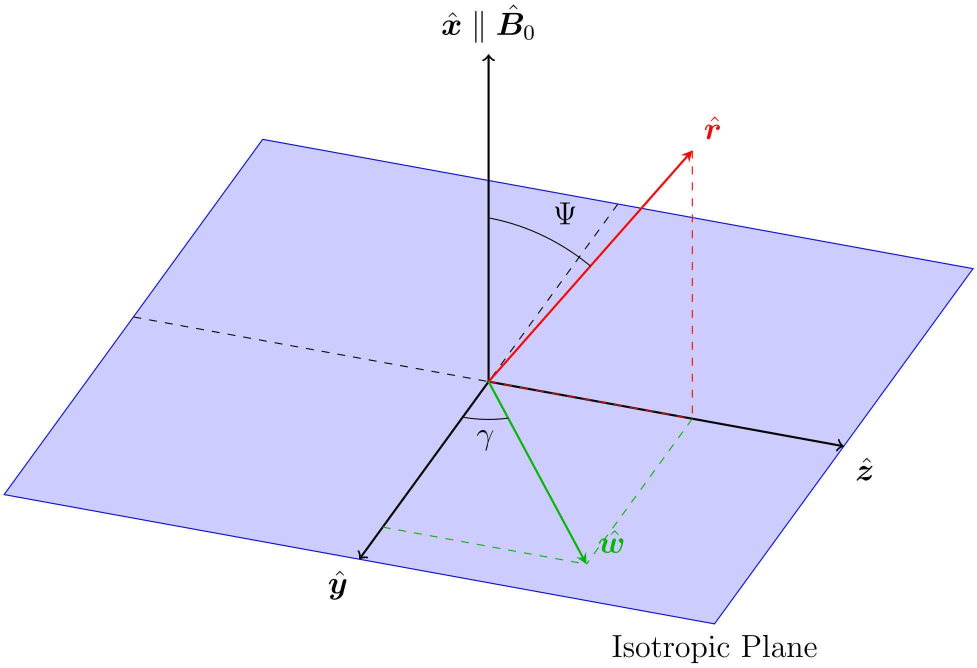

Figure D.3: Two dimensional isotropic (axisymmetric) turbulence where the Cartesian coordinate system $(\hat{\boldsymbol{x}}, \hat{\boldsymbol{y}}, \hat{\boldsymbol{z}})$ is chosen, such that the radial and magnetic field plane (r, B_0) lie in the $(\hat{\boldsymbol{x}}, \hat{\boldsymbol{z}})$ plane, with the $\hat{\boldsymbol{x}}$-axis aligning with the background magnetic field (the field-aligned coordinate system). Additionally plotted is the integration vector or the separation vector $\hat{\boldsymbol{w}}$ which lies arbitrarily in the isotropic plane.

The integration direction $\hat{\boldsymbol{w}}$ is in the turbulent plane at an angle γ to the $\hat{\boldsymbol{y}}$ axis (Figure D.3). In general

$$\hat{\boldsymbol{w}} = \cos\gamma\hat{\boldsymbol{y}} + \sin\gamma\hat{\boldsymbol{z}} \tag{D.82}$$

Once again, we have a choice to make with the direction of integration $\hat{\boldsymbol{w}}$, which corresponds to a choice of the angle γ, we can either choose the unit vector to be in the radial-magnetic field plane (r, B_0) or we can let $\hat{\boldsymbol{w}}$ be normal to both the radial $\hat{\boldsymbol{r}}$ and magnetic field $\hat{\boldsymbol{B}}_0$ directions. We will be focusing on integration in the (r, B_0) plane (section 2.2). Similar to subsection D.3.2 we will fix the $\hat{\boldsymbol{x}}$-axis onto the magnetic field $\hat{\boldsymbol{B}}_0 = \hat{\boldsymbol{x}}$ and the radial direction $\hat{\boldsymbol{r}}$ into the $(\hat{\boldsymbol{x}}, \hat{\boldsymbol{z}})$ plane. Integrating in the (r, B_0) plane corresponds to choosing $\gamma = 90°$, in other words $\hat{\boldsymbol{w}} = \hat{\boldsymbol{z}}$. We will need to applying a rotation about the $\hat{\boldsymbol{y}}$-axis by the winding angle Ψ to get the integration vector $\hat{\boldsymbol{w}}$ in the radially-aligned coordinate system

$$\hat{\boldsymbol{w}}' = \Omega_y(\Psi)\hat{\boldsymbol{w}} = \sin\Psi\sin\gamma\hat{\boldsymbol{r}} + \cos\gamma\hat{\boldsymbol{\theta}} + \cos\Psi\sin\gamma\hat{\boldsymbol{\phi}} \tag{D.83}$$

so, with $\gamma = 90°$, $\hat{\boldsymbol{w}}' = \sin\Psi\hat{\boldsymbol{r}} + \cos\Psi\hat{\boldsymbol{\phi}}$. We can now move onto solving the gradient terms. But first, the divergence terms are straightforward to work out

$$-\nabla_j\left(\frac{\boldsymbol{U}_j}{2} \pm \boldsymbol{V}_{A,j}\right)\int_0^\infty \boldsymbol{R}_{ii}^{Ds}(w)\mathrm{d}w = -\frac{1}{r}\left(U \pm V_{Ar}\right)L_D\hat{\boldsymbol{w}}_i'\hat{\boldsymbol{w}}_i' \overset{\text{trace}}{=} -\frac{L_D}{r}\left(U \pm V_{Ar}\right) \tag{D.84}$$

$$-\nabla_j\left(\frac{\boldsymbol{U}_j}{2} \mp \boldsymbol{V}_{A,j}\right)\int_0^\infty \boldsymbol{H}_{ii}^{\pm}(w)\mathrm{d}w = -\frac{1}{r}\left(U \mp V_{Ar}\right)L_\pm\hat{\boldsymbol{w}}_i'\hat{\boldsymbol{w}}_i' \overset{\text{trace}}{=} -\frac{L_\pm}{r}\left(U \mp V_{Ar}\right) \tag{D.85}$$

The mean flow gradient terms are the following

$$2\nabla_i \boldsymbol{U}_j \int_0^\infty \boldsymbol{R}_{ij}^{Ds}(w)\mathrm{d}w = 2\frac{U}{r}Tr\Bigg\{ \begin{bmatrix} 0 & 0 & 0 \\ 0 & 1 & 0 \\ 0 & 0 & 1 \end{bmatrix} L_D \hat{\boldsymbol{w}}_i' \hat{\boldsymbol{w}}_j' \Bigg\} \tag{D.86}$$

$$= 2L_D\frac{U}{r}Tr\Bigg\{ \begin{bmatrix} 0 & 0 & 0 \\ 0 & 1 & 0 \\ 0 & 0 & 1 \end{bmatrix} \begin{bmatrix} \sin^2\Psi & 0 & \sin\Psi\cos\Psi \\ 0 & 0 & 0 \\ \sin\Psi\cos\Psi & 0 & \cos^2\Psi \end{bmatrix} \Bigg\} \tag{D.87}$$

$$\overset{\text{trace}}{=} 2L_D\frac{U}{r}\cos^2\Psi \tag{D.88}$$

$$2\nabla_i \boldsymbol{U}_j \int_0^\infty \boldsymbol{H}_{ij}^{\pm}(w)\mathrm{d}w \overset{\text{trace}}{=} 2L_{\pm}\frac{U}{r}\cos^2\Psi \tag{D.89}$$

and the mean magnetic field gradient terms are the following

$$2\frac{1}{\sqrt{4\pi\rho}}\nabla_i \boldsymbol{B}_{0,j} \int_0^\infty \boldsymbol{R}_{ij}^{Ds}\mathrm{d}w \tag{D.90}$$

$$= 2L_D Tr\Bigg\{ \left(\begin{bmatrix} -2 & 0 & 0 \\ V_{Ar}'/V_{Ar} & 1 & 0 \\ 0 & 0 & 1 \end{bmatrix} \frac{V_{Ar}}{r} + \begin{bmatrix} 0 & 0 & \frac{2R_0-r}{r-R_0} \\ 0 & 0 & V_{A\phi}'/V_{A\phi} \\ -1 & -\cot\theta & 0 \end{bmatrix} \frac{V_{A\phi}}{r} \right)$$

$$\times \begin{bmatrix} \sin^2\Psi & 0 & \sin\Psi\cos\Psi \\ 0 & 0 & 0 \\ \sin\Psi\cos\Psi & 0 & \cos^2\Psi \end{bmatrix} \Bigg\} \tag{D.91}$$

$$\overset{\text{trace}}{=} 2\frac{L_D}{r}\left(V_{Ar}\left(-2\sin^2\Psi + \cos^2\Psi\right) + V_{A\phi}\left(\frac{2R_0 - r}{r - R_0}\sin\Psi\cos\Psi - \sin\Psi\cos\Psi \right) \right) \tag{D.92}$$

$$= 2\frac{L_D}{r}\left(V_{Ar}\left(3\cos^2\Psi - 2\right) + V_{Ar0}\left(\frac{\Omega R_0}{U}\right)\left(\frac{3R_0}{2r} - 1\right)\sin\theta\sin 2\Psi \right) \tag{D.93}$$

$$2\frac{1}{\sqrt{4\pi\rho}}\nabla_i \boldsymbol{B}_{0,j} \int_0^\infty \boldsymbol{H}_{ij}^{\pm}\mathrm{d}w$$

$$= 2\frac{L_\pm}{r}\left(V_{Ar}\left(3\cos^2\Psi - 2\right) + V_{Ar0}\left(\frac{\Omega R_0}{U}\right)\left(\frac{3R_0}{2r} - 1\right)\sin\theta\sin 2\Psi \right) \tag{D.94}$$

Therefore, the mixing terms result in

$$\int_0^\infty \mathbf{\Pi}_{ii}^{\pm}(w)\mathrm{d}w = -\frac{L_D}{r}\left(U \pm V_{Ar}\right) + 2U\frac{L_D}{r}\cos^2\Psi$$
$$\pm 2\frac{L_D}{r}\left(V_{Ar}\left(3\cos^2\Psi - 2\right) + V_{Ar0}\left(\frac{\Omega R_0}{U}\right)\left(\frac{3R_0}{2r} - 1\right)\sin\theta\sin 2\Psi\right) \tag{D.95}$$
$$= \frac{1}{r}\left(U\left(2\cos^2\Psi - 1\right) \pm V_{Ar}\left(6\cos^2\Psi - 5\right) \pm V_{Ar0}\left(\frac{\Omega R_0}{U}\right)\left(\frac{3R_0}{2r} - 1\right)\sin\theta\sin 2\Psi\right) L_D \tag{D.96}$$

$$\int_0^\infty \mathbf{\Sigma}_{ii}^{\pm}(w)\mathrm{d}w$$
$$= \frac{1}{r}\left(U\left(2\cos^2\Psi - 1\right) \mp V_{Ar}\left(6\cos^2\Psi - 5\right) \mp V_{Ar0}\left(\frac{\Omega R_0}{U}\right)\left(\frac{3R_0}{2r} - 1\right)\sin\theta\sin 2\Psi\right) L_\pm \tag{D.97}$$

Lastly, the term involving the dot product between the integration direction $\hat{\boldsymbol{w}}$ and the large scale Alfvén field $\boldsymbol{V}_A$ is zero due to the integration direction being perpendicular to the magnetic field.

$$-2D\boldsymbol{w}\cdot\boldsymbol{V}_A = 0 \tag{D.98}$$

D.5 Steady State System of Equations

One may suppose that the energies $Z_\pm^2, D$ and the correlation lengths $L_\pm, L_D$ do not evolve over time (*i.e.,* steady state) and only evolve over radial distance (we are ignoring the θ and ϕ dependence in $Z_\pm^2, D, L_\pm$, and L_D). Also, assuming two dimensional isotropic turbulence the following is the coupled system of six equations describing the radial transport of turbulence

$$\frac{\mathrm{d}Z_\pm^2}{\mathrm{d}r} = -\frac{U \pm V_{Ar}}{U \mp V_{Ar}}\frac{Z_\pm^2}{r} - \frac{1}{U \mp V_{Ar}}M^\pm D + \frac{1}{U \mp V_{Ar}}N_\pm + \frac{1}{U \mp V_{Ar}}S_\pm \tag{D.99}$$
$$\frac{\mathrm{d}D}{\mathrm{d}r} = -\frac{D}{r} - \frac{1}{2}\frac{1}{U}\left(M^+Z_-^2 + M^-Z_+^2\right) + \frac{1}{U}N_D + \frac{1}{U}S_D \tag{D.100}$$
$$\frac{\mathrm{d}L_\pm}{\mathrm{d}r} = -\frac{U \pm V_{Ar}}{U \mp V_{Ar}}\frac{L_\pm}{r} - \frac{1}{U \mp V_{Ar}}M_L^\pm L_D + \frac{1}{U \mp V_{Ar}}N_\pm^L + \frac{1}{U \mp V_{Ar}}S_\pm^L \tag{D.101}$$
$$\frac{\mathrm{d}L_D}{\mathrm{d}r} = -\frac{L_D}{r} - \frac{1}{2U}\left(M_L^-L_+ + M_L^+L_-\right) + \frac{1}{U}N_D^L + \frac{1}{U}S_D^L \tag{D.102}$$

where the 2 dimensional mixing terms are

$$M_{2D}^{\pm} = \frac{1}{r}\left[U\cos^2\Psi \pm V_{Ar}\left(3\cos^2\Psi - 2\right) \pm V_{Ar0}\left(\frac{\Omega R_0}{U}\right)\left(1 - \frac{3R_0}{2r}\right)\sin\theta\sin 2\Psi\right] \tag{D.103}$$

$$M_{2D,L}^{\pm} = \frac{1}{r}\left[U\left(2\cos^2\Psi - 1\right) \pm V_{Ar}\left(6\cos^2\Psi - 5\right) \pm V_{Ar0}\left(\frac{\Omega R_0}{U}\right)\left(\frac{3R_0}{2r} - 1\right)\sin\theta\sin 2\Psi\right] \tag{D.104}$$

and the 3 dimensional mixing terms are

$$M_{3D}^{\pm} = \frac{1}{r}\left(\frac{U}{3} \mp V_{Ar}\right) \tag{D.105}$$

$$M_{3D,L}^{\pm} = \mp 2\frac{V_{Ar}}{r} \tag{D.106}$$

Appendix E

Other Models

It is useful to compare results from our six-equation models to earlier results. Here we summarise two such models and solve their equations through our equation solver to reproduce their results.

E.1 Adhikari Model

Using a structural similarity assumption with the Cauchy-Scharz inequality, a different six equation model for the evolution of solar wind has been proposed by Zank et al. [64]. Adhikari et al. [1, 4] takes the system of equations introducted by Zank et al. and makes the following assumptions. The first is setting $a = \frac{1}{2}$, $b = \frac{1}{2}$ to attempt to retain two dimensional turbulence, the second assumption assumes the equivalent of the gradient mixing term is zero $\Gamma = \hat{\boldsymbol{w}}\hat{\boldsymbol{w}}\left(\nabla \boldsymbol{U} \pm \frac{1}{\sqrt{4\pi\rho}}\nabla \boldsymbol{B}_0\right) = 0$ which produces the following system of equations in steady state

$$(U \mp V_{Ar})\frac{\mathrm{d}Z_\pm^2}{\mathrm{d}r} + (U \pm V_{Ar})\,\frac{Z_\pm^2}{r} + (U \mp V_{Ar})\,\frac{D}{r} = N^\pm + S^\pm \tag{E.1}$$

$$\begin{aligned} &U\frac{\mathrm{d}D}{\mathrm{d}r} + U\frac{D}{r} + \frac{1}{2}V_{Ar}\frac{1}{Z_+Z_-}\left(Z_+^2\frac{\mathrm{d}Z_-^2}{\mathrm{d}r} + Z_-^2\frac{\mathrm{d}Z_+^2}{\mathrm{d}r}\right) \\ &+\frac{1}{2}\,(U + V_{Ar})\,\frac{Z_+^2}{r} + \frac{1}{2}\,(U - V_{Ar})\,\frac{Z_-^2}{r} = -\alpha_D N^D + S^D \end{aligned} \tag{E.2}$$

$$(U \mp V_{Ar})\,\frac{\mathrm{d}L_\pm}{\mathrm{d}r} + (U \mp V_{Ar})\,\frac{L_\pm}{r} + \frac{1}{2}\,(U \mp V_{Ar})\,\frac{L_D}{r} = -\alpha_\pm N_L^\pm + S_L^\pm \tag{E.3}$$

$$\begin{aligned} &U\frac{\mathrm{d}L_D}{\mathrm{d}r} + U\frac{L_D}{r} + V_{Ar}\sqrt{\frac{L_+}{L_-}}\frac{\mathrm{d}L_-}{\mathrm{d}r} - V_{Ar}\sqrt{\frac{L_-}{L_+}}\frac{\mathrm{d}L_+}{\mathrm{d}r} \\ &+ (U + V_{Ar})\,\frac{L_+}{r} + (U - V_{Ar})\,\frac{L_-}{r} = N_L^D + S_L^D \end{aligned} \tag{E.4}$$

The nonlinear terms chosen by Adhikari et al. is the following

$$N^\pm = \frac{Z_\pm^2 Z_\mp}{\lambda_\pm} \tag{E.5}$$

$$N^D = D\left(\frac{Z_+}{\lambda_-} + \frac{Z_-}{\lambda_+}\right) \tag{E.6}$$

$$N_L^\pm = 0 \tag{E.7}$$

$$N_L^D = 0 \tag{E.8}$$

with the Kármán-Taylor parameters chosen as $\alpha_\pm = \beta_\pm = 2$, $\alpha_D = 1$. The source terms were chosen as

$$S^\pm = 2C_{sh}U\frac{Z_\pm^2}{r} + \frac{f_D n_H^\infty U V_A}{n_{sw}^1 \tau_{ion}^1} e^{L_{cav}/r} \tag{E.9}$$

$$S^D = 2C_{sh}U\frac{D}{r} \tag{E.10}$$

$$S_L^\pm = 0 \tag{E.11}$$

$$S_L^D = 0 \tag{E.12}$$

with $C_{sh} = 7.35$. Adhikari et al. defines the proton temperature evolution in steady state as

$$\frac{\mathrm{d}T}{\mathrm{d}t} + U\frac{\mathrm{d}T}{\mathrm{d}r} + (\gamma - 1)\frac{2UT}{r} = \frac{1}{9}\frac{m_p}{k_B}\alpha\left(\frac{Z_+^2 Z_-}{\lambda_+} + \frac{Z_-^2 Z_+}{\lambda_-} + D\left(\frac{Z_-}{\lambda_+} + \frac{Z_+}{\lambda_-}\right)\right) \tag{E.13}$$

where $\gamma = 5/3$ is the adiabatic index, m_p is the proton mass, k_B is the Boltzmann constant and α is chosen to be 1 and controls the heat dissipation from the nonlinear terms.

Below, we have reproduced the plots from Adhikari et al. [1] plotted with data provided by Adhikari et al. [1] where the blue plusses is data from 0.29 AU to 5 AU from the Helios 2 and Ulysses spacecraft, the orange plusses is data from 1 AU to 75 AU taken from the Voyager 2 spacecraft. Figure E.1 shows the energy over radial distance to 100 AU where the top left shows the inward fluctuation energy Z_+^2 in $(km/s)^2$ and the top right shows the outward Z_-^2 in $(km/s)^2$. The bottom left panel shows the normalized energy difference σ_D and the bottom right panel shows the normalized cross helicity σ_c. Figure E.2 shows the correlation lengths in km from 0.29 AU to 100 AU, the top panels show the inward λ_+ and outward λ_- correlation lengths from left to right respectively whereas the bottom panel shows the correlation length for the energy difference λ_D. Figure E.4 shows the proton temperature measured in Kelvin to 100 AU. [1] switches the initial conditions for Z_+^2 and Z_-^2, we have plotted the correct choices for Z_+^2 and Z_+^2 following the data Table 4.1 except, we have set $D_0 = -200$ to prevent D from becoming positive which results in $\lambda_D \to \infty$ as $\lambda_D = \frac{L_D}{D}$. The spike seen in λ_D, Figure 5.3 is due to σ_D approaching 0, but it does not become 0.

E.2 Breech Model

The Breech et al. [13] model is a three equation model built from simplifications of Zhou and Matthaeus [66]. The equations are effectively reduced to three by using only one correlation length $\lambda = \lambda_+ = \lambda_-$ and assuming that the normalized energy difference is constant $\sigma_D \approx 1/3$ giving $D \approx \sigma_D Z^2$. The Breech et al. model is written as

$$U\frac{\mathrm{d}Z^2}{\mathrm{d}r} + \frac{Z^2}{r} + M\sigma_D\frac{Z^2}{r} = N + S \tag{E.14}$$

$$U\frac{\mathrm{d}\sigma_c}{\mathrm{d}r} - M\sigma_D\frac{\sigma_c}{r} = N_C + S_c \tag{E.15}$$

$$U\frac{\mathrm{d}\lambda}{\mathrm{d}r} = N_\lambda + S_\lambda \tag{E.16}$$

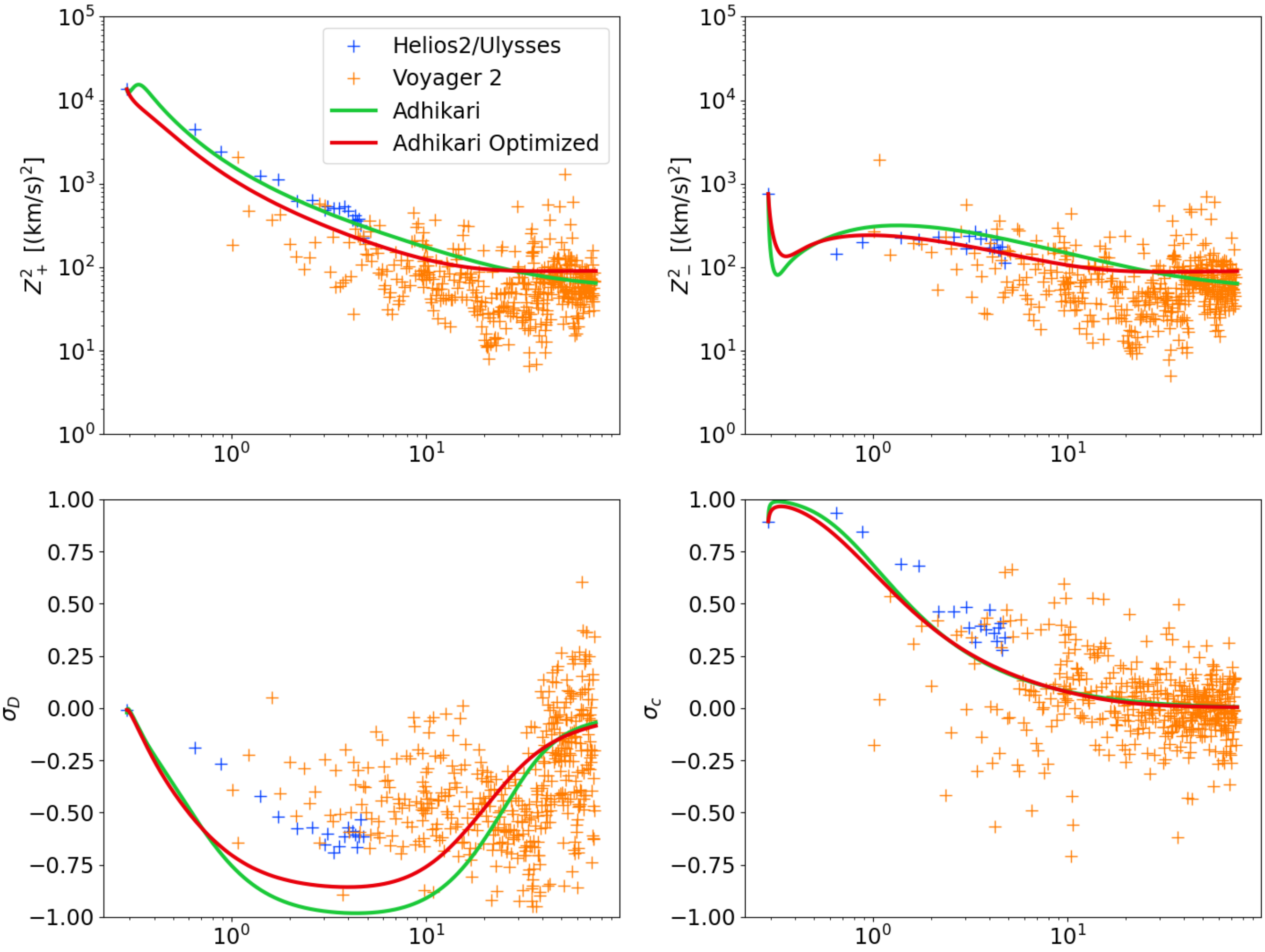

Figure E.1: Reproduced plot from Adhikari et al. [1] showing the backward and forward propagating energies, the normalized energy difference and the normalized cross helicity. The green line is the Adhikari et al. model plotted with data from the Helios 2/Ulysses (blue) and Voyager 2 (orange) spacecraft indicated by the plus markers. The red line is the optimized parameters.

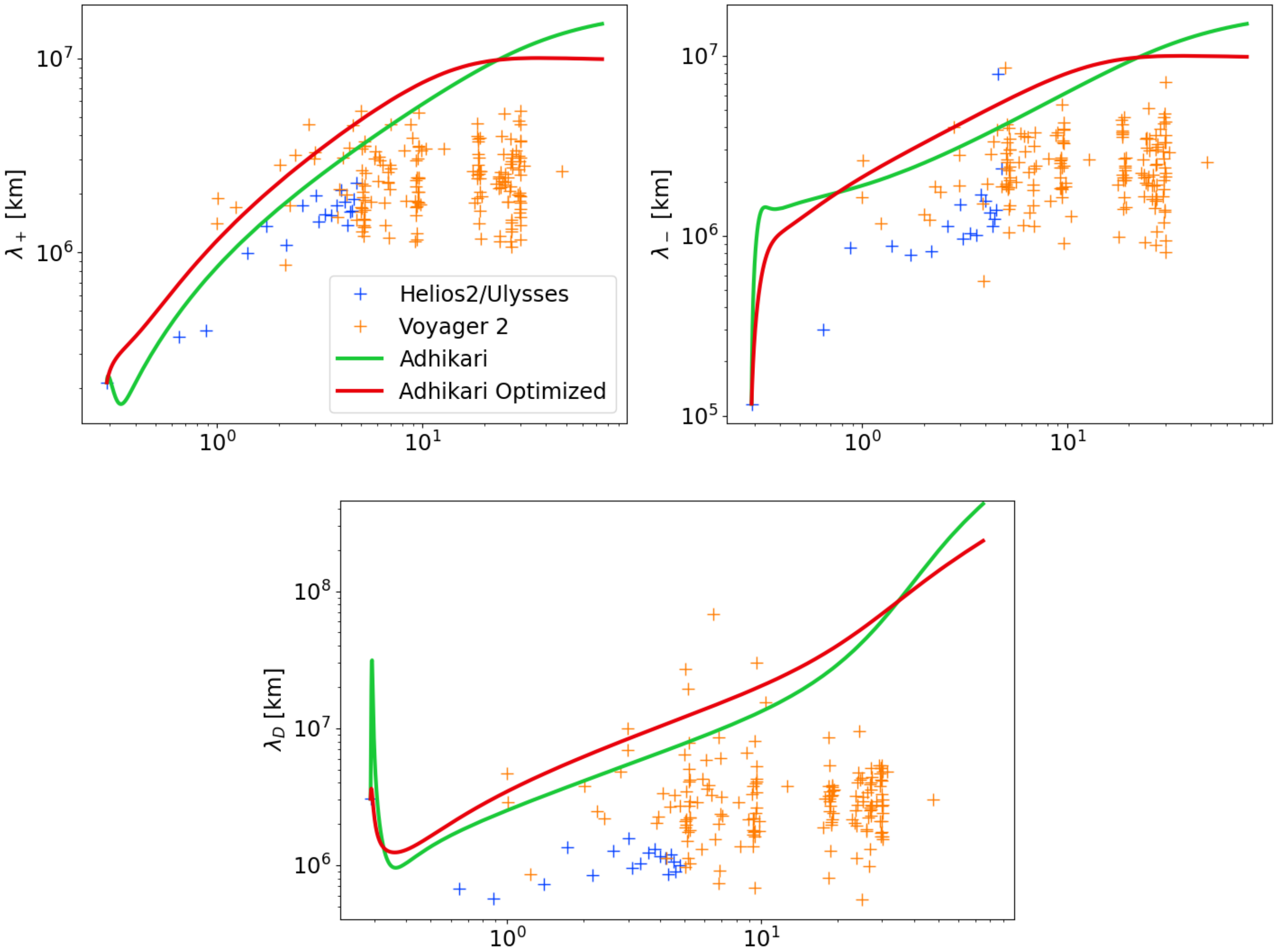

Figure E.2: Reproduced plot from Adhikari et al. [1] showing the correlation length of the backward and forward correlation lengths and the correlation length for the energy difference. The green line is the Adhikari et al. model plotted with data from the Helios 2/Ulysses (blue) and Voyager 2 (orange) spacecraft indicated by the plus markers. The red line is the optimized parameters.

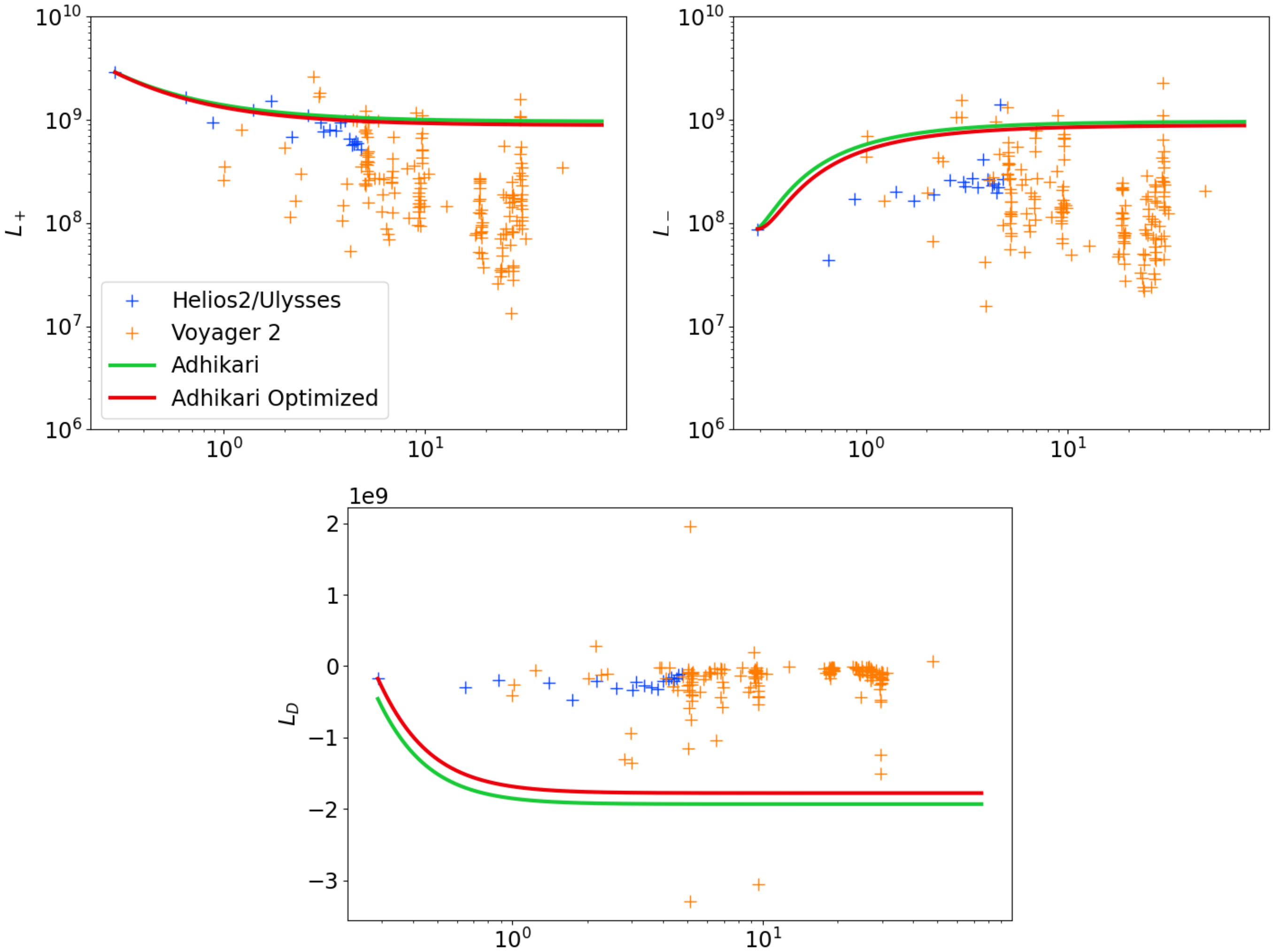

Figure E.3: Reproduced plot from Adhikari et al. [1] showing the correlation integrals of the backward and forward correlation lengths and the correlation length for the energy difference. The green line is the Adhikari et al. model plotted with data from the Helios 2/Ulysses (blue) and Voyager 2 (orange) spacecraft indicated by the plus markers. The red line is the optimized parameters.

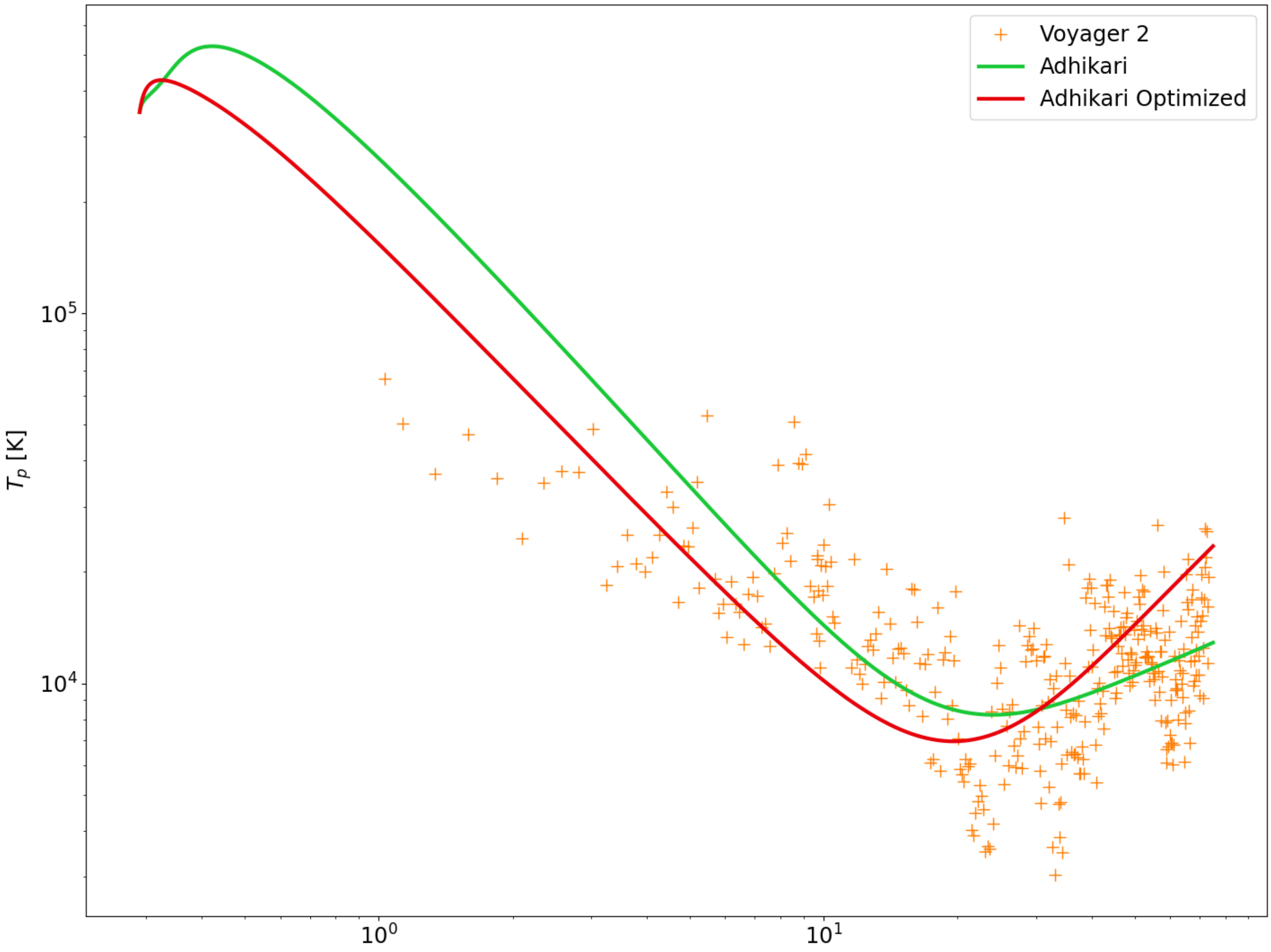

Figure E.4: Reproduced plot from Adhikari et al. [1] showing the proton temperature. The green line is the Adhikari et al. model plotted with data from the Voyager 2 (orange) spacecraft indicated by the plus markers. The red line is the optimized parameters.

with $Z^2 = \frac{Z_+^2+Z_-^2}{2}$ and $\sigma_c = \frac{Z_+^2-Z_-^2}{Z_+^2+Z_-^2}$. M is the mixing term and is also assumed to be constant. The nonlinear terms were chosen as

$$N = \alpha f^+ \frac{Z^3}{\lambda} \tag{E.17}$$

$$N_C = \alpha f' \frac{Z}{\lambda} \tag{E.18}$$

$$N_\lambda = \beta f^+ Z \tag{E.19}$$

where

$$f^\pm(\sigma_c) = \frac{\sqrt{1-\sigma_c}}{2}\left(\sqrt{1+\sigma_c} \pm \sqrt{1-\sigma_c}\right) \tag{E.20}$$

and $f' = \sigma_c f^+ - f^-$. The source terms used were

$$S = C_{sh}\frac{UZ^2}{r} + U\dot{E}_{PI} \tag{E.21}$$

$$S_c = -C_{sh}\frac{U\sigma_c}{r} - U\dot{E}_{PI}\frac{\sigma_c}{Z^2} \tag{E.22}$$

$$S_\lambda = -\frac{\beta}{\alpha}U\dot{E}_{PI}\frac{\lambda}{Z^2} \tag{E.23}$$

where $\dot{E}_{PI}$ is the rate at which the energy is added proportional to the rate of creation of new protons, the pickup ion driving

$$\dot{E}_{PI} = \frac{f_D V_A n_H}{n_{sw}\tau_{ion}} e^{-L_{cav}/r} \tag{E.24}$$

The temperature equation introduced by Breech et al. is an adiabatic cooling temperature equation modified with an increase proportional to the nonlinear decay of the energy

$$\frac{\mathrm{d}T}{\mathrm{d}r} = -\frac{4}{3}\frac{T}{r} + \frac{1}{3}\frac{m_p}{k_B}\frac{\alpha}{U}f^+\frac{Z^3}{\lambda} \tag{E.25}$$

where m_p is the proton mass, k_B is the Boltzmann constant.

We have plotted the above equations using the initial conditions from Table E.1 as well as $\alpha = 0.4, \beta = 0.2, C_{sh} = 1, \sigma_D = -1/3, M = 1/2$. Figure E.5 plots the forward Z_-^2 and backward Z_+^2 fluctuation energy along with the constant normalized energy difference σ_D and the normalized cross helicity. Figure E.6 shows the single correlation length plotted against radial distance to 100 AU and Figure E.7 shows the proton temperature.

Parameters	Initial Values
Z_0^2	6757.5 [(km/s)^2]
$\sigma_{C,0}$	-0.894
λ_0	0.0011045 [AU]
T_0	3.5×10^5 [K]
R_0	0.29 [AU]

Table E.1: Solar wind initial conditions at 0.29 AU based off Helios 2 data

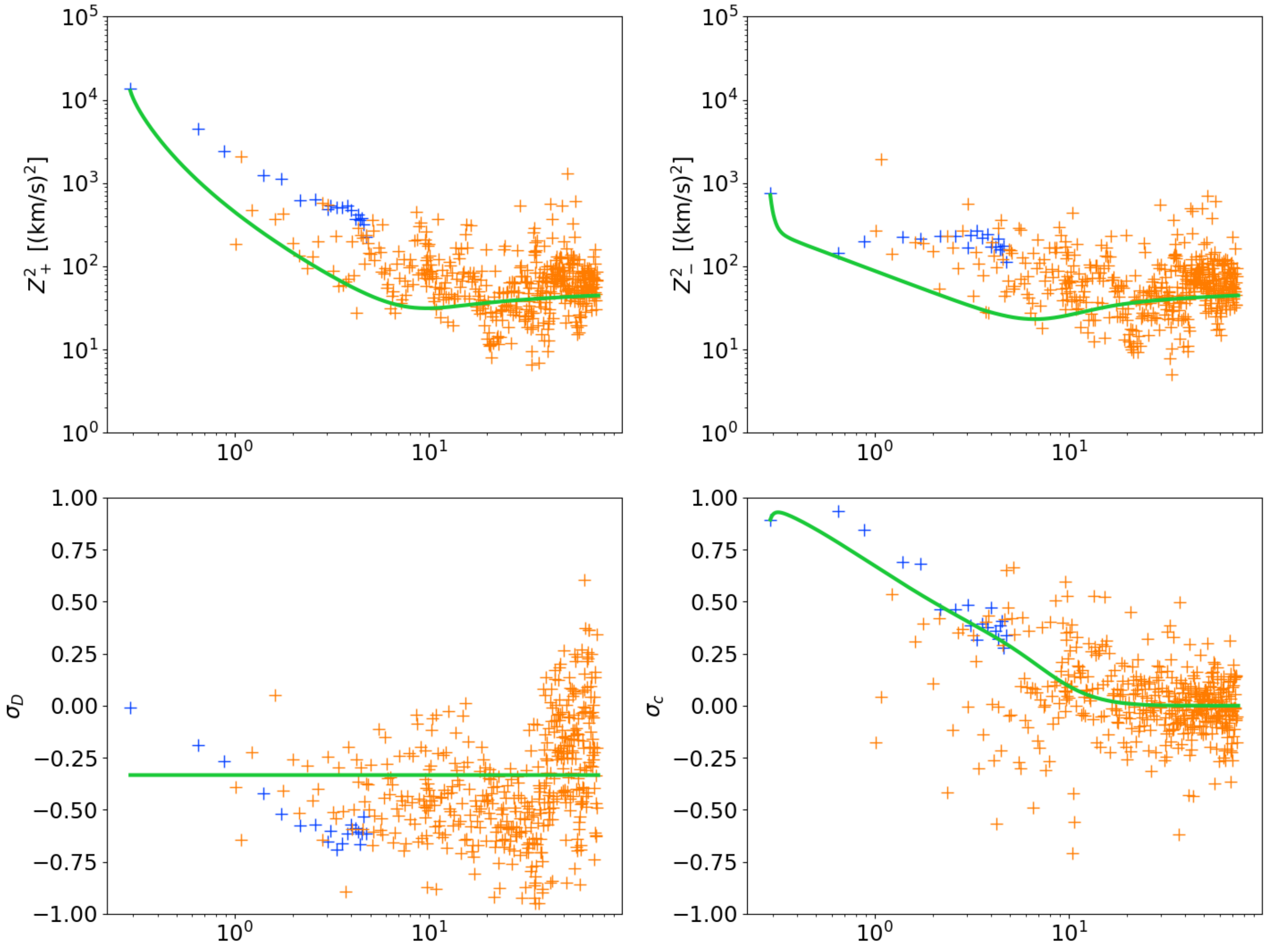

Figure E.5: Energies of the Breech et al. [13] model (green) plotted against radial distance from 0.29 to 100 AU along with data from the Helios 2/Ulysses (blue) and Voyager 2 (orange) spacecraft indicated by the plus markers.

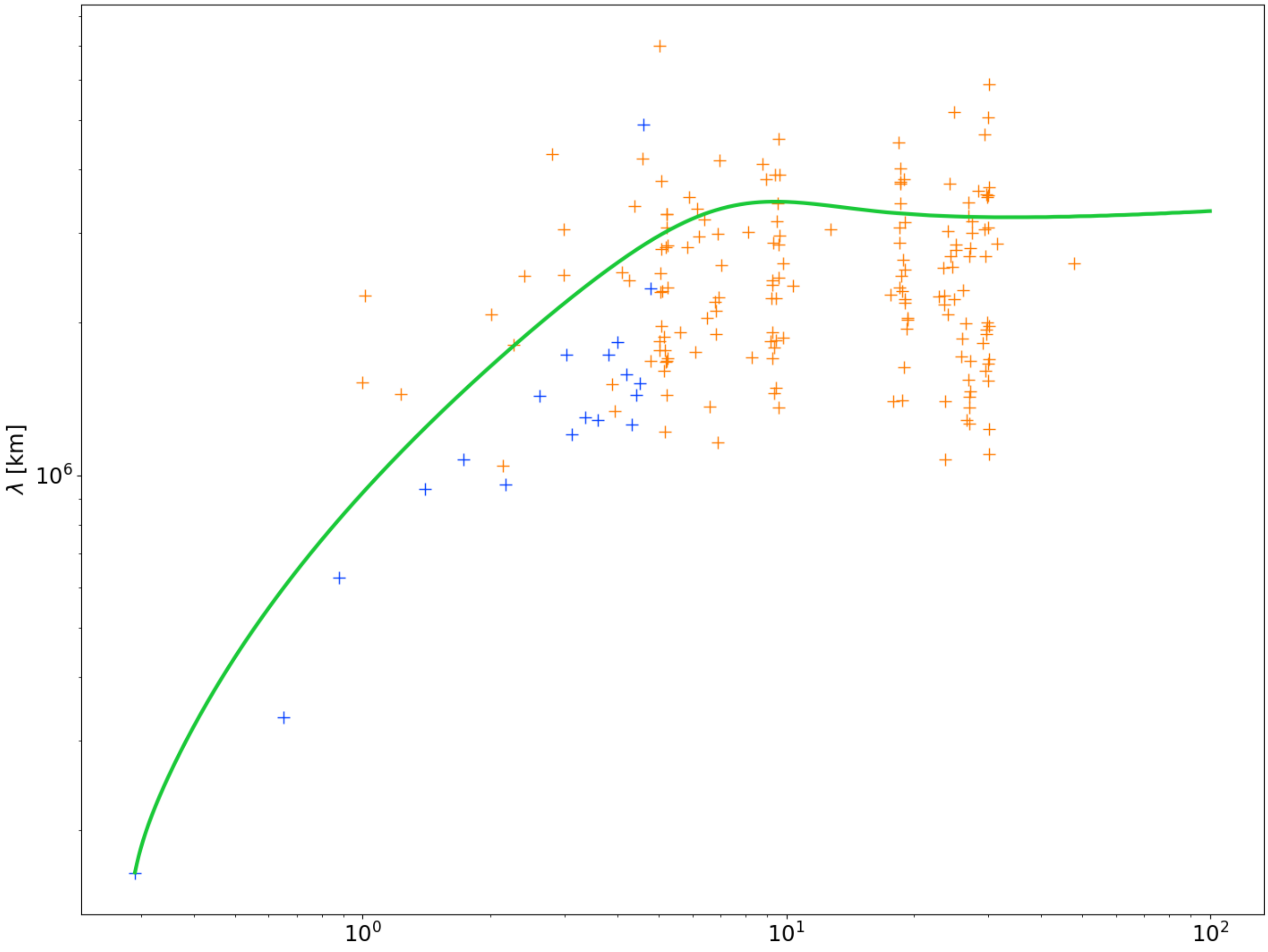

Figure E.6: Correlation length of the Breech et al. [13] model (green) plotted against radial distance from 0.29 to 100 AU along with data from the Helios 2/Ulysses (blue) and Voyager 2 (orange) spacecraft indicated by the plus markers.

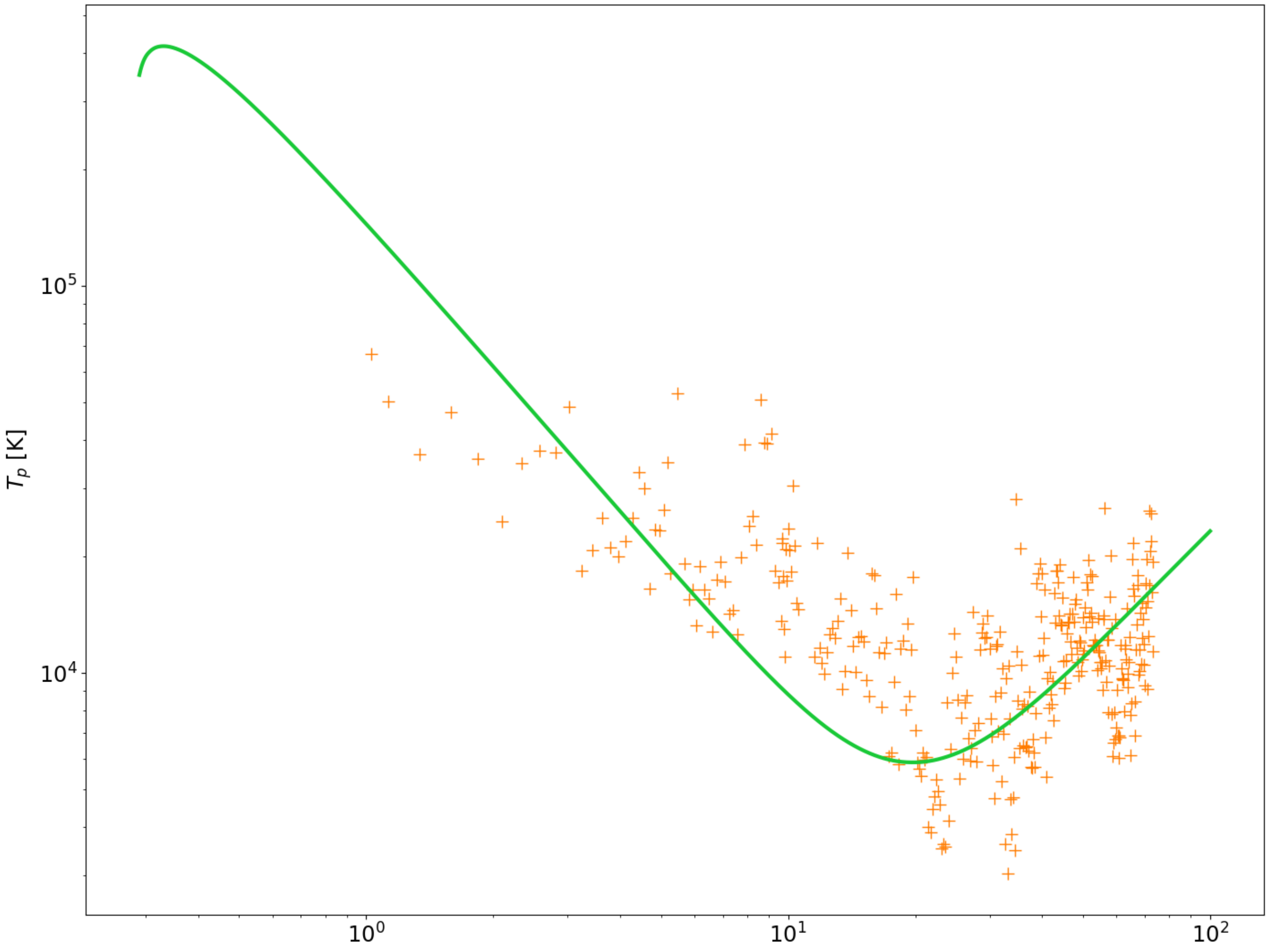

Figure E.7: Temperature of the Breech et al. [13] model (green) plotted against radial distance from 0.29 to 100 AU along with data from the Helios 2/Ulysses (blue) and Voyager 2 (orange) spacecraft indicated by the plus markers.